UNIVERSIDAD COMPLUTENSE DE MADRID

FACULTAD DE CIENCIAS FÍSICAS

DEPARTAMENTO DE FÍSICA ATÓMICA, MOLECULAR Y NUCLEAR

TESIS DOCTORAL

Impact of the air-fluorescence yield on the energy scale of the Pierre Auger Observatory

Efecto del rendimiento de fluorescencia atmosférica en la escala de energía del Observatorio Pierre Auger

MEMORIA PARA OPTAR AL GRADO DE DOCTOR
PRESENTADA POR

José Ramón Vázquez Peñas

Directores

Fernando Arqueros Martínez

Jaime Rosado Vélez

Madrid, 2015

Universidad Complutense de Madrid

Facultad de Ciencias Físicas

Impact of the Air-Fluorescence Yield on the energy scale of the Pierre Auger Observatory

Efecto del rendimiento de fluorescencia atmosférica en la escala de energía del Observatorio Pierre Auger.

Tesis presentada por José Ramón Vázquez Peñas
para obtener el grado de Doctor en Física

Directores:
Fernando Arqueros Martínez
Jaime Rosado Vélez

Departamento de Física Atómica, Molecular y Nuclear

Agradecimientos

Aunque sea mi nombre el que aparezca en la portada, esta tesis no habría podido culminarse sin una gran cantidad de personas que me han ayudado en el camino. De no ser por esa gente que, fuera y dentro de los muros de la facultad, han conseguido empujarme hasta terminar y no han dejado que me rinda. Si ellos no hubiesen confiado en mí, hoy no estaría escribiendo estos agradecimientos.

Gracias por supuesto al Profesor Fernando Arqueros, por apostar por mí desde una lejana clase de quinto de carrera hasta hoy. Gracias a Jaime Rosado por sus ideas y su impulso, sin él esta tesis no habría sido igual. Gracias a María, por ayudarme en mis inicios, sin ella nunca habría podido convertirme en doctor. Gracias a Diego, por conseguir que siempre diera el máximo. Gracias a Nacho, por tantas noches compartidas en el centro de control de Auger, en la a la vez tan lejana y cercana Malargüe. Muchas gracias a Ernesto, siempre a mi lado incluso cuando cambió nuestro despacho por otro en Argentina. Y gracias a Hernán Wahlberg, al que considero también parte de nuestro grupo en Madrid, que además de apoyarme me hizo conocer los sitios mas auténticos de Buenos Aires.

Quiero dar las gracias al grupo Auger de Roma Tor Vergata, por haberme hecho salir de mi zona de confort y hacerme sentir que podá desarrollar mi carrera lejos del entorno protector de Madrid. Muchas gracias a Valerio Verzi, por su estímulo constante y por haberme convertido en un físico experimental y no un simple analizador de datos. A Gonzalo Rodríguez, por tantas charlas interesantes en el despacho de Tor Vergata. Gracias a Claudio Di Giulio y Gaetano Salina, por hacerme sentir siempre parte del grupo de Roma.

Gracias de todo corazón a Beatriz Seoane, la primera persona que conocí en la facultad y la que más me he ayudado a conseguir mis metas. Estés donde estés siempre te siento a mi lado.

Gracias a mis “nosomosamigos” por estar ahí desde el principio y porque sé que van a seguir hasta el final. A Blanca, desde que tengo memoria ha sido mi amiga. A Diego, por todas las tardes y todas las noches en Madrid. A Fer, por contagiarme siempre de su locura maravillosa. A Erik, Mike y Dani que, como yo, saben lo que es sufrir por un doctorado.

A Juanko y Galindo por las noches intentando cambiar el mundo desde la barra de un bar. A Tomás y Fran, dos personas a las que envidio por su capacidad para conseguir siempre lo que se proponen. A Darío, por sus mil y un intentos de hacerme comprender que las cosas no son tan graves como parecen. A Julia y Raquel, siempre dispuestas a que todo el mundo se lo pase bien. A Jaime, por hacerme ver que las personas a veces sí pueden cumplir sus sueños. A Gonzalo, por su futuro como chef. A Abel y Juanillo, que me han demostrado lo lejos que puedes llegar cuando te gusta tu trabajo.

Gracias al resto de doctorandos de la facultad de física, por estos años increíbles. A todo el DomiLab, internos y afiliados. Vivy, Marco, Édgar, Domin, Javi, Punki Ricardo y tantos otros. Gracias por las risas. A Mariano, que fue sucesivamente compañero de instituto, de carrera y de doctorado. A los compañeros de la facultad y del peor equipo de baloncesto de la historia: Guille, Javi, Alvarito... A Edu, otro búho que estudiaba mejor de madrugada. Gracias a todos por hacerme sentir menos solo en esto.

Quiero agradecer también a los que comparten conmigo la adicción por juntar letras. Ahora que he terminado este libro espero volver a retomar todos los asuntos pendientes. Sin Santi, Edu, Fidel, Alfredo, Julián y Alemo no habría podido llegar a donde he llegado en mi otra "profesión".

Y por último, aunque esta tesis es para ellos, muchas gracias a mi familia. A mis padres, porque sin ellos no sería lo que soy (y no sería en general). A mi hermana Ángela, también mi compañera de piso, que es la persona que más ha tenido que aguantarme mi constante mal humor. Sé que vas a cambiar las cosas. Quiero recordar también a mis abuelos Segundo y Josefa, que no han podido ver esta tesis terminada pero que sé que estarían muy orgullosos de lo que he conseguido. Gracias, en general, a todo el clan de los Vázquez Peñas por su apoyo.

Gracias a los que nombro porque no quiero que estos agradecimientos sean eternos. Gracias en definitiva a todo aquel que creyó alguna vez en mí. Aunque solo fuera un poquito y rápido se le pasara.

Contents

List of Figures

List of Tables

Chapter 1

Introduction

More than one hundred years have passed since the discovery of the cosmic rays. During this century, cosmic rays have been proved to be a very fruitful field of research, both for high energy physics and astrophysics. Prior to the construction of the first particle accelerators, cosmic rays were the only source of high energy particles and the positron and pion were first discovered using cosmic rays. They have also provided valuable information in astrophysics phenomena. In spite of this long and rich history, there are still open questions regarding the origin, acceleration mechanism and mass composition of cosmic rays, specially for the ones with the most extreme energies, above 10^{18} eV, the so-called Ultra-High Energy Cosmic Rays (UHECRs). These particles are believed to be of extra-galactic origin, and their flux is so low that approximately one cosmic ray of these macroscopic energies reaches the atmosphere of the Earth per square kilometer and year. This extremely low flux makes necessary the construction of very extense detectors in order to collect a sample big enough to study the many interrogants still open about their nature.

When one of these UHECRs impinges the atmosphere it interacts with an atmospheric nucleus, producing secondary particles and initiating a cascade of interactions that propagate along the atmosphere until they decay or reach the ground. The result of this process is what is known as an Extensive Air Shower (EAS) and its features are related to the properties of the incident UHECR.

The Pierre Auger Observatory, with a total area of 3000 km^2 is currently the largest cosmic ray detector made by mankind and it has been taking data since 2004. Located in Malargüe (Argentina) it covers the southern hemisphere sky using a hybrid technique. The Surface Detector (SD), composed of around 1600 water Cherenkov tanks, samples the particles of the EAS that arrive to ground level. The Fluorescence Detector (FD) registers the fluorescence light produced by the atmospheric nitrogen molecules that are excited by

the cascade particles.

The SD is calibrated using the calorimetric measurements provided by the FD. A correct determination of the energy deposition via the fluorescence light is of the uttermost importance, as all the analyses performed at the Pierre Auger Observatory rely on the energy estimation provided by the FD. The fluorescence yield (FY) is the parameter that gives the conversion factor between the energy deposition and the number of fluorescence photons produced in the atmosphere. An international combined effort in the past few years has improved the knowledge on the absolute value and the dependences of this parameter, which has been the main source of uncertainty in the primary energy determination of the Pierre Auger Observatory. It is believed that the FY selection is also one of the main source of discrepancies between the UHECR spectrum measured by the Pierre Auger Observatory and the one measured by Telescope Array (located in Utah, USA), the other UHECRs observatory operated presently.

In this work the impact of the FY data used for shower reconstruction has been studied, in particular its effect on the primary energy and the shower maximum depth. To this end, an analytical procedure has been developed and real data of the Auger Observatory has been analyzed using dedicated algorithms.

This thesis is organized as follows. In chapter 2 a brief review of the history and current knowledge of cosmic rays will be presented, with a focus on UHECRs and the questions that are still open in the field. Chapter 3 will be devoted to a description of the Pierre Auger Observatory, the facility that has provided most of the data used for this thesis. The SD and FD are reviewed throughfully, along with a brief summary of the reconstruction techniques used for each detector. In chapter 4 the physical processes related to the fluorescence emission are discussed, the available measurements of the air-fluorescence yield are presented and methods for evaluating its impact in the shower reconstruction are described. In chapter 5 the impact of the new measurements of the temperature and humidity dependences of FY will be evaluated. In chapter 6 the effect of this study on the energy scale of the Pierre Auger Collaboration will be presented, along with the new analyses that have made possible the reduction of the systematic uncertainty in the energy determination. In chapter 7 a comparison between Auger and Telescope Array will be shown. Finally, the conclusions of the thesis will be presented in chapter 8. At the end of the document (Appendix A) there is a description of the module developed for the analysis of this thesis that is now part of the $\overline{\text{Off}}\underline{\text{line}}$ framework, the official software of the Pierre Auger Collaboration.

Chapter 2

Cosmic Rays

At the beginning of the 20^{th} century Theodor Wulf designed and built an electrometer to detect the air ionazition due to energetic charged particles from radioactive sustances. It was well known that even in the absence of nearby radioactive sources the electrometers detected a residual background signal. He predicted that this ionization came from natural radiation sources on the ground and then, if he moved far enough from the ground, he would detect less radiation. To test this hypothesis, in 1910 he compared the ionization at the bottom and the top of the Eiffel Tower [33]. He found out that the rate of ionization did not decrease with altitude at the expected rate. In 1911, Domenico Pacini [34] made measurements at different altitudes, including underwater, and concluded that an important part of the radiation was due to other sources than the radioactivity of the Earth. Their results, however, were not widely accepted. Radioactivity had been discovered in 1896 and the general consensus was that the measurements were compatible with the terrestrial origin of the radiation and discrepancies were due to residual radioactive components in the electrometers or an incomplete knowledge of the absorption properties of the air.

In 1912 Victor Hess performed a series of measurements with altitude by personally taking more precise electrometers aloft in a balloon. He systematically measured the radiation at altitudes up to 5300 m [35]. He found an increment of ionization radiation with height and inferred that radiation were mostly coming from outer space. He repeated the measurements during nights and even during a solar eclipse, finding no substantial difference and concluding that the main source was other than the Sun. Werner Kolhörster confirmed these results in 1913-1914 [36] flying up to 9 km. Hess received the 1936 Nobel prize for this discovery.

In 1920 Robert Millikan coined the term "cosmic rays" to name this radiation as he believed that the primary particles were gamma rays, the most penetrating radiation known

at the moment. He proposed that these gamma rays were produced in interstellar space as by-products of the fusion of hydrogen atoms into the heavier elements, and that secondary electrons were produced in the atmosphere by Compton scattering of gamma rays. A heated debate with Arthur Compton emerged, as he thought that cosmic rays were high energy charged particles. Compton was proved right in 1927, when Jacob Clay [37] observed a variation of cosmic ray intensity with latitude, which indicated that the primary cosmic rays were deflected by the geomagnetic field and must therefore be charged particles, not photons. Thomas H. Johnson [38], Luis Álvarez and Arthur Compton himself [39] and Bruno Rossi [40] confirmed these results and also proved that most primaries were positively charged. Using balloons at high altitudes, Marcel Schein *et al.* [41] showed that primary particles with positive charge were atomic nuclei moving close to the speed of light. The relative abundance of nuclei up to Z $\sim$ 40 was determined, finding hydrogen and helium to be the most frequent primaries, and elements more massive than iron to be very rare. The term cosmic rays remained to define these charged nuclei of extraterrestrial origin.

This significant discovery initiated a close and fruitful connection between astronomy and particle physics since cosmic rays provided particle physicists with high energetic particles before the advent of particle accelerators. The observation of cosmic rays in cloud chambers led to the discovery of yet unknown particles where the positron and the muon were the first of them. In 1932, Anderson observed in his cloud chamber the antiparticle of the electron as a result of cosmic ray interactions [42], the first evidence of antimatter, whose existence had been recently postulated by Dirac [43]. Anderson was awarded along Hess with the Nobel prize in 1936. Shortly after this landmark, Neddermeyer and Anderson [44] and Street and Stevenson [45] discovered the muon while looking for evidences of a particle predicted by Yukawa [46] and associated with the strong nuclear force that finally turned out to be the pion, discovered in 1947 [47].

Rossi also observed in 1934 that the rate of coincidences between detectors distributed on an horizontal plane were higher than expected [48]. In 1938 Pierre Auger [49] and Kolhöster *et al.* [50] confirmed these results. They interpreted the measurements as the result of a shower of secondary particles caused by the collision of high-energy primary particles with air nuclei discovering the so-called Extensive Air Showers (EASs). The confirmation of the phenomenon suspected by Rossi was possible using electronics with microsecond time resolution. Based on the recently developed electromagnetic cascade theory, Auger deduced that some detected EASs were initiated by cosmic rays with energies around 10^{15} eV.

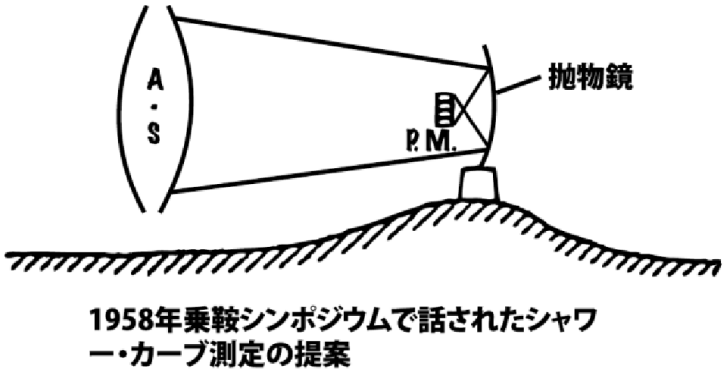

Figure 2.1: Sketch for the proposal of the first fluorescence detector. The text translates as "*Parabolic mirror*" and "*A proporsal for the curve measurement in Norikura symposium, 1958*". Reproduction from Proceedings of Norikura Meeting in Summer 1957 taken from [1]

The replacement of Geiger counters by faster detectors like plastic scintillators, provided information about shower direction and made possible the construction of larger ground arrays like the pioneering experiments of Volcano Ranch [51], SUGAR [52] or Haverah Park [53]. The large area of detection made possible the study of cosmic rays with energies around 10^{17} eV, where the low flux made impossible a direct detection using balloons. In 1963 Linsley [51] reported the first event with an energy of 10^{20} eV.

The fluorescence technique has been succesfully employed for the last 30 years, although the idea of using the atmospheric excitations of nitrogen to detect UHECRs has been explored since the 1940s, during the Manhattan Project nuclear bomb tests, when the so-called "Teller light" was first detected associated to an atomic explosion. Shower particles deposit their energy exciting N_2 molecules that emit fluorescence light when they relax to their ground state. Fig. 2.1 shows a concept sketch of a PMT camera viewing the fluorescence light induced by an EAS collected with mirror. This design is very similar to the fluorescence telescopes used today by the Pierre Auger Observatory and Telescope Array. In 1962, Suga [54] and Chudakov [55] suggested the possibility of using the Earth's atmosphere as a giant calorimeter in order to obtain information about the incident cosmic rays. The Cornell Wide Angle system, proposed and built by K. Greisen and colleagues at the eponimous university during the 1960s was the pilot experiment to test the feasibilty of the technique [56]. It consisted of three detectors set up in the vicinity of the university campus, each station comprised of five photomultiplier tubes. The system was operational for around 1000 h. Light flashes were recorded, but they could not be attributed to air showers beyond doubt. In 1969 the INS-Tokyo experiment recorded clear fluorescence light

signals from an extensive air shower with an energy exceeding $5 \cdot 10^{19}$ eV [57].

In 1976 fluorescence light was detected in coincidence with an air shower registered by the surface array of Volcano Ranch. The prototypes employed led eventually to the development of the Fly's Eye detector, the first independent fluorescence detector. The Fly's Eye Observatory [58] consisted of two stations separated 3.3 km. Each one was comprised of front aluminized spherical mirrors to collect the light, with Winston light collectors and photomultipliers mounted in the focal plane of the mirror in hexagonal groups as sensing units or "eyes". The projection of each hexagonal "eye" onto the celestial sphere resembled the compound eye of an insect, hence the name of Fly's Eye. Whenever the first telescope recorded an event, it sent an infrared pulse flash of light towards the second telescope, which recorded pulse integrals and arrival times. The shower track geometry was reconstructed either from hit patterns and timing information by a single Fly's Eye detector or by steroscopic viewing and relative timing by both Fly's Eyes. The experiment operated succesfully from 1981 to 1993 and for the first time applied the fluorescence technique to explore the properties of UHECRs on a large scale.

The High Resolution Fly's Eye (HiRes), located in Utah (USA), was the succesor of the Fly's Eye experiment [59] and operated between 1997 and 2007. The last generation of UHECR detectors that operate today, like the Pierre Auger Observatory and Telescope Array employ a hybrid design that combine both the surface and fluorescence techniques to obtain larger statistics and improved reconstruction of the air shower produced by the incident cosmic ray.

After more than a century of cosmic ray physics, the field still has some unknowns, specially concerning the UHECRs. As mentioned before, the incoming rate of these particles is strongly dependent on energy, and the low flux at the most extreme energies makes difficult to answer questions like:

- What is the origin of the most relevant features of the cosmic-ray energy spectrum?
- Is there an end of the energy spectrum? At which energy does it occur?
- What are the sources of UHECRs? Is the flux at these energies isotropic or is it possible to link the cosmic rays with their sources, leading to a potential cosmic ray astronomy? What are the acceleration mechanisms that make possible to achieve energies of 10^{20} eV?
- What is the mass composition of cosmic rays as a function of energy? Is it predominantly light-like or are there heavy elements? Is it pure or is made of a mixture of species?

Measuring the cosmic ray flux, composition and arrival directions at the highest energies is fundamental to separate the different scenarios of origin and propagation of cosmic rays. In this chapter a review of the state-of-the-art knowledge in the field will be made, including possible answers to the aforementioned questions, with a focus on the most energetic cosmic rays in section 2.3.

In section 2.1 a brief review of the physics of Extensive Air Showers will be made. As a direct measurement of cosmic rays of this extreme energies is not feasible, shower observables must be used to infer the energy, composition and origin of UHECRs.

2.1 Ultra High Energy Extensive Air Showers

The extremely low flux of UHECRs makes almost impossible the direct detection of primary cosmic rays, either using balloons or space-based detectors. Only ground detectors have the extensive collection area needed to obtain enough statistics at these extreme energies. However, as discovered by Pierre Auger [49], when a primary cosmic ray impinges the atmosphere it starts a series of interactions that induces an Extensive Air Shower (EAS). The goal of detectors like the Pierre Auger Observatory is to characterize the properties of these showers and obtain through them the primary energy, particle type and arrival direction of the primary cosmic ray.

When a high energy cosmic ray reaches the atmosphere it suffers an hadronic interaction with an atmospheric nucleus with a mean free path of about tens of gcm^{-2}. From this primary interaction a large number of secondary particles, mainly pions, are produced. In turn, some of these hadrons, mainly charged pions, can interact again giving rise to the *hadronic component* of the shower. The neutral pions decay into photons before interacting, due to their short lifetime. The photons convert into $\mathrm{e}^{+}\mathrm{e}^{-}$ pairs which radiate through bremsstrahlung process. The so-called *electromagnetic component* of the shower is composed of these photons, electrons and positrons. The generation of EM particles continues until their energy drops below a certain threshold called the critical energy E_{C} [60]. Below this limit the dominant energy losses are due to ionization rather than by bremsstrahlung and the Compton scattering dominates the photon interactions instead of the pair production. When the average energy of particles equals E_{C} the showers reaches the maximum number of particles.

If each hadronic interaction produces two charged pions and a neutral one, about a 1/3 of the energy is transferred to the EM component in each generation. Equivalent to the EM processes, the multiplication in the hadronic component occurs until the energy of charged pions drops below a certain critical energy. Below this limit pions decay yielding

muons. It is demonstrated that the number of steps needed to reach this energy limit is enough to transfer most of the primary particle energy to the EM component [61].

A third component of the shower, called the *muonic component*, is generated by the decay of the charged pions previously mentioned. A significant part of the energy of the shower is carried by these muons and the neutrinos (that are also produced in the pion decay) while crossing the atmosphere almost without interactions. This fraction of the total energy is called the *invisible energy*, as it cannot be recorded by current cosmic ray telescopes.

However, as most of the energy of the shower is carried by the electromagnetic component, it is possible to develop telescopes that record the fluorescence light produced by atmospheric molecules excited by this component. The energy deposited by these particles in the atmosphere accounts for around 90% of the energy of the primary UHECR [61]

2.1.1 Longitudinal development

The longitudinal development represents the number of shower particles as a function of atmospheric slant depth X, that is, the total mass thickness of air traversed by the shower. The atmospheric slant depth at a given height z, measured from the ground level, depends on the shower geometry and on the atmospheric density $\rho(z)$:

$$X(z) = \int_z^\infty \rho(z') \frac{\mathrm{d}z'}{\cos(\theta)} \tag{2.1}$$

where θ is the zenith angle of the shower.

The longitudinal development of a shower was parameterized by Gaisser and Hillas [62], and is thus called the Gaisser-Hillas function:

$$N(X) = N_{\max} \left(\frac{X - X_0}{X_{\max} - X_0} \right)^{X_{\max} - X_0/\lambda} \cdot \exp\left(\frac{\mathrm{X_{max}} - \mathrm{X}}{\lambda} \right) \tag{2.2}$$

where $N(X)$ is the number of charged particles of the shower, mainly electrons, at a given atmospheric depth X, $X_{\max}$ is the slant depth at which the number of charged particles reaches a maximum, $N_{\max}$ and finally, X_0 and λ are shape parameters without physical meaning.

In Fig. 2.2 different longitudinal profiles simulated with CORSIKA [63] are shown for different incident primaries and different hadronic interaction models. It can be observed that for a vertical shower induced by a nuclei of 10^{19} eV the shower maximum X_{max} is around 700 gcm^{-2}. This value is almost at the level of the ground, marked in Fig. 2.2 as

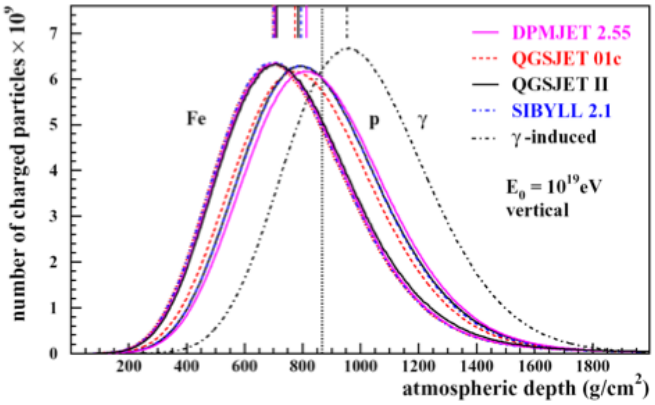

Figure 2.2: Simulated longitudinal profiles for proton, iron and photon primaries with an initial energy of 10^{19} eV and arriving at a zenith angle of $\theta = 0^{\circ}$. The dashed line marks the ground level. Figure taken from [2]

a dashed line. This means that a proton-initiated shower of this energy will be in a stage of maximum development when it reaches ground.

2.1.2 Lateral development

As a cosmic ray shower develops in the atmosphere the particles spread out around the shower axis due to combined effect of the Coulomb scattering and the transverse momentum in the succesive interactions and decays. The most energetic particles are collimated along the shower axis constituting the core of the shower. However, low energy photons and electrons, as well as muons, extend far away from the core forming a halo of particles that can be detected up to few kilometers from the axis when the shower finally strikes the ground.

The particle distribution is symmetric around the shower axis and its density falls off with the distance to the core on a scale determined by the Moliere radius, r_M [64]. The Moliere radius decreases with increasing density of the medium and, in the case of the Pierre Auger Observatory, it is about 100 meters at ground level [65]. On average, 90% of the total energy is contained in a cylinder with radius r_M around the shower axis.

The lateral distribution of shower particles as a function of the distance to the shower axis r can be approximated by the NKG function due to Nishimura, Kamata and Greisen [66, 67]:

$$\rho(r) \propto \left(\frac{r}{r_M}\right)^{s-2} \cdot \left(1 + \frac{r}{r_M}\right)^{s-4.5} \tag{2.3}$$

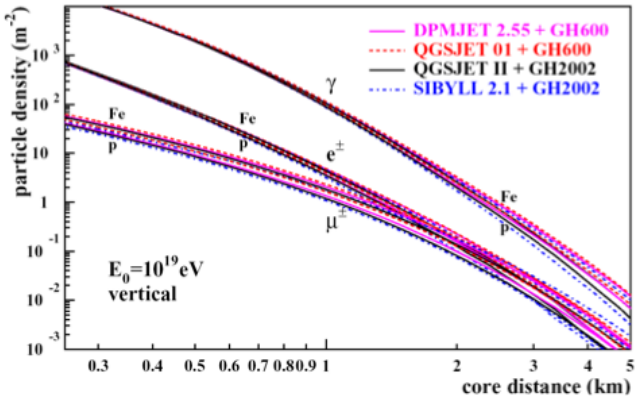

Figure 2.3: Simulations of the lateral distribution of shower particles (photons, electrons and muons) for proton and iron induced showers as predicted by different hadronic models. Figure taken from [2]

where s is the so-called *shower age* defined as:

$$s = \frac{3X}{X + 2X_{\max}} \tag{2.4}$$

Eq. (2.3) describes the radial distribution of shower particles in a plane located at given depth in the atmosphere. The lateral distribution at ground level for some simulated showers induced by protons and iron nuclei is shown in Fig. 2.3. Only the main components, that is, photons, electrons and muons are considered.

This density distribution is usually sampled using an array of particle detectors spread out on the ground. The particular features of the measured signal will depend on the specific characteristics of the ground detector employed.

2.2 Cosmic rays below the ankle

All the solar system, including the Earth, is exposed to a constant flux of cosmic radiation, with energies that extends 13 decades from 1 GeV to about 100 EeV (10^{20} eV. 1 EeV = 10^{18} eV). This flux, J, as a function of energy, E, is called the spectrum and follows a power law ($J \propto e^{-\gamma}$) without any further structure. The spectral index, γ, is almost constant above the GeV, with $\gamma \simeq 2.7$ and spans 34 decades in flux.

The total spectrum (Fig. 2.4) can be divided, attending to the cosmic ray origin, in three main zones. Solar cosmic rays are the least energetic ones, up to 1 GeV. The sources capable of accelerate nuclei over these energies are outside our solar system, but still in

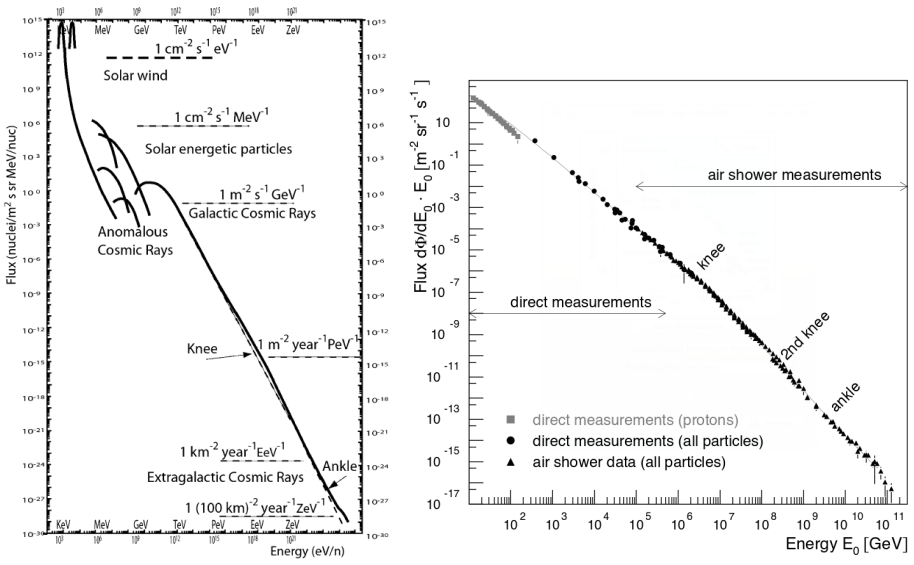

(a) (b)

Figure 2.4: Left: All cosmic ray spectrum showing the three main regions attending to sources: solar, galactic and extragalactic. The approximate position of the knee and the ankle are shown. Figure taken from [3]. Right: Experimental measurements of the cosmic ray spectrum, showing the type of detector. Figure taken from [4]

the vicinity of our galaxy. In this region a steepening of the flux curve, where the spectral index changes to $\gamma \simeq 3.1$, occurs at around $3.5 \cdot 10^{15}$ eV. This feature is called the *knee*. Around $4 \cdot 10^{18}$ the spectrum presents a new change of the slope called the *ankle*, where the flux reflattens again. Features of cosmic rays above this energy will be reviewed in section 2.3.

2.2.1 Solar cosmic rays

Solar cosmic rays, originate in violent events, like solar flares and coronal mass ejections, stirred up by the sun. Their energies are usually up to 100 MeV, although exceptionally they can reach 10 GeV. The flux is strongly affected by the solar cycle, varing various order of magnitude depending on the activity of the Sun. The abundance of nuclei of different elements matches the solar atmosphere one, with protons and helium nuclei as the most common species. At the end of these energies there is a change in mass composition that does not match neither the solar cosmic rays nor the galactic cosmic rays. These anomalous cosmic rays are richer in helium and oxygen and are most likely produced by neutral atoms in the interestellar space.

Figure 2.5: Jack Kirby and Stan Lee used the concerns about the unshielded exposure to cosmic ray radiation as the origin of Marvel Comics' first superhero team, the Fantastic Four. Figure taken from [5]

The most known effect of solar cosmic rays are the northern lights. Earth's magnetic field direct the "solar wind" to the atmosphere near the magnetic poles. The charged particles interact with the atmosphere exciting oxygen atoms and nitrogen mollecules that produce light via fluorescence emission. Solar cosmic rays are also relevant for manned space missions, as the cosmic radiation can constitute an important hazard for humans in space. This concern was used by Stan Lee and Jack Kirby for the origin of Marvel Comics' first superhero team, the Fantastic Four, who obtained superpowers after unshielded exposure to this radiation. Although such effects belong to the realm of fiction, astronauts have reported spontaneous flashes of light when they close their eyes outside the magnetosphere. This phenomena is attributed to cosmic rays, either due to a direct interaction with the optic nerve or visual centres in the brain or to Cherenkov radiation created as the cosmic ray particles pass through the vitreous humor of the astronauts' eyes.

2.2.2 Galactic cosmic rays

At larger energies, galactic cosmic rays (GRCs) become the main component. They are believed to be accelerated at supernova remnants (SNRs) in our galaxy. Their large size and long life make possible the acceleration of particles to these energies using a process called Fermi acceleration or diffusive shock acceleration [68], based on a mechanism first introduced by Fermi in 1949 [69].

In this mechanism, similar to the one that accelerate the solar cosmic rays, particles get accelerated in the strong shock fronts of the SNRs. The charged particles travel from the upstream (unshocked) region and back, gaining an amount of energy $\Delta E \propto E$ with each cycle, although exiting the shock front without return is also possible. The longer the particles remain in the shock, the higher energy they can achieve. After a time T, the maximum energy a particle can achieve is $E_{max} \sim Ze\beta_s TV_s$, where V_s is the velocity of the shock, $\beta_s = V_s/c$, B is the intensity of the magnetic field and Ze the charge of the particle [70]. This process is called a Fermi-I or first order Fermi mechanism because the efficiency of the acceleration is linear with β_s. Using typical values of Type II supernovae exploding in the average intergalactic medium the maximum achivable energy yields $E_{max} \approx Z \cdot 10^{14}$eV [71], although recent measurements have established that for some types of supernovae it could reach up to $E_{max} \approx Z \cdot 5$PeV [72].

GCRs are mainly protons ($\simeq 85\%$) and nuclei ($\simeq 15\%$), although electrons, positrons and antiprotons are also present. At around $4 \cdot 10^{15}$ eV the spectral index changes from $\gamma \simeq 2.7$ to $\gamma \simeq 3.1$, as it was mentioned before. This steepening of the spectrum is called the knee. KASCADE-Grande [6] has recently measured the spectra for different groups of elements, and found knee-like structures for all of them at energies growing with mass, as can be seen in Fig. 2.6. The observed spectra seem to be compatible with the assumption of power laws and a cut-off energy proportional to the nuclear charge. This implies that the knee in the all-particle energy spectrum is caused by a cut-off of the light elements. The shape of the all-particle spectrum at higher energies is then determined by the subsequent cut-offs of all elemental species in cosmic rays. Most likely, the astrophysical origin of the knee is a combination of the maximum energy reached in the acceleration process and leakage from the Galaxy during propagation.

At around 400 PeV the spectrum exhibits a further steepening down to $\gamma \sim 3.3$ called the *second knee*. This trait continues up to 10^{18} eV, where the spectral index reflattens to $\gamma \sim 2.7$ (the ankle). At these energies the standard theories about SNRs does not explain the presence of GCRs. Different theories have been proposed to explain this. Hillas [73] introduced a second galactic component accelerated at certain types of supernovae, mixed with extragalactic sources. A significant presence of elements heavier than iron with Z up to 92, the so-called poly-gonato model [74], has been proposed as an alternative explanation as the second knee energy, E_{2k}, is $E_{2k} \sim 92 \cdot E_k$. Berezinsky *et al.* [75] proposed that the dip in the spectrum is caused by electron-positron pair production of extragalactic cosmic rays on cosmic microwave background photons.

The structure and the intensity of the galactic magnetic field set an upper limit for

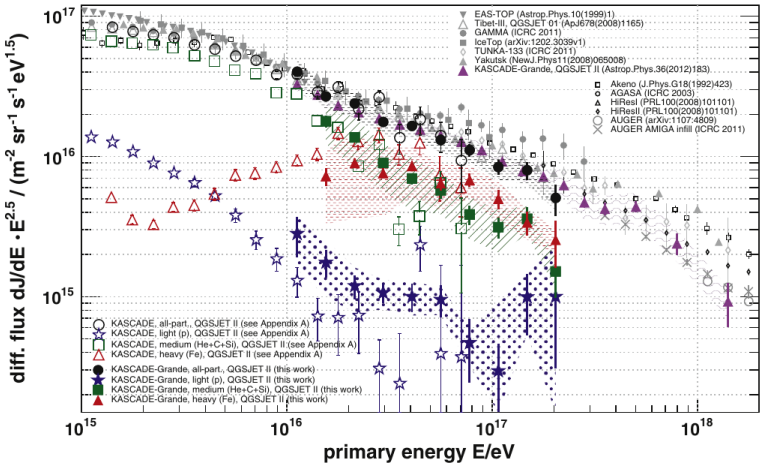

Figure 2.6: Galactic cosmic ray spectra obtained by KASCADE-Grande and other experiments. Spectra for different groups of elements are shown Figure taken from [6]

galactic cosmic ray confinement. Cosmic rays with energies above $3 \cdot 10^{18} B_\mu$ eV, where B_μ is the average magnetic field in μG, have a Larmor radius bigger than 3 kpc, the size of our galaxy. This cut-off seems to have a confirmation in the cosmic ray spectrum, as it corresponds to the ankle region.

2.3 Ultra-High Energy cosmic rays

2.3.1 UHECR energy spectrum

The origin and nature of cosmic rays with energies above the ankle are not well understood yet. The estimation of maximum energies for galactic sources are all below 10^{18} eV. This suggests that at some point between the knee and the ankle SNRs stop to be the main sources. This transition from galactic to extragalactic sources has been proposed as an explanation of the re-flattening of the spectrum.

The efficient acceleration of microscopic particles like cosmic rays to macroscopic energies of 10^{20} eV is still an open question. The so-called *bottom-up* scenarios propose that low energy particles are accelerated to these extreme energies at the source or near them. The main mechanisms proposed are the previously mentioned diffusive shock acceleration and acceleration in very intense electric fields.

Considering acceleration by diffusive shocks, in a similar way to galactic cosmic rays in SNRs, the maximum energy, $E_{\max}$, attainable by a particle of charge Ze and a magnetic

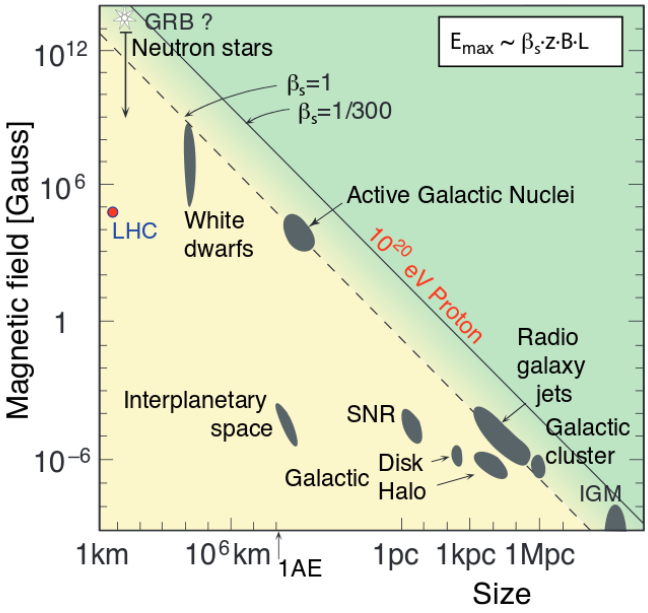

Figure 2.7: Hillas plot [7] of astrophysical sources where cosmic rays could be accelerated. Figure taken from [4]

field strength B and size of the region of the shock R is:

$$E_{max} \simeq Z\beta \left(\frac{R}{\text{kpc}}\right) \cdot \left(\frac{B}{\mu\text{G}}\right) [\text{EeV}] \tag{2.5}$$

where β is the shock velocity in units of c. All the possible sources are represented in the Hillas plot (Fig. 2.7). Active Galactic Nuclei (AGN), Gamma Ray Bursts (GRB), radio lobes of RB II galaxies and neutron stars are the most likely candidates.

Top-down scenarios, on the other hand, are based on mechanisms that would produce particles with energies above 100 EeV. The existence of Topological Defects or supermassive exotic particles have been theorized as alternative sources for UHECRs. The decay of these particles would produce a cascade of very energetic photons, light leptons and neutrinos, along with protons and neutrons, that would not need to be accelerated. All these scenarios show a very identifiable footprint: photons and neutrinos should dominate the spectrum at the highest energies. As it will be showed on section 2.3.3, these scenarios have been disfavored by recent experimental measurements.

To overcome the very low number of expected events it is mandatory to build facilities with a large detection area or to operate smaller experiments for long periods of time. Telescope Array and the Pierre Auger Observatory, the two biggest UHECR detectors

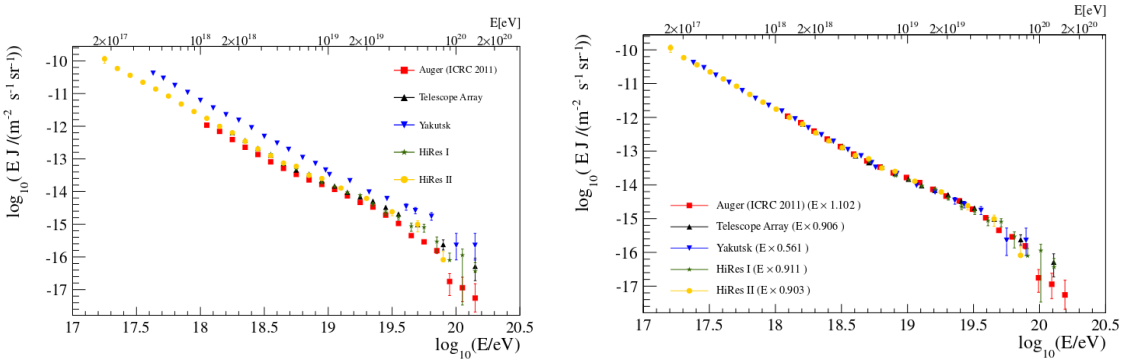

(a) (b)

Figure 2.8: Left: Uncorrected energy spectra, with the flux multiplied by E, of UHECRs measured by different experiments. Right: Same as left, after an energy re-scale by a factor α showed in the legend. Figures taken from [8] (see reference for details).

operating, cover an area of 762km^2 and 3000km^2 respectively. JEM-EUSO is a space-based cosmic ray detector that aims to monitor large fractions of the atmosphere. Latest measurements of the UHECR spectrum are shown in Fig. 2.8. As it is shown in this figure, the measurements of the UHECR spectrum by different experiments shows apparent differences and, if the energy is re-scaled by a given factor, the spectra become perfectly compatible within the uncertainties. This suggests that the problem is basically related to the energy scale of the different experiments. In Chapter 7 of this thesis it will be shown the impact of the fluorescence yield parameter on this problem.

Due to this scarcity of available data, UHECRs composition and their sources are not as well known as those of GCRs or solar cosmic rays. The rest of this chapter will be devoted to summarize the most recent developments on the field.

The GZK cut-off

Recent measurements have confirmed an end of the spectrum at very high enery. The existence of a cut-off of the cosmic ray energy spectrum at around $10^{19.6}$ eV was predicted independently in 1966 by Greisen [76] and Zatsepin and Kuzmin [77], named the GZK cut, due to the interaction of UHECRs with the Cosmic Microwave Background Radiation (CMBR), discovered one year before by Penzias and Wilson [78]. Ultra-high energy protons

interact via photo-pion production and pair production with the CMBR:

$$\begin{aligned} p + \gamma_{\mathrm{CMBR}} \longrightarrow \triangle^{+}(1232) &\longrightarrow \pi^{0} + p \\ &\longrightarrow \pi^{+} + n \\ &\longrightarrow p + e^{-}e^{+} \end{aligned}$$

The energy threshold for these processes is $\sim 10^{19.6}$ and 10^{18} eV respectively. However the energy loss for the pion production is much larger than the pair production one, so the energy losses are dominated by this process.

UHE nuclei also interact with the CMBR and the infra-red background (IRB), losing enery via photodesintegration and pion production.

$$\begin{aligned} A + \gamma_{\mathrm{CMBR,IRB}} &\longrightarrow (A - nN) + nN \\ &\longrightarrow A + e^{-}e^{+} \end{aligned}$$

where N is a nucleon. The main channel is n=1, where a proton or a neutron is produced. Double-nucleon emission is possible, but is one order of magnitud less important than single-nucleon emission [79]. The energy loss due to IRB interaction is only effective below $5 \cdot 10^{19}$ eV, while interaction with CMBR photons dominate above $2 \cdot 10^{20}$ eV. Between these energies pair production becomes the most important source of energy loss in UHE nucleons that interact with the cosmic background. If the cosmic rays are mainly nuclei a GZK-like cut is expected, although its shape and energy threshold will differ from the proton one. The short energy loss lengths indicate that cosmic rays with energies above 10^{20} eV should come from sources within a ~ 100 Mpc sphere.

Fig. 2.9 shows recent experimental measurements by both the Pierre Auger Observatory [80] and Telescope Array [9] that confirm the presence of a cut at around 10^{20} eV previously reported by HiRes [81]. Only AGASA [82] showed no evidence of flux supression. In any case, it is not possible to rule out the maximum energy attainable at the source as the cause for this cut-off of the spectrum.

2.3.2 UHECR composition

One of the problems of ground based UHECR detectors is that, due to the large fluctuations on shower development, is not possible to determine accurately the mass A of individual cosmic rays. Only statistical tendencies on the nature of UHECRs can be asserted through the study of shower observables. It is possible, however, to distinguish between charged nuclei and other types of primary particles, as the EAS produced by photons or neutrinos

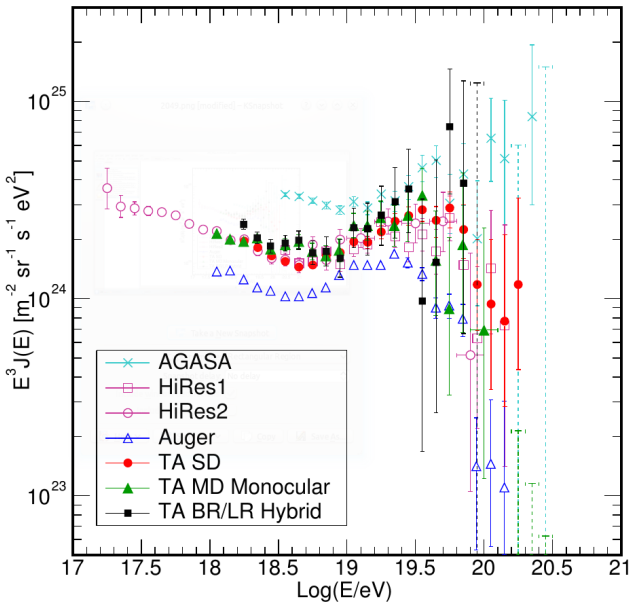

Figure 2.9: End of the cosmic ray spectrum measured by different experiments. The GZK cut-off is clearly shown for all experiments except AGASA. Figure taken from [9]

have very distinctive signatures. They will be reviewed in section 2.3.3.

As mentioned before, some shower observables are sensitive to mass composition and can be used to discriminate between primary species. The longitudinal development, recorded by fluorescence telescopes, shows differences dependending on the nature of the primary cosmic ray. The most common used feature is the depth at which the shower reaches its maximum, X_{max}. Proton-induced showers have an average shower maximum depth, $\langle X_{max} \rangle$, about 100 gcm^{-2} larger than showers initiated by iron nuclei. The standard deviation, $\sigma(X_{max})$, of the distribution also gives information about the mass composition, as proton showers are expected to have larger fluctuations (up to 40 g $\cdot$ cm^{-2}) than iron ones.

The limited duty cycle of fluorescence detectors makes difficult to get significant results for a statistical analysis, specially at the highest energies. Ground arrays do not have this handicap, but cannot directly record X_{max} and must therefore employ other observables. For example, the azimuthal asymmetry of the time distribution of the signal from different detectors gives information on the longitudinal development of the shower. The electromagnetic component of the shower is attenuated in its path through the atmosphere while the muonic component remains nearly unaffected. This effect can be employed to define a parameter, sec(θ_{max}), sensitive to the mass composition [83]. Another method also based

on the muon signal at ground is the Muon Production Depth (MPD), which allows the reconstruction of the muon production profile and the depth at which it reaches a maximum, X^{μ}_{max}. The average of this observable, $\langle X^{\mu}_{max} \rangle$, is another mass sensitive parameter [84].

The Pierre Auger Collaboration has reported a trend with energy towards heavy composition with increasing energy compared with EAS simulations in all the observables, as can be seen in Fig. 2.10. This trend has not been confirmed by Telescope Array, that has shown a proton dominated composition up to the highest energy, as can be seen in Fig. 2.11a. HiRes also reported a composition dominated by lighter species (Fig. 2.11b). A common effort between Auger, TA, HiRes and Yakutsk collaborations have proved [14] that these measurements are compatible withing the systematics uncertainties, with Auger and HiRes measurements below $10^{18.5}$ as the only exceptions. This incompatibility depends on the hadronic interaction model employed for the Monte Carlo predictions.

2.3.3 The multi-messenger component: neutrinos, photons and neutrons

It could be said that solar photons were the first "cosmic rays" ever detected. Today photon observations cover an impressive range of energies up to about 100 TeV [85–87] and new gamma-ray observatories like the Cherenkov Telescope Array (CTA) [88] have been proposed, opening new energy windows for astrophysical discoveries. The first extraterrestrial neutrino, on the other hand, was detected only in 1968 by the Homestake experiment. Recently, the Antarctica-based IceCube experiment has detected the first astrophysical neutrinos of energies above 50 TeV [89].

Both UHE photons and neutrinos are thought to be typically produced as decay secondaries from higher energy cosmic rays. These cosmic rays may interact with matter, like gas around a source, or with background photons like those from the CMBR. These interactions produce pions. Neutrinos can be formed when these charged pions decay, while neutral pions decay into photons. For example, the GZK process produces neutrinos in 1/3 of the cases and UHE photons in 2/3 of the cases. In the top-down models, pion emerge from the decay of or annihilation of exotic particles, that again produce photons and neutrinos.

In constrast to charged cosmic rays, UHE photons and neutrinos propagate along a straight line since they are not deflected by magnetic fields. This gives rise to an opportunity of discovering sources by directional pointing. As neutrinos, to a good approximation, do not interact, they can be used to trace back cosmological sources.

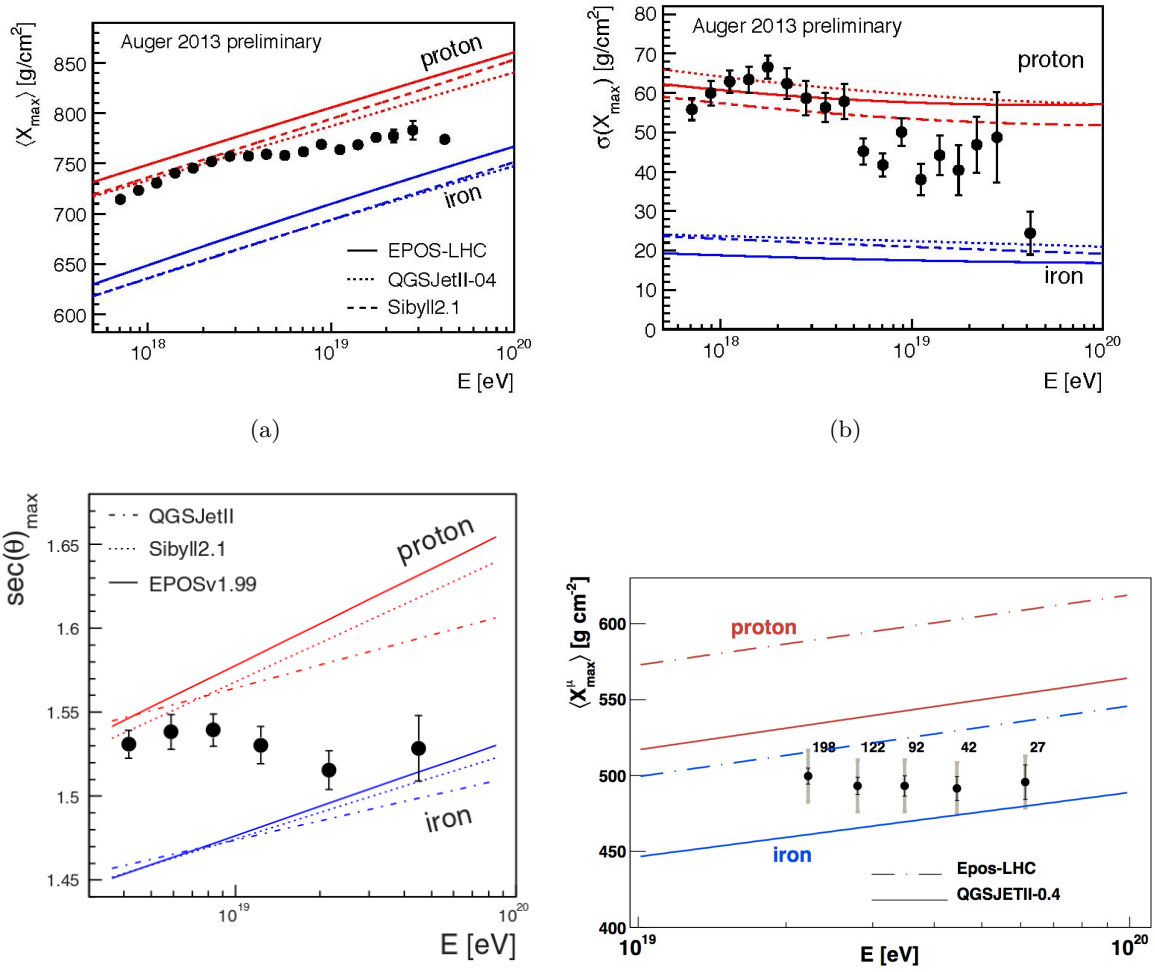

Figure 2.10: UHECRs mass composition observables (see text for details) as a function of energy reported by the Pierre Auger Collaboration. Statistical uncertanties shown as error bars. Systematic uncertanties are represented as a band. Predictions from various hadronic models for proton and iron are presented as different types of lines. Figures a and b taken from [10]. Figure c taken from [11]. Figure d taken from [12]

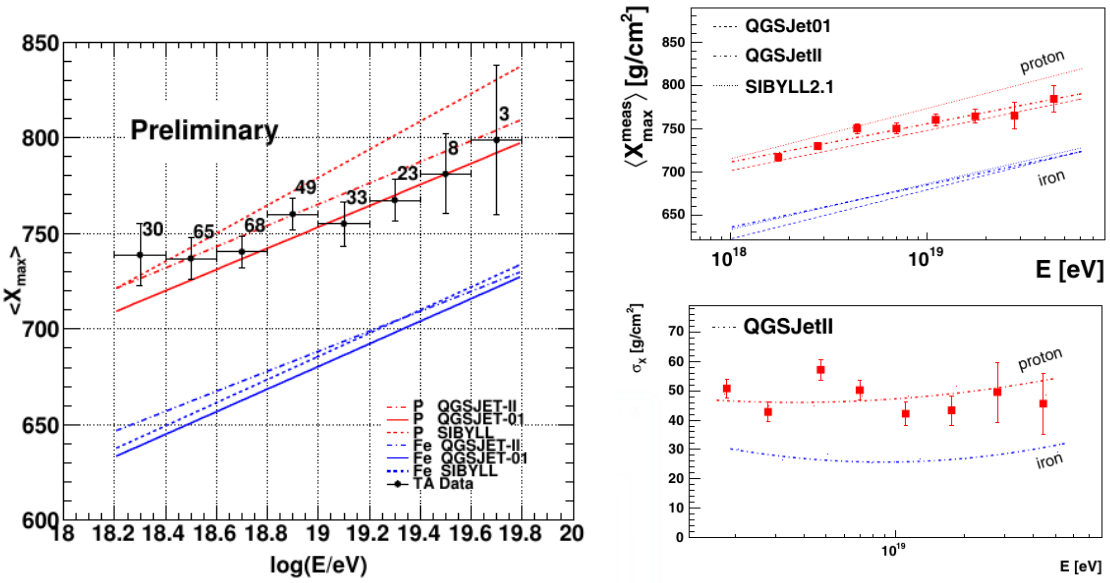

(a) (b)

Figure 2.11: Left: Average X_{max} of MC and data measured by the fluorescence detectors of Telescope Array stereoscopically. Figure taken from [13]. Right: Average X_{max} and $\sigma(X_{max})$ measured by the HiRes Collaboration for MC and Data. Figure taken from [14]

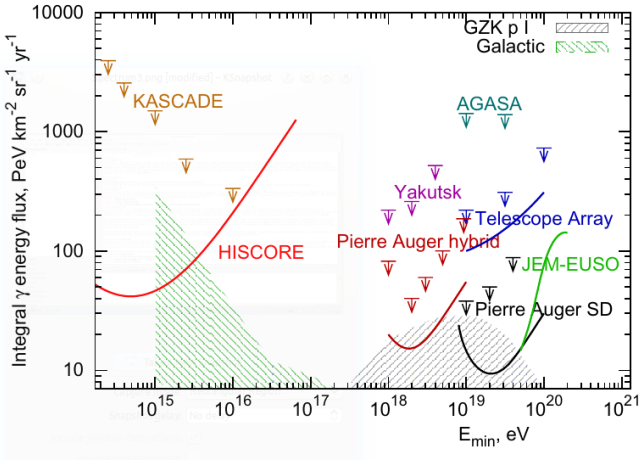

Figure 2.12: Limits to the photon flux from $\sim 10^{14}$ eV to $\sim 10^{20}$ eV. Experimental results and expected sensitivites (continous line) for different detectors are shown. Figure taken from [15]

Photons

UHE photons can be searched using cosmic-ray ground detectors, as they produce extensive air showers, like hadrons, that can be detected by ground based experiments. Photon-induced showers can be differentiated from hadron-induced showers using composition observables like X_{max}. As photon showers lack the hadronic component they develop deeper in the atmosphere and have much less muons than hadronic showers. Generally, any technique good for hadronic composition study is adequate for photon search (as long as electromagnetic showers can trigger the detectors).

So far no photon has been found at the highest energies since the number of photon candidates found can be attributed to hadronic background (deep proton-induced showers). The existing photon flux, along with the predictions from the models, is shown in Fig. 2.12. Also shown are estimates of the sensitivity with data until 2015 as derived by scaling the current limits to account for the relative exposure, and assuming the number of background events remain constant.

This lack of photons put a strong constraint in top-down models based on the decay of heavy particles. The bottom-up mechanism based on accelartion near the sources is thus a more likely origin of UHECRs.

Neutrinos

The observation of UHE neutrinos is limited by exposure, not by background. Using Monte Carlo simulations it has been established that neutrino identification at ground arrays can be performed with high efficiency as long as the search is restricted to very inclined showers (typically above 60°), starting deep in the atmosphere and thus close to the ground [90] or with upward-going showers [91]. In principle this search could be also done with fluorescence detectors that can identify very penetrating inclined showers. However fluorescence detectors can only work during moonless nights. As a consequence, this reduce the exposure to UHE neutrinos compared to ground array particle detectors.

All experiments working in the EeV range aim at detecting the cosmogenic neutrino flux produced in interaction of UHECRs above 50 EeV with the CMBR. Despite the existence of these neutrinos should be guaranteed by the observation of both projectiles of that energy and target photons, the level at which this flux is realized in nature is dependent on many unknown parameters such as the composition of UHECRs at the sources, the spatial distribution of the sources and their evolution with time, the features of the UHECR spectra at the production sites, etc. This leads to a wide range of predictions as can be seen in Fig. 2.13. In particular, if the primary UHECR flux at the sources is dominated by iron, the expected neutrino flux is at least one order of magnitude smaller than in the case of proton dominated flux.

In the EeV range only one candidate, compatible with background has been reported by ANITA [92]. No other candidates have been found by any other experiment. This allows us to put a limit in the neutrino flux. The differential neutrino flux for different experiments, along with the different flux predictions, is presented in Fig. 2.13.

Neutrons

In addition to photons and neutrinos, other neutral charged particles could potentially be used in the search for UHECR point sources. In principle, neutron-induced showers are indistinguishable from air showers produced by protons. A flux of neutrons from discrete source would cause an excess of cosmic-ray events around the direction to the source. So far no significant excess of air showers attributable to neutron fluxes has been detected using the Pierre Auger Observatory [93] and flux upper limits have been derived.

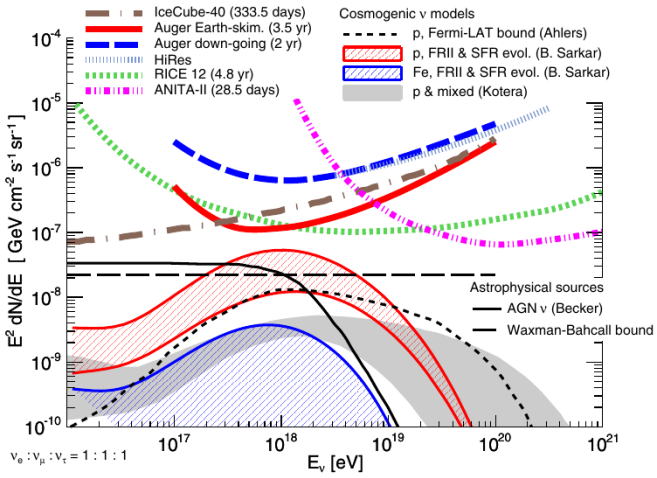

Figure 2.13: Differential neutrino flux for different experiments, along with the different theoretical predictions. Figure taken from [15], see reference for details

2.3.4 Origin and propagation of UHECRs

To understand the nature of UHECRs a good knowledge of the sources is required. However, as UHECRs are charged particles, magnetic fields are expected to deflect their trajectories. If all the information linking the UHECRs with their source is lost in this process, an isotropic distribution of the arrival directions is expected. However, cosmic rays with the highest energies are expected to keep their original direction within an angle deviation that depends on the distance to the source, the magnetic field traversed and primary charge and mass. Thus, the measurement of anisotropies in the distribution of arrival directions, combined with the chemical composition and the spectral features of UHECRs, could provide invaluable information about the sources and acceleration mechanisms. A precise determination of arrival directions is fundamental to assess the possible clustering of events from particular directions.

The data collected by the HiRes experiment in the North Hemisphere in stereo mode (with both detectors working simultaneously) were analyzed searching for these anisotropies [94]. In this mode the angular resolution for cosmic rays pointing directions is around 0.8^{o}. The datasample was divided in three subsamples. Events with energies greater than 10 EeV and 40 EeV were compatible with an isotropic flux with a confidence level of 95%. Events with energy over 57 EeV are nearly consistent with an isotropic flux, favoring heavy deflections at extragalactic magnetic fields and no correlation with AGNs.

AGASA had an energy dependent angular resolution, ranging from 4^{o} at $10^{18.5}$ eV down

to 1.3° at 10^{20}. The AGASA collaboration reported small scale anisotropies, observing 1 triplet and 6 doublets with an energy threshold of $4 \cdot 10^{19}$ eV within angular windows of 2.5°, while only 2 doublets were expected from an isotropy hypothesis [95]. This clustering in the AGASA data set is weaker than expected, according to more recent analyses. They claimed an hypothesis of isotropically distributed arrival directions [96], consistent at the 8% level with the data. No AGN correlation were found, but rather a confirmation of compatibility of AGASA data with isotropy [97].

More recent experiments like the Pierre Auger Observatory and Telescope Array have shown different results. The Pierre Auger Observatory is able to reconstruct the arrival direction of cosmic rays with an accuracy of about 1°. Point-like source searches have resulted in evidence for anisotropy in the distribution of arrival direction at the highest energies [98], although recent analyses using new data suggest a weaker signal than expected [99]. The arrival directions of the events with energies above 55 EeV show correlation within an angular scale of 3° with the positions of nearby AGNs from the Veron-Cetty & Veron (VCV) catalog [100], above what is expected from random chance coincidences in an isotropic scenario. 28 out of the 84 events with energies above the threshold correlate with AGNs. That corresponds to a fraction of correlating events of $(33 \pm 5)\%$ [101]. For an isotropic distribution of sources, the rate of correlating events expected is 21%.

Telescope Array SD angular resolution for events with $E > 10$ EeV is around 1.5°. The first data set after 40 months of full Telescope Array SD operation shows 11 correlating events out of 25 (44%) with the VCV catalog [102]. The expected number of random coincidences is 5.9, corresponding to a fraction of 21%. The probability of this excess given an isotropic distribution due to chance is around 2%. Both the Pierre Auger Observatory and Telescope Array data are in good agreement [101], and the combined chance probability of observing such correlation is at the 10^{-3} level.

The weakness of the anisotropy, combined with the low flux of photons, points to a scenario where AGNs are possible point sources of UHECRs, with a large isotropic background.

Chapter 3

The Pierre Auger Observatory

The Pierre Auger Observatory, located in the "Pampa Amarilla" near the town of Malargüe in the province of Mendoza (Argentina) at about 1400 m a.s.l., is the largest facility in the world dedicated to the study of UHECRs. It is a hybrid experiment that uses two different and well established techniques to detect cosmic rays: an array of water Cherenkov tanks, the so-called Surface Detector (SD), combined with fluorescence telescopes, the so-called Fluorescence Detector (FD). This design is conceived to measure with high statistical significance the flux, arrival direction and composition of cosmic rays above 0.01 EeV. It has been collecting data since 2004 and it was completed in 2008. The site was chosen because of its relatively flat orography and high quality sky conditions.

The SD is composed of 1600 water tanks, disposed in an hexagonal grid and separated 1500 m each, and covers about 3500 km^2. The SD is overlooked by 27 fluorescence telescopes deployed in 4 different sites. The SD samples the tail of the EAS at the ground from the Cherenkov light produced when the shower particles cross the water tanks, while the FD registers the fluorescence light emitted by the de-excitation of atmospheric nitrogen. This hybrid technique allows to compensate the individual disadvantages of both detectors. The FD reconstruct the full longitudinal profile of the shower, providing a calorimetric measure of the cosmic ray energy. The small FD duty cycle ($\approx$ 10% considering moonless nights) is compensated by the high statistics of the SD data (100% duty cycle). The shower size at ground measured by the SD is converted into cosmic ray energy using the FD measurements and then avoiding the use of simulations. This allows a significant reduction of the systematic uncertainties because the simulations include the extrapolation of hadronic interaction models well beyond the accelerator energies.

In addition to the FD and SD other instruments are installed to expand the energy spectrum to lower energies as well as to explore new detection techniques. AMIGA is

intended to extend the efficiency of the SD to lower energies to about 10^{17} eV with a better mass discrimination. It is composed of an infill array of 61 water Cherenkov tanks separated 750 m with muon counters buried beneath them. The FD low-energy extension, called HEAT, is composed of 3 fluorescence telescopes titled 30^o to detect EAS that develop higher in the atmosphere. AERA is an array of radio antennas who aims to detect the geosynchroton emission of radio waves from EAS in a frequency range from 30 to 80 MHz. AMBER, EASIER and MIDAS are prototypes developed to measure the so-called molecular bremsstrahlung emission in the GHz band.

As the atmosphere affects the fluorescence emission, a good knowledge of its properties is needed to ensure a reliable reconstruction of the shower. To do so a series of atmospheric monitoring stations are installed across the observatory. Four LIDAR stations located near the FD sites detect clouds and aerosols analyzing the backscatter of light from laser pulses. Two additional laser facilities, the CLF (Central Laser Facility) and XLF (Extreme Laser Facility) are installed in the middle of the array. They shoot UV laser tracks that are recorded by the FD and used to estimate the aerosol distribution of the atmosphere at different heights. A program of balloon measurements was used to obtain precise measurements of the atmosphere above the Observatory This has been substituted by the station of Global Data Assimilation System (GDAS) of the Global Forecast System located near the array.

A schematic layout of the Observatory is presented in Fig. 3.1. The water Cherenkov tanks that constitute the Surface Detector are represented as gray dots, while the blue lines correspond to the field of view of the fluorescence telescopes, marked as blue dots. Enhancements and atmospheric facilities are also represented.

3.1 The Surface Detector

The surface detector of the Pierre Auger Observatory is composed of 1660 Cherenkov tanks that cover a total area of 3500 km^2. They are disposed on an hexagonal grid with a spacing of 1.5 km. The water tanks detect the secondary particles produced by a cosmic rays at the ground level and were chosen for their robustness and low cost. They have a fairly uniform exposure up to large zenith angles and are sensitive to both charged particles and high energetic photons. Water Cherenkov tanks have been succesfully used in pioneering experiments like Haverah Park [53] and is also employed by the High Altitude Water Cherenkov observatory (HAWC) [103].

The basic unit of the SD is shown on Fig. 3.2. Each Cherenkov detector consists of a rotationally mounted opaque polyethylene tank with 3.6 m diameter and 1.55 m height,

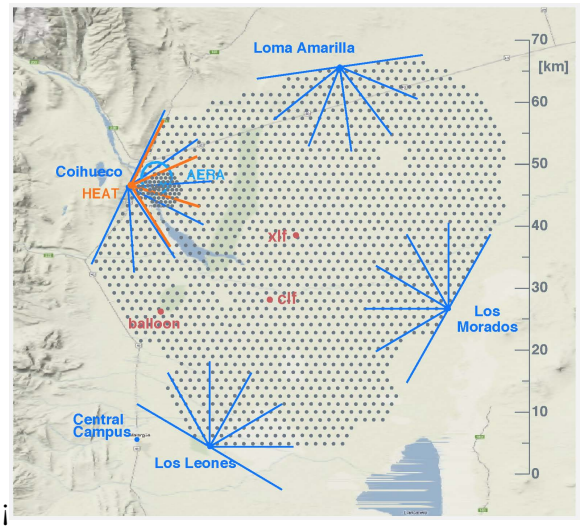

Figure 3.1: Schematic layout of the Pierre Auger Observatory. Gray dots represent the water tanks of the SD. The FD are labeled in blue. Atmospheric monitoring stations are marked in red. The HEAT and infill low energy extensions, and the AERA enhancement near the FD site of Coihueco are also represented.

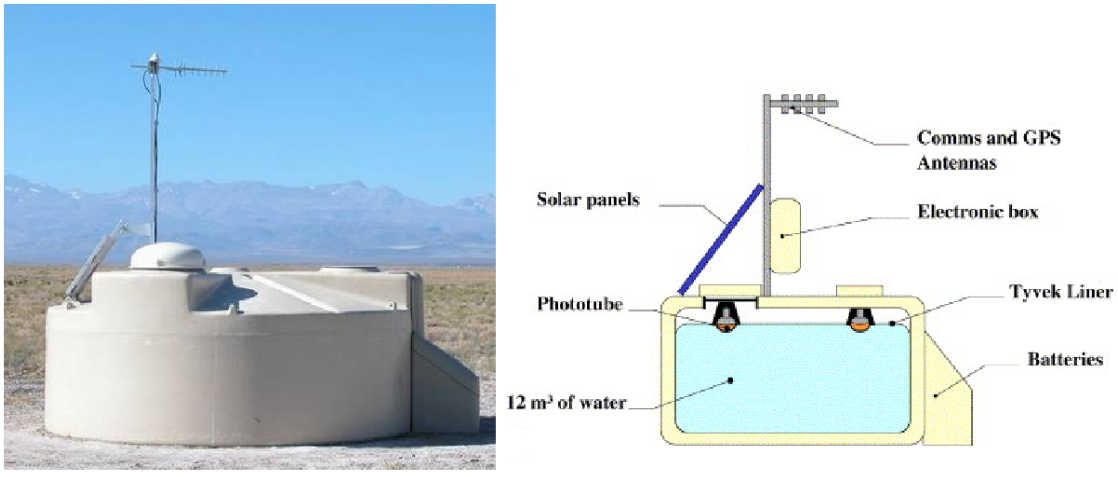

Figure 3.2: Left: Photograph of a water Cherenkov tank deployed on the field. Right: Schematic view of the station components.

enclosing a liner filled with 12000 liters of high purity water. The liner is a plastic cylindrical bag with 1.2 m height that serves as a secondary seal against external sources. The inner Tyvek surface of the liner gives excellent diffuse reflectivity of Cherenkov light. To the outside the liner is black and has been designed to provide a barrier against water and light.

Tanks are equipped with three 9" XP1805 Photonis photomultiplier tubes (PMT), disposed simmetrically at 1.2 m from the center of the tank and observing the water volume through clear polyethylene windows. Two signals are extracted from each PMT, a $\times 32$ amplified signal from the last dynode and a signal from the anode. This design provides enough dynamic range to cover with good precision total signals from the highest ($\approx$ 1000 particles μs^{-1} near the shower core) down to the lowest ($\approx$ 1 particle μs^{-1} far from the shower core). The readout of the six signals from each tank is digitized at 40 MHz (25 ns bins) using 10 bit Flash Analog to Digital Converters (FADCs). All the electronics are mounted locally at each station and are contained in a box situated on top of the tank. The local electronics are controlled by CPU which also controls a Programmable Logic Device used to select signals according to the trigger conditions implemented for individual stations. Timing synchronization, crucial for determining the shower direction, is achieved using a commercial Motorola GPS receiver which provides the event time with a precision of around 8 ns.

Power is supplied by two solar panels connected to 12 V batteries which are situated in a box in the shadow of the tank. A communication antenna connects the tank to the Central Data Acquisition System (CDAS). Each detector is autonomous and can operate independently of the rest of the detectors of the array.

3.1.1 SD calibration

The three PMTs detect the Cherenkov radiation produced by the shower particles giving rise to a digitalized signal. This electronic signal generated by a shower particle depends not only on the light deposited by the particle but also on other parameters like the water quality, liner response or PMT efficiency. Therefore equal light produced by a given particle in a water tank (or even in the same tank) will not generate the same signal. A precise calibration of the PMTs is thus mandatory, but the large number of detectors and distance between them makes not feasible an inter-detector calibration. Instead, the signal measured by each tank is normalized to a reference calibration unit.

The selected calibration unit is the Vertical Equivalent Muon (VEM or Q_{VEM}), defined as the signal produced by a vertical and through-going (VCT) muon. The goal of the

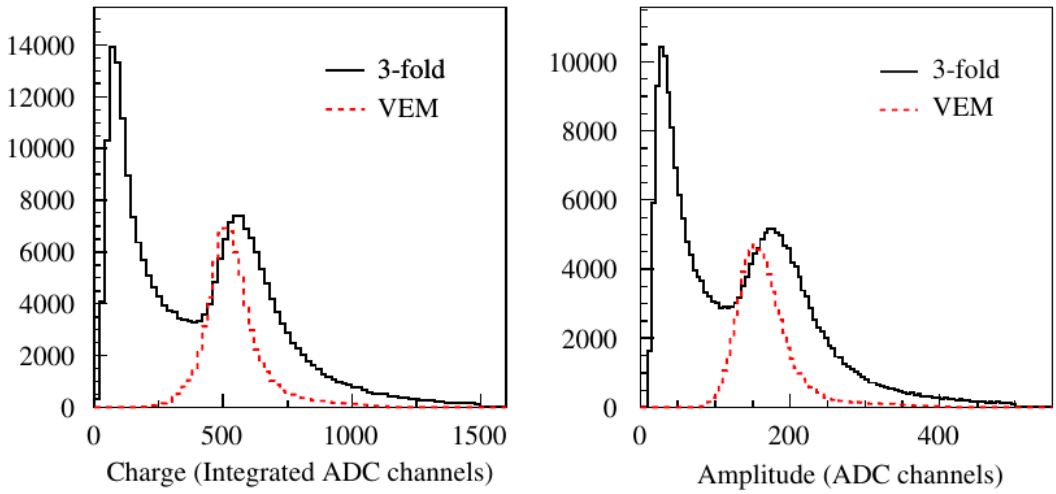

Figure 3.3: Charge and pulse height histograms from an SD station with the signal from 3 all PMTs summed. The dashed histogram is produced by an external muon telescope providing the trigger to select only VCT muons. The first peak in the black histogram is caused by low energy particles. The second peak is due to VCT atmospheric muons. Figure taken from [16]

calibration is to obtain the value of 1 VEM in electronic units (integrated counts) and setting a common trigger-threshold in detector-independent units. For this purpose, the signals of atmospheric muons, a well understood uniform background across the array, are employed.

Since the SD in its normal configuration has no way to select VCT muons, a reference tank equipped with two movable scintillators has been used to establish the relation between the signal of a VEM and the peak of the histogram obtained from omni directional muons crossing the tank ($Q_{\mathrm{VEM}}^{\mathrm{peak}}$). Fig. 3.3 (left) shows the charge histogram from an SD station, the signal from all 3 PMTs summed, originated by background muons (black solid line) and the charge histogram generated by VCT muons (red dashed line) by coincidence between the two scintillators of the reference tank. The conversion factor between the peak in the charge histogram for background muons and the charge corresponding to the sum of the 3 PMTs is approximately at 1.09 VEM, i.e. $Q_{\mathrm{VEM}}^{\mathrm{peak}} = 1.09\ Q_{VEM}$ and at 1.03 ± 0.02 for each PMT.

To maintain a uniform trigger condition for the whole array, atmospheric muons are also used to establish a common reference unit for threshold levels. In this case pulse height histograms (Fig. 3.3 (right)), those storing the maximum values of the measured FADC

are used. Atmospheric muons also produce a peak in this histogram ($I_{\mathrm{VEM}}^{\mathrm{peak}}$) which is used as a common reference unit for threshold levels. Additionally, the initial end-to-end gains of the 3 PMTs, i.e. $I_{\mathrm{VEM}}^{\mathrm{peak}}$, must be roughly equivalent to ensure that the signals recorded from the 3 PMTs are similar in amplitude.

Finally, the calibration procedure must also be able to determine the baselines of all the six FADC inputs and the gain ration between the dynode and the anode to convert the raw FADC traces into integrated channels.

The calibration is operated online every minute, and sent to CDAS every 6 minutes for monitoring. In addition, high statistics histograms of the charge distribution from muons and average pulse shapes are sent every time a station records an event.

3.1.2 SD trigger

The SD data acquisition (DAQ) trigger must fulfill both physical and technical requirements. The main limitation to the rate of recordable events comes from the wireless communication system which connects the surface detector to the central campus. The maximum sustainable rate of events in the whole array is < 1 per hour and tank, to be compared with the 3 kHz counting rate per station due to atmospheric muon flux. The trigger thus must reduce the single station rate without inducing loss of physical events. It must also allow data acquisition down to the lowest possible energy. To deal with all these requirements the design of the SD DAQ trigger has been realised in a hierarchical form, where at each level the single station rate becomes less and less, by means of discrimination against background stricter and stricter. At the same time, the DAQ is designed to allow the storage of the largest possible number of EAS candidates.

The ultimate discrimination of EAS from chance events due to combinatorial coincidences among the surface detectors is performed off-line through a selection of physics events and of detectors participating in each of them.

Local triggers

Two levels of triggers (called **T1** and **T2**) are formed at each detector upon the analysis of the signals of the PMTs. Two independent modes are implemented as **T1**, having conceived in a complimentary way the electromagnetic and muonic component of an air-shower.

The first T1 mode is a simple threshold trigger (**TH**) which requires the coincidence of the three PMTs each above $1.75 I_{VEM}^{peak}$. This trigger is used to select large signals that are not necessarily spread in time and is particularly effective for the detection of inclined showers that have traversed a large amount of atmosphere and are consequently dominatly

muonic. The TH-T1 trigger is used to reduce the rate due to atmospheric muons from ≈ 3 kHz to ≈ 100 Hz.

The second T1 mode is designated "time-over-threshold" trigger (**ToT**) and requires a minimum of 13 bins (325 ns) in 120 FADC bins of a sliding window of 3 μs are required to be above a threshold of $0.2I_{VEM}^{peak}$ in 2 of the 3 PMTs. This trigger is intended to select sequences of small signals spread in time and is thus optimized for the detection of near-by low energy showers dominated by the electromagnetic component, or for high energy showers where the core is distant. The ToT rate at each detector is < 2 Hz.

The **T2** is applied in the station controller to reduce to about 20 Hz the rate of events per detector. This reduction is done to cope with the bandwidth of the communication system between the detectors and the central campus. All ToT-T1 triggers are promoted to T2 status, whereas the T1-TH trigger are requested to pass an higher threshold of $3.2I_{VEM}^{peak}$ in coincidence among the three PMTs.

Array triggers

T2 triggers are combined with those from other detectors and examined for spatial and temporal correlations, leading to an array trigger (**T3**). This third level trigger initiates the central data acquisition and storage. Once a T3 is formed all FADC signals are sent to the CDAS as well as those from detectors passing the T1 but not the T2 provided that they are within 30 μs of the T3.

The T3 is realized in two modes. The first T3 mode requires the coincidence of at least three detectors that have passed the ToT condition and that meet the requirement of a minimum of compactness, namely one of the detectors must have one of its closest neighbors and one of its second closest neighbors triggered. It is called "ToT2C_1&3C_2", where C_n indicates the nth set of neighbors (see Fig. 3.4). Once the spatial coincidence is verified, timing criteria are imposed: each T2 must be within $(6 + 5C_n)$ μs of the first one. An example of such T3 is shown in Fig. 3.4 left. The rate of this T3 with the full array in operation is around 1600 events per day. This trigger is extremely pure since 90% of the selected events are real showers and it is mostly efficient for showers below 60^o. The second mode requires a four-fold coincidence by any T2 with a moderate compactness. Namely, among the four fired detectors, within appropriate time windows, at least one must be in the first set of neighbors from a selected station (C_1), another must be in the second set (C_2) and the last one can be as far as the fourth set C_4. This trigger is called "2C_1&3C_2&4C_4". Concerning timing criteria the same logic as the ToT2C_1&3C_2 is applied. An example of this T3 configuration is shown in Fig. 3.4 right. Such a trigger is efficient for the detection

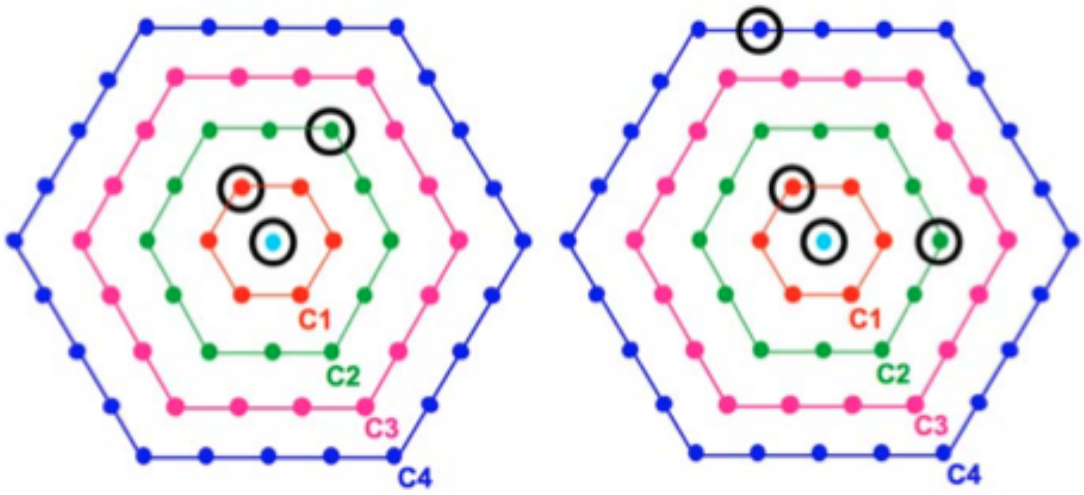

Figure 3.4: Example of T3 configurations: the 3-fold T3 mode ToTT2C$_1$&3C$_2$ is shown on the left and 4-fold mode 2C$_1$&3C$_2$&4C$_4$ on the right (see text for definitions). C_1, C_2, C_3, C_4 indicate the first, second, third and fourth sets of neighbors. Figure taken from [17]

of horizontal showers that, being rich in muons, generate in the detectors signals that have a narrow time spread with triggered detectors having wide-spread patterns on the ground. With the full array configuration this trigger detects about 1200 events a day, out of which about 10% are real showers.

The next level of trigger concern the physics selection. The **T4** trigger is needed to select real showers from the set of stored T3 data. Two criteria are defined, with different aims. The first T4 criterion, so-called 3ToT, requires three nearby stations passing the T2-ToT in a triangular pattern. The number of chance coincidences passing 3 ToT condition over the full array is < 1 per day, thanks to very low rate of T2-ToT. Due to their compactness, events with zenith angle below 60^o are selected with an efficiency more than 98%. An example of this configuration is shown in Fig. 3.5 top. The second T4 criterion, so-called 4C1, requires four nearby stations with any kind of T2 trigger. This trigger is used to detect showers with larger zenith angles and brings $\approx 100\%$ efficiency for showers below 60^o. An example of 4C1 is shown in Fig. 3.5 bottom. In both cases is also required that the stations fit to a plane shower moving at the speed of light.

The finite size of the array makes necessary a final fiducial trigger, **T5** that selects events well contained within the array and ensures a proper core reconstruction. It requires the detector with the highest signal to be surrounded by an hexagon of working stations. This is called the 6T5 trigger. A less restrictive criterion, called 5T5, requires only 5

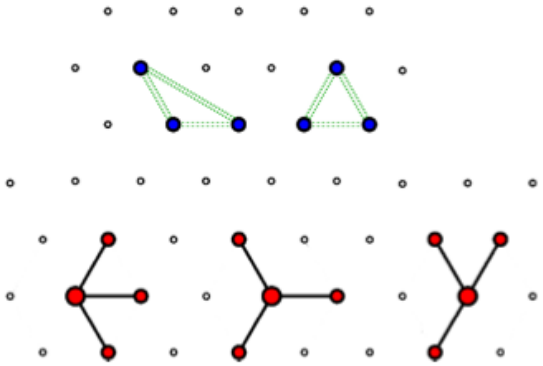

Figure 3.5: Minimal T4 configurations: 3ToT (solid lines, top) and 4C1 (dashed lines, bottom). Figure taken from [18]

working stations around the hottest detector. Due to the large numbers of detectors of the surface array, a 1% of them is expected to malfunction at any time, even with constant maintenance. Thus, the T5 trigger will discard events that, even if contained within the array, fall close to a non-working station.

The full trigger chain, from T1 to T5, is summarized in Fig. 3.6

3.1.3 SD reconstruction

Events that fulfill the T5 trigger conditions have enough information to reconstruct their arrival direction and energy of the primary cosmic ray. The time distribution of the signals from the surface detectors is used to reconstruct the arrival direction and front curvature while energy is obtained from the lateral distribution of the signals.

SD geometrical reconstruction

Not all the triggered stations are used in the reconstruction. Only the so-called *candidate* stations are used. Stations with a random trigger are removed and those that have no data are flagged as accidental. Also, the stations that have been triggered due to a lightning are removed as well. Those lightning events are detected as a series of oscillation in the FADC traces of the three PMTs. If the signal does not exceed 1000 FADC counts and makes more than 3 baselines crossings the event is considered to come from a lightning and thus removed.

Finally, the timing compatibility of the stations is checked. An EAS can be considered as a front of particles propagating at the speed of light c along a straight direction de-

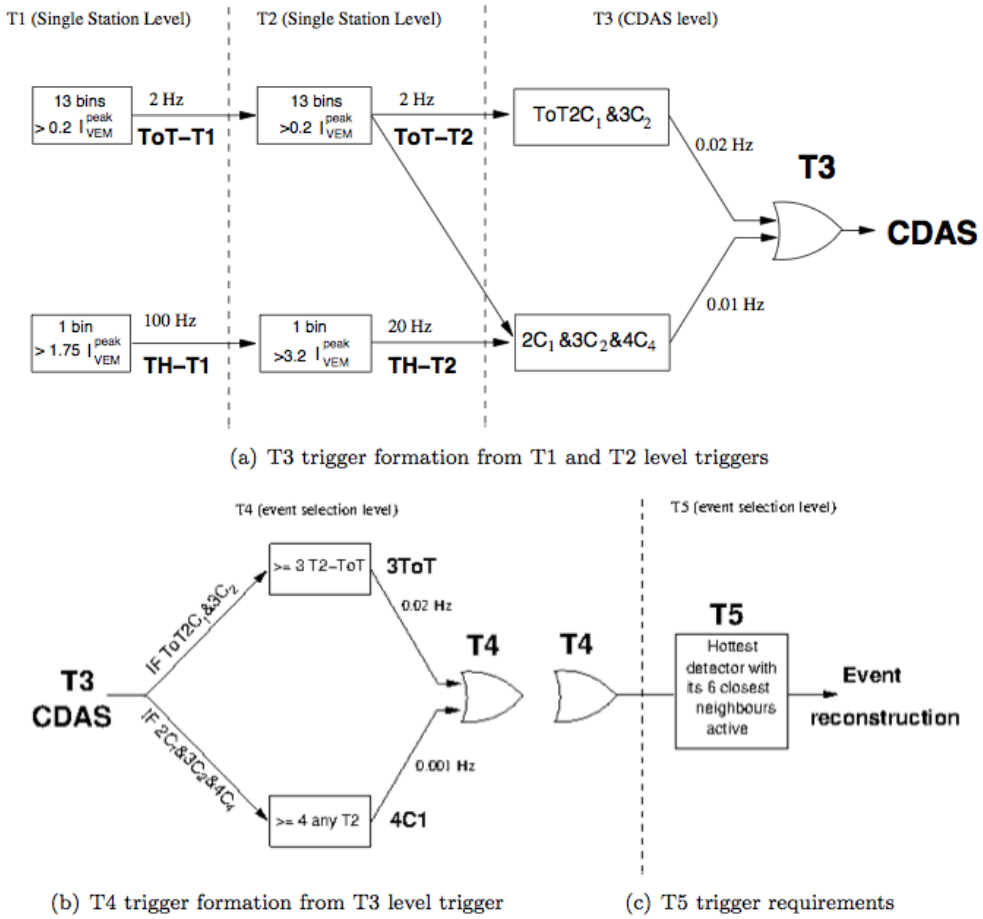

(a) T3 trigger formation from T1 and T2 level triggers

(b) T4 trigger formation from T3 level trigger

(c) T5 trigger requirements

Figure 3.6: Schematics of the hierarchy of the trigger systeme of the Pierre Auger Observatory, from local trigger (T1) to fiducial trigger (T5). Figure taken from [17]

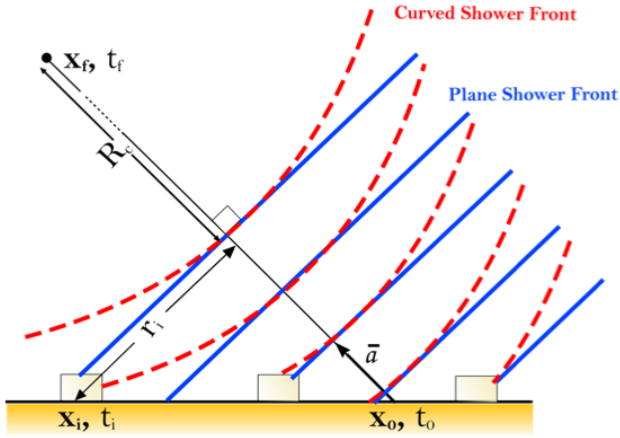

Figure 3.7: Shower geometry including parameters used in the SD reconstruction

termined by the arrival direction of the primary particle. In a first step this shower front is approximated as a planar disk perpendicular to the shower axis direction $\vec{a}$. Given the reconstruction *seed* (The 3C1 stations with largest sum of station signals) we require the planar front to be compatible with the speed of light:

$$c(t_1 - t(\vec{x_i})) = (\vec{x_1} - \vec{x_i})\vec{a},\ i \in \{1, 2, 3\} \tag{3.1}$$

where $\vec{x_i}$ and t_i are the position and the time of the i^{th} station. The station with the highest signal is used as the origin of position and time $(\vec{x_1}, t_1)$. This equation defines two projections that determine a linear system from which a provisional axis $\vec{a}$ is obtained. With this $\vec{a}$ and t_1 station times are checked for compatibility with the shower front arrival. The predicted time arrival t_{sh} at $\vec{x_i}$ is:

$$t_{sh}(\vec{x_i}) = t_1 - \vec{a}(\vec{x_i} - \vec{x_1})/c \tag{3.2}$$

For each station i the difference between the predicted time arrival and actual start time, i.e. the station delay Δt_i, must satisfy the condition:

$$-1000\text{ns} < \Delta t_i < 2000\text{ns} \tag{3.3}$$

Stations outside this interval are flagged as *accidentals* and discarded. Also, stations with no neighbors within 1800 m or only one within 5000 m are considered isolated and removed as well.

The signal-weighted barycenter of the stations that remain is used as the origin $\vec{b}$ and is used a first estimate of the core position. Similarly, the weighted bary-time is set as the time origin. A shower track can be visualized as a point $\vec{x_i}(t)$ moving with the speed of light c along the straight line with (normalized) axis $\vec{a}$ and passing the origin at time t_0. In this approximation the time when the shower passes through some station on the ground $t(\vec{x_i})$:

$$ct(\vec{x_i}) = ct_0 - (\vec{x_i} - \vec{b})\vec{a} \tag{3.4}$$

The shower plane is obtained minimizing the sum of the squares of the time differences between the measured signal start time t_i and the predicted one $t(\vec{x_i})$ given by (3.4):

$$\chi^2 = \sum_i \left(\frac{t_i - t(\vec{x_i})}{\sigma_{t_i}} \right)^2 \tag{3.5}$$

where σ_{t_i} is the station variance in the start time t_i [104]. This equation has three parameters, two components of $\vec{a}$, the third component is given by the normalization constraint, and t_0. An approximate linear solution can be obtained if the z-component of the stations is neglected [18] .

A more realistic approximation is obtained assuming a spheric (curve) shower front with radius of curvature R_C (see Fig. 3.7). In this case the expected arrival time $t(\vec{(}x_i))$ will be given by:

$$ct(\vec{x_i}) = ct_0 - (\vec{x_i} - \vec{b})\vec{a} + \frac{\rho_i^2}{2R_C} \tag{3.6}$$

where $\rho_i = |\vec{a} \times (\vec{x_i} - \vec{b})|$ is the perpendicular distance to the axis, A first approximation to R_C is obtained assuming that the time propagation of the shower front is described as an expanding sphere centered at the position of the first interaction, without any assumption about the ground impact point [18]. Since the position of the shower core is required, the curvature fit is only performed after the LDF fit described in the next section that provides the core position. After this is done the function to be minimized is

$$\chi^2 = \frac{1}{\sigma_{t_i}^2} \sum_i [c(t_i - t_0) - |R_C\vec{a} - \vec{x_i}|]^2 \tag{3.7}$$

SD energy reconstruction via LDF

In the Volcano Ranch experiment the energy of an event was obtained from the total number of particles, this last one estimated by integrating the signal of the SD over all

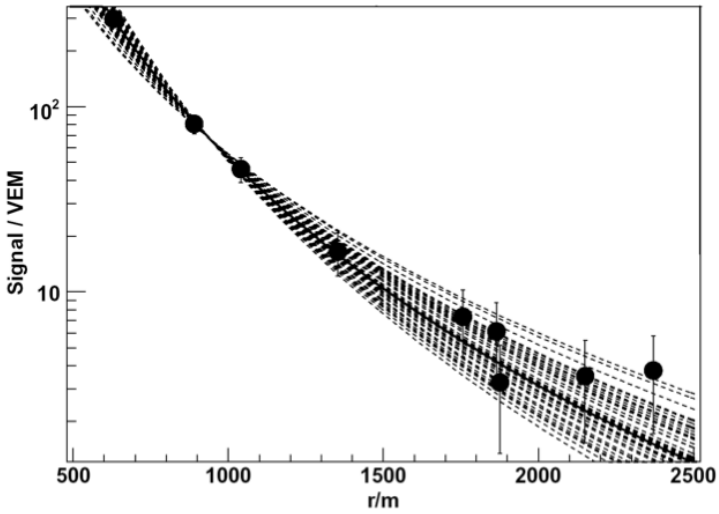

Figure 3.8: Stations signals as a function of distance (marked as black dots) for a simulated event and the reconstructed LDFs using different values of β (dashed lines). Figure taken from [19]

distances using an empirically determined Lateral Distribution Function (LDF). However, the large fluctuations in the shower development and inaccuracies in the assumption of the LDF resulted in large uncertainties in the determination of the energy. To avoid this problem, Hillas [105] proposed to use the signal at some reference distance from where the particle density is subjected to smaller fluctuations than those of the total number of particles.

Later [19] it was demonstrated that at this optimal distance $r_{\rm opt}$, that depends mainly on the spacing of the array, the fluctuations in the expected signal due to a lack of knowledge of the LDF is minimized. For example, at the Haverah Park experiment a $r_{\rm opt}$ of 600 m was used while in the Pierre Auger Observatory, with 1.5 km spacing, this core distance has been found to be at 1000 m. This is shown in Fig 3.8, where a single simulated event is reconstructed 50 times using the LDF defined by (3.8) with different values of the slope parameter β. As can be appreciated, the different parameterizations used to described the expected signal crossing at a distance close to 1000 m. Finally it should be pointed out that this optimal distance r_{opt} fluctuates from event to event increasing up to 1500 m when there are saturated stations.

Different types of LDF have been proposed. The LDF used at the Pierre Auger Observatory to describe the expected signal $S(r)$ in VEM units at a core distance r is a modified

NKG function [66, 67]:

$$S(r) = S(1000)\left(\frac{r}{1000}\right)^{\beta}\left(\frac{r+700}{1000+700}\right)^{\beta} \tag{3.8}$$

where r is measured in m. $S(1000)$, defined as the signal in VEM units at 1000 m from the shower core is chosen as the normalization factor of the LDF. β is the slope of the LDF and is given by [18]:

$$\beta = \begin{cases} a + b(\sec\theta - 1) & \text{if } \sec\theta < 1.55 \\ a + b(\sec\theta - 1) + f(\sec\theta - 1.55)^2 & \text{if } \sec\theta > 1.55 \end{cases} \tag{3.9}$$

The values of the constant parameters a, b and f can be found in the reference.

The parameters which best fit the measured signal S_i at a given station to the expected signal $S(\rho_i)$ are obtained by minimizing the χ^2 function:

$$\chi^2 = \sum_i \left(\frac{S_i - S(\rho_i)}{\sigma_{S_i}}\right) + \sum_{i,\text{zero signal}} S(\rho_i) \tag{3.10}$$

where σ_{S_i} is the accuracy of the signal, which has been parameterized as function of the axis zenith angle θ as $\sigma_{S_i} = (0.32 + 0.42\sec\theta)\sqrt{S_i}$ [106]. The first term of (3.10) runs over stations with signal while the second one has been added to take into account stations with zero signal but with a non-negligible probability to measure a signal lower than the threshold. Some stations, especially those that are near the core, can have a saturated signal. Several procedures have been developed to avoid these traces being lost [107–109]. From this minimization process the parameter S_{1000} and a precise position of the core are obtained.

Finally, to obtain the energy of the primary cosmic ray a conversion of S_{1000} to energy units is required. For a reconstruction with only SD data, this conversion needs predictions from Monte Carlo simulation that are heavy dependent on hadronic models and assumptions of the primary mass. A much more precise method, using data from the FD will be described in section 6.1.

3.2 The Fluorescence Detector (FD)

The detection of UHECR using nitrogen fluorescence emission is a well established technique, pioneered by K. Greisen and colleagues at the "Cornell Wide-Angle System" [56] during the 1960s and used by experiments like Fly's Eye [58], HiRes [59] or Telescope

Array [110]. The JEM-EUSO mission [111], expected to be launch during 2017, intends to use this technique to detect EAS developing in the atmosphere from space.

The FD of the Pierre Auger Observatory comprises four observation sites -Los Leones, Los Morados, Loma Amarilla and Coihueco- located atop small elevations on the perimeter of the SD array. Six independent telescopes, each with a field of view of $30^o \times 30^o$ in azimuth and elevation, are located in each FD site. The telescopes face towards the interior of the array so that the combination of the six telescopes provides 180^o coverage in azimuth (see Fig. 3.1). This arrangement of the four sites was the optimum solution to the primary design goal ensuring 100% FD triggering efficiency above 10^{19} eV over the entire area of the surface detector. At the Malargüe site a large flat area, ideal for deployment of the SD, is bordered with a number of small hills suitable for FD sites. The arrangement of four inward-looking FD sites is a cost-effective way of ensuring full coverage without wasteful overlaps, and of minimizing the average distance to detected air showers, thus reducing uncertainties in atmospheric transmission corrections.

FD data-taking is only possible under specific environmental conditions. The light-sensitive cameras must be operated on dark nights with low wind and without rain. Thus, the FD is only operated during nights with a moon fraction below 60% beginning at the end of the astronomical twilight till the beginning of the next astronomical twilight. The observation period lasts 16 days per month, with an average observational time of about 10 h (ranging from about 14 h in June to 5 h in December). Taking into account the atmospheric conditions, the duty cycle of the FD is reduced to around 11%.

Fig. 3.9 depicts an individual FD telescope inside the building site. Nitrogen fluorescence light enters through a large UV-passing filter window. The light is focused by a 10 square meter mirror onto a camera of 440 pixels with photomultiplier light sensors. Light pulses in the pixels are digitized every 100 ns, and a hierarchy of trigger levels culminates in the detection and recording of cosmic ray air showers.

3.2.1 Optical System

The basic elements of the optical system in each FD telescope are a filter at the entrance window, a circular aperture, a corrector ring, a mirror and a camera with photomultipliers. The system is housed in a clean climate- controlled building, where an air-conditioning system is set to stabilize the temperature at 21°C. This helps to minimize thermal dilation of the system and to maintain the alignment of mechanical and optical components.

The window is an optical filter made of Schott MUG-6 glass. This absorbs visible light while transmitting UV photons from 290 nm up to 410 nm wavelength, which includes

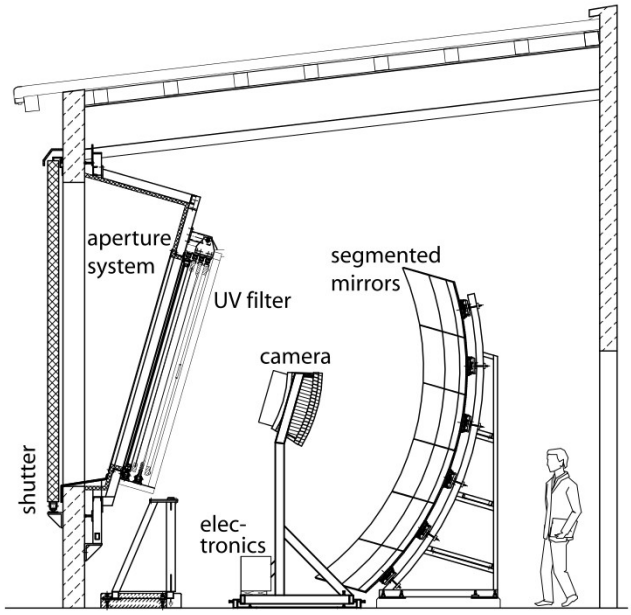

Figure 3.9: Schematic view of a fluorescence telescope from the Pierre Auger Observatory. Figure taken from [20]

almost all of the nitrogen fluorescence spectrum (See Fig. 3.10). Without this filter window, the fluorescence signals would be lost in the noise of visible photons.

The aperture, the corrector ring, the mirror, and the PMT camera constitute a modified Schmidt camera design that partially corrects spherical aberration and eliminates coma aberration. The size of the aperture is optimized to keep the spot size due to spherical aberration within a diameter of 15 mm, i.e. 90% of the light from a distant point source located anywhere within the $30^o \times 30^o$ FOV of a camera falls into a circle of this diameter. This corresponds to an angular spread of 0.5^o. In comparison, the FOV of a single camera pixel is 1.5^o.

Due to its large area (13 m^2), the mirror is segmented to reduce the cost and weight of the optical system. Two segmentation configurations are used. The first one is a tessellation of 36 rectangular anodized aluminum mirrors of three different sizes (used at the 12 telescopes at the Los Leones and Los Morados sites) with an additional layer of $AlMgSiO_5$ alloy to improve reflectivity, and an aluminum-oxide layer to provide additional protection. The second is a structure of 60 hexagonal glass mirrors (of four shapes and sizes) with vacuum-deposited reflective coatings (employed at the remaining 12 telescopes in the buildings at Coihueco and Loma Amarilla) with a reflective aluminum layer covered by an

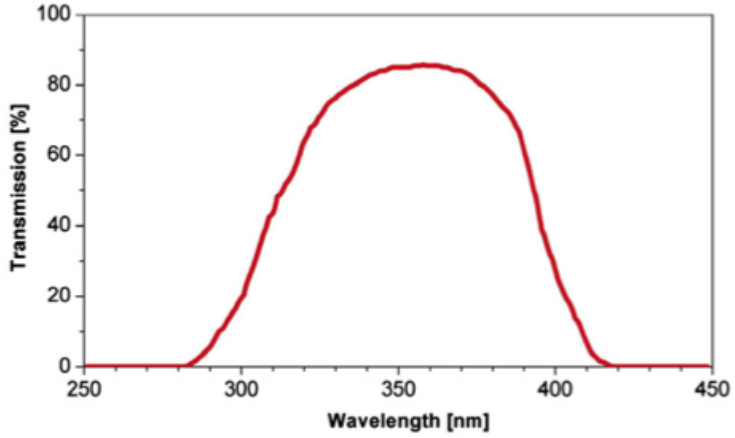

Figure 3.10: The measured transmission curve of the sample of the MUG-6 filter in the range between 250 and 450 nm.. Figure taken from [20]

additional layer of SiO_2. In both cases, the spherical inner radius of mirror segments was specified as 3400 mm, and mirror segments with measured radii in the range between 3400 and 3420mm were accepted and used for the construction. The reflectivity for both configurations has been measured at several points of each segment, and the average reflectivity at $\lambda = 370$ nm exceeds 90%.

A novel solution of the optical system with a "corrector ring" was designed to keep the advantage of a large aperture of the Schmidt system, and simultaneously simplify the production of the element, minimize its weight and cost, while maintaining the spot size within the limits of aforementioned design specification. The aperture area of the telescope with the corrector ring is almost doubled with respect to the optical system without any correcting element. The corrector ring is the circumferential part of the corrector plate of a classical Schmidt camera with one planar side and the other with an aspheric shape corresponding to a 6th-order polynomial curve. Such a surface is difficult to manufacture and therefore some optimizations were adopted to simplify the lens production. Eventually, a spherical approximation specially designed for the fluorescence detector was chosen to fulfill both price and performance requirements. The simplified corrector ring is located at the aperture and covers the annulus between radii of 0.85 and 1.1 m. Since the rings have an external diameter of 2.2m, their manufacture and transportation to the site in a single piece would have been very difficult. Therefore, each lens was divided into 24 segments of BK7 glass manufactured by Schott.

The camera is the sensitive element of a telescope. It is composed of a matrix of 440

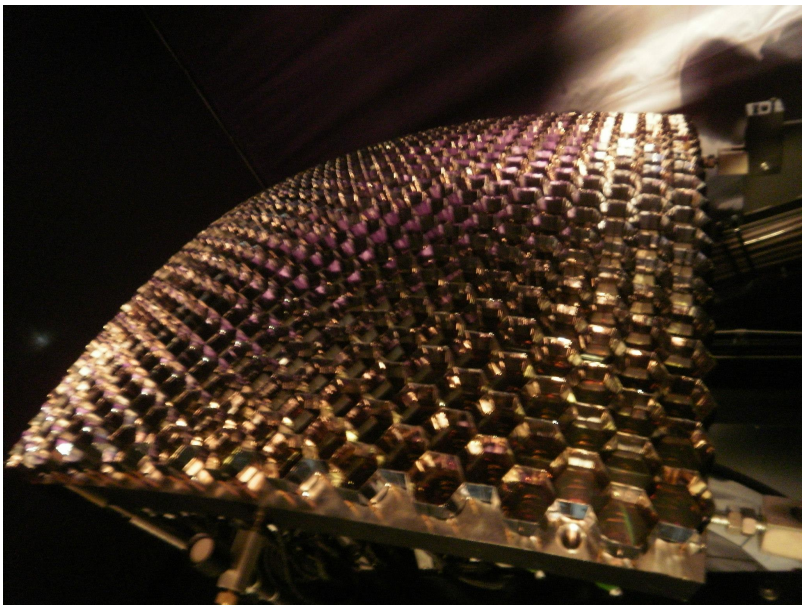

Figure 3.11: Picture of a camera at Los Leones site completely assembled with all PMTs and light collectors in place.

pixels located on the focal surface of the telescope. The camera pixels are arranged in a matrix of 22 rows by 20 columns. The corresponding field of view is of 30° in azimuth (full acceptance of one row) and 28.1° in elevation (full acceptance of one column). A cosmic ray shower is imaged on the camera as a line of activated pixels having a track-like geometrical pattern and also a clear time sequence. Each pixel is realized by a photomultiplier with a light collector. An hexagonal photomultiplier tube (PMT), model XP3062 manufactured by Photonis, is used to instrument the camera. Although their hexagonal shape represents the best approximation to the pixel geometry, a significant amount of insensitive area is nevertheless present between the photocathodes. To maximize light collection and guarantee a sharp transition between adjacent pixels, the hexagonal PMTs are complemented by light collectors. The basic element for the pixel light collector is a specially designed analog of a Winston cone realized by a combination of six "Mercedes stars". Each Mercedes star has three arms oriented 120° apart, which is positioned on each pixel vertex. Six Mercedes stars collect the light for a given pixel.

3.2.2 FD trigger

The FD telescopes are used to record fluorescence signals of widely varying intensity atop a sizeable, and continuously changing, light background. This presents a significant challenge

for the design of the electronics and data acquisition system (DAQ), which must provide a large dynamic range and strong background rejection, while accepting any physically plausible air shower. The DAQ must also allow for the robust, low-cost, remote operation of the FD telescopes. And finally, the absolute FD-SD timing offset must be sufficiently accurate to enable reliable hybrid reconstruction.

The FD electronics are responsible for anti-alias filtering, digitizing, and storing signals from the PMTs. The PMT signals are received by a set of 20 front-end boards, each one serving 22 pixels of a camera column, hosted in a crate placed on the floor below the camera. The signals are digitized continuously by 10 MHz 12 bit ADCs. The digital part of the front-end board is use to implement a First Level Trigger which involves decisions at the level of individual pixels. A Second Level Trigger logic is implemented on a separated board which read the pixel triggers generated for each channel in the 20 First Level Trigger boards. Synchronization with the front-end board is provided by a GPS clock. The Mirror PC, a robust, diskless, industry PC associated with each telescope, is used to perform the data readout and the Third Level Trigger. Finally, a single computer called the EyePC merges triggers from the six telescopes and send them to the CDAS in Malargüe.

Hardware triggers

The First Level Trigger (**FLT**) is generated using a threshold cut on the ADC signal of each pixel. A moving "boxcar" of the last n ADC samples is compared to a 14-bit threshold, where n is a fixed number of time bins that can be chosen in the range $5 < n < 16$. The threshold is dynamically adjusted to mantain a fixed pixel rate (the so-called hitrate) of 100 Hz. When the sum exceeds the threshold a pixel trigger is generated. The hit rate is measured in parallel by counters for each channel. It is used to adjust the threshold in such manner that the hit rate is kept constant at 100 Hz. under variable light conditions, such as the presence of moon and stars in the field of view of the camera. Finally, the multiplicity (the number of pixels triggered simultaneously within 100 ns) is calculated for each FLT and the full camera. The chronological sequence of multiplicity values carries information about the temporal development of the camera image.

The Second Level Trigger (**SLT**) searches for track segments at least five pixels in length. It makes use of the patterns shown on Fig. 3.12 and the rotation and mirror images of these segments. During data acquisition, some tracks will not pass through every pixel center, and therefore some PMTs along the track may not record enough light to trigger. To allow for this situation and to be fault-tolerant against defetctive PMTs, the algorithm requires only four triggered pixels out of five. Counting all different four-fold

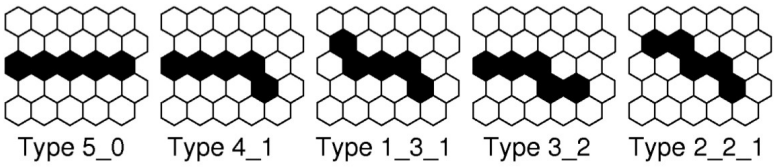

Figure 3.12: Fundamental five-pixel patterns used in the SLT. Figure taken from [20]

patterns originating from the five-pixel track a total number of 108 patterns is considered.

Software triggers

The DAQ system can handle data from three different sources: external lights (mainly artificial light sources used for atmospheric monitoring like the Central Laser Facility), calibration events, test pulses and real events. The two first types of event have an special trigger flag and are storaged in dedicated raw data files. In contrast, true shower data have to pass an additional Third Level Trigger (**TLT**) optimized to get rid of noise events like lightnings, triggers cased by muon impacts on the camera and randomly triggered pixels. In a first step the algorithm reads only the multiplicity of the events and remove noise events with more than 25 pixels. These cuts remove approximately 99% of SLTs provocated by lightnings. The correlation between the spacial arrangement and peak signal times of triggered pixels is used to discard noisy channels far off the light track on a second step. Although the exact behavior of the algorithm depends on the actual sky and atmopsheric conditions, approximately 94% of all background events are correctly identified by the TLT and less than 0.7% true showers are rejected.

Events passing the TLT trigger are sent to the EyePC, which merges coincident events from adjacent telescopes and then send an hybrid trigger, called **T3**, to the CDAS in Malargüe. The T3 acts as an external trigger for the surface array. The T3 algorithm is used to calculate a prelimanry shower direction and ground impact time with a simple online reconstruction. Whenever a T3 FD trigger is received by the CDAS, a request is sent to the SD for signals recorded close to the time at ground estimated by the FD. For each T3 trigger, the SD stations nearest the FD building (comprising approximately one quarter of the array) are read out. The FD and SD data are merged offline for subsequent hybrid analysis.

3.2.3 FD Calibration

As the number of fluorescence photons that arrive to the telescope are proportional to the deposited energy by the primary cosmic-ray, a reliable absolute calibration of the FD telescopes is essential. To ensure this a precise conversion of ADC counts to photons for each PMT must be measured. It is therefore necessary to have some method for evaluating the response of each pixel to a given flux of incident photons from the solid angle covered by that pixel, including the effects of aperture projection, optical fiber transmittance, reflection at optical surfaces, mirror reflectivity, pixel light collection, efficiency and area, cathode quantum efficiency, PMT gain, pre-amp and amplifier gains, and digital conversion. While this response could be assembled from independently measured quantities for these effects an alternative method in which a cumulative effect is measured in an end-to-end calibration is employed. There are four different and complementary procedures to ensure this:

Absolute drum calibration

The absolute calibration of the FD uses a calibrated 2.5 m diameter, 1.4 m deep light source, known as "drum" due to its shape, which is mounted at the telescope aperture. The source provides a pulsed photon flux of knwon intensity and uniformity across the aperture, and simultaneously triggers all the pixels in the camera. To produce diffuse light inside the drum, illumination is provided by a pulsed UV LED (375 ± 12 nm), mounted against the face of a 2.5 m diameter $\times$ 2.5 long Teflon™cylinder. An absolute calibration of the drum light source intensity is done using UV-silicon photodetectors.

Uniformity of the light emission from the drum surface is important, since the pixels in the FD camera view the aperture at varying angles. In addition, for each pixel, a different part of the aperture is blocked by the camera itself. The measured drum non-uniformities are small, indicating that the FD pixels see similar intensities integrated over the drum surface. While perfect drum uniformity is desirable, the present non-uniformities are acceptable small and well mapped over the surface of the drum. A ray-tracing program shows less than 1% variation in the total flux seen by the pixel, and corrections are applied for these variations.

The drum technique has been cross-checked for some pixels using remote laser shots at 337 and 355 nm. A laser pulse is shot vertically into the air with a known intensity. A calculated fraction of photons is scattered to the aperture of the FD detector. This yields a known number of photons arriving to the detector for each pixel, which views a segment of the laser beam. The response of each pixel to the known number of photons constitutes

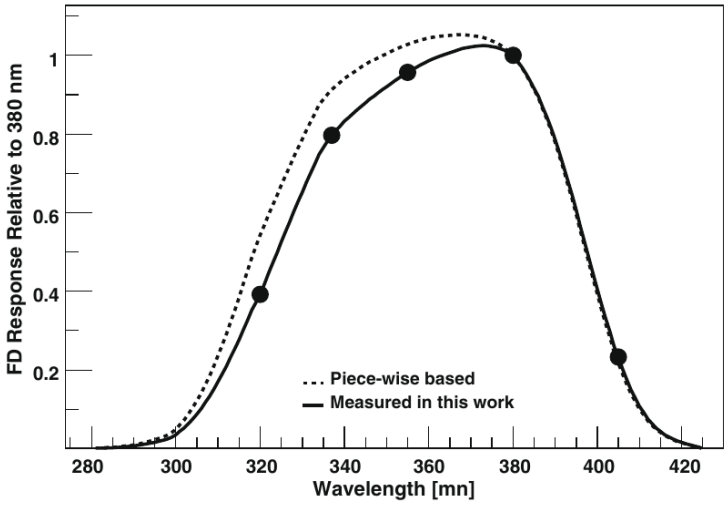

Figure 3.13: The measured FD wavelength response (solid line) compared with a curve generated in a piecewise fashion from manufacturer's data for each FD component (dashed line). Experimental measurements at five wavelengths are shown; the solid line is constrained to pass through these points. Figure taken from [21]

an absolute end-to-end calibration for those pixels.

Multi-wavelength calibration

The response of the different components of the FD is wavelength-dependent (see Fig. 3.10 for the response of the optical filter for an example), as is the fluorescence emission. Instead of a piecewise measurement of the response an end-to-end measure is obtained using different wavelengths. A flasher xenon light that covers a broad UV spectrum is mounted in the back of the drum. Relative drum intensities at wavelengths of 320, 337, 355, 380 and 450 nm have been made with the same reference PMT used for in the absolute measurements. At each wavelength the recorded response for the reference PMT, combined with the PMT quantum efficiency and corrected for light source and filter width effects, yields a quantity that is proportional to the number of photons emitted from the drum. The FD response detected using the various filters, with the drum placed in the aperture, can be combined with the results from the laboratory to form the curve of relative camera response shown in Fig. 3.13.

The relative curve for all wavelengths (solid line in Fig. 3.13) is the result of an iterated spline fit beginning with a response curve predicted from the manufacturer's specifications for the FD components (dashed line). The shape of this initial curve is dominated by the

quantum efficiency of the PMTs and the UV filter transmission. The final fit includes effects of the notch filter transmission width (15 nm FWHM), the reference PMT QE, the xenon light source emission spectrum and the relative drum intensity for each filter, all measured at the lab, and the observed FD response to the drum for each filter. The relative uncertainty at each wavelength on the curve is 5%

Relative FD calibration

The relative optical calibration system is used to monitor detector response and to track absolute calibration between drum calibrations. The system is used before and after each night of FD operation. Three positions (A, B and C) are illuminated for each camera, monitoring different groups of detector components. Light is distributed through optical fibers, from permanent installed light sources. The A fiber light source is located at the center of each mirror of the FD building, illuminating directly the camera face. The B source fibers are split near each camera, with the light directed at the mirror. The C source fibers terminate outside the aperture directed outwards. Tyvek sheets are mounted inside of the aperture shutters. The sheets are positioned such that they are opposite the fiber when the shutters are closed, and the diffuse light scattered off the Tyvek enters the aperture.

Light source on a flying platform

Recently [112], a new technique to study the optical properties of fluorescence and atmospheric Cherenkov telescopes and measure the point spread function of the Auger telescopes has been developed. A portable, point-like 375 nm light source is placed in the field of view of a telescope by an autonomous flying platform, an octocopter. The GPS and pressure-sensor-based positioning system of the octocopter can be programmed to place the light source at different distances and altitudes for a duration of up to 20 min. By illuminating the telescopes from different angles, their optical properties can be tested. Unlike the drum calibration, the pixels in the camera are not all simultaneously illuminated, and thus, a more precise determination of the response of the individual components of the telescope can be performed.

3.2.4 Hybrid Reconstruction

A hybrid detector achieves the best geometrical accuracy by using timing information from all the detector components, both FD pixels and SD stations. Each element records a

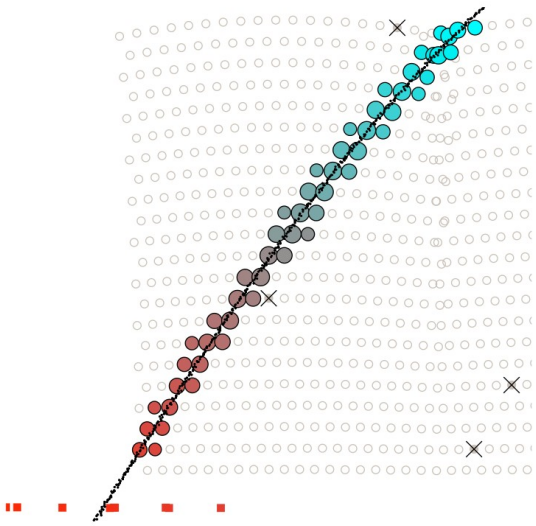

Figure 3.14: Light track of a hybrid event as seen by the fluorescence telescopes. The different colors indicate the timing sequence of the triggered pixels. The full line is the fitted shower-detector plane (see text for explanation). The red squares in the bottom represent the SD stations that also triggered in this event. The crosses mark the camera pixels that had a signal within the time of the trigger, but were marked by the reconstruction algorithm as too far either in distance (to the SDP) or in time (to the time fit). Figure taken from [20]

pulse of light from which is possible to determine the time of the pulse and its uncertainty. Each trial geometry for the shower axis yields a prediction for the signal arrival times at each detector component. Differences between actual and predicted times are weighted using their corresponding uncertainties, squared and summed to construct a χ^2 value. The hypothesis with the minimum value of χ^2 is the reconstructed shower axis.

In the FD, the cosmic rays are detected as a sequence of the triggered pixels on the camera. An example of an event propagating through two adjacent FD telescopes is presented in Fig. 3.14. The first step in the analysis is the determination of the shower-detector plane (SDP). The SDP is the plane that includes the location of the eye and the line of the shower axis (see Fig. 3.15). Experimentallly, is the plane through the eye which most nearly contains the pointing directions of the FD pixels centered on the shower axis (see fitted line in Fig. 3.14). Using a known axis provided by the CLF, the SDP reconstruction error can be evaluated by comparing the space angle between the normal vector to the experimentally determined SDP and the known true normal vector. This uncertainty in the SDP is of the order of 0.5^{o} depending on, for example, the length of the observed track on the camera.

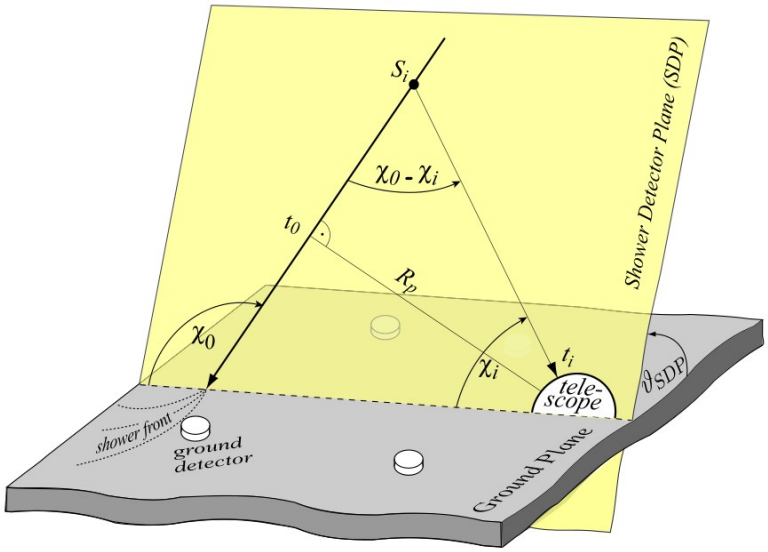

Figure 3.15: Illustration of the geometrical shower reconstruction from the observables of the FD. Figure taken from [22]

Next, the timing information of the pixels is used for reconstructing the shower axis within the SDP. As illustrated in Fig. 3.15, the shower axis can be characterized by two parameters: the perpendicular distance R_p from the camera to the track, and the angle χ_0 that the tracks makes with the horizontal line in the SDP. Each pixel that observes the track has a pointing direction which makes an angle χ_i with the horizontal line. Let t_0 be the time when the shower front on the axis passes the point of closest approach R_p to the camera. The light arrives at the camera at the time:

$$\widehat{t_i} = t_0 + \frac{R_p}{c} \tan\left(\frac{\chi_0 - \chi_i}{2}\right) \tag{3.11}$$

The best fit for the set of parameters R_p, χ_0 and t_0 will be obtained by minimizing the difference between the expected $\widehat{t_i}$ and the t_i measured by the FD:

$$\chi^2_{\mathrm{FD}} = \sum_i \left(\frac{\widehat{t_i} - t_i}{\sigma_{t_i}}\right)^2 \tag{3.12}$$

Using the fast sampling electronics, this monocular reconstruction may achieve excellent accuracy. However, this accuracy is limited when the measured angular speed $d\chi/dt$ does not change much over the observed track length. An example is shown in Fig. 3.16. For

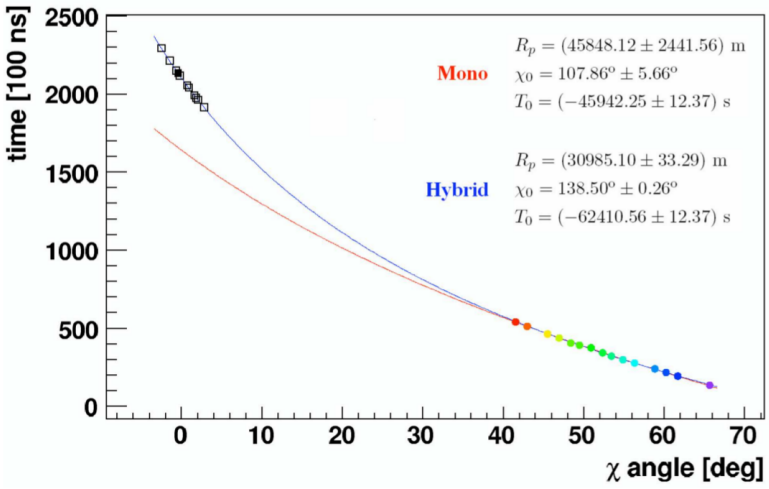

Figure 3.16: Functional form that correlates the time of arrival of the light at each pixel with the angle between the pointing direction of that particular pixel and the horizontal line within the SDP. FD data (color points) and SD data (squares) are superimposed to the monocular (red line) and hybrid (blue line) reconstruction fits. The full square indicates the SD station with the highest signal. Figure taken from [20]

these events (usually short tracks) there is a small curvature in the funcional form of Eq. (3.11) such that there is a family of possible (R_p, χ_0) axis solutions. R_p and χ_0 are tightly correlated, but neither value is well constrained. This leads to uncertainty in other showers parameters, including the reconstructed shower energy.

The fit degeneracy can be broken by combining the timing information from the SD stations with that of the FD telescopes. The arrival time of the shower to a SD station can be considered as an additional "pixel" at ground levels imposing a time constraint and thus breaking the degeneracy in the FD-only (or mono) solution. Assuming a shower front, the expected arrival time $\widehat{t}_{\text{ground}}$ of the shower to a surface station is given by:

$$\widehat{t}_{\text{ground}} = t_0 + \frac{\vec{R}_{\text{ground}} \cdot \vec{n}_{\text{axis}}}{c} \tag{3.13}$$

where $\vec{R}_{\text{ground}}$ is the vector from the eye to the SD station and $\vec{n}_{\text{axis}}$ is an unitary vector in the shower direction. A χ^2 function, similar to Eq. (3.12) can be defined for the SD timing information:

$$\chi^2_{\text{SD}} = \frac{1}{R^2_{\text{core}}} \left(\frac{t_{\text{ground}} - \widehat{t}_{\text{ground}}}{\sigma_{t_{\text{ground}}}} \right)^2 \tag{3.14}$$

where t_{ground} and $\sigma_{t_{\text{ground}}}$ are the trigger time of the SD station and its time-variance,

and $R_{\rm core}$ is the distance from the surface station to the shower core. Finally, the fit is performed minimizing the sum of the contributions given by the FD and SD detectors (equations (3.12) and (3.14)):

$$\chi^2 = \chi^2_{\rm FD} + \chi^2_{\rm SD} \tag{3.15}$$

The fit uses the timing information from one station, usually the one with the highest signal. In fact, this is the only stage in the so-called hybrid reconstruction procedure where the SD information is used. As an example, Fig 3.16 shows the same event reconstructed first with fluorescence information (mono, red line) using Eq. (3.11) and using the hybrid costraint (blue line) from Eq.(3.13).

Using the timing information from the telescope pixels together with the surface stations to reconstruct real air showers, a core location resolution of 50 m. is achieved. The typical resolution for the arrival direction of cosmic rays is $0.6^{\rm o}$.

Once the geometry of the shower is known, the light collected at the aperture as a function of time can be converted to energy deposit at the shower as a function of slant depth. For this purpose, the light attenuation from the shower to the telescope needs to be estimated and all contributing light sources need to be disentangled: fluorescence light, direct and scattered Cherenkov light, as well as multiple-scattered light. This procedure will be explained in detail in section 4.4.

In principle, the total energy deposited by the electromagnetic component of the shower can be obtained from the integral of the energy deposited at each level:

$$E_{\rm em} = \int_0^\infty \frac{{\rm d}E}{{\rm d}X} dX \tag{3.16}$$

The determination of the electromagnetic energy via this equation could be only performed in the rare cases when the full shower profile was observed. However, the limited FoV of the telescopes does not allow to observe the full profile and therefore a function to extrapolate the profile outside the FoV is needed. The usual choice is the well-known Gaisser-Hillas function (Eq. (2.2) in section 2.1) that in terms of energy deposition can be written as:

$$\frac{{\rm d}E}{{\rm d}X}(X) = \frac{{\rm d}E}{{\rm d}X_{\rm max}} \cdot \left(\frac{X - X_0}{X_{\rm max} - X_0} \right)^{(X_{max} - X_0)/\lambda} \cdot \exp\left(\frac{\rm X_{max} - X}{\lambda} \right) \tag{3.17}$$

where $\frac{{\rm d}E}{{\rm d}X_{\rm max}}$ is the total energy deposited at the shower maximum depth. To obtain the calorimetric energy of the shower the reconstructed shower profile must be fitted to this G-H function and integrating it. To obtain the primary energy the so-called "invisible energy" needs to be taken into account. Although most of the energy is transferred to the

electromagnetic component of the shower, a significant fraction is carried by undetected neutrinos and muons that need to travel long distances to deposit their energy. Another contribution comes from the hadrons that arrives at ground level carrying a fraction of energy that does not produce fluorescence radiation. To estimate the fraction of the total energy that corresponds to invisible energy a novel parameterization [113] that does not rely on Monte Carlo simulations (and thus, is independent of the selected hadronic model) is used:

$$\frac{E_{\rm inv}}{1\rm EeV} = 0.174 \left(\frac{E_{\rm em}}{1\rm EeV} \right)^{0.914} \tag{3.18}$$

3.3 Atmospheric Monitoring

A ground-based cosmic ray experiment like the Pierre Auger Observatory uses the atmosphere as a calorimeter. Thus, atmopsheric conditions have to be properly monitored since they affect both the longitudinal and the lateral development of the shower. The FD is particularly sensitive to the atmosphere properties since the emission of fluorescence light depends on variables like temperature, pressure or humidity. Furthermore, a precise determination of the fluorescence light emitted by a cosmic ray and measured by telescopes must also take into account the attenuation of the light in its passage from the emission point to the detector. The effect of these atmosphere properties on the detection of cosmic rays using the fluorescence technique will be reviewed on Chapter 4.

To obtain a reliable calorimetric information from the fluorescence stations, the atmospheric conditions at the experiment's site need to be constantly monitored. In order to do so, an extensive atmospheric monitoring program is carried out at the Pierre Auger Observatory.

3.3.1 Lidar

Four elastick backscatter lidar (an acronym for LIght Detection And Ranging) stations [114] are located near each of the FD sites. A lidar register and analyze the backscattered light pulses by the atmosphere and provides information on clouds and aerosols. Each system includes an UV laser source and three 80 cm diameter parabolic mirrors to focus the back-scattered laser light onto a PMT tube. The laser and mirrors are mounted on a steering frame that allows a complete scanning of the sky. They are configured to operate in two different modes. In the default operational mode, the LIDAR system is continuously scanning the sky outside the FoV of the fluorescence telescopes in two orthogonal planes, one of them parallel to the back wall of the fluorescence building, with

a maximum zenith angle of 45°, or in discrete scans at a few fixed locations to obtain larger statistics. These data provide useful info about cloud coverage, inhomogeneities or the vertical aerosol distribution. In the second mode, the so-called *shoot-the-shower*, the system interrupts the autoscan to study the air region where an interesting air shower has been developed in order to determine the light transmission between the shower location and the FD. In this case the shots are directed inside the FoV of the telescopes. For a good quality hybrid event the shower plane, obtained in a preliminary fast reconstruction, is sent to the corresponding LIDAR system in order to activate the shoot-the-shower procedure. In this case, the system scans the vicinity of the air shower providing real-time information about the atmospheric conditions.

3.3.2 CLF/XLF

The Pierre Auger Observatory has two-high powered laser facilities called the Central Laser Facility (CLF) and the eXtreme Laser Facility (XLF) [115], both located near the geometrical center of the SD array. Both facilities contain a frequency-tripled YAG laser that has a wavelength of 355 nm, which is near the middle of the nitrogen spectrum that is produced by air showers, making it optimal for the testing and calibration of the FDs.

The laser facilites have been designed to perform important tasks for the study of the atmosphere as well as detector performance:

- **Atmospheric monitoring:** the laser tracks can be used to measure the Vertical Aerosol Optical Depth (VAOD) as a function of height in an independent way from LIDAR systems. Sets of laser shots fired every quarter hour are combined to provide an hourly measurement of the aerosol distribution with height that is stored in a database.

  Since both CLF and XLF vertical shots are simultaneously detected by all four FD stations, the VAOD can be obtained from signals measured in different positions at the perimeter of the array. Comparisons between them will provide a monitoring of the horizontal uniformity of the atmosphere across the aperture of the observatory.

- **Photometric resolution:** both laser shots and air shower energies can be reconstructed using the FD in a similar way. The data proccesing requires that the signal must be corrected for detector gain and atmospheric transmission. Since the laser energy is measured for each shot with a calibrated monitor, the comparison with the reconstructed energy gives an estimate of the end-to-end photometric resolution and

fixes the period, depending on viewing conditions, where the energy reconstruction is more reliable.

- **Cross-check of the absolute calibration:** for nights with a negligible aerosol content, the comparison of the measured and reconstructed laser energy can be used as a cross-check for the standard drum calibration, as was explained in section 3.2.4.
- **Geometry reconstruction accuracy:** the geometry of laser shots can be reconstructed in a similar way that EAS tracks. Besides giving an estimate of the angular resolution since the true laser location and pointing direction are known, both facilities can be used to debug and improve the software employed for geometrical reconstruction of the showers.
- **Other applications:** in addition to the previously mentioned applications, both facilities can be used to measure the relative timing between different FD eyes as well as between FD and SD. They can also be used as a simple test to know if the cameras are properly working and if they are able to detect light arriving from the array center. Sweeps of inclined shots are also used to test the FD mirror pointing directions.

3.3.3 Rapid Atmospheric Monitoring System

As mentioned before, weather conditions near ground, and the height-dependent atmospheric profiles of temperature, pressure, water vapor pressure affect the production of fluorescence light and the Rayleigh scattering of the light between the air shower and the detector. To obtain precise measurements of these parameters intermittent meteorological radio soundings were carried out at the Pierre Auger Observatory site [116]. The profiles from the weather balloons were averaged to obtain local monthly models. To obtain a precise measurement of atmospheric profiles with radio soundings (and thus ensure a high-quality reconstruction of the most interesting events) shortly after the detection of particularly high-energy air-showers, a system called *Balloon-the-shower* was developed. This system, however, needed a lot of human and material resources and a less expensive alternative was investigated [117].

The Global Assimilation Data System (GDAS) is an atmospheric model developed at the National Centers for Environmental Prediction (NCEP). It is the system used by the Global Forecast System (GFS) model to place observations into a gridded model space for the purpose of starting, or initializing, weather forecasts with observed data. The data comes from instruments sited at locations on every continent. Land-based (in situ)

observations include temperature, dew point, relative humidity, precipitation, wind speed and direction, visibility, atmospheric pressure, and types of weather occurrences such as hail, fog, and thunder. Because of the lateral homogeneity of the atmospheric variables across the Auger array, only the 35° S, 69° W point of the grid (located near the north-eastern part of the array) is needed to describe the atmospheric conditions.

In addition, on top of every FD site, IR cloud cameras are installed. They provide 2D images of the whole field of view every five minutes. Combined with the LIDAR measurements, they are used to obtain a three-dimensional map of the clouds above the Observatory. Finally, the F/Photometric Robot Atmospheric Monitor (FRAM) is an optical telescope located near Los Leones FD site. Its primary objective is the determination of the wavelength dependence of the extinction caused by Rayleigh and Mie scattering. Since its installation in 2005, the FRAM telescope has also been involved in automatic observations of optical transients of gamma-ray bursts.

3.4 Low Energy enhancements

The SD array of the Pierre Auger Observatory reaches full efficiency above $10^{18.5}$ eV. Using the hybrid trigger of the FD explained in Section 3.2.2, this threshold can be lowered to $E \sim 10^{18}$ eV. However, a better discrimination between astrophysical models requires the knowledge of the evolution of the cosmic ray composition along the transition region starting at the second knee ($E \sim 10^{17}$ eV). With the aim of extending the efficiency of the Observatory down to this energy, several improvements over the original design have been developed.

3.4.1 AMIGA

The Auger Muon Infill Ground Array (AMIGA) [118] consists of a more dense array of water Cherenkov tanks deployed inside the regular 1.5 km regular array, near the Coihueco site, complemented with muon counters buried underneath. A total of 61 tanks with a 750 m grid spacing that extend the full efficiency down to $E = 3 \cdot 10^{17}$ eV are already deployed and taking data [119]. The array of scintillators, that will be buried next to each station is now being installed. The first unitary cell, composed of 30 m^2 counters is expected to be completeb in the near future and will be used to validate the detection technique and detection design.

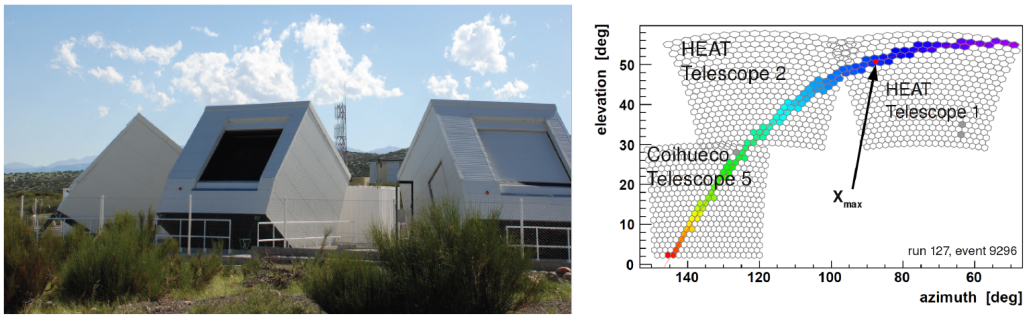

(a) (b)

Figure 3.17: Left: Photo of the three HEAT buildings in tilted mode. Right: Example of a low energy event display recorded by two HEAT and one Coihueco cameras. Figures taken from [23].

3.4.2 HEAT

The High Elevation Auger Telescope (HEAT) [23], located near the Coihueco fluorescence building, is composed of three telescopes with the same Schmidt optics as the standard Auger FD that can be tilted 30° (as seen in Fig. 3.17a) using an electrically driving hydraulic system. When tilted, they have a field of view from 30° to 60° in elevation. Showers with energy below 10^{18} eV develop higher in the atmosphere and can not be detected with enough quality by the regular FD telescopes. Working together, HEAT and Coihueco telescopes have a combined FoV of $0° - 60°$ as they record different and complementary parts of these low-energy showers, as can be seen inFig. 3.17b . The location, near AMIGA, also makes possible a combined low-energy hybrid spectrum.

3.5 New UHECR detection techniques

As a world-class UHECR detection facility, the Pierre Auger Observatory has a lot of advantages as a test site for the feasibility of new detection techniques, based on radio and microwave emissions. Both the SD array and FD telescopes can be used to trigger prototype detectors or cross-check event features detected by these prototypes.

3.5.1 AERA

Although the emission of radio pulses in the MHz band was first detected in the 1960s [120], the realization of comprehensive radio detector was not feasible until the development of fast-digital oscilloscopes in the past two decades. The Auger Engineering Radio Array

(AERA) [24] was designed to instrument a sensitive area of 10km^2 with 160 stations and isthus the first detector with sufficient collecting area to make possible the measurement of radio signals of air showers beyond 10^{18} eV. As an engineering array, AERA main mission is testing different technical solutions to optimize the radio technique for future large scale observatories. All the stations have the ability to self-trigger on radio signal although a 100 % has not been achieved yet and an external trigger like the SD array is needed. Recently the Auger collaboration has approved an upgrade to AERA, that will cover all the Infill array. The deployment of new stations will begin in March 2015.

All stations feature two antennas, one aligned in the geomagnetic north-south direction and one in the east-west direction. The signals of both antennas are supressed in the frequency range outside 30 MHz and 80 MHz by an analogue bandpass filter. After amplification, the signals of both antennas are sampled with ADCs, digitally stored and transferred to the CDAS. AERA is already taking data and have measured several events in coincidence with both the SD and FD detectors that could increase the reconstruction accuracy for the primary mass.

3.5.2 Microwave detectors: EASIER. AMBER and MIDAS

The microwave emission by UHECRs via the so-called "molecular bremsstrahlung" process is a recently discovered phenomenon [121] that have opened the possibility of new detection techniques. Various detectors that try to measure this alleged radiation in the GHz band have been already installed in the Pierre Auger Observatory [25]:

AMBER (Air shower Microwave Bremsstrahlung Experimental Radiometer) and MIDAS (MIcrowave Detection of Air Showers) are imaging telescopes like an FD, instrumenting an array of feed horn antennas at the focus of a parabolic dish. The major difference between both prototypes is the triggering system. MIDAS uses a self-triggering system while AMBER works with a modified version of the SD T3 trigger. AMBER prototype was first tested at University of Hawaii and is now installed near the Coihueco FD site, while it has been taking data for almost two years. MIDAS, first tested at the University of Chicago, is installed near Los Leones and has been taking data since the beginning of 2013.

EASIER (Extensive Air Shower Identification using Electron Radiometer) uses a different approach. It is a radio detector array integrated in the SD regular array that not only detects radiation in the GHz band but also, like AERA, detects the radio pulses in the MHz band. It takes advantage of the SD communication and trigger system. 61 antennas have been deployed in the field so far and they have already recorded three signals

in coincidence with the SD detectors.

(a) AERA antenna

(b) EASIER antenna mounted on an SD detector

(c) AMBER

(d) MIDAS

Figure 3.18: Photos of the different Auger detectors in the MHz and GHz bands. Fig. 3.18a taken from [24], Figs. 3.18b and 3.18c taken from [25]

Chapter 4

Effect of the Fluorescence Yield on the air-shower reconstruction

Charged particles of the air shower, mainly electrons/positrons, produce fluorescence radiation that is detected by ground based telescopes. Using this technique, fluorescence telescopes register the longitudinal development of the EM component of the shower providing two relevant parameters. The first one is the total energy deposition, that is a calorimetric measure of the shower energy. The primary energy of the cosmic ray can be evaluated adding the invisible energy (nearly model independent). In addition, the atmospheric depth at which the shower reaches its maximum, $X_{\max}$, is directly measured by this techniqueand as is well known, for a given energy, this parameter is related with the mass of the primary cosmic ray.

In this technique the key parameter is the so called air-fluorescence yield, FY, that is, the number of fluorescence photons produced per unit of energy deposited in the atmosphere. Actually, the fluorescence yield is characterized by a number of parameters: the absolute value at certain reference conditions, the relative intensities of the molecular bands of the air-fluorescence spectrum and and the various parameters determining the atmospheric dependences. They have been measured in dedicated laboratory experiments and available measurements show non-negligible disagreements. Since the shower reconstruction is very sensitive to these parameters, a change in the FY assumption might have implications in the results, in particular the energy spectrum and mass composition of cosmic rays.

The processes involved in fluorescence emission and its atmospheric dependences will be discussed in section 4.1. The available FY data will be presented in section 4.2. The effect of the selected FY on the shower reconstruction can be predicted using a simple

analytical approach developed in this work, published in [122], that will be presented in section 4.3. An accurate evaluation of the effect of the FY on the shower parameters needs the reconstruction of MC or real showers. The analysis procedure used by the Pierre Auger Collaboration is detailed in 4.4 including the implementation of several FY values. As a simple example, both methods (i.e., the analytical approach and the detailed reconstruction analysis) will be applied to evaluate the effect of a change in the absolute FY recently applied by the Auger collaboration as well as the effect of implementing some atmospheric dependencies.

Two UHECR experiments using different asumptions of FY are expected to obtain results in disagreement. In section 4.5 we will show that for the comparison of the corresponding energy scales, the wavelength dependence of the optical efficiency of the telescope matters, a result published in [123]. An analytical procedure similar to that of section 4.3 including the effect of the optical efficiencies will be discussed. Also, it will be shown the application of this procedure to the analysis of real data.

4.1 Fluorescence Yield

Electrons passing through the atmosphere deposit energy due to inelastic collisions with air molecules. A small fraction of the energy deposit gives rise to the production of nitrogen fluorescence in the spectral range of interest (290-430 nm). This radiation is also quenched by air molecules in a way that depends on the atmospheric conditions. A simple expression for the FY and its atmospheric dependences will be presented next.

4.1.1 Physical processes involved in the generation of air-fluorescence light

Fig. 4.1 shows a scheme of the molecular levels of N_2 and N_2^+. As is well known, each electronic state is split in vibrational levels v. In addition, each vibrational level is split in rotational sub-levels following a complex structure. Electron collisions excite molecular nitrogen in the ground state to upper levels. Down going arrows in Fig. 4.1 represent optically allowed transitions. Each electronic transition gives rise to an spectral band system, each band corresponding to a given combination of upper and lower vibrational levels v–v'. The width and shape of these molecular bands is determined by the rotational structure.

In the spectral range of interest, nitrogen fluorescence comes basically from the Second Positive system $C^3\Pi_u \rightarrow B^3\Pi_g$ of N_2 and the First Negative System $B^2\Sigma_u^+ \rightarrow X^2\Sigma_g^+$

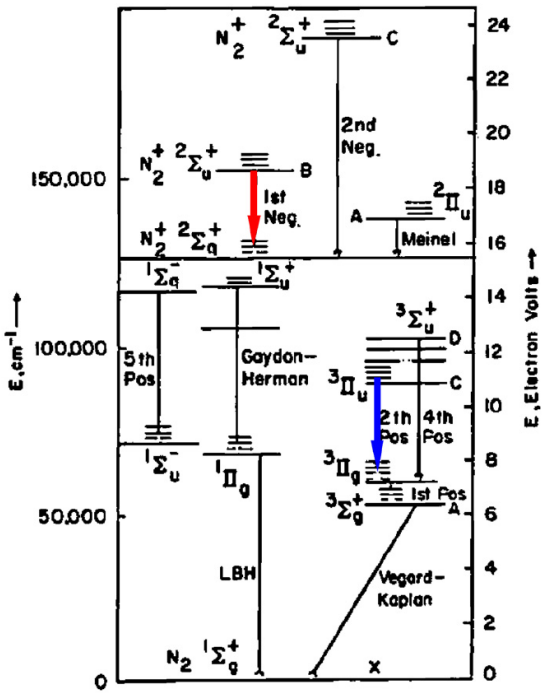

Figure 4.1: Molecular levels of N_2 and N_2^+. Broad arrows represent the main optical transitions. Figure taken from [26]

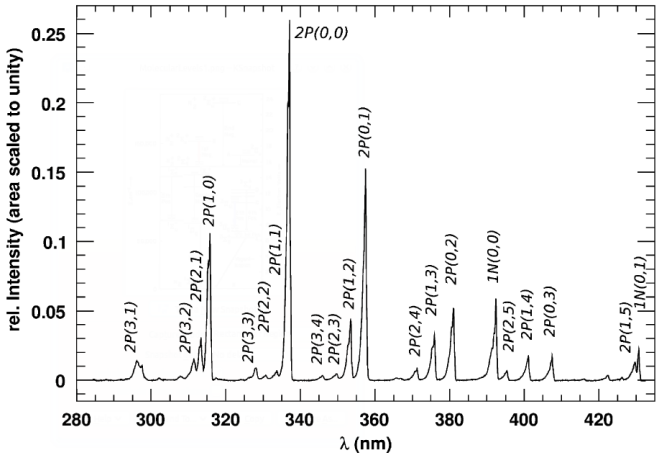

Figure 4.2: Air-fluorescence spectrum excited by 3 MeV electrons at 800 hPa as measured by the AIRFLY Collaboration. [27]

of N_2^+ (see Fig. 4.1) which in the air-fluorescence community are usually denoted as the 2P and 1N systems, respectively. Apart from these transitions, the weak bands of the N_2 Gaydon-Herman (GH) system have been observed in the air-fluorescence spectrum. Fig. 4.2 shows the air-fluorescence spectrum between the 280 and 430 nm obtained by the AIRFLY collaboration [27] at atmospheric pressure.

Upon passage of an electron, the probability of exciting a nitrogen molecule from its ground state to an excited level v is given by the excitation cross section σ_v. In the absence of other processes, the number of v–v' photons emitted per incident electron and unit path lenght is given by:

$$\varepsilon_{vv'} = N\sigma_v \frac{A_{vv'}}{A_v} = N\sigma_v B_{vv'} = N\sigma_{vv'} \tag{4.1}$$

where N is the number of nitrogen molecules per unit volume, $B_{vv'}$ is the ratio between the partial $A_{vv'}$ and total $A_v = \sum_{v'} A_{vv'}$ radiative transition probabilities, called the *branching ratio* and $\sigma_{vv'}$ is the so-called optical cross section.

4.1.2 Fluorescence quenching and atmospheric dependencies

Non-radiative molecular de-excitation by collision with other molecules of the medium is also possible. This process is known as *collisional quenching* and becomes more important with increasing pressure. The total de-excitation probability is the sum of the radiative transition probability A_v and the collisional transition probability A_v^c and therefore, the probability of v–v' photon emission diminishes as the pressure grows. At a given tempera-

ture, $A_v^c(P)$ is proportional to the collision rate and thus to the pressure P. It is possible to define a characteristic pressure P', at which the probability of collisional de-excitation equals the radiative one, $A_v^c(P') = A_v$,

$$A_v^c = A_v \frac{P}{P'_v} \tag{4.2}$$

This collisional quenching introduces an additional pressure dependence in $\varepsilon_{vv'}$. If we replace A_v by $A_v + A_v^c(P)$ into Eq. (4.1) we obtain .

$$\varepsilon_{vv'}(P) = N\sigma_{vv'} \frac{1}{1 + P/P'} \tag{4.3}$$

where $1 + P/P'$ is the so-called Stern-Volmer correction factor.

For shower reconstruction purposes it is more convenient to measure the fluorescence yield in terms of number of fluorescence photons emitted per unit deposited energy. If we introduce the deposited energy per unit track lenght, $(\mathrm{d}E/\mathrm{d}x)_{\mathrm{dep}}$, into Eq.(4.3) we obtain the fluorescence yield Y_λ for a photon of wavelength λ emitted in a transition v–v':

$$Y_\lambda(P, t, h) = \frac{\varepsilon_{vv'}}{(\mathrm{d}E/\mathrm{d}x)_{\mathrm{dep}}} = Y_\lambda^0 \frac{1}{1 + P/P'_v(T, h)} \tag{4.4}$$

where Y_λ^0 represents the fluorescence yield for that molecular band in the absence of quenching, that is, at $P \to 0$.

All atomic and molecular components of the atmosphere can act as quenchers for excited nitrogen (e.g. oxygen, water vapor, nitrogen itself); oxygen molecules in particular are very efficient quenchers of air fluorescence. For a given molecular band, the characteristic pressure for a mixture of gases follows the law

$$\frac{1}{P'_{\mathrm{air}}} = \sum_i \frac{f_i}{P'_i} \tag{4.5}$$

where f_i is the fraction of molecules of type i (including nitrogen) and the partial characteristic pressures P'_i can be described as:

$$P'_i = \frac{kT}{\tau^{\mathrm{r}}} \frac{1}{\sigma_{\mathrm{N}i}\overline{v}_{\mathrm{N}i}}, \quad \overline{v}_{\mathrm{N}i} = \sqrt{\frac{8kT}{\pi\mu_{\mathrm{N}i}}} \tag{4.6}$$

In these relations k is Boltzmann constant, T the temperature of the gas, $\tau^{\mathrm{r}} = 1/A_v$ the radiative lifetime of the corresponding upper level, $\sigma_{\mathrm{N}i}$ is the cross section for collisional

de-excitation of the excited nitrogen molecule by molecules of type i, and $\overline{v}_{\mathrm{N}i}$ and $\mu_{\mathrm{N}i}$ are the relative velocity and reduced mass of the two body system N–i, respectively.

For dry air Eq. (4.5) might be simplified as a sum of nitrogen and oxygen with $f_{\mathrm{N}} = 0.79$ and $f_{\mathrm{O}} = 0.21$. However, it is more practical to obtain a measure of P'_{air}, instead of a characteristic pressure for each component, i.e. P'_N and P'_O for nitrogen and oxygen, respectively.

A particular interesting case is the effect of water vapor, as it is an efficient quencher with an altitude-dependent presence in the atmosphere. The characteristic pressure of humid air, P'_{hum}, containing a fraction f_{w} of water vapor, that is, a water vapor pressure $P_{\mathrm{w}} = f_{\mathrm{w}}P$ is related to that of dry air, P'_{dry}, by:

$$\frac{1}{P'_{\mathrm{hum}}} = \frac{1}{P'_{\mathrm{dry}}\left(1 - \frac{P_{\mathrm{w}}}{P}\right)} + \frac{P_{\mathrm{w}}}{P}\frac{1}{P'_{\mathrm{w}}} \tag{4.7}$$

Apart from pressure and humidity, air fluorescence depends on a third atmospheric variable, that is, temperature, T. Eq. (4.6) shows a net temperature dependence of P' growing with $\sqrt{T}$. However, $\sigma_{\mathrm{N}i}$ is expected to be a function of the kinetic energy of the colliding particles and, thus, of T. Although data on this temperature dependence is still scarce a $\sigma_{\mathrm{N}i} \propto T^{\alpha}$ power law can be assumed [124]. Recent measurements have confirmed this additional temperature dependence of the fluorescence emission [125, 126]. Taking this into account, the temperature dependence of P' in dry air becomes:

$$P'(T) = P'(T_0)\left(\frac{T_0}{T}\right)^{\alpha-1/2} \tag{4.8}$$

where $P'(T_0)$ is the characteristic pressure measured at a reference temperature, T_0. Quenching collision is a very complex problem of molecular physics and our knwoledge on the various fluorescence dependences relies on experimentally determined P' values.

4.2 Fluorescence Yield data

The reconstruction of the EAS parameters using the fluorescence technique requires a set of fluorescence yield data, obtained from dedicated laboratory measurements. This dataset can be enumerated as follows:

1. The absolute value in dry air at a reference pressure P_0 and temperature T_0 integrated over the spectral range of the telescope. Alternatively, the absolute value for a single intense band (e.g. $\lambda = 337$ nm, corresponding to the 2P(0,0) transition) at a given

pressure can be used.

2. The relative band intensities in dry air at same P_0 and T_0, from which the fluorescence yields for the other bands of the spectrum, Y_λ, can be calculated.

3. The values of P' in dry air at the reference temperature for all bands. Measurements of P'_N and P'_O could also be used for this purpose.

4. The values of P'_w for all bands.

5. The T dependence of $\sigma_{\mathrm{N}i}$ for all bands. In principle, values of α_λ for each quencher, including water vapor, would be necessary. This information is, however, still very limited.

A data set containing 1, 2 and 3 allows obtaining the total fluorescence yield for dry air as a function of P at T_0. If the T dependence of $\sigma_{\mathrm{N}i}$ is neglected, the value of Y for dry air at any given P, T conditions can also be calculated with these date. Adding 4 the air-fluorescence yield can be calculated for humid air. Finally, 5 provides a more accurate extrapolation at temperatures far from the reference one (e.g. at high altitude).

4.2.1 Fluorescence yield datasets

Although many measurements of the fluorescence parameters are avalaible in the literature (see [127–129] for some examples) this work will be focused on the air-fluorescence yield datasets that have been employed by UHECR experiments.

Kakimoto-Bunner

The first air-fluorescence yield dataset for cosmic rays applications were reported by Bunner in the late 60s [56]. His values for the relative intensities for nitrogen bands were still used in the HiRes experiment, along with the much modern values for P' and absolute yield reported by Kakimoto *et al.* [130]. This Kakimoto-Bunner dataset consists in the absolute FY measured by Kakimoto *et al.* distributed following the spectrum measured by Bunner (see Fig. 4.3c). Instead of the P' formulation described in section 4.1, Kakimoto *et al.* used two parameters, A and B, to describe the atmospheric dependences of the FY. In particular, B is related to P' through:

$$\rho B\sqrt{T} = P/P' \tag{4.9}$$

where ρ is the air density. Both the humidity effect and the temperature dependence of the collisional cross-section were neglected in this dataset. More details about this dataset can be found in [131].

Nagano-AIRFLY dataset

The Pierre Auger collaboration used this dataset in the period 2004-2012. The scale of the fluorescence yield is given by the absolute value of the 337 nm band, $Y_{337} = 6.38$ ph/MeV, at 800 hPa and 293 K as measured by Nagano *et al.* [132]. The fluorescence yield at a given wavelength, Y_λ, is obtained using the relative intensities of the spectrum bands I_λ ($I_{337} = 1$) along with the corresponding characteristic pressures P'_λ measured in [27] by the AIRFLY collaboration. The AIRFLY collaboration has also measured the most comprehensive set of α and P'_w parameters [125] which were implemented in the Auger data analysis Y_λ at any atmospheric condition is obtained as:

$$\begin{aligned} Y_\lambda(P,T,P_w) &= Y_\lambda(P_0,T_0,0)\cdot\frac{1+P_0/P'(T,P_w)}{1+P/P'(T,h)} \\ &= Y_{337}(P_0.T_0,0)\cdot I_\lambda(P_0.T_0,0)\cdot\frac{1+P_0/P'_\lambda(T,P_w)}{1+P/P'_\lambda(T,P_w)} \end{aligned} \tag{4.10}$$

AIRFLY dataset

In 2012 the Auger collaboration updated the absolute value of the 337 nm band to the more precise result measured by the AIRFLY collaboration [133]. The new value at the same atmospheric conditions (800 hPa, 293 K) is $Y_{337} = 7.07$ ph/MeV, 10% larger than the previous one. The rest of the parameters, including relative intensities, P' values and atmospheric dependences, remain the ones measured by AIRFLY and described in the previous section. The Auger dataset is shown in Fig. 4.3a.

Kakimoto-FLASH dataset

The Telescope Array collaboration is presently using the integral absolute fluorescence yield value for the 280-420 nm interval measured by Kakimoto *et al.* [130], completed with the measurements by the FLASH collaboration [134] for those bands that fall out of the spectrum measured by Kakimoto *et al.* The relative intensities are those measured by FLASH, while the P' values are obtained from the Kakimoto measurements. The value for the 337 nm band at 1013 hPa and 293 K is 4.29 ph/MeV (see Fig. 4.3b). Neither the dependence of the collisional cross section nor the humidity effect is implemented in this dataset.

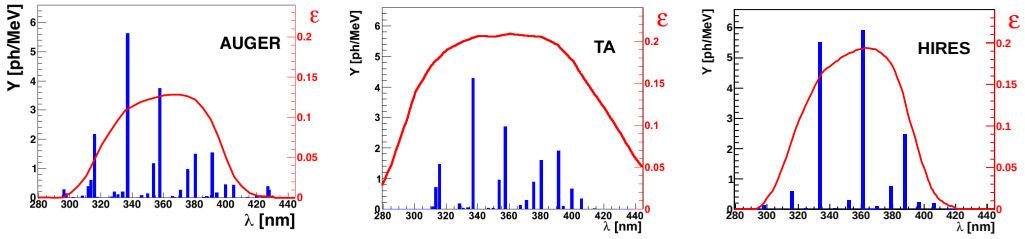

(a) (b) (c)

Figure 4.3: Comparison of AIRFLY (left), Kakimoto-FLASH (center) and Kakimoto-Bunner (right) measurements of the air-fluorescence yield at 1013 hPa and 293 K (blue bars). The red line correspond to the optical efficiency, ε, of the fluorescence detectors for both experiments.

4.2.2 Optical efficency of the telescopes

The optical efficiency of the telescopes, ε, as will be explained in the next section, is also important to evaluate the impact of the fluorescence yield selection. ε is wavelength dependent and intrinsic to the telescope design (see section 3.2.1 for the Auger telescopes). In Fig. 4.3 the optical efficiency of the Auger, TA and HiRes telescopes is plotted together with the corresponding FY assumed by these experiments. It should be noted that although the AIRFLY dataset includes more molecular bands than the Kakimoto-FLASH one, the narrower filter employed in the Auger telescopes compensates in practice the differences between both datasets.

4.3 Effect of the FY on shower reconstruction: Analytical method

In this section a theoretical method to evaluate the effect of a change in the FY selection on the reconstructed shower parameters will be shown. This method will give information about the changes due exclusively to this FY selection. A more detailed method using real data will be explained in section 4.4, taking into account other dependences not related to the FY.

Assuming a certain longitudinal profile of deposited energy $\mathrm{d}E/\mathrm{d}X$, the number of fluorescence photons generated in the wavelength interval of the telescope per unit slant depth is determined by:

$$\frac{\mathrm{d}n_\gamma^{\mathrm{gen}}}{\mathrm{d}X} = \frac{\mathrm{d}E}{\mathrm{d}X} \cdot Y(X) \tag{4.11}$$

The total calorimetric energy E can be obtained from the integral of the longitudinal profile, and therefore:

$$E = \int_0^\infty \frac{1}{Y(X)} \frac{\mathrm{d}n_\gamma^{\mathrm{gen}}}{\mathrm{d}X} \mathrm{d}X \tag{4.12}$$

If the fluorescence yield assumption is now changed to a new data set $Y'(X)$ the profile of deposited energy consistent with the fluorescence profile is

$$\frac{\mathrm{d}E'}{\mathrm{d}X} = \frac{\mathrm{d}E}{\mathrm{d}X} \frac{Y(X)}{Y'(X)} \tag{4.13}$$

and thus the calorimetric energy associated to the new fluorescence yield selection will be:

$$E' = \int_0^\infty \frac{\mathrm{d}E}{\mathrm{d}X} \frac{Y(X)}{Y'(X)} \mathrm{d}X \tag{4.14}$$

Therefore, in principle, the effect of changing the fluorescence yield selection on the primary energy can be evaluated by comparing (4.12) and (4.14). On the other hand, the effect on the X_{max} value can be obtained by comparing the shape of $\mathrm{d}E/\mathrm{d}X$ and $\mathrm{d}E'/\mathrm{d}X$ profiles.

Only a small fraction of the fluorescence photons generated by the shower reaches the PMT camera of the fluorescence detector. In the first place, the number of photons is strongly reduced by a geometrical factor $G(X) = A/(4\pi R^2(X))$ where A is the collection area of the telescope and R is the distance from the emission point to the telescope location. In addition, the atmosphere scatters a non-negligible fraction of photons on their way to the telescope. Finally, the optical elements of the telescope also absorb a certain fraction of photons reaching the telescope window. Both atmospheric transmission and optical efficiency are wavelength dependent. Therefore the profile of deposited energy is calculated from the profile of observed photons using the expression:

$$\frac{\mathrm{d}E}{\mathrm{d}X} = \frac{\mathrm{d}n^{\mathrm{obs}}}{\mathrm{d}X} \frac{1}{G(X)} \frac{1}{\sum_{\Delta\lambda} \varepsilon_\lambda T_\lambda(X) Y_\lambda(X)} \tag{4.15}$$

where ε_λ is the relative optical efficiency of the fluorescence detector at wavelength λ, $T_\lambda(X)$ the relative optical transmission for this wavelength at the atmospheric layer X and $Y_\lambda(X)$ is the corresponding fluorescence yield at the atmospheric conditions of the atmospheric layer X. Using this, expression (4.13) becomes:

$$\frac{\mathrm{d}E'}{\mathrm{d}X} = \frac{\mathrm{d}E}{\mathrm{d}X} \frac{\sum_{\Delta\lambda} \varepsilon_\lambda T_\lambda(X) Y_\lambda(X)}{\sum_{\Delta\lambda} \varepsilon_\lambda T_\lambda(X) Y'_\lambda(X)} \tag{4.16}$$

The variation of both E and X_{max} due to a change in the fluorescence yield selection is not

sensitive to the fine details of the longitudinal development of $\mathrm{d}E/\mathrm{d}X$ and thus, instead of using real data, the longitudinal development of deposited energy will be parameterized using a Gaisser-Hillas profile (described in Eq. (3.17)). Using Eq. (4.16) a new longitudinal profile is obtained that is then fitted to a Gaisser-Hillas function. E' is obtained integrating the fitted profile while $X_{\max}$ is one of the parameters of this fitted profile.

To study the effect of the fluorescence yield, typical parameters of a selection of proton and iron showers with a zenith inclination, θ, and fixed total energies of 10^{19} eV and 10^{20} eV have been used. The values of the $X_{\max}$, X_0 and λ parameters obtained in [135] by fitting the average longitudinal development of a sample of CORSIKA showers have been used in this work. The value of $(\mathrm{d}E/\mathrm{d}X)_{X_{\max}}$ is obtained as a normalization constant to account for the total deposited energy.

For a given energy, the shower reaches its maximum development at an altitude which grows with θ and therefore, since the fluorescence yield varies with altitude (through pressure, temperature and humidity) the impact of the fluorescence yield selection depends on shower geometry. The effect of atmospheric transmission increases with the distance between the telescope and the shower axis and its effect is wavelength-dependent. To study this, results have been obtained for several shower to telescope distances. The atmosphere has been modelled using the average monthly models measured at the Auger site [136].

4.3.1 Example applications

Two illustrative examples will be shown next. The first one is the update from the absolute value of the Nagano-Airfly dataset previously used by the Auger Collaboration to the present one. The second one, a comparison between the Nagano-Airfly dataset and the Kakimoto-Bunner dataset employed by the HiRes collaboration, will illustrate the importance of the optical efficiency of the telescope in the evaluation of the impact of the fluorescence yield selection on the energy scale.

Nagano - AIRFLY absolute 337 nm value comparison

As mentioned before, in 2013 the Auger collaboration changed the absolute value of the Y_{337} from the 6.38 ph/MeV measured by Nagano *et al.* to the new value measured by Airfly, 10% higher. Fig. 4.4 shows the application of the method to an iron shower with a 60$^{\mathrm{o}}$ zenith angle and total energy of 10^{19} eV for the January atmospheric model. The black solid line represents the original Gaisser-Hillas profile and the blue dotted profile is the result from Eq. (4.16). The increase of 10% in the absolute FY translates into a 10% decrease in energy, as inferred from Eq. (4.10) and (4.14). The effect is only a scale factor

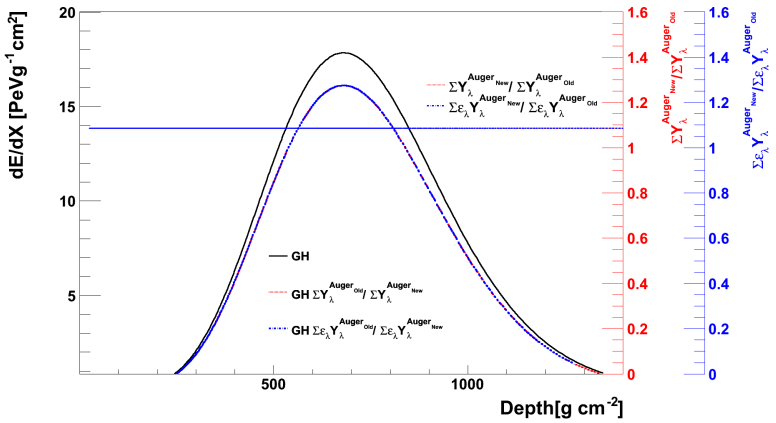

Figure 4.4: Effect of replacing the Nagano absolute yield by the AIRFLY one on shower reconstruction. The ratio of these FY values (right red vertical axis) is indepedent of atmospheric depth even if the optical efficiency of Auger is included (blue vertical axis). The shower profile for a 10^{19} eV iron shower of 60deg zenith angle (black line) is modified (blue line) when divided by the FY ratio (see text for details).

in the reconstruced profile, with no change in the $X_{\max}$ value, because the ratio of sums in Eq. (4.16) is a constant (axis on the right), that is, it depends neither on the optical efficiency of the telescopes nor the atmosphere. The process has been repeated for different showers obtaining identical results, as expected.

Obviously the ratio between fluorescence yields is independent of atmospheric depth and thus the $X_{\max}$ value remains unaffected. The same results have been obtained for other analytical profiles and atmospheric condition.

Nagano-Airfly vs Kakimoto-Bunner comparison

The comparison between the K-B and N-A FY datasets has been studied for the same iron shower and atmospheric model as the previous case. The modified profile dE′/dX is shown in Fig. 4.5 under two hypoteses: a constant optical efficency in the whole spectral range (red dashed line) and implementing the optical efficency of the Auger telescopes, which is very similar to the HiRes one (blue dashed line). The respective correction factors $\sum Y_\lambda^{\mathrm{K-B}}/\sum Y_\lambda^{\mathrm{N-A}}$ and $\sum \varepsilon_\lambda Y_\lambda^{\mathrm{K-B}}/\sum \varepsilon_\lambda Y_\lambda^{\mathrm{N-A}}$ for both hipoteses are also plotted (axis on the right) as a function of depth. If the effect of the optical efficiency is ignored, the difference in the energy, $(E^{\mathrm{K-B}} - E^{\mathrm{N-A}})/E^{\mathrm{N-A}}$, is 16%. When the optical efficency of Auger FD is taken into account, the energy difference is reduced down to about 7%.

The $X_{\max}$ variation is related to the slope of the FY ratio versus depth function. The $X_{\max}$ value increases (decreases) if the slope of the above-mentioned correction factor at

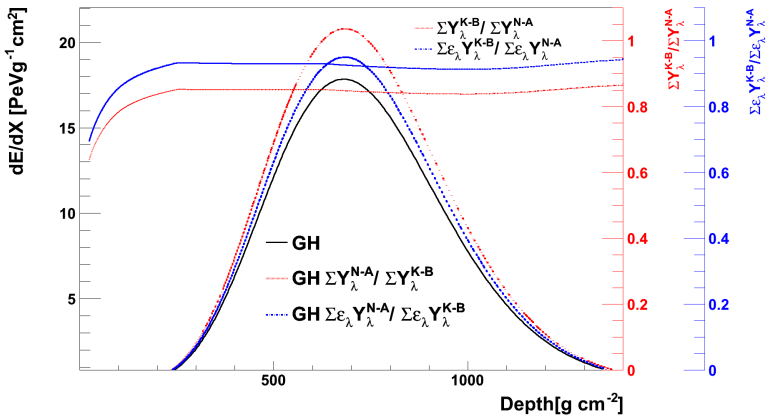

Figure 4.5: Same as Fig. 4.4 for the effect of replacing the Nagano-Airfly yield by the Kakimoto-Bunner one. Since the former includes atmospheric dependences while the later does not, the FY ratio depends on atmospheric depth and the optical filter and thus the shape of the reconstrcuted profile is affected (see text for more details).

$X = X_{\max}$ is negative (positive). In the example, the $X_{\max}$ of the K-B dataset is 2 gcm^{-2} less deep than the original one for both assumptions of the optical efficiency. This effect is mainly due to the humidity and colissional cross section temperature dependence, a feature that will be further explained in chapter 5.

4.4 Detailed reconstruction

The procedure described in the previous section neglects relevant ingredients of the shower reconstruction, in particular the contribution of the Cherenkov light. In a real shower a non-negligible fraction of the detected light is due to the Cherenkov effect. A change in the FY is not expected to translate directly to the shower energy due to this Cherenkov light. Therefore, a detailed reconstruction that takes into account these effects, like the one the Pierre Auger Collaboration uses with the raw data obtained by the FD telescope, is mandatory to obtain more accurate results.

A reconstruction algorithm must, first, transform the ADC counts and arrival times detected by the PMTs of the telescopes into a profile of detected photons, and then, calculate the energy deposit profile knowing the Fluorescence Yield.

The Auger Collaboration has developed the Offline Software Framework [137], which does this operation as well as the geometrical reconstruction explained in section 3.2.4 and the SD reconstruction. In this section, the Offline framework will be described, with a focus on the FD reconstruction processes. A simple example of its application and a

comparison of the resuls with those obtained with the analytical method of section 4.3 will be presented at the end of this section.

4.4.1 The $\overline{\text{Off}}\underline{\text{line}}$ reconstruction framework

The $\overline{\text{Off}}\underline{\text{line}}$ framework, implemented in C++, has been developed to provide the necessary tools for the analysis of data gathered by the observatory, including simulation and reconstruction tasks. It consists of three principal parts:

1. **Modules**: The different tasks to be developed within the Pierre Auger Collaboration can be usually factorized into several sequences of self-contained processing steps. Each one of these tasks are carried out by processing algorithms, the so-called modules, which can be assembled and sequenced through instructions provided in an XML file. This modular design allows users to build a wide variety of applications by combining modules, as well as an easy way to exchange some of the modules by custom ones developed by the user.

2. An **event data model** which accumulates all simulation and reconstruction information (raw, calibrated, reconstructed and Monte Carlo data). Furthermore, through this event data model, modules can communicate and relay data to one another.

3. **Detector description**: which provides a unified interface with non-event information about the configuration and performance of the observatory, as well, as atmospheric conditions as a function of time.

A dedicated module for the fluorescence yield calculation has been developed as part of this thesis. This module, called AirFluorescenceModel.xml is presently used in the official Auger reconstruction. Details about the module can be found in Appendix A.

4.4.2 Raw signal to photon conversion

The PMTs of the FD only record light signals that the associated electronics use to provide digitilized intensities and arrival times. This raw signal must be converted to fluorescence photons in order to evaluate the primary energy of the shower. As explained in section 3.2.3 the PMTs are calibrated using a 370 nm light source. This calibration convert the ADC intensity counts registered by a PMT into 370 nm-equivalent photons per 100 ns per square meter:

$$F_{370}(t) = \frac{\text{ADC} \times \text{K}}{A} \tag{4.17}$$

where K is the pixel calibration constant obtained using the drum and A is the diaphragm area perpendicular to the telescope axis. The component of the flux for a wavelenght i can be obtained using:

$$f_i(t) = F_{370}\frac{\varepsilon_{370}}{\varepsilon_i}w_i \tag{4.18}$$

where ε_i is the detector efficiency for wavelenght i and w_i is a relative fluorescence factor at wavelenght i, such as $\sum w_i = 1$. The purpose of w_i is to make sure that the fluxes f_i have the expected spectrum for fluorescence light after transmission from the eye. It can be defined as:

$$w_i = \frac{Y_i T_i \varepsilon_i}{\sum Y_i T_i \varepsilon_i} \tag{4.19}$$

where Y_i is the fluorescence yield at the source and T_i is the atmospheric transmission factor from the source to the detector. The number of equivalent 370 nm photons is thus:

$$F_{370} = \frac{1}{\varepsilon_{370}}\sum f_i \varepsilon_i \tag{4.20}$$

The light at the telescope for this band, $f_i(t)$, can be transformed to the light at the track at depth X using

$$l_i(X) = \frac{f_i}{T_i G} = \frac{F_{370}}{T_i G}\frac{\varepsilon_{370}}{\varepsilon_i}w_i \tag{4.21}$$

where G is the geometrical factor that takes into account the isotropic nature of fluorescence emission.

4.4.3 Deposited energy evaluation

The analytical method simplifies the light production processes occurring in the atmosphere and assumes that the light registered by the telescopes comes from fluorescence. Most of the charged shower particles travel faster than the speed of light in air, leading to the emission of Cherenkov ligth. Thus, the signal coming from an air shower will be composed of both fluorescence and Cherenkov light contributions.

Traditionally, Cherenkov light was iteratively substracted from the measured total light [58]. This method have some drawbacks, however. It does not converge for events with large amounts of Cherenkov radiation and the uncertainties of the substracted signal are difficult to propagate. An alternative procedure used by the HiRes collaboration [138] is to assume that the longitudinal profile of the shower follows a functional form, calculate the corresponding light emission and vary the parameters of the shower curve until an agreement with observed light is obtained. This avoids the convergence problems, al-

though can only be used if the showers indeed follow the functional form assumed in the minimization.

The Auger collaboration employs an analytical least square solution for the estimation of the longitudinal energy deposit profile of air showers from the observed light signal, in which both fluorescence and Cherenkov light contributions are treated as signal [28].

The directly observed (non-scattered) fluorescence light emitted at a certain slant depth X_i arrives at the detector at a time t_i. Given the fluorescence yield Y_i^f at this slant depth, the observed fluorescence flux at the detector, y_i^f can be written as:

$$y_i^f = d_i Y_i^f w_i \Delta X_i \tag{4.22}$$

where d_i is the attenuation factor that includes the atmospheric transmition, the detector efficiency and the geometrical factor, while w_i denotes the energy deposited per unit depth at slant depth X_i.

The number of Cherenkov photons emitted at the shower is proportional to the number of charged particles above the Cherenkov threshold energy. Unlike the fluorescence emission, Cherenkov photons are emitted in a narrow cone along the particle direction. However, they cover a considerable angular range with respect to the shower axis are deflected from the primary particle direction due to multiple scattering. Given the fraction $f_{\mathrm{C}}(\beta_i)$ of Cherenkov photons per solid angle emitted at an angle β_i with respect to the shower axis, the light flux at the detector aperture originating from direct Cherenkov light is:

$$y_i^{\mathrm{Cd}} = d_i Y_i^{\mathrm{C}} f_{\mathrm{C}}(\beta_i) \Delta X_i N_i^{\mathrm{e}} \tag{4.23}$$

where N_i^{e} denotes the number of electron and positrons above a certain energy cut-off, which is constant along the full shower track and should not be confused with the Cherenkov emission energy threshold. Details of the Cherenkov light production like this threshold are included in the Cherenkov yield factor, Y_i^{C}.

Due to the forward peaked nature of the Cherenkov light production, an intense Cherenkov light beam builds up along the shower as it traverses the atmosphere. If a fraction $f_{\mathrm{s}}(\beta_i)$ of the beam is scattered towards the observer it can contribute significantly to the total light received at the detector. In a simple one-dimensional model the number of photons in the beam at depth X_i is just the sum of Cherenkov light produced by all previous depths X_j attenuated on the way from X_j to X_i by ϑ_{ji}. Similar to the direct

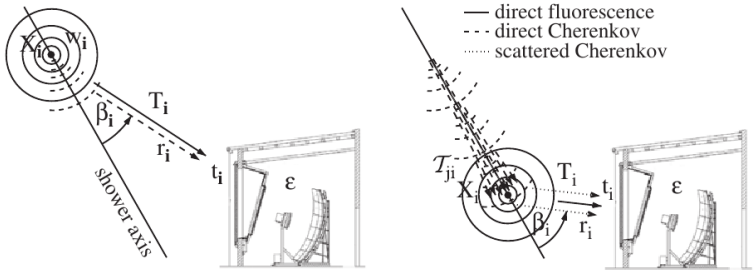

Figure 4.6: Illustration of the isotropic fluorescence light emission (solid circles), Cherenkov beam along the shower axis (dashed arcs) and the direct (dotted lines) Cherenkov light contributions. Figure taken from [28]

contributions, the scattered light received at the detector is then:

$$y_i^{\mathrm{Cs}} = d_i f_{\mathrm{s}}(\beta_i) \sum_{j=0}^{i} \vartheta_{ji} Y_j^{\mathrm{C}} \Delta X_j N_j^{\mathrm{e}} \tag{4.24}$$

Finally, the total light received at the detector at the time t_i is obtained by adding the scattered and direct light contributions:

$$y_i = y_i^{\mathrm{f}} + y_i^{\mathrm{Cd}} + y_i^{\mathrm{Cs}} \tag{4.25}$$

An schematic of the different contributions to the total flux can be found in Fig. 4.6.

The aim of the profile reconstruction is to estimate the energy deposit and/or electron profile from the light flux observed at the detector. At first glance this seems hopeless, since at each depth there are two unknown variables, w_i and N_i^{e} and only one measured quantity, y_i. Since the total energy deposit is just the sum of the energy loss of electrons, w_i and N_i^{e} are related via:

$$w_i = N_i^{\mathrm{e}} \alpha_i \tag{4.26}$$

where α_i is the average energy deposit per unit depth per electron at shower age $s_i = 3/(1 + 2X_{\max}/X_i)$. With this one-to-one relation between the energy deposit and the number of electrons, the shower profile is readily calculable from the Eq (4.25). For the solution to the problem, it is convenient to rewrite the relation between energy deposit and light at the detector in matrix notation. Let $\mathbf{y} = (y_1, y_2, ..., y_n)^T$ be the n-component vector of the measured photon flux at the aperture and $\mathbf{w} = (w_1, w_2, ..., w_n)^T$ the energy

deposit vector at the shower track. Using the expression:

$$\mathbf{y} = \mathbf{C}\mathbf{w} \tag{4.27}$$

the elements of the *Cherenkov-fluorescence matrix* $\mathbf{C}$ can be found in a comparison with the coefficients in Eqs. (4.22), (4.23) and (4.24):

$$C_{ij} = \begin{cases} 0, & i < j \\ c_i^d + c_{ii}^s, & i = j \\ c_{ij}^s, & i > j \end{cases} \tag{4.28}$$

where

$$c_i^d = d_i(Y_i^{\mathrm{f}} + Y_i^{\mathrm{C}} f_{\mathrm{C}}(\beta_i)/\alpha i)\Delta X_i \tag{4.29}$$

and

$$c_{ij}^s = d_i f_{\mathrm{s}}(\beta_i)\vartheta_{ji} Y_j^{\mathrm{C}}/\alpha j \Delta X_j \tag{4.30}$$

The solution to Eq. (4.27) can be obtained by inversion, leading to the energy deposit estimator, $\hat{\mathbf{w}}$:

$$\hat{\mathbf{w}} = \mathbf{C}^{-1}\mathbf{y} \tag{4.31}$$

Due to the triangular estructure of the Cherenkov-fluorescence matrix the inverse can be calculated quickly even for matrixes with large dimensions. As the matrix elements in Eq. (4.28) are always ≥ 0, $\mathbf{C}$ is never singular.

4.4.4 Dataset and event selection

The impact of the fluorescence yield selection on real data has been performed (unless specified) using golden hybrid events from December 2004 to September 2010 using $\overline{\text{Off}}\underline{\text{line}}$ v2r9p1-Valentine. Golden events, that is, events that simultaneously pass FD and SD reconstruction requirements, are selected to ensure a proper reconstruction of the event. This impact has been determined changing the fluorescence yield parameters in the reconstruction chain and comparing the new reconstructed parameters with the ones obtained by the default configuration. To this end a dedicated air-fluorescence module has been developed in this work (see Apendix A). In order to speed up the data processing, a sample of around 70000 events has been pre-selected following detector-related requirements:

- There must be a measurement of the VAOD to ensure that the effects of the optical transmission are properly taken into account.

- Calibration data must be present. Due to different technical issues, calibrations performed at the beginning and end of the data-taking nights are sometimes lost or corrupted.
- Events with saturated pixels are skipped as the energy cannot be accurately reconstructed.
- To prevent monocular events with random SD triggers, only events with the station used for reconstruction lying within 750 m from the shower axis are accepted.
- The time residual of the hottest station must be below 300 ns.

Once the showers have been reconstructed the study of the fluorescence yield selection has been limited to a sample of well reconstructed showers. This sample has been selected applying similar cuts to those used to obtain the hybrid spectrum of the Pierre Auger Observatory.

- The reconstructed value of $X_{\max}$ is required to lie within the observed track range to ensure a reliable reconstruction.
- For similar reasons, the uncertainty in $X_{\max}$ must be below 40 gcm^{-2}.
- As the algorithm used for the profile reconstruction propagates both light flux and geometrical uncertainties, the uncertainty in the energy is a good estimator to reject poorly reconstructed showers. The relative uncertainty in the energy must be below 20%.
- The maximum percentage of Cherenkov light allowed is 50%. As will be shown, this magnitude affects greatly the impact of the fluorescence yield selection in the energy.
- Events recorded by different bays at a site lost a fraction of light at the boundaries. Showers with a hole greater than 20% of the total shower track are rejected.
- Fog or the presence of a cloud can distort significantly the profile shape. To avoid this, the Gaisser-Hillas fit must have a reduced χ^2 under 2.5.
- Profiles with an insignificant shower maxima (mainly due to low energy showers) are rejected by requiring that χ^2 of a linear fit to the longitudinal profile is bigger than the χ^2 of the Gaisser-Hillas fit by at least four ($\chi^2_{\text{linear}} - \chi^2_{\text{GH}} > 4$).
- Finally, very inclined showers, with a zenith angle θ over 60$^{\text{o}}$ are rejected, as they need an special reconstruction that is out of the scope of this work.

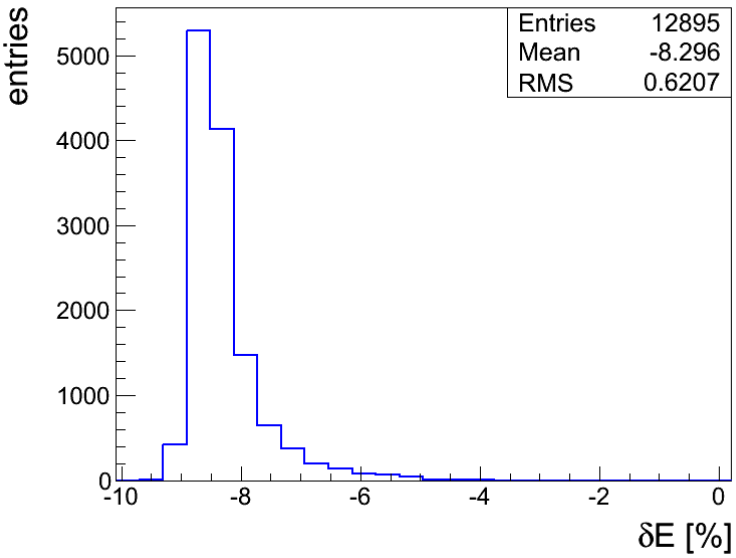

Figure 4.7: Comparison of the new and old Y_{337} value employed as the official Auger Fluorescence Yield and their impact in the energy reconstruction for a dataset of real data events recorded by the Pierre Auger Observatory.

Around 15000 showers survive these quality cuts. The number varies depending on the case of study, as the change in fluorescence yield affects the whole reconstruction process and some of these conditions may not be satisfied.

4.4.5 Example application: Nagano - AIRFLY absolute 337 nm value comparison

The same comparison performed in section 4.3.1 for the change in the absolute value of Y_{337} has been performed for the dataset presented in the previous section using the $\overline{\text{Off}}\underline{\text{line}}$ framework. Results of this comparison on the energy can be found in Fig. 4.7, 4.8, 4.9 and 4.10. where δE, defined as:

$$\delta E[\%] = 100 \times \frac{E_{\text{new}} - E_{\text{old}}}{E_{\text{old}}}; \tag{4.32}$$

and $\Delta_{X_{\text{max}}}$, defined as:

$$\Delta X_{\text{max}} = X_{\text{max,new}} - X_{\text{max,old}} \tag{4.33}$$

and their dependences are displayed.

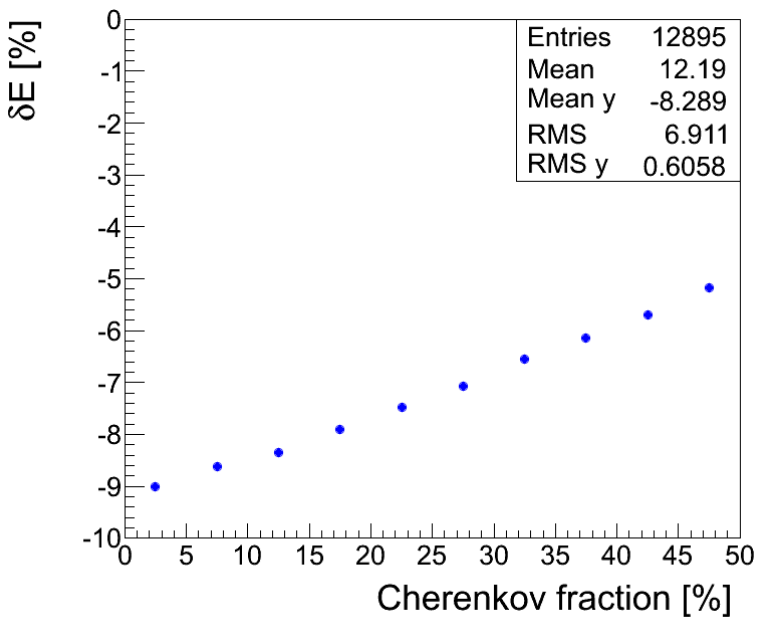

Figure 4.8: Dependence of the energy variation, δE between the Y_{337} values employed by the Pierre Auger Observatory with the Cherenkov light percentage.

As can be seen, the effect on the energy is a 8%, compared to the 10% obtained with the analytical method. This difference is mainly due to the presence of Cherenkov light, as explained in section 4.4.3. Fig. 4.8 shows that δE depends on the amount of Cherenkov light of the event. The change on Y_{337} does not affect the Cherenkov contribution, only the fluorescence light.

The effect on $X_{\max}$ is shown on Fig. 4.9. As expected, is almost negligible, below 2 gcm^{-2}. The change in the absolute value of Y_{337} affects homogeneously the fluorescence yield along the atmosphere, as it was seen on Fig.4.4 and neither geometrical dependences nor seasonal ones can be found, as it is shown on Fig. 4.10

4.5 The effect of the optical efficiency in the relative energy scales

In sections 4.3 and 4.4 a procedure to evaluate the effect on the reconstructed energy due to a change in the FY in a given experiment has been presented. However, in practice, different experiments not only assume different fluorescence spectra but also use optical filters with different wavelength responses, a factor than can affect the relative energy scales. For

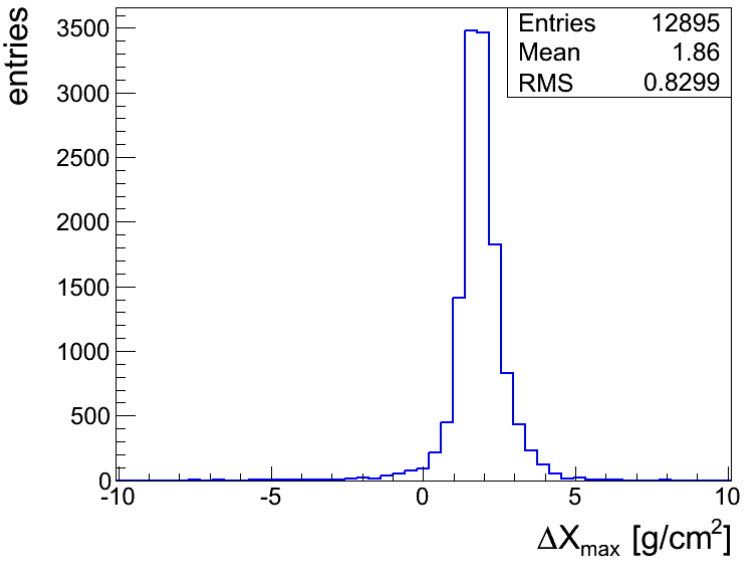

Figure 4.9: Comparison of the new and old Y_{337} value employed as the official Auger Fluorescence Yield and their impact in $X_{\max}$ reconstruction for a dataset of real data events recorded by the Pierre Auger Observatory.

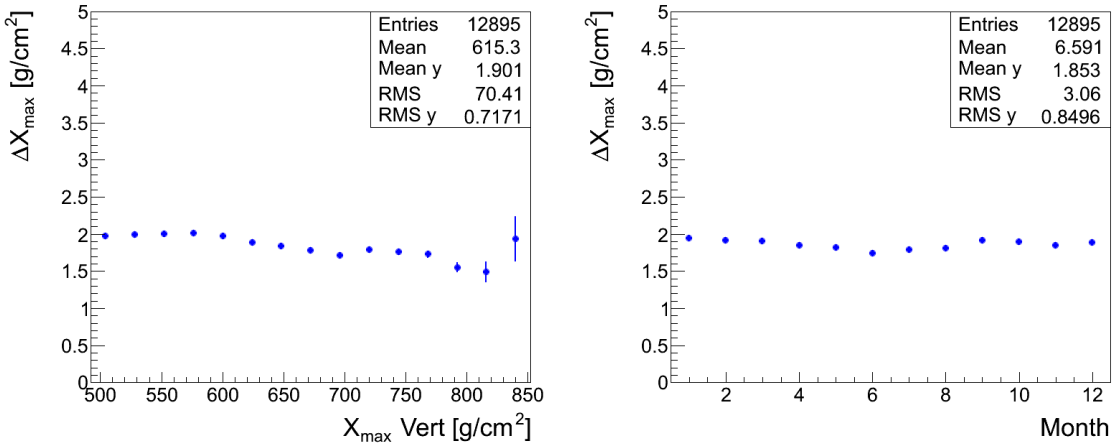

(a) (b)

Figure 4.10: (Left) Dependence of the $X_{\max}$ variation, $\Delta X_{\max}$ between the Y_{337} values employed by the Pierre Auger Observatory with the vertical $X_{\max}$. (Right) Same as left, but the dependence of $\Delta X_{\max}$ with the month is shown.

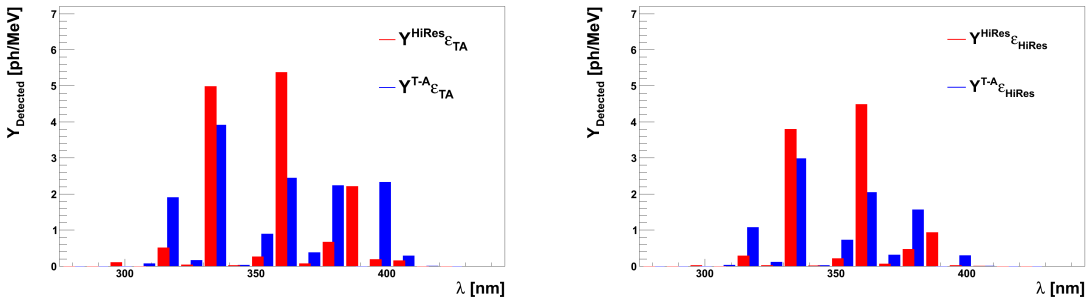

(a) (b)

Figure 4.11: (Left) Comparison of the HiRes and TA yields at 800 hPa and 293K after crossing the TA optical filter. (Right) Same as left, but using HiRes efficiency. In this case, the integral over all the spectrum yields 10.34 ph/MeV for HiRes and 9.17 ph/MeV for TA, a 11% difference in the opposite direction.

example, the Kakimoto-Bunner dataset, employed by HiRes, and Kakimoto-FLASH one, employed by TA have an almost identical absolute value of the total fluorescence yield integrated over all the wavelength interval (Telescope Array add some intensities in the 400-420 nm interval, although their effect is almost negligible), although their spectra are different. For a very wide filter, like the one employed by TA, this difference is not important, but a narrower filter, like the one employed by HiRes (and still used in one of the TA FD telescopes) produces an 11% difference in the integrated yield, as can be seen in Fig 4.11.

In this section a method to evaluate the study of the effect on the relative energy scales of two different experiments that employ different FY dataset will be presented. A brief discussion of this problem can also be found in [139].

4.5.1 The analytical approach

As described in section 4.3, the energy deposit profile of a shower is related to the fluorescence profile observed by a telescope of a cosmic ray experiment through Eq. (4.15). Therefore, the total number of fluorescence photons detected by the telescope is proportional to the calorimetric energy of the shower, that is, $N = C \cdot E$, where the proportionality factor C is given by

$$C = \int_{\text{fov}} \mathrm{d}X \, f(X) G(X) \sum_{\lambda} \varepsilon_{\lambda} T_{\lambda}(X) Y_{\lambda}(X) \tag{4.34}$$

where $f(X)$ is the normalized energy deposit profile and the integration extends over all slant depths. Note that all the dependencies on geometry, atmospheric parameters, etc. of the integrated signal N are included in this parameter C. Therefore, in this analytical approach, the reconstruction of the shower energy is equivalent to solve the integral (4.34) assuming that $f(X)$ is known.

Now, let us assume two telescopes placed at the same location and with same field of view, but with different efficiencies ε_1 and ε_2. For a given shower, the integrated signals N_1 and N_2 recorded by these telescopes will be different, although the *true* calorimetric energy E will be reconstructed from both signals, provided that the FY and all the parameters needed for the reconstruction are properly characterized. However, if different yields Y_1 and Y_2 are assumed for each telescope, the reconstructed energies E_1 and E_2 will be different as well. This can be expressed with the following relations:

$$\begin{aligned} N_1 &= C[\varepsilon_1\,, Y]\, E = C[\varepsilon_1\,, Y_1]\, E_1 \\ N_2 &= C[\varepsilon_2\,, Y]\, E = C[\varepsilon_2\,, Y_2]\, E_2\,, \end{aligned} \tag{4.35}$$

where the $C[\varepsilon\,, Y]$ factors are given by introducing the corresponding ε and Y values in equation (4.34). Therefore, the ratio of the reconstructed energies is

$$\frac{E_2}{E_1} = \frac{C[\varepsilon_1\,, Y_1]}{C[\varepsilon_2\,, Y_2]}\frac{N_2}{N_1} = \frac{C[\varepsilon_1\,, Y_1]}{C[\varepsilon_2\,, Y_2]}\frac{C[\varepsilon_2\,, Y]}{C[\varepsilon_1\,, Y]}\,. \tag{4.36}$$

In principle, this E_2/E_1 ratio can only be evaluated if either the signals N_1 and N_2 of both telescopes for the same shower are available or the *true* yield Y is known. Nevertheless, if one of the two telescopes is assumed to use the *true* yield, e.g., $Y_1 = Y$, equation (4.36) is reduced to

$$\frac{E_2}{E_1} = \frac{C[\varepsilon_2\,, Y_1]}{C[\varepsilon_2\,, Y_2]}\,. \tag{4.37}$$

Note that Y_1 only needs to describe the *true* relative fluorescence spectrum and the atmospheric dependences so that equation (4.37) holds, because a constant factor in the yield cancels out in the ratio of equation (4.36). This equation for $\varepsilon_1 = \varepsilon_2$ is almost equivalent to the procedure described in section 4.3 to obtain the change in energy. The only difference is that here $f(X)$ is assumed to be known, that is, the impact of a change of the FY on the shape of the energy profile is neglected.

4.5.2 Application to real data

Eq. (4.35) to (4.37) can be applied with some limitations to the analysis of real data of two cosmic ray experiments using a reconstruction algorithm like the one of the Pierre Auger Collaboration, described in section 4.4. The above analytical model assumes a pure fluorescence signal, whereas Cherenkov light also contributes to the signal of a real shower. The relationships (4.15) and (4.34) should be generalized and thus Eq. (4.37) is only expected to be valid if this Cherenkov contribution is small. As mentioned before, the FY selection is supposed to affect only the reconstructed energy, not the shape of the profile. Nevertheless, this assumption is justified by the fact that the FY selection has a small impact on reconstruction of the shape of the energy deposit profile, as shown before. Finally, the model does not account for other differences between the two cosmic ray experiments apart from their FY datasets and optical efficiencies.

According to Eq. (4.37), the relative energy scale of two cosmic ray experiments using different FY datasets corresponds to the change in the energy scale of experiment 2 when replacing its FY dataset by that of experiment 1, which is assumed to be the true one. Next, it is shown that this can also be evaluated using data registered by experiment 1 exclusively. If the optical efficiency of experiment 2 is introduced in the reconstruction algorithm of experiment 1 and data are analyzed using both FY datasets Y_1 and Y_2, the two fake energies E_1^* and E_2^* will be reconstructed. Nevertheless, they should satisfy the following relation

$$N_1 = C[\varepsilon_2, Y_1]E_1^* = C[\varepsilon_2, Y_2]E_2^* \tag{4.38}$$

Therefore, combining this with Eq. (4.37) we obtain

$$\frac{E_2}{E_1} = \frac{E_2^*}{E_1^*} \tag{4.39}$$

That is, the relative difference in these parameters E_1^* and E_2^* also provides the relative energy scale of both experiments.

Validation with Monte Carlo showers

Some tests have been carried out using air showers simulated with the CORSIKA code [63]. Fluorescence signals of the telescope have been generated for these showers using the software of the Auger experiment and assuming that the yield of Auger is the *true* one. Two kind of telescope signals have been simulated: using the optical efficiency of Auger (i.e., default Auger signals) or replacing the optical efficiency of Auger by that of TA,

emulating in this case the signal that TA would have recorded. These fluorescence signals of Auger and TA have been reconstructed with the Auger software for both assumptions of FY and optical efficiency. In this way we can obtain, for instance, the energies $E_{\rm Auger}$ and $E_{\rm TA}$, equivalent to E_1 and E_2 in Eq. (4.39) respectively, that Auger and TA would reconstruct for the same shower.

A CORSIKA shower initiated by a Fe nuclei of 10 EeV and a zenith angle $\theta = 26^\circ$ will be used as an example. This shower reaches its maximum development at an atmospheric depth of 679 g cm^{-2} and its axis crosses the ground at 25 km from the telescope with an azimuthal angle $\phi = 169^\circ$. Using this air shower, Auger and TA signals have been simulated 30 times each to calculate the average and RMS of the corresponding reconstructed energies.

The first test is to check that the primary energy is properly reconstructed irrespectively of the implemented optical efficiency. To this end, the same efficiency (either that of Auger or that of TA) and the same yield (i.e., that of Auger) were employed in both the simulation of the signal and its reconstruction. Fully compatible average energies of 9.44 ± 0.14 and 9.48 ± 0.18 EeV were found for the Auger and TA signals respectively. This energy is in agreement with the MC input within the expected uncertainties of the reconstruction. We will use 9.44 ± 0.14 EeV as E_1 in equation (4.39).

The E_2 energy has been obtained from the emulated TA signal when both the yield and efficiency of TA are used in the reconstruction. The result was $E_2 = E_{\rm TA} = 11.02 \pm 0.21$ EeV, that is, 17% larger than $E_{\rm Auger}$.

To test the procedure, the same event has been simulated 30 times calculating the fake energies E_1^* and E_2^* in Eq. (4.39), that is, those obtained from the simulated Auger signal when the TA efficiency is used in the reconstruction in combination with the yields of TA and Auger, respectively. These results were $E^*_{\rm TA} = E_2^* = 8.70 \pm 0.12$ EeV and $E^*_{\rm Auger} = E_1^* = 7.48 \pm 0.11$ EeV, and therefore, the relation $E_2/E_1 = E_2^*/E_1^*$ is fulfilled, as expected:

$$\frac{E_2}{E_1} = 1.167 \qquad \frac{E_2^*}{E_1^*} = 1.163 \tag{4.40}$$

Chapter 5

Impact of the atmospheric dependences of the Fluorescence Yield

Ground-based UHECR experiments that employ the fluorescence technique use the atmosphere as a giant calorimeter. This means that an accurate description of the atmosphere and its properties is mandatory to reduce the systematic uncertainties. To do so, the Pierre Auger Observatory employs a series of facilities, described in section 3.3. As the atmosphere is itself part of the experimental set-up, a complete knowledge of its properties is crucial to correctly reconstruct the EASs. The fluorescence technique is specially sensitive to atmospheric conditions. Note that the optical properties of the atmosphere affect the fluorescence light transmission and also the FY is strongly dependent on atmospheric properties, specially pressure, temperature and humidity as a consequence of non-radiative processes, that is, molecular de-excitation without the emission of a photon (see section 4.1.2).

The pressure dependence of this quenching is parameterized using P' values obtained at atmospheric conditions. In general, the effect of using different P' available values is not very relevant (A comparison between different P' datasets can be found in [122]). For instance, in this work it has been found that the energy deviation when the AIRFLY P' dataset is replaced by that of MACFLY [129] is less than 1%.

While the pressure dependence of the FY has been known and studied for decades, a comprehensive knowledge and experimental measurements for the humidity and temperature dependences were not available until recently. The recent results measured by

the AIRFLY Collaboration [125] have been implemented in the fluorescence yield dataset employed by the Pierre Auger Collaboration. This is the first time a fluorescence detector has taken into account these dependences. As described in section 4.2 both HiRes and TA neglect these effects.

In this work the effect of these dependences on the shower parameters reconstructed by Auger will be evaluated. To do so a comparison of the FY values of the AIRFLY FY values neglecting and including the humidity and temperatures effect along the atmosphere will be examined. After that, the analytical method explained in section 4.3 using the FY will be applied to a variety ofGaisser-Hillas profiles in different atmospheric conditions to obtain a theoretical approximation of the effect of these dependences to the reconstructed E and $X_{\max}$ values. Finally, these theoretical expectations will be confirmed using real data of the Pierre Auger Collaboration providing accurate and reliable results on the impact of these atmospheric paramenters on the shower reconstruction.

Sections 5.1 and 5.2 will be devoted to the study of the temperature dependence of the collisional cross-section through the α parameter, using equation 4.8, and the humidity contribution to the fluorescence quenching via the P'_w following equation 4.7, respectively. Finally, in section 5.3 both dependences will be combined to obtain a complete description of the effect of the atmospheric parameters in the reconstructed shower.

5.1 The temperature dependence of the collisional cross section

The fluorescence yield Y_λ depends on temperature through the P' parameter. In general, P' for a mixture of gases like air can be written following equations (4.5) and (4.6). The well known temperature proportionality between P' and $\sqrt{T}$ is explicitly stated in these equations. Assuming constant density, this results in higher quenching rate constants for increasing temperature due to the molecular Brownian motion.

From molecular physics, a second temperature dependence is expected. The cross-sections for collisional quenching of excited molecular nitrogen with nitrogen, σ_{NN}, and oxygen, σ_{NO}, depend on the relative velocity of the colliding molecules and therefore the average value varies with temperature. The expected behaviour follows a power-law temperature $\sigma \propto T^\alpha$, where α is nearly constant in the temperature interval of interest. This T dependence of the collisional cross-section had been neglected during the last decades as Bunner claimed an evidence for only a weak temperature dependence [56]. However, as reviewed in [140], considerable effects had been found earlier [141, 142]. In the past few

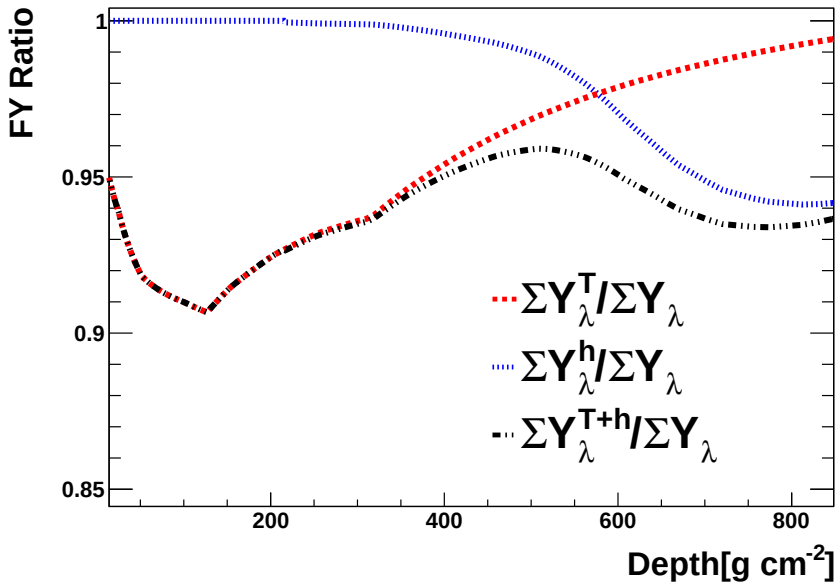

Figure 5.1: Effect of the humidity and a T-dependent collisional cross-section on the Airfly FY. In this plot the ratio of fluorescence yields for the month of January vs the atmospheric depth is shown.

years different measurements of this dependence have been reported [125, 126]. In this chapter the term temperature dependence will be applied to this collisional cross-section dependence.

5.1.1 FY ratio

An approximation of the temperature dependence of the FY can be asserted just by evaluating the ratio between the fluorescence yield assuming $\alpha = 0$, Y, and the same magnitude with the appropiate α values, Y^{T}. At a given atmospheric conditions, the ratio of energy deposition is given by the FY ratio, Y^{T}/Y, as can be easily derived from equation (4.13):

$$\text{FY Ratio} = \frac{Y^{\mathrm{T}}(X)}{Y(X)} \tag{5.1}$$

Thus, the dependence of this ratio with X will be translated to the modified Gaisser-Hillas profile. This dependence is shown in the dashed red line of Fig. 5.1.

As expected, the effect of the temperature is almost negligible near the ground (that is, for higher X values) where T is similar to the reference one, T_0. The ratio is reduced down to 0.9 in the upper layers of the atmosphere, where the temperature is much lower. This means that showers that develop higher (i.e., with a larger zenith angle, θ), will be

more affected by this dependence than vertical showers, that tend to deposit the bulk of the energy near the ground. In the next section this prediction will be tested using the analytical method explained in section 4.3.

5.1.2 Analytical approach

Following the method described in sec. 4.3, the temperature effect on the reconstructed shower profile has been studied. As an example, Fig. 5.2 shows the case of a 10^{19} eV Fe shower in the austral summer atmosphere (mean atmospheric profile for the month of January measured at the Auger site in Argentina), for two different incident angles, 30º (left) and 60º (right). The geometry-dependent effect of the atmospheric transmission has been neglected. Including temperature results in an increase of the reconstructed energy. The energy deviation δE (defined like in Eq. 4.32) for these cases turns out to be 6% for the "inclined" shower and 2.5% for the "vertical" one. As expected, inclined showers are more affected by this temperature correction.

This procedure has been repeated for different shower profiles and the same behaviour is found irrespective of primary energy or mass composition, as can be seen in Fig. 5.3a. A small seasonal dependence is observed during the austral winter, probably due to the lower temperatures of the atmosphere during the central months of the year, that further enlarge the $(T_0/T)^{1/2-\alpha}$ factor.

The $\Delta X_{\max}$ value (defined in eq. 4.33), on the other hand, does not present this geometrical dependence, and it is around -5 gcm^{-2} for all the studied showers. The variation on $X_{\max}$ is related to the shape of the FY ratio near the shower maximum. If this ratio increases with atmospheric depth, at $X = X_{\max}$ the change in the Gaisser-Hillas function at $X < X_{\max}$ is larger than the change at $X > X_{\max}$ and the maximum is slightly moved towards smaller X. The slope of the function FY versus depth is always positive and thus, the T effect always results in a decrease of $X_{\max}$. The small differences between the showers (including seasonal variation) are due to the rate of change of the FY ratio. The larger the slope of the function, the larger $\Delta X_{\max}$ becomes.

5.1.3 Real data reconstruction

The theoretical predictions on δE and $\Delta X_{\max}$ are confirmed when the temperature dependence of the FY is studied using the $\overline{\text{Off}}\underline{\text{line}}$ framework and dataset described in section 4.4.4. In Fig. 5.4 the histograms of these magnitudes for the events that survive the quality cuts are shown. The expectations on $\Delta X_{\max}$ are confirmed, as the mean value of a sample of more than 15000 events is -5 gcm^{-2}, with a small RMS value of 1 gcm^{-2}.

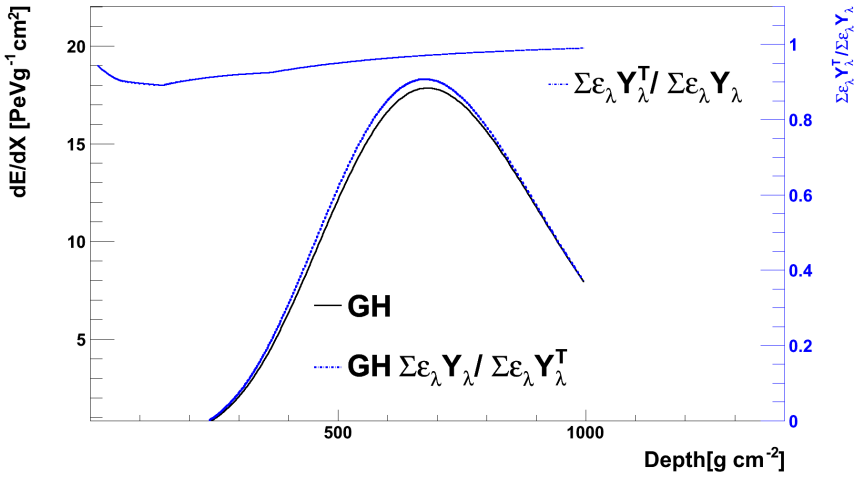

(a)

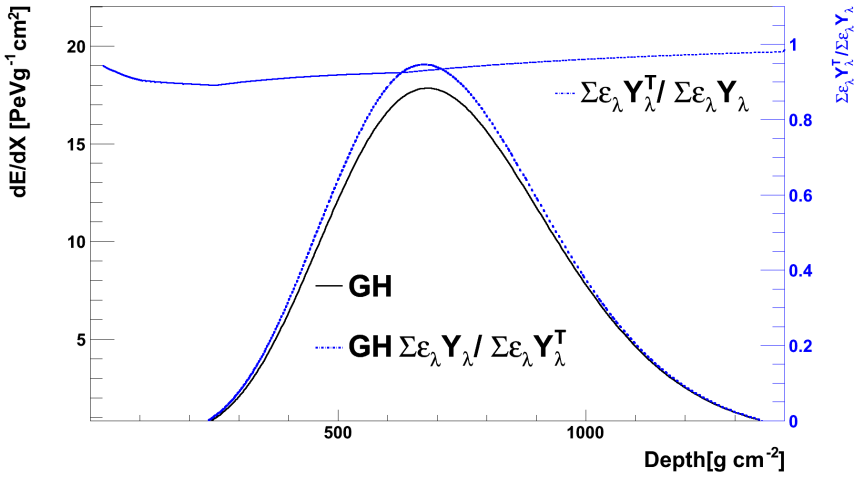

(b)

Figure 5.2: Effect of including the temperature dependence of the cross-section in the profile of the deposited energy for 30° (top) and 60° (bottom) for a Fe shower of 10^{19} eV using the mean January atmospheric profile measured at the Auger site. The dependence of the FY with the slant depth varies with the angle. For these calculations the optical efficiency of the Auger telescopes have been assumed.

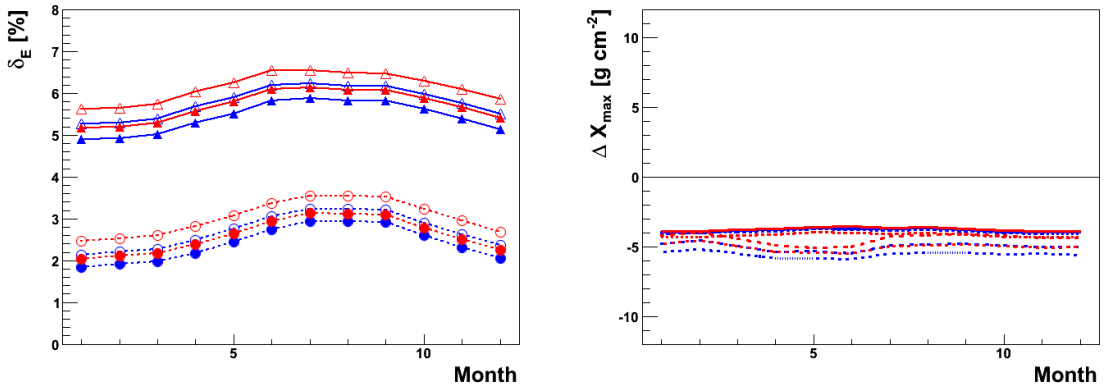

(a) (b)

Figure 5.3: (Left) Energy deviations vs Month due to the temperature dependence of the cross-section in the FY for proton (blue) and iron (red) showers of 10^{19} eV (open symbols) and 10^{20} eV (full symbols), for two different zenith angles, θ. Dashed lines correspond to 30° showers while full lines correspond to 60° showers. The dependence of δE with the incident angle is clearly shown. (Right) Same as left, for the variation on the reconstructed $X_{\max}$

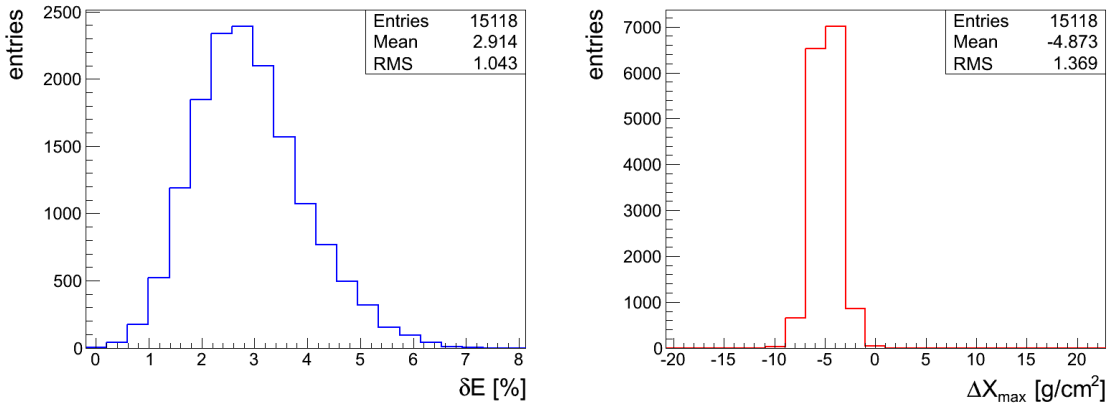

(a) (b)

Figure 5.4: Reconstructed values of δE (left) and $\Delta X_{\max}$ (right) for a datasample of real showers detected by the Pierre Auger Observatory. Neither geometry selection nor energy cuts have been applied.

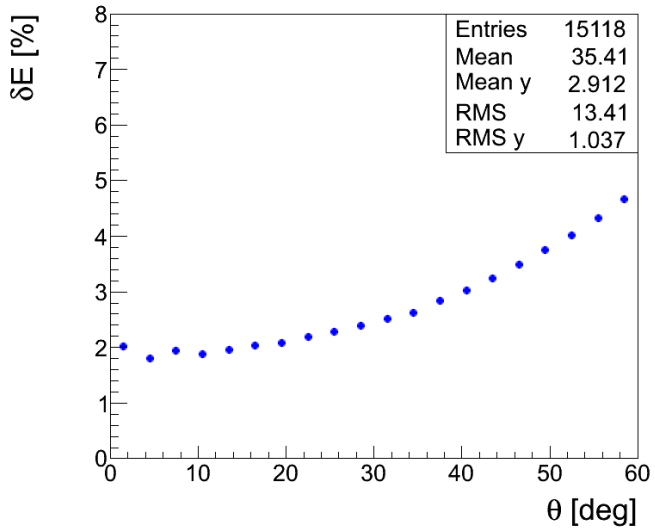

Figure 5.5: Dependence of δE with the zenith angle in real data for the cross-section temperature dependence of the FY

The interpretation of the results on δE are not so straightforward. The mean value is around 3%, just between the predictions for 30º showers and those for 60º. The expected dependence of this magnitude with θ is confirmed in Fig. 5.5. For the more vertical showers described in section 5.1 the mean value of δE is around 2%, a value compatible with the theoretical one. For the inclined showers δE almost reaches 5%, somewhat less than the theoretical prediction. As explained before, the analytical prediction does not take into account the Cherenkov light and tends to overestimate the energy shifts. Also, showers with the same θ value can develop at different altitudes since the more energetic ones develop deeper. To understand this, the dependence of δE with vertical depth at the maximum is shown in Fig.5.6. In this case, even for the deepest showers, δE is only slightly above 5%

In conclusion, including the T effect to the FY evaluation results in an energy increase of about 3% growing with zenith angle while the shower maximum depth decreases by about 5gcm^{-2}.

5.2 Humidity dependence of the Fluorescence Yield

Water vapor is an always changing constituent of the Earth's atmosphere. With respect to the fluorescence emission, the H_2O molecules serve as an additional quenching partner for the excited N_2 molecules. Hence, equation (4.5) must be extended by a term accounting

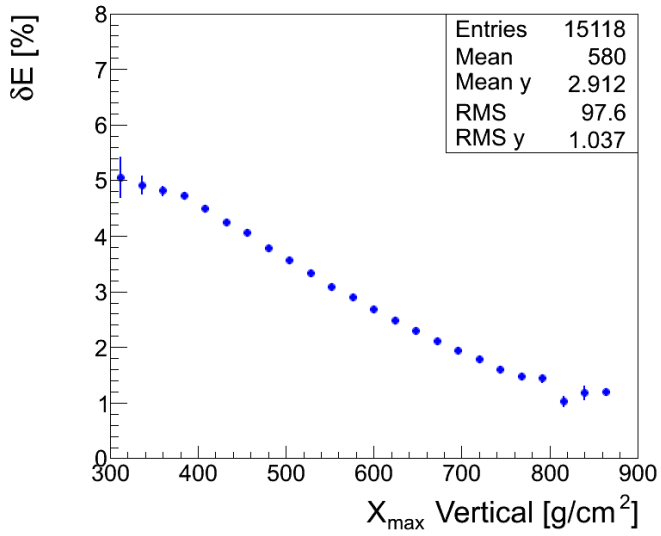

Figure 5.6: Dependence of δE with the vertical depth of the shower maximum in real data for the cross-section temperature dependence of the FY

for collisional cross section due to water vapor, yielding equation (4.7).

The first measurements of this dependence were reported by Pancheshnyi *et al.* [143]. In the last few years several groups have carried out different experiments in order to obtain more precise values of this magnitude (e.g.[144–146]). In this work the effect of the P'_w values reported by the AIRFLY collaboration [125] in the shower reconstruction parameters will be evaluated following the same procedure employed in section 5.1.2.

5.2.1 FY ratio

In Fig. 5.1 the FY ratio for the humidity effect is represented with a blue dashed line. It behaves the opposite way of the temperature effect: in the upper layers of the atmosphere the FY is constant, as there is no water vapor in those regions. Near the ground, on the other hand, water vapor is much more abundant, and thus the FY ratio goes down to 5% in the January atmosphere. It should be noted that the humidity profile in the atmosphere is much more variable than the temperature one (as will be shown in the next section), and so is the effect on the FY.

In any case, the shape of the dependence of the FY with depth is similar independently of the humidity variation. That means that vertical showers that develop near the ground are expected to be more affected by humidity than inclined ones.

5.2.2 Analytical approach

Fig. 5.7 confirms the expectations derived from the FY ratio. Although 60° showers are slightly affected by the humidity contribution to the FY (+0.6% energy variation in the case depicted in Fig. 5.7a), the effect in δE for vertical showers goes up to 4%.

The behaviour of $\Delta X_{\max}$ in this case is more interesting. For the vertical shower the variation on $X_{\max}$ is +7 gcm^{-2} while the variation on the inclined shower is smaller although on the same direction ($\Delta X_{\max} \leq +1$ gcm^{-2}). As explained before, this is due to the slope of the FY ratio funcion in the maximum. Near the ground is much steeper than upper in the atmosphere, and thus the change is larger for vertical showers.

This calculation has been repeated for all months (Fig. 5.8). The seasonal variation of the humidity dependence is more important than the temperature one for vertical showers. Both δE and $\Delta X_{\max}$ peak in March and are generally larger during the first part of the year due to higher relative humidity near the ground during those months. Inclined showers do not show this dependence, as the humidity in the upper layers of the atmosphere remains almost constant during the year.

5.2.3 Real data reconstruction

The effect of water vapor quenching has been tested in real data obtained by the Pierre Auger Observatory too. Fig. 5.9 shows the effect on the reconstructed energy and $X_{\max}$. The distributions of both magnitudes present long tails due to the high variation of the water vapor content between different shower tracks. Like in the temperature dependence case, the different dependences of both δE and $\Delta X_{\max}$ are very important to obtain a correct interpretation of the results.

In Fig. 5.10a the dependence of the energy variation with θ is shown. The most vertical showers, with zenith angles below 30°, present the most important energy variation, peaking around 3%, while for inclined ones δE is reduced to around 1%. These values, although a little smaller, confirm the theoretical expectations. The same trend is found in $\Delta X_{\max}$ (Fig. 5.10b). While the reconstructed $X_{\max}$ is almost unaffected for inclined showers, vertical ones are shifted by as much as 6 gcm^{-2}.

The seasonal dependence (Fig. 5.11) for the humidity is more important than the one found for the cross-section temperature dependence of the FY. Both δE and $\Delta X_{\max}$ are noticeably larger during the first part of the year (summer-autummn) than in the middle of it. This trend was also found using the analytical method.

In summary, the humidity effect on the FY gives rise to an increase of energy (about 2%) and $X_{\max}$ (about 4 gcm^{-2}). In both cases the effect decreases with zenith angle and

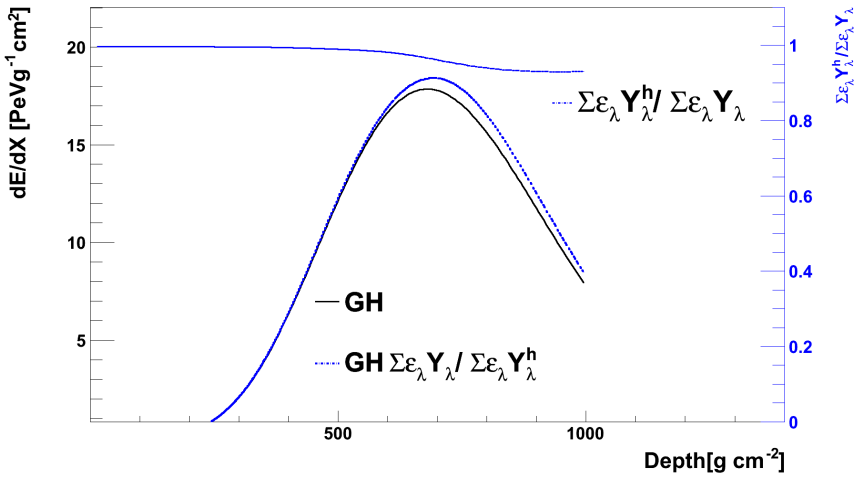

(a)

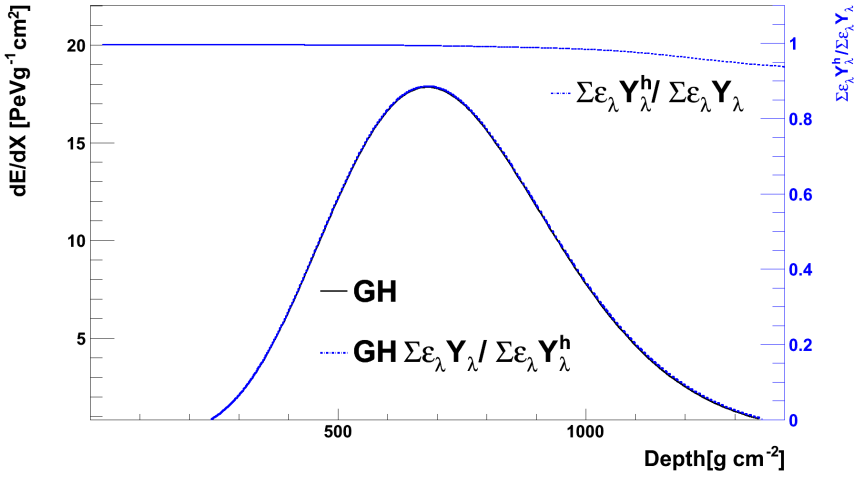

(b)

Figure 5.7: Effect of including the humidity contribution in the shower reconstruction for 30º (top) and 60º (bottom). See Fig. 5.2 for details.

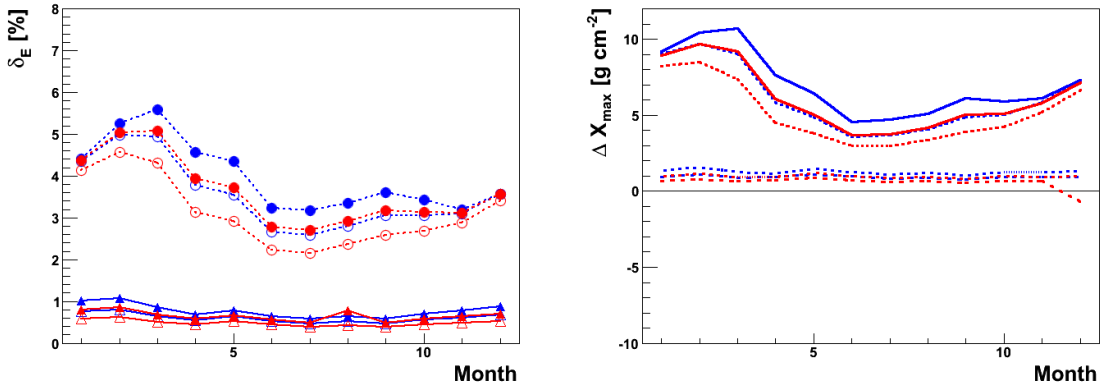

(a) (b)

Figure 5.8: Same as Fig. 5.3 for the humidity effect on the reconstructed energy.

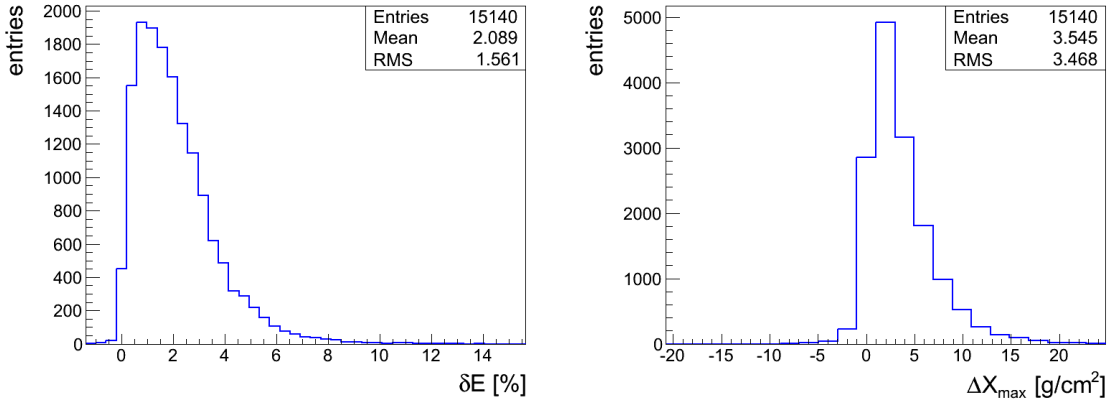

(a) (b)

Figure 5.9: Same as Fig. 5.4 for the humidity dependence of the FY.

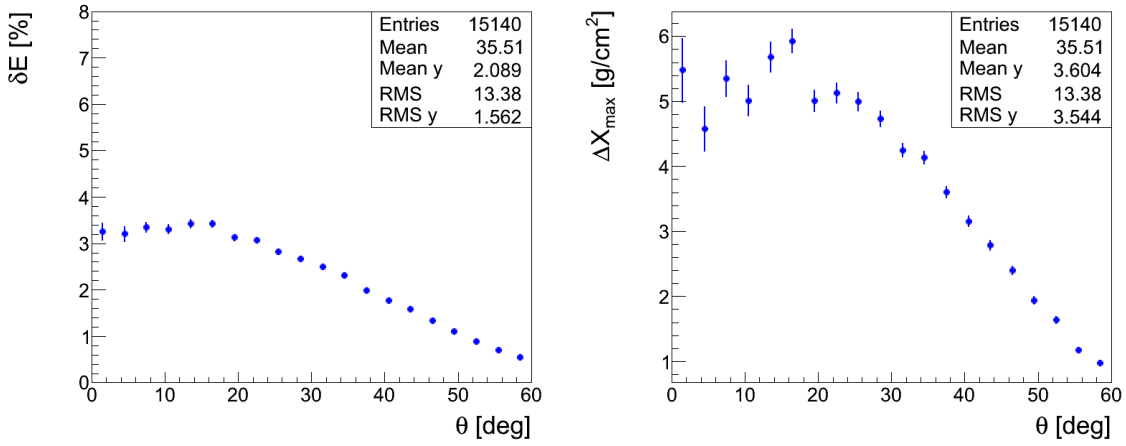

(a) (b)

Figure 5.10: Dependence of δE (left) and $\Delta X_{\max}$ (right) with the zenith angle in real data for the humidity dependence of the FY

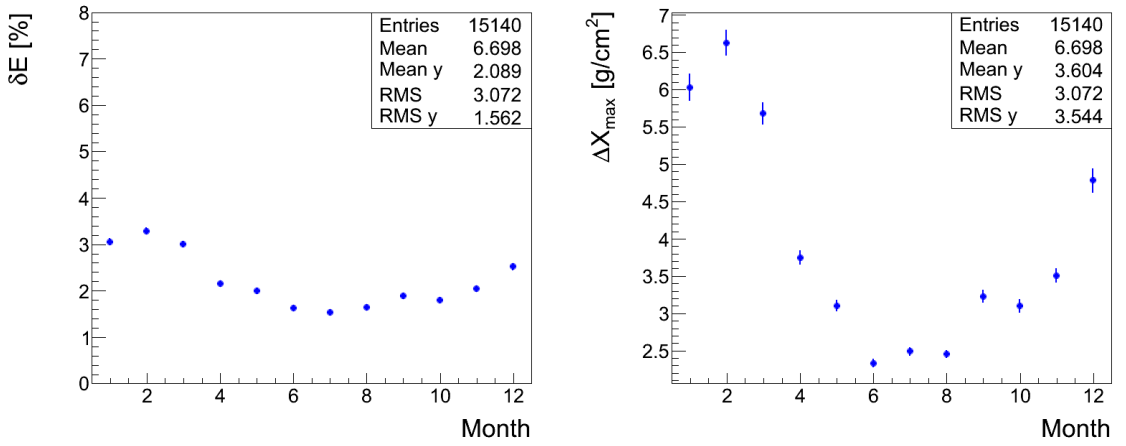

(a) (b)

Figure 5.11: Seasonal dependence of δE (left) and $\Delta X_{\max}$ (right) in real data for the humidity dependence of the FY.

is seasonal dependent.

5.3 Temperature and humidity combined effect

Once the individual effect of both atmospheric dependences of the FY have been studied and their impact in the shower reconstruction is well understood, the combined effect of both parameters will be studied in this section following the same procedure. As both effects on δE are in the same direction, the combined effect will be larger than the individual ones.

5.3.1 FY ratio

The solid black line in Fig. 5.1 represents the FY ratio after taken into account the contribution of both α and P'_w. It is almost a direct product of both humidity and temperature ratios. That means that showers that develop deeper in the atmosphere will be dominated by the humidity effect while those that develop in the upper layers of the atmosphere will show the trends previously described for the temperature effect. That means that δE will be shifted regardless of geometry while $\Delta X_{\max}$ behaviour will be dependent of the shower maximum depth.

5.3.2 Analytical approach

As described in sections 5.1 and 5.2, the angle dependence of δE for the humidity effect is opposite to that of the temperature and therefore this dependence for their combined effect is expected to be somewhat compensated. This is confirmed in Fig. 5.12 where it is shown that both the 30º (left) and 60º (right) profiles of the same 10^{19} eV Fe shower employed in the previous sections are shifted similarly, with a δE of 6.8% for the 30º and 6.5% for the 60º one. The vertical shower maximum is moved towards the ground ($\Delta X_{\max} \approx +3.5$ gcm^{-2}), while in the inclined one the maximum is shifted the same amount but in the opposite direction ($\Delta X_{\max} \approx -3.5$ gcm^{-2}).

The energy trend is repeated for all the selected profiles, independently of the season, as can be seen in Fig. 5.13a and Fig. 5.13b. There are, however, some differences due to the variability of the humidity during the year, mainly due to the humidity contribution. δE for 30º showers is somewhat larger from January to March than in the rest of the monthly profiles, a shift that can also be seen in $\Delta X_{\max}$. In this case, it should be noted that the effect on the shower maximum can even change direction during the central month of the

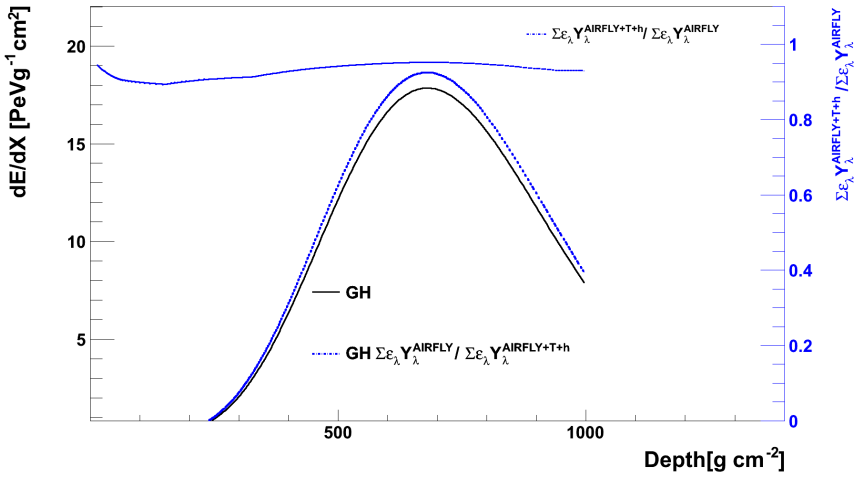

(a)

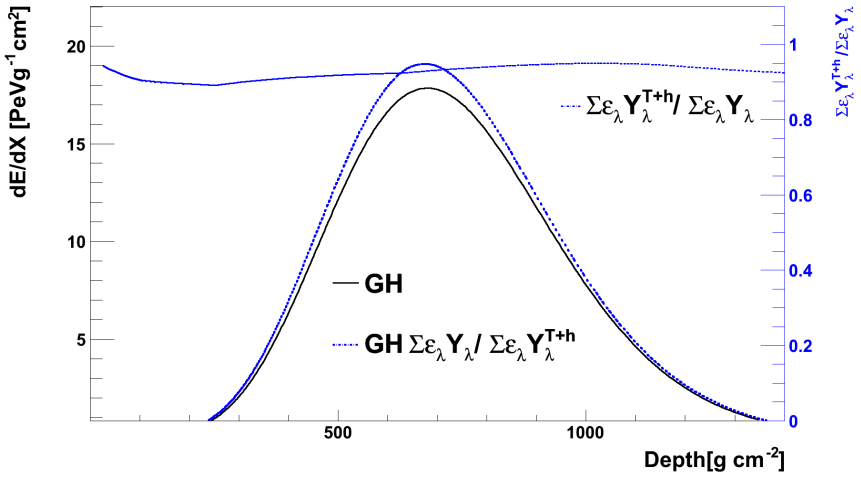

(b)

Figure 5.12: Effect of including both the temperature dependence of the cross-section and the humidity contribution in the shower reconstruction for 30° (top) and 60° (bottom) for the same cases of Fig. 5.2.

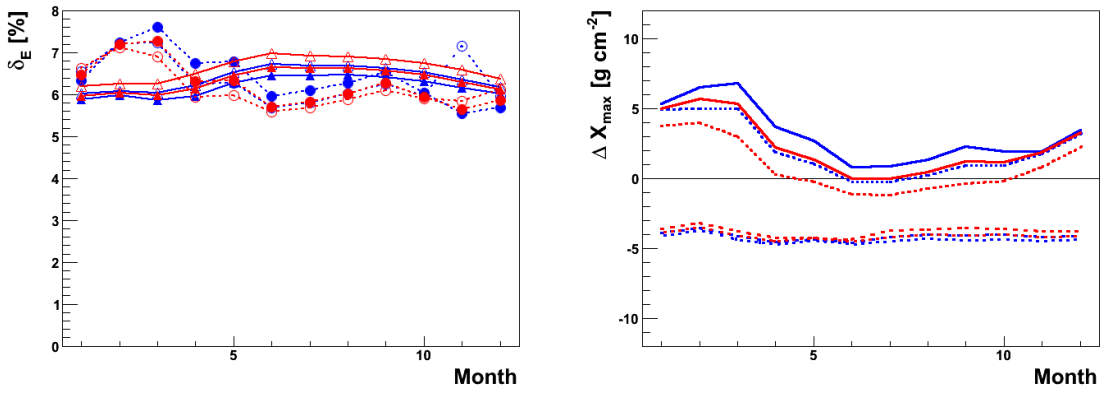

(a) (b)

Figure 5.13: Same as Fig. 5.3 for the combined effect of humidity and temperature.

year for some showers. The atmosphere is dryer these months, and the temperature effect dominates even for showers that develop near the ground.

5.3.3 Real data reconstruction

The combined effect of both atmospheric dependences of the FY has also been studied using real data. In Fig. 5.14a is shown that δE distribution is centered in 5% with an RMS of 1.2%. This results are below the theoretical expectations shown in Fig. 5.13a as expected. As can be seen in Fig. 5.15, there are no visible dependences of δE with neither the geometry nor the season. Temperature and humidity effects combined affect δE equally for inclined and vertical showers, and the atmospheric variability is also compensated when both dependences are taken into account.

$\Delta X_{\rm max}$, on the other hand, does not present such an uniform distribution, as can be seen in Fig. 5.14b. The distribution, centered in $\Delta X_{\rm max} = -1.5$ gcm^{-2} is much wider than the energy one, with a RMS of 3.6 gcm^{-2}, although the tails of the distribution reach up to ± 20 gcm^{-2}. Unlike δE, the humidity and temperature dependences of the FY affect in $X_{\rm max}$ in opposite directions. When the temperature effect is more important than the humidity one (i.e. showers that develop upper in the atmosphere) $\Delta X_{\rm max}$ is negative. When the humidity effect dominates (i.e. vertical showers that develop near the ground) $\Delta X_{\rm max}$ becomes positive.

This trend is easily spotted in Fig. 5.16a. $\Delta X_{\rm max}$ for showers with low θ (those that develop near the ground and are thus dominated by the humidity contribution) is positive, reaching $+2$ gcm^{-2}, while inclined showers (that tend to develop upper in the atmosphere)

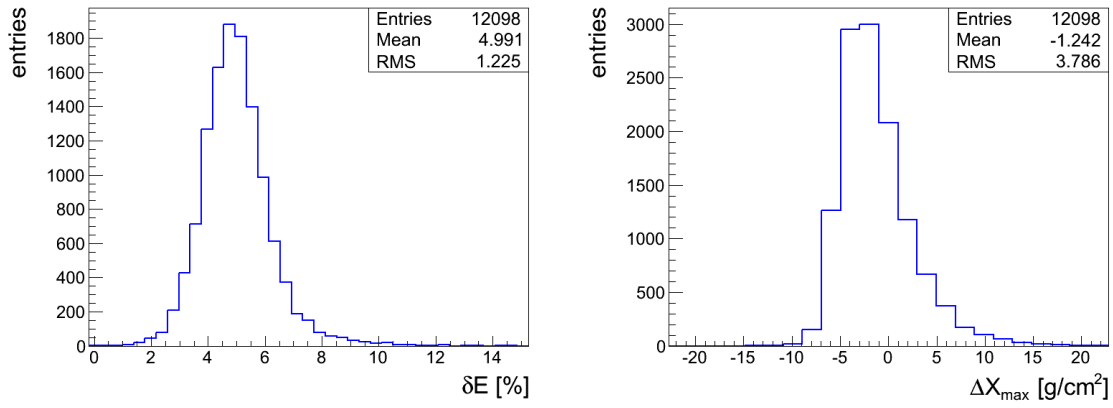

(a) (b)

Figure 5.14: Same as Fig. 5.4 for both the temperature dependence of the cross-section and the humidity dependence of the FY.

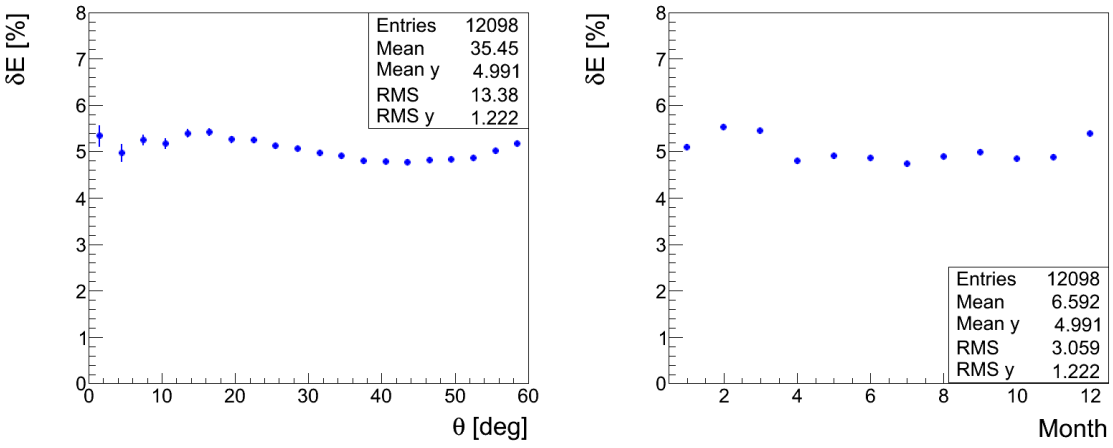

(a) (b)

Figure 5.15: Angular (left) and seasonal dependence (right) of δE in real data for both the temperature dependence of the cross-section and the humidity dependence of the FY.

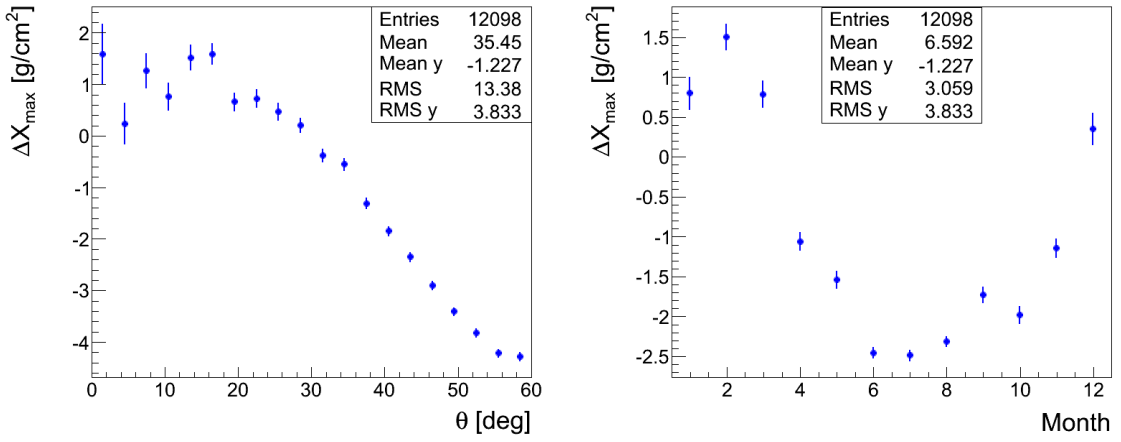

(a) (b)

Figure 5.16: Angular (left) and seasonal dependence (right) of $\Delta X_{\max}$ in real data for both the temperature dependence of the cross-section and the humidity dependence of the FY.

present a negative $\Delta X_{\max}$ that can go as down as -6 gcm^{-2}.

Seasonal variability is also important for $\Delta X_{\max}$. In Fig. 5.16a is shown that during the central part of the year (austral winter months) $\Delta X_{\max}$ becomes negative. During the first part of the year the trend is exactly the opposite, with a positive $\Delta X_{\max}$.

These features are compatible with the theoretical predictions of section 5.3.2. The complete datasample is composed of showers with different zenith angles and energies. In general, the higher the energy the deeper the shower will develop. As low energy showers are more abundant in the datasample employed for the study, there is a trend towards showers that develop in the upper layers of the atmosphere and are thus more affected by the temperature dependence than the humidity one. In any case, the qualitative theoretical predictions are fulfilled when the real data study is performed.

In conclusion, when both the temperature and humidity dependences are taking into account the reconstructed energy increases by about 5% independently of the shower geometry, while the $X_{\max}$ variation is correlated with the shower maximum depth. For showers that develop near the ground $X_{\max}$ increases by around +2 gcm^{-2}, while for those that develop higher in the atmosphere the maximum depth decreases about 5 gcm^{-2}.

Chapter 6

The new energy scale of the Pierre Auger Observatory

The FY studies presented in the previous chapter are part of a combinated effort by the Hybrid Reconstruction task of the Pierre Auger Collaboration that aimed at improving the reconstruction of the FD events and reducing the associated uncertainties. This is crucial for the Auger Observatory, as the FD energy is used to calibrate the SD. This joint effort has crystallized in an internal GAP note [29], an ICRC contribution [31] and a future paper in preparation.

In this chapter these recent results will be presented, with a focus on the effect of the FY on the Auger energy scale. In section 6.1 the method for calibrating the SD using the FD energy will be presented, along with the methodology used to evaluate the recent changes in the energy scale and their associated uncertainties. Section 6.2 will be devoted to the impact of the most recent measurements of the FY on the Auger energy scale. In section 6.3, other improvements in the determination of the Auger energy scale will be summarized. Finally, in section 6.4, all the results will be combinated to present the new energy scale of the Pierre Auger Observatory.

6.1 The SD calibration curve

The $S(1000)$ parameter, as mentioned in section 3.1.3, is used to characterize the energy of a cosmic ray shower detected by the SD array. However, $S(1000)$ depends on the stage of the shower development and therefore, on the zenith angle. The signal recorded by the array decreases with increasing zenith angle due to the attenuation of shower particles in the atmosphere and geometrical effects. The function that describes $S(1000)$ as a function

of zenith angle is called the *attenuation curve*.

This curve provides a mean to convert $S(1000)$ signal generated by a shower arriving at a given zenith angle θ to the $S(1000)$ that would have been generated at a reference angle, $\hat{\theta}$. In the Pierre Auger Observatory $\hat{\theta}$ has been fixed at 38°, the median of the zenith angle distribution of the SD events. The attenuation curve is obtained using the so-called Constant Intensity Cut (CIC) method [147] by fitting it to a second polynomial in $x = \cos^2(\theta) - \cos^2(\hat{\theta})$:

$$\mathrm{CIC}(\theta) = 1 + \mathrm{a}x + \mathrm{b}x^2 \tag{6.1}$$

The attenuation curve yields then

$$S_{38} = \frac{S(1000)}{\mathrm{CIC}(\theta)} \tag{6.2}$$

where S_{38} is the $S(1000)$ signal that would have been generated by the shower if it had arrived at a zenith angle of 38°. This parameter is the one used to obtain the relation between the FD energy, E_{FD} and the SD signal for golden events, following the relationship:

$$E_{\mathrm{FD}} = AS_{38}^{B} \tag{6.3}$$

The A and B parameters are obtained by performing a maximum likelihood fit to the real data [148]. The changes in the FD energy and their associated uncertainties, both correlated and uncorrelated, are propagated to the SD using this calibration curve. In fact, the uncorrelated errors should be propagated through the FD energy resolution, which is used to calculate the likelihood in the calibration fit, while the correlated errors should be propagated by coherently shifting all FD energies by the errors and then evaluating the change of the SD energy scale.

The calibration curve has been obtained for the dataset described in section 4.4.4. The SD only becomes fully efficient for energies above 3 EeV, so the events with eneries below this saturation threshold are not included. The parameters of the calibration curve obtained prior to the upgraded reconstruction are $A = (1.68 \pm 0.05) \cdot 10^{17}$ eV and $B = 1.036 \pm 0.009$ for a total number of selected events of 838. This is in total agreement with the results presented previously [149] ($A = (1.68 \pm 0.05) \cdot 10^{17}$ eV, $B = 1.037 \pm 0.009$ and 839 events).

6.2 Changes in the energy scale of the Pierre Auger Observatory due to the FY

Previously, the Pierre Auger Collaboration used the fluorescence spectrum and atmospheric dependences of the FY measured by the AIRFLY collaboration and the absolute value of the 337 nm band measured by Nagano *et al.*, a dataset called in this work the Nagano-AIRFLY dataset. The Nagano value for the 337 nm band has an uncertainty of 14%. This was the largest contribution to the total uncertainty of the Auger energy scale, that amounted 22%. In 2013, the AIRFLY collaboration published a much precise value for this magnitude with a reported uncertainty of only 4%.

The atmospheric dependences of the FY that were studied in the previous chapter have been introduced in the Auger scale in 2012 [117]. However, the impact of their uncertainties was not previously taken into account, as they were negligible compared with the uncertainty associated to the absolute value of the 337 nm band. The reduced uncertainty of the new AIRFLY value made necessary a complete evaluation of all the parameters involved in the FY, that is, P', α and P'_w

6.2.1 Effect of the new 337 nm band absolute value

As was already mentioned in section 4.4.5, when the absolute value of Airfly (around 11% higher than the one from Nagano *et al.*) is used, the energy is lowered by around 8% with a slight dependence on the energy, as can be seen in Fig. 6.1. This result is expected taking into account the contribution of the Cherenkov light in the energy reconstruction. For lower energy showers the Cherenkov contribution is higher than in more energetic ones and thus the change in the energy is smaller. It is worth noting that this change is within the boundaries of the previous uncertainty that, as mentioned before, was 14%.

This huge uncertainty is drastically reduced with the new AIRFLY value. Fig. 6.2 (left) shows how much the energy changes when the absolute yield of 337 nm band is shifted by its uncertainty. The new uncertainty on the energy scale becomes, on average, $+3.4\%/-3.1\%$. Since the absolute yield is known with such precission, the effect of the uncertainties of the relative band intensities has to be evaluated. An upper limit on this uncertainty component has been estimated by taking half of these uncertainties as fully correlated, as suggested by the AIRFLY Collaboration [27]. The showers have been thus reconstructed by changing all relative intensities by plus/minus half the error. Fig. 6.2 (right) shows that the resulting uncertainty in the energy scale is around 1%.

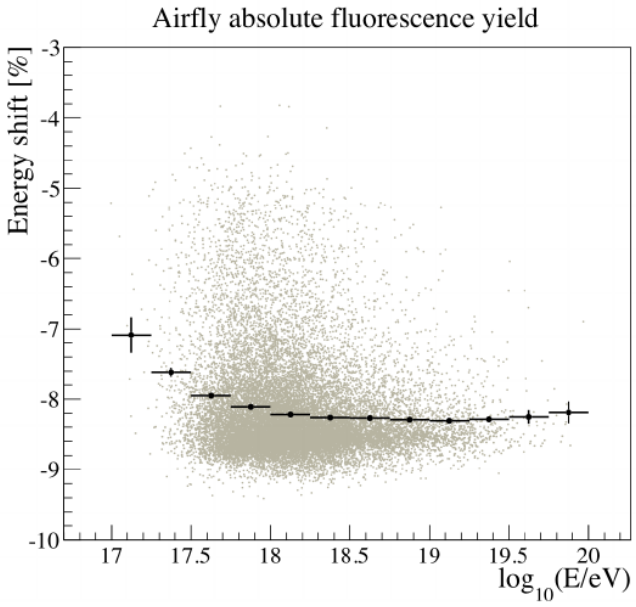

Figure 6.1: Change of the shower energies when introducing the new absolute yield of the 337 nm band measured by the AIRFLY experiment with respect to the old value measured by Nagano *et al.*. Figure taken from [29]

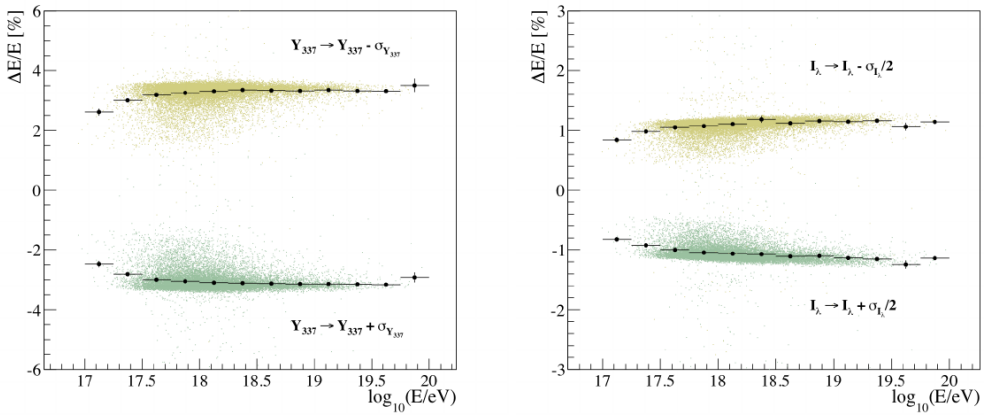

Figure 6.2: Propagation to the shower energies of the systematic uncertainties on the absolute fluorescence yield (left) and on half of the uncertainties on the λ band intensities (right). Figure taken from [29]

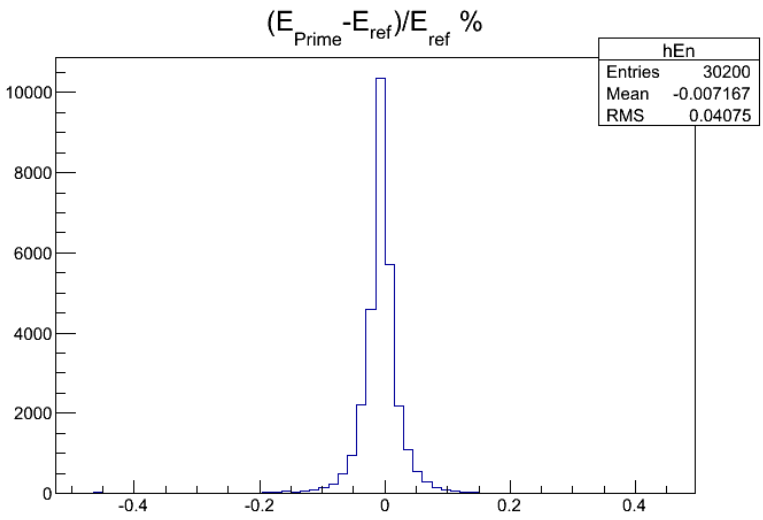

Figure 6.3: Propagation to the shower energies of the uncorrelated systematic uncertainties on the P'values. See text for details.

6.2.2 P' uncertainties

The errors in $P'_{\rm air}$ have two components, one correlated and one uncorrelated [27]. Both have been propagated to the energy scale taking into account the different grades of correlation. The uncorrelated errors have been propagated by generating 50 different sets of $P'_{\rm air}$ assuming a Gaussian distribution of the errors. The data sample to perform this analysis was reduced to a representative subsample of around 550 events to reduce computation time. The uncertainty in the energy has then been evaluated by taking the RMS of the energy shift distribution obtained by reconstructing the showers with the different sets of parameters (Fig 6.3). The uncertainty on the energy arising from these uncorrelated errors is found to be 0.05%

Correlated errors, on the other hand, have been evaluated following a similar procedure to the one followed to evaluate the relative intensities of the spectrum, that is by reconstructing the subsample by changing all $P'_{\rm air}$ values by plus/minus the correlated errors. The effect on the energy scale, as can be seen in Figs. 6.4a and 6.4b, is around 0.1%.

6.2.3 Uncertainties in the temperature parameter α

The uncertainties in the cross-section temperature dependence and the humidity dependence had both been evaluated using a similar procedure than the one followed in chapter 5. A first theoretical prediction of the effect of a change in the atmospheric parameters on

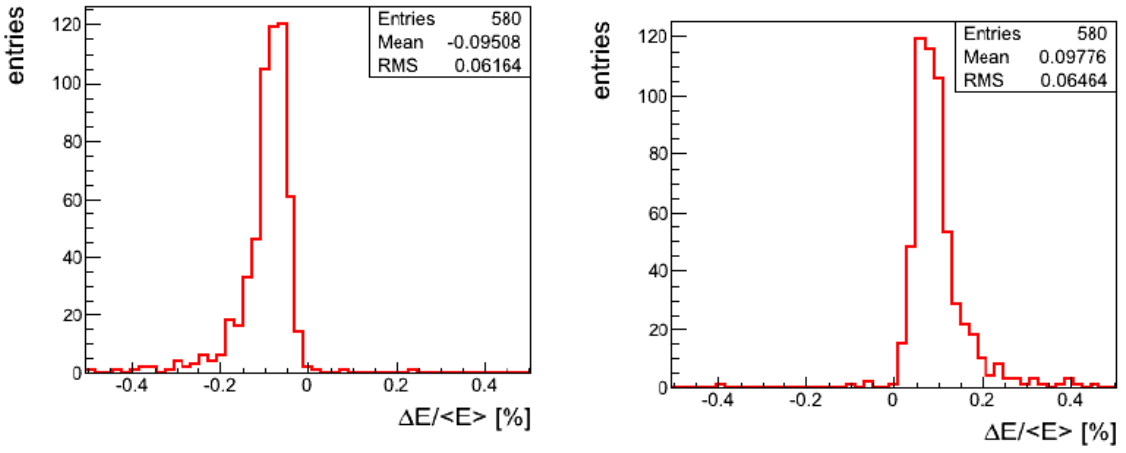

(a) (b)

Figure 6.4: Propagation to the shower energies of the correlated systematic uncertainties on the P'values. See text for details

the FY was performed by checking the variation in the FY ratio between the official Airfly dataset and the same dataset with a shift in the α and P'_w atmospheric parameters equivalent to their reported uncertainties. For simplicity, the P'_w and α values for all the fluorescence bands were shifted in the same direction, even though their errors are not correlated.

In the case of the α parameters, the shift was applied considering a mean relative uncertainty of 10%, that is, $\alpha \pm \sigma_T$ with $\sigma_T = 0.1 \cdot \alpha$. The results of this change in the FY ratio are presented in Fig. 6.5 (red lines). As expected, the changes are only important in the upper layers in the atmosphere, that is, low depths. Near the ground the effect is completely negligible. This means that inclined showers will be more affected by the uncertainties in α than the vertical ones. Also it is worth noting that no clear differences are found between austral summer (Fig. 6.5a) and winter (Fig. 6.5b).

The effect of the temperature dependence uncertainties have been evaluated following the method presented in section 4.3 for G-H profiles from typical iron showers of 10^{18} eV and 10^{19} eV and two different incident zenith angles, 30° and 60°. To obtain an even more conservative estimate of the impact of the α uncertainties in the reconstructed shower energies, the modified profiles have been calculated with $\alpha \pm 1\sigma_T$ and $\alpha \pm 2\sigma_T$ for all the monthly profiles measured at the Auger site. The results of this analysis are shown in Fig. 6.6, when a $\pm 1\sigma_T$ is applied. The effect on 30° showers is small, but not negligible ($\delta E \approx 0.5\%$) while the inclined showers are much more affected ($\delta E \approx 1\%$) with no

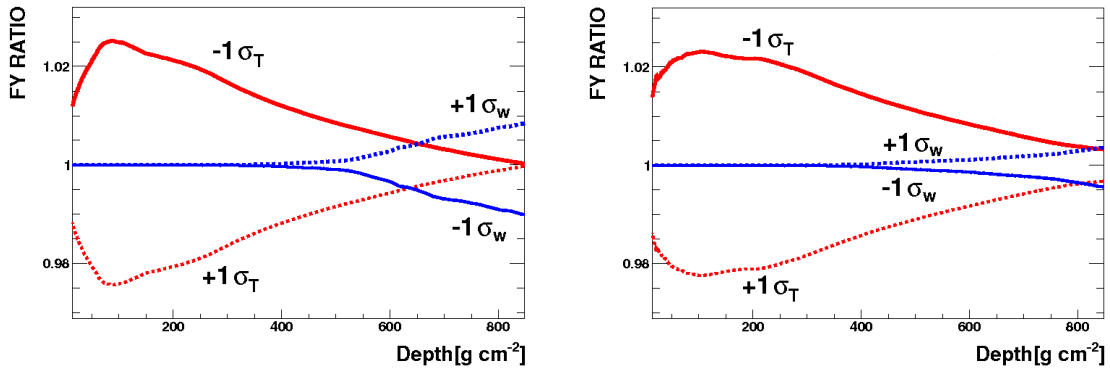

(a) (b)

Figure 6.5: FY ratio, defined as Y'/Y, where Y is the FY obtained with the Airfly database and Y' is the FY from the Airfly database modified by $\pm 1\sigma$ for February (left) and August (right) in the P'_w parameter (blue) and the α parameter (red). Figure taken from [30]

apparent season dependence. If this effect is doubled, that is, when a $2\sigma_T$ shift is applied, a $\delta E \approx 1\%$ is found for vertical showers, while the 60^o showers show a much important shift in energy, reaching $\delta E = 3\%$. A small seasonal dependence is found for such large deviations.

The evaluation of the temperature uncertainties with real data has been done following the same process employed to evaluate the uncorrelated uncertainties of P'_{air}. Fifty different α datasets were generated assuming a gaussian distribution of the errors. These datasets were employed to reconstruct a subsample of 550 events. The results were compared with the ones obtained with the official Airfly dataset. The error associated with the temperature dependence of the FY would be the RMS of the $(E_{\text{error}} - E_{\text{Airfly}})/E_{\text{Airfly}}$ distribution.

Fig. 6.7 shows said distribution. The uncertainty associated to α are found to be 0.3%, way less than the conservative theoretical prediction. The dependence with both energy and incident zenith angle has also been studied. While there is no indication of energy dependence (Fig. 6.8a), an slightly dependence with θ is found as expected (Fig. 6.8b).

6.2.4 Uncertainties in the humidity parameter, P'_w

The uncertainties associated with the humidity dependence of the FY are evaluated using the same procedure as the one employed for α. Again, although the uncertainties for each fluorescence band are not correlated, an uniform shift, estimated as the average of all P'_w errors will be used as a conservative estimation. Thus, the associated uncertainty to P'_w to

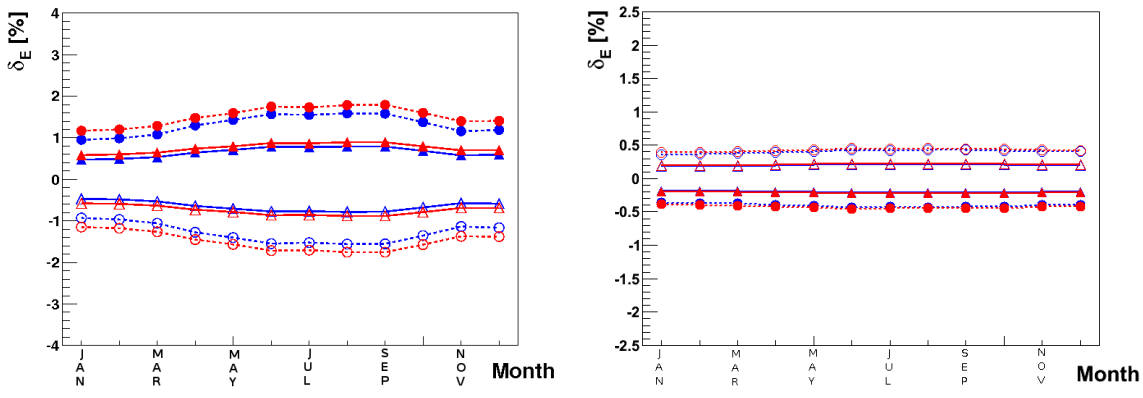

(a) (b)

Figure 6.6: Energy deviation vs Month when α is shifted $\pm 1\sigma$ (triangles) and $\pm 2\sigma$ (circles) for 30° (left) and 60° (right). Full symbols correspond to a negative shift in α. Figure taken from [30]

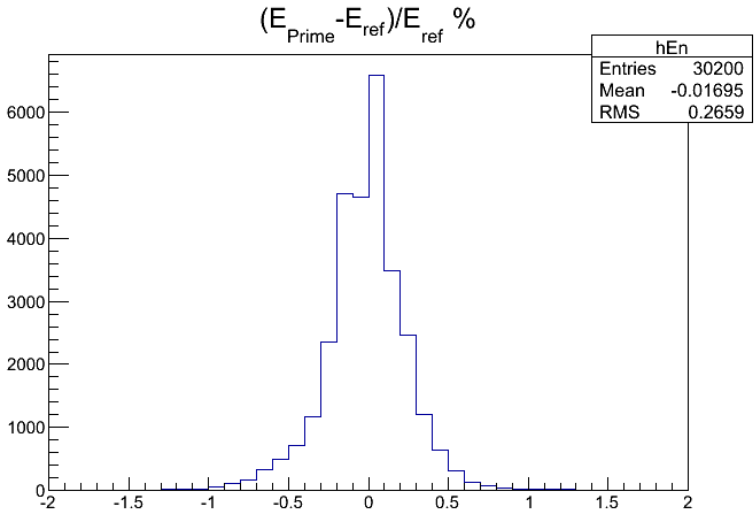

Figure 6.7: Propagation to the shower energies of the systematic uncertainties on the α values when using the modified set of parameters with respect to the measured ones. See text for details.

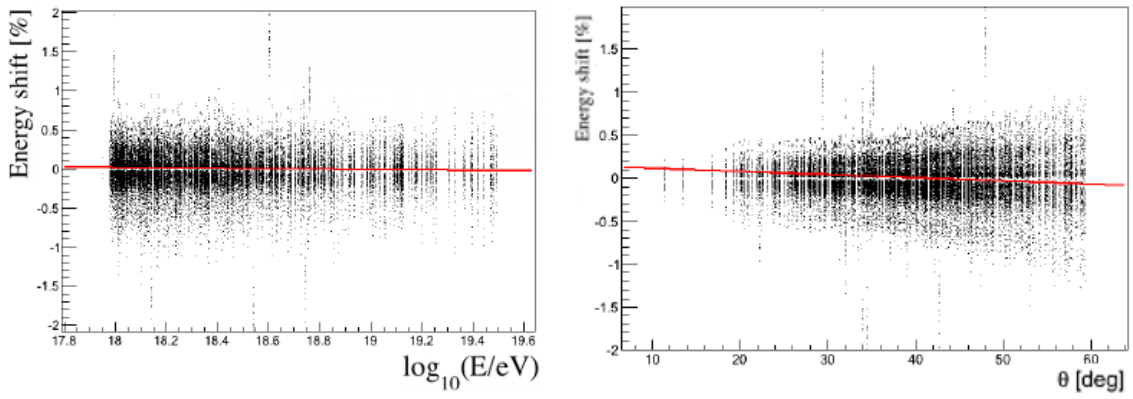

(a) (b)

Figure 6.8: Propagation to the shower energies of the systematic uncertainties on the α values versus energy (left) and zenith angle (right) when using the modified set of parameters with respect to the reported ones. See text for details.

obtain theoretical predictions, σ_w is estimated as $\sigma_w \approx 0.25 P'_w$. in Fig. 6.5 the blue lines show the effect of shifting P'_w by $\pm\sigma_w$. The change is completely negligible in the upper layers of the atmosphere, and only noticiable very near the ground. This means that only vertical showers that develop near the ground will be affected by this effect. The seasonal variation in this case is more important than the one found for α.

In Fig. 6.9 the analytical prediction of the effect of the P'_w uncertainties is shown for a $\pm 1\sigma_w$ shift (triangles) and $\pm 2\sigma_w$ shift (circles). 60º showers (Fig. 6.9b) remain almost unaffected by both shifts in the P'_w, because those showers develop higher in the atmosphere and thus are less affected by the humidity. On the other hand, for 30º showers (Fig. 6.9b), δE reaches 0.5% for a $\pm 1\sigma_w$ shift, while it can reach up to 1.5% depending on the season when a $\pm 2\sigma_w$ shift is applied.

The same analysis employed for the evaluation of the reconstructed energy uncertainties associated to the α parameters have been applied to P'_w. 50 different datasets have been randomly generated assuming a gaussian distribution of the errors for each band. The selected subsample of events has been subsequently reconstructed for each database and compared with the official one. The results are shown in Fig. 6.10.

In Fig. 6.11 the dependence of δE with energy and incident angle are shown. There is a slight dependence with θ, as expected, but also with the primary energy. This can be related to the fact that more energetic showers develop deeper in the atmosphere and thus are more affected by the humidity. In any case, this dependence is quite small and can be

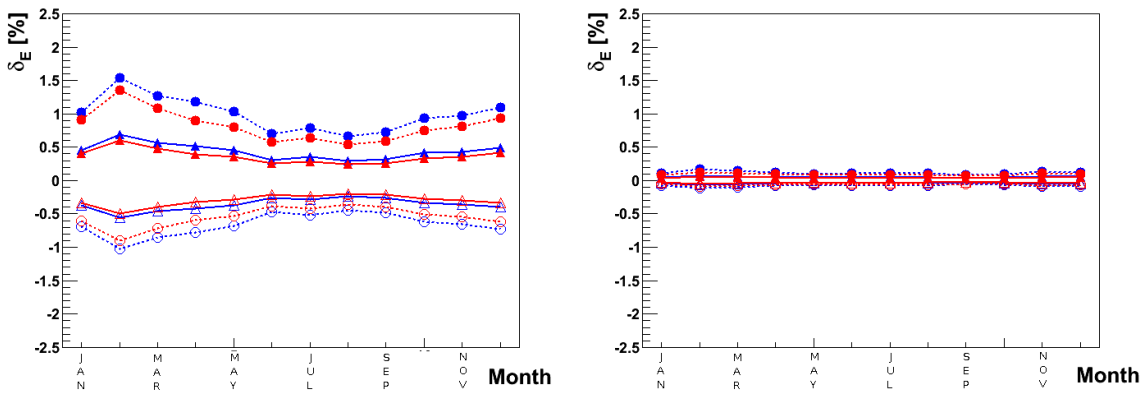

(a) (b)

Figure 6.9: δE vs Month when P'_w is shifted $\pm 1\sigma$ (triangles) and $\pm 2\sigma$ (circles) for 30° (left) and 60° (right). Full symbols correspond to a positive shift in P'_w. Figure taken from [30]

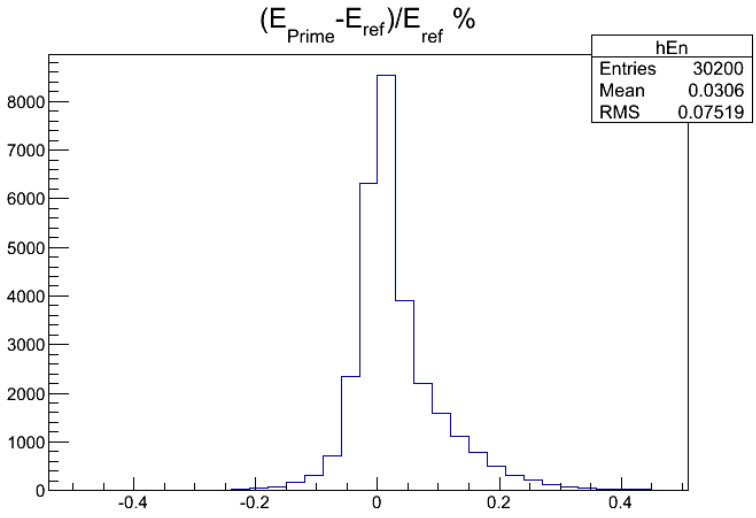

Figure 6.10: Propagation to the shower energies of the systematic uncertainties on the P'_w values when using the modified set of parameters with respect to the reported ones. See text for details.

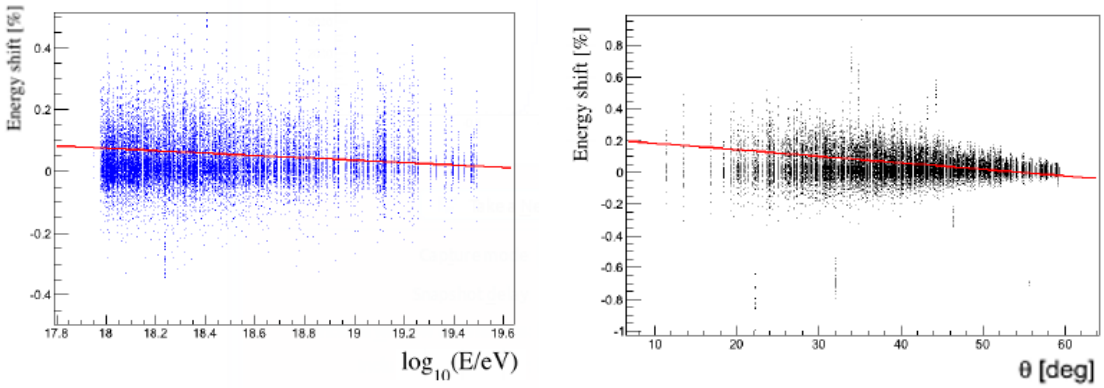

(a) (b)

Figure 6.11: Propagation to the shower energies of the systematic uncertainties on the P'_w values versus energy (left) and zenith angle (right)when using the modified set of parameters with respect to the reported ones. See text for details.

neglected.

The uncertainties associated to the P'_w parameter is then estimated using the RMS of the δE distribution. An 0.1% value associated to the errors in P'_w is added to the total uncertainty in the energy scale, independently of energy, as a result.

Another source of uncertainties is the dependence of P'_w with temperature. Like any other P', the behaviour with temperature should be corrected with an α_w due to the collisional cross-section dependence with temperature, that is $P'_w \propto (T_O/T)^{\alpha_w - 1/2}$. However, this parameter is very difficult to measure and no experimental values have been reported yet. An estimation of the effect of neglecting this dependence can be done by using the α values for dry air for each band. This introduces an 0.05% uncertainty in the energy scale.

6.3 Other changes in the energy scale

The new measurements of the FY are only one of the many improvements in the Auger energy scale that have been studied by the Hybrid Reconstruction task of the Pierre Auger Collaboration. Although they are out of the scope of this thesis, a brief review of the most important ones is presented in this section.

6.3.1 FD calibration

Recently, a new study of the optical properties of the FD telescopes have been carried out using an isotropic point-like source mounted on flying platform [150]. For a fixed position of the light source, it has been discovered that the reflectivity of the PMT surface causes an optical *halo* extending over the full focal surface of the telescope. The calibration constants have been corrected for this effect increasing by about 3% with shower energy.

As was explained in section 3.2.3, the FD telescopes are calibrated absolutely with a drum-shaped light placed in front of the diaphragm. This end-to-end calibration of all elements of the telescope is performed periodically. A new calibration curve using the drum device has also been introduced. In the past, the optical efficiency of each component of the telescope was used instead. This revised efficiency increases the shower energies by about 4%. The absolute calibration is made at 375 nm and has an uncertainty of 9% fully correlated between different showers. The aim of the Pierre Auger Collaboration is to reduce the uncertainty to 5% following the progress reported in [151]. The uncertainties in the efficiency curve propagated to the shower energies introduces a correlated uncertainty of 3.5%

The response of the PMTs to the relative calibration before and after each night are used to track the absolute calibration between the drum measurement periods. The associated uncertainties to this tracking are 3% for the uncorrelated part and 2% for the correlated one.

6.3.2 Atmosphere

An accurate measurement of the transmission factors during data acquisition is necessary for a reliable reconstruction of the shower and for proper measurements of the physical properties of the primary particle (energy, mass composition, etc). The hourly estimates of the aerosol optical depth profile used to calculate the aerosol transmission factor [152] have been improved recently [153]. The uncertainty in these profiles has two components, one correlated and another uncorrelated between different showers. These components give rise to an uncertainty in the energy that grows with energy from 3% to 6%. Other correlated uncertainties related to aerosols are those from measurements of the phase function and from the wavelenght dependence of the scattering cross-section and amount to 1% and 0.5% respectively. Another uncorrelated uncertainty of 1% is associated to the spacial variability of the aerosol across the site [154].

The fluctuations associated to the use of the GDAS model for the parameterization of the atmosphere [117] have been evaluted, giving rise to an uncorrelated uncertainty of

around 1% and a correlated one of about 1%.

6.3.3 Longitudinal profile reconstruction

The event reconstruction method has been slightly changed due to an improved technique for the determination of the energy deposit in the atmosphere. As explained in section 4.4, knowing the shower geometry, the FD absolute calibration, the attenuation of the light flux in the atmosphere and by estimating the number of Cherenkov photons detected by the FD, it is possible to calculate the energy deposit with a fit to the dE/dX data using a Gaisser-Hillas function. This enables an estimate of the energy deposit even outside the field of view of the telescopes and therefore yields the energy deposited in the atmosphere.

Because of the intrinsic shower width and the optical point spread function of the telescopes, part of the incoming light is spread away from the image axis in the field of view of non-selected pixels. The contribution of this light to the dE/dX is calculated by estimating the size of the shower image at the telescope diaphragm. Two models are used for the fluorescence [155] and Cherenkov [156] light. We have now introduced a further correction which takes into account the angular spread close to the shower axis produced by the optical elements of the FD telescope [150]. The folding of this point spread function with the intrinsic shower width spreads the light more than predicted by the two models that only take into account the shower width. This effect has been parameterized by analysing shower data and it increases the shower energy by 9% for lower energies down to 5% as energy increases. A conservative correlated systematic uncertainty of 5% has been assigned to the light collection.

A further complication arises from the light that arrives to the telescope after being scattered multiple times in the atmosphere. To avoid an overestimation of the shower energy, this light must be substracted from the profile of detected photons. This multiple scattering has been parameterized using [157] and the uncertainty of it affects the shower energies in a fully correlated way by about 1% [154].

A new maximum likelihood fit, taking into account realistic fluctuations of the signal in the PMTs has also been developed. This increases the shower energies by about 2%. To improve the fit of the dE/dX, a Gaussian constraint is imposed to the parameters that define the Gaisser-Hillas function. Changing this constraint by one standard deviation, a fully correlated uncertainty in the shower energy that ranges from 3.5% to 1% decreasing with energy has been evaluated. Other errors arise from the statistical error of the dE/dX fit, which decreases with energy from 5% to 3%, and an average uncertainty of 1.5% that arises from the uncertainty in the shower axis geometry. Both effects are uncorrelated.

Finally, the full reconstruction technique has been tested using Monte Carlo simulations. On average, the reconstructed energies differ from the true ones by about 2%. This bias has been considerated another uncorrelated uncertainty.

6.3.4 Missing energy

The final update in the reconstruction concerns the invisible energy [113], $E_{\rm inv}$. Previously, the Auger collaboration used an estimate based entirely on simulated showers [158] while the new one is derived from data. This significantly reduces the dependence on the hadronic interaction models and mass composition. $E_{\rm inv}$ can be calculated for each shower using the FD measurement of the longitudinal profile and the SD signal at 1000 m from the axis, S_{1000}. This can only be reliably estimated for shower energies above $3 \cdot 10^{18}$, for which the SD is fully efficient. Below this energy, S_{1000} is biased by upward fluctuations of the shower signals and, in this case, $E_{\rm inv}$ is extrapolated from the analytical functions for showers above $3 \cdot 10^{18}$ eV.

The same set of showers used to calibrate the SD energies is used to find the relation between $E_{\rm inv}$ and the calorimetric energy $E_{\rm cal}$:

$$E_{\rm inv} = a_0 (E_{\rm cal}[\mathrm{EeV}])^{a_1} \tag{6.4}$$

The fit is performed by minimising a χ^2 function which takes into account the fluctuations of both the FD and the SD measurements yielding the parameters $a_0 = (0.174 \pm 0.001) \cdot 10^{18}$ eV and $a_1 = 0.914 \pm 0.008$. The correlation coefficient of the two parameters is -1.

The number of muons measured with the SD [159] is higher than that predicted by the simulations formerly used to derive the invisible energy. This contribution to the primary energy now ranges between 15% at 10^{18} eV and 11% at the highest energies, while the previous predictions were $11\% \div 8\%$. With the new estimation the total energy for the highest showers increases about 4%. Analysis of the systematic uncertainties of the invisible energy [113] shows a correlated uncertainty in the total energy that decreases with energy from 3% to 1.5%.

Due to the stochastic nature of air showers, the invisible energy is also affected by shower-to-shower fluctuations. These are parameterized according to [28], introducing an uncorrelated uncertainty of 1.5%.

Changes in FD energies at 10^{18} and 10^{19} eV		
AIRFLY Fluorescence Yield	−8.2%	−8.3%
New optical efficiency	4.3%	3.7%
Calibration database update without halo	−0.5%	−1.1%
Optical halo correction	3.2%	3.2%
Subtotal (FD calibration)	7.0%	5.8%
Likelihood fit of the profile	2.2%	2.2%
Lateral width correction	9.5%	10.1%
Subtotal (FD profile reconstruction)	11.7%	12.3%
New missing energy	6.9%	5.6%
TOTAL	17.4%	15.4%

Table 6.1: Changes to the energy of showers at 10^{18} and 10^{19} eV.

6.4 The new energy scale of the Pierre Auger Observatory

The changes in the event reconstruction presented in this chapter have an impact in the energy determination and the associated uncertainty for both FD and SD events. All changes that concern the FD energies are summarized in Table 6.1 for two reference energies: 10^{18} and 10^{19} eV. Figure 6.12 shows the cumulative energy shift as a function of the shower energy when the effects described in this chapter are taken into account. It is worth noting that the aerosol optical depth profiles described in section 6.3.2 do not affect the shower energies significantly and thus are not included in the figure. The new energy scale is consistent with the old one within the reported systematic uncertainty of 22% [149]. In fact, each individual contribution to the change in the energy scale is consistent with the uncertainties reported previously for each sector of the reconstruction (14% for the fluorescence yield, 9.5% for the FD calibration, 10% for the longitudinal profile reconstruction and 4% for the invisible energy).

The new calibration curve parameters obtained after the fit are $A = (0.190 \pm 0.005) \cdot 10^{18}$ eV and $B = 1.025 \pm 0.007$ for a total number of 1475 showers with a correlation coefficient of -0.98. The RMS of the distribution of AS_{38}^{B}/E_{FD} is about 18.5%. It is dominated by low-energy showers and is compatible with the expected resolution obtained from the quadratic sum of all the uncertainties listed in Table 6.2

The large number of hybrid showers detected by the Pierre Auger Observatory over 9 years has allowed several consistency checks [160]. The SD energy estimator ($E_{SD} = AS_{38}^{B}$ for a given value of S_{38}) has been studied by making calibrations fits to data collected during different time periods and/or under different conditions. E_{SD} is found to be stable within 5%, significantly above the statistical uncertainties. Even though these variations

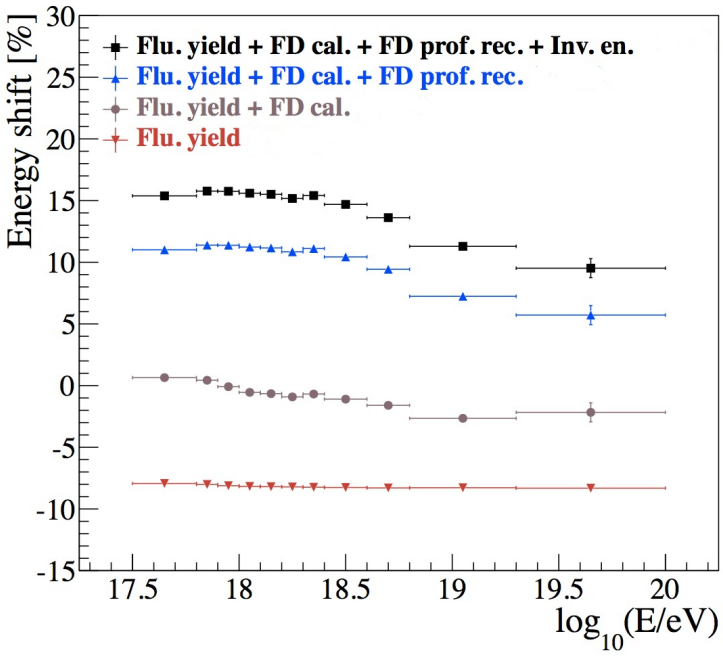

Figure 6.12: Cumulative energy shift as a function of the shower energy when various effects are introduced. Figure taken from [31]

Uncertainties entering into the SD calibration fit	
Aerosol optical depth	$3 \div 6\%$
Horizontal uniformity	1%
Atmosphere variability	1%
Nightly relative calibration	3%
Statistical error of the profile fit	$5 \div 3\%$
Uncertainty in the shower geometry	1.5%
Subtotal (FD energy resolution)	$7 \div 8\%$
Statistical error of the S(1000) fit	$12 \div 3\%$
Uncertainty in lateral distribution function	5%
Shower-to-shower fluctuations	10%
Subtotal (SD energy resolution)	$17 \div 12\%$

Table 6.2: Uncertainties uncorrelated between different showers affecting the energy estimator

Systematic uncertainties on the energy scale	
Absolute fluorescence yield	3.4%
Fluorescence spectrum and quenching parameters	1.1%
Subtotal (Fluorescence Yield)	3.6%
Aerosol optical depth	$3 \div 6\%$
Aerosol phase function	1%
Wavelength dependence of aerosol scattering	0.5%
Atmospheric density profile	1%
Subtotal (Atmosphere)	$3.4 \div 6.2\%$
Absolute FD calibration	9%
Nightly relative calibration	2%
Optical efficiency	3.5%
Subtotal (FD calibration)	9.9%
Folding with point spread function	5%
Multiple scattering model	1%
Simulation bias	2%
Constraint in the Gaisser-Hillas fit	$3.5 \div 1\%$
Subtotal (FD profile reconstruction)	$6.5 \div 5.6\%$
Invisible energy	$3 \div 1.5\%$
Statistical error of the SD calibration fit	$0.7 \div 1.8\%$
Stability of the energy scale	5%
TOTAL	14%

Table 6.3: Systematic uncertainties on the energy scale

of E_{SD} are consistent with the quoted systematic uncertainties, another uncertainty of 5% is introduced to take into account this effect.

As mentioned before, the FD uncertainties correlated between different showers should be propagated to the SD energy scale by shifting all FD energies coherently by their uncertainties. This means that the correlated uncertainties propagate entirely to the SD energies. Table 6.3 lists all uncertainties on the Auger energy scale. Most of them have a mild dependence on energy. When this dependence is non-negligible, a variation of the uncertainty in the energy range between $3 \cdot 10^{18}$ eV and 10^{20} eV is presented. The total uncertainty is about 14% and approximately independent of the energy. This is a significant improvement from the previous energy scale uncertainty of 22% [149].

Chapter 7

The impact of the FY selection on TA and Auger

The Telescope Array project (TA) is an UHECRs hybrid detector located in Millard County, Utah, USA that observes the sky of the northern hemisphere since 2007. The surface detector is composed of more than 500 scintillators evenly distributed across a 762 km^2 array with 1.2 km grid spacing. The fluorescence detector comprises three fluorescence telescopes, one of them refurbished from the HiRes experiment. Since 2012, the Pierre Auger and the TA collaborations have started to work together in order to understand the discrepancies between both experiments in the energy spectrum, mass composition and arrival direction of UHECRs. The first joint result sof both collaborations, as well as other UHECR experiments like Yakutsk, were presented in the UHECR Conference celebrated at the CERN in 2012 [14, 15, 161, 162], and in the 33^{rd} ICRC celebrated in Sao Paulo [163]. Also, a first joint journal paper has been recently published [164].

In Fig. 2.8 (see section 2.3.1) it has been shown that the differences between the spectra of these UHECR experiments, can be explained if a scale factor is applied. The FY is an external parameter and thus, one source of discrepancy that can be easily evaluated. In this chapter the impact of the FY selection in the relative scales of TA and the Pierre Auger Observatory will be evaluated using both an analytical method and a detailed reconstruction using the $\overline{\text{Off}}\underline{\text{line}}$ framework, following the procedures explained in sections 4.3 and 4.4. Since TA and Auger use different optical filters and assume different wavelength spectra, the procedure presented in 4.5 has been applied.

The impact of the FY selection in the shape of the longitudinal profile has also been studied, in particular the effect on the $X_{\max}$ value. Finally both energy and $X_{\max}$ deviations have been combined to study the effect on the elongation curve.

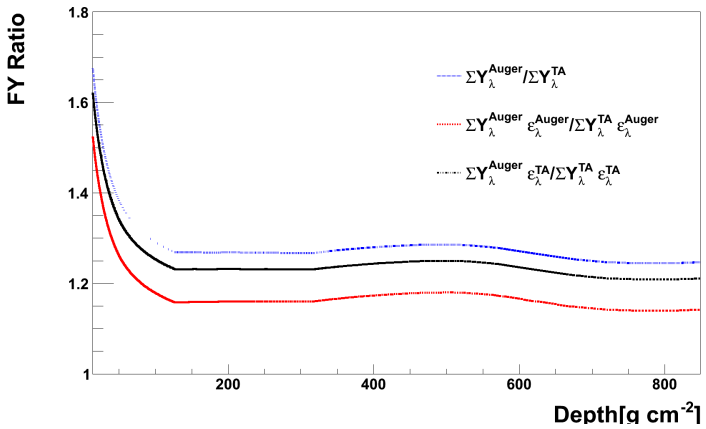

Figure 7.1: Comparison between the AIRFLY and the Kakimoto-FLASH FY databases versus atmospheric depth for the month of January (blue line). Red and black lines represent the corresponding ratios when the fluorescence light is filtered by the optical system of Auger and TA, respectively.

7.1 Differences between FY datasets

As mentioned in section 4.2, the dataset employed to describe the FY and its dependences is composed of many different parameters. The dataset employed by Auger, reviewed through this thesis, is the one measured by the AIRFLY collaboration, while Telescope Array employs the absolute FY and P' values measured by Kakimoto *et al.* and the relative intensities obtained by the FLASH collaboration that characterize the spectrum.

The main difference between both datasets is the absolute value of the FY. For the 337 nm band, the FY assumed by TA is about 30% smaller than that of Auger and this should be translated into a comparable energy overestimate of TA. Other FY parameters like the wavelength spectrum and atmospheric dependences assumed by both experiments are different in such a way that the large discrepancy in the absolute FY is partly compensated.

Also, it is important to remark that the eficiency of the fluorescence telescopes, which is determined by the optical filters, mirrors, PMTs, etc., is a function of wavelength. In Fig. 4.3 the wavelength dependence of the optical efficiencies of Auger and TA are shown. While TA efficiency is much wider and has almost no effect on the observed wavelength spectrum, the Auger efficiency is much narrower, reducing the observed interval down to 320-400 nm. Moreover, the atmosphere scatters the light following a λ^{-4} law, further affecting the differences between the spectra. A correct determination of the differences between energy scales of Auger and Telescope Array must take into account these effects.

The effect of the optical filter on the wavelength-integrated FY is displayed as a function

of the atmospheric depth in Fig. 7.1. It can be seen that the filter, in particular the one of Auger, reduces the difference in the integrated FY values. The shape of the function showed in the figure can be explained from the results presented in section 5.3. The combined effect of the temperature and humidity dependence in the FY is almost constant regardless of atmospheric depth. Only at very high altitudes (i.e. very low depth) the FY ratio gets larger due to the shallow atmosphere (i.e. low values of P) that makes relevant the differences in P' values. However, the energy deposit at these altitudes is marginal and thus these deviations are completely irrelevant to the reconstructed energy.

As shown in Fig. 7.1, the shape of these plots in the region around the maximum development of showers is nearly flat and thus using the FY of TA should not lead to a significant impact on the $X_{\max}$ reconstruction.

7.2 Theoretical expectations from an analytical method

The effect on the reconstructed energy of replacing the FY of Auger by that of TA in the Auger telescopes can easily be evaluated by means of the procedure described in section 4.5. Assuming the same telescope $\varepsilon_1 = \varepsilon_2 = \varepsilon_{\text{Auger}}$ in Eq. (4.36), the ratio between the default Auger energy, E_{Auger}, and that expected using the TA yield, E_{TA} becomes:

$$E_{\text{TA}}/E_{\text{Auger}} = C_{\text{Auger}}/C_{\text{TA}} \tag{7.1}$$

where C_{Auger} and C_{TA} are defined by Eq. (4.34) with the same optical efficiency, i.e., the Auger one, and the FY of Auger, Y_{Auger} ,and that of TA, Y_{TA}, respectively.

The C_{Auger} and C_{TA} integrals have been evaluated for a number of showers with different Gaisser-Hillas profiles $f(X)$ and with different arrival directions. The shower geometry is defined by the zenith angle θ, the azimuthal angle ϕ and the distance D from the telescope to the impact point at ground. The field of view of the telescope is assumed to cover 30° in elevation and 180° in azimuth, with the shower impact point being just in front of the telescope (see figure 7.2). The atmospheric transmission $T_\lambda(X)$ is calculated using data from [165]. Atmospheric profiles of the Malargüe monthly model have been used to parameterize the pressure, temperature and humidity profiles.

Following the criterium used along this thesis, the percentage energy difference is defined for this comparison as:

$$\delta E = 100 \times \frac{E_{\text{TA}} - E_{\text{Auger}}}{E_{\text{Auger}}}\,, \tag{7.2}$$

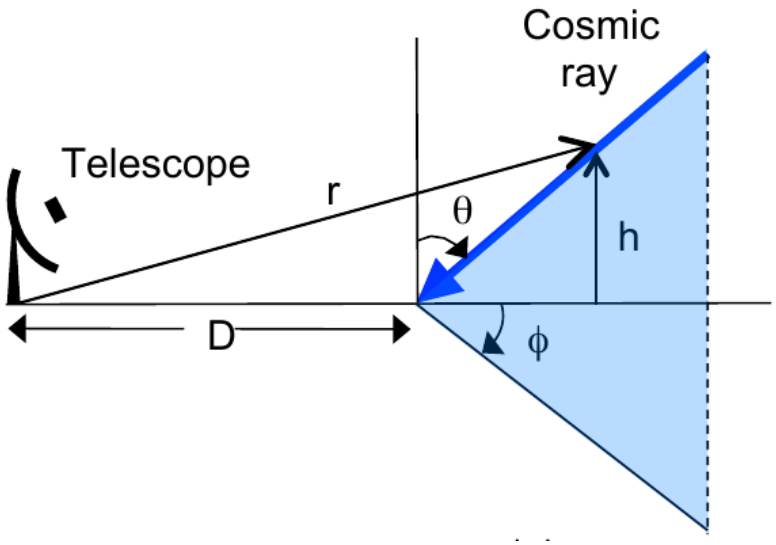

Figure 7.2: Diagram showing the definitions of the geometrical parameters used in this section.

This energy deviation is expected to depend on the average mass thickness of air $\langle r \rangle$ that separates the shower and the telescope, because the different wavelength spectra assumed by both experiments (i.e., Y_λ in equation (4.34)) are modified by the atmospheric transmission through Rayleigh scattering in a different manner. In addition, differences in the quenching parameters (i.e., P' values) can make δE to be dependent on the average height $\langle h \rangle$ where the fluorescence light is produced. So we use:

$$\langle r \rangle = \int_{\text{fov}} \mathrm{d}X \, f(X) r(X) \, ; \quad \langle h \rangle = \int_{\text{fov}} \mathrm{d}X \, f(X) h(X) \tag{7.3}$$

where the weighted averages are restricted to the fraction of shower within the telescope field of view.

In Fig. 7.3, the energy deviation for July is represented as a function of $\langle r \rangle$ and $\langle h \rangle$ for typical proton G-H profiles of 10^{19} and 10^{20} eV with three azimuth angles ϕ. The selected $\langle r \rangle$ and $\langle h \rangle$ are chosen to reproduce typical data obtained at the Pierre Auger Observatory. These analytical results show that the energy deviation ranges from about 12% to 17%, depending on both $\langle r \rangle$ and $\langle h \rangle$ due to the different wavelength spectra and atmospheric dependences respectively, as already mentioned. In general, the larger the distance traversed by the shower photons, the smaller the energy deviation. That means that showers that develop deeper in the atmosphere (and thus has a larger X_{max}) tend to

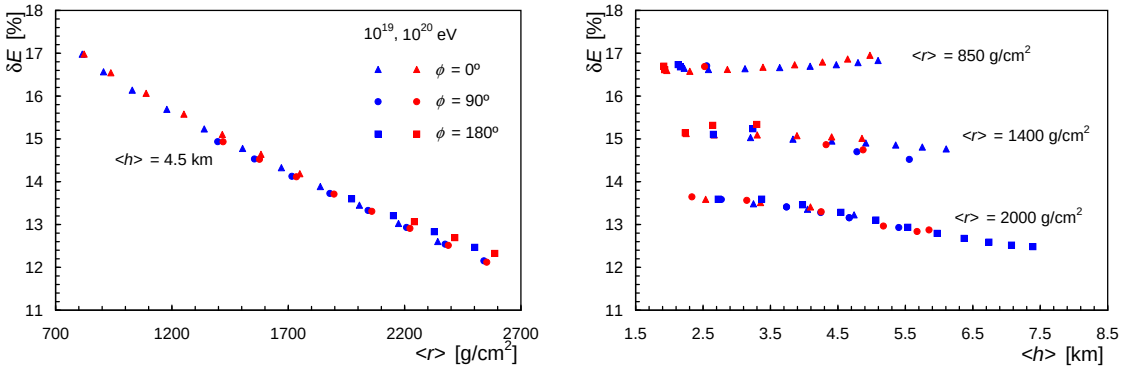

(a) (b)

Figure 7.3: Theoretical percentage difference in the reconstructed energies when the FY of Auger is replaced by that of TA for two shower energies and several combinations of the θ, ϕ, D parameters. Energy deviations have been calculated for the July month. Results are plotted as a function of $\langle r \rangle$ for a given $\langle h \rangle$ value (left) and as a function of $\langle h \rangle$ for several values of $\langle r \rangle$ (right).

have a smaller δE than those that develop higher for similar telescope-shower distances, due to the more dense atmosphere near the ground. This effect is clearly shown in Fig. 7.3b.

The calculation has been repeated assuming $\varepsilon_1 = \varepsilon_2 = \varepsilon_{\rm TA}$ in Eq. (4.36). Results are shown in Fig. 7.4. The energy deviation increases by 4.5 per cent units with respect to the previous case, because the flatter optical efficiency of TA amplifies the effect of a change of the FY.

These theoretical results do not account for many ingredients of the reconstruction algorithm of real data, in particular, the Cherenkov light. As was explained in Chapter 4, the Cherenkov signal expected for a shower of given energy and geometry is independent of the FY, and thus, the actual energy deviation due to a change in the FY should be somewhat smaller than the linear effect expected theoretically.

Apart from a scale factor in the reconstructed shower profile, a change in the FY may affect its shape if the corresponding atmospheric dependences are different. This is the case between the Auger and TA yields and thus a deviation in the reconstructed $X_{\rm max}$ values is expected. Theoretical predictions on the absolute difference in $X_{\rm max}$, that is,

$$\Delta X_{\rm max} = X_{\rm max}^{\rm TA} - X_{\rm max}^{\rm Auger}\,, \tag{7.4}$$

have been evaluated for various G-H profiles following the procedure described in section 4.3

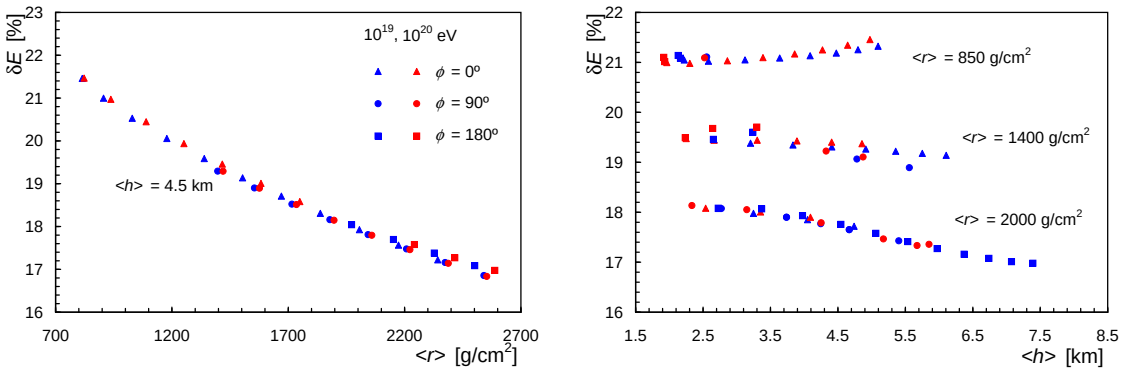

(a) (b)

Figure 7.4: Same as Fig. 7.3 taken into account the different optical efficiencies of the Auger and TA telescopes.

with different incoming directions and atmospheric conditions. As an example, in Fig. 7.5 the results for a proton with $X_{\max} = 755$ g cm^{-2} as a function of $h_{\max}$ (determined by θ) are shown. The calculation has been carried out for two orientations ϕ and two atmospheric conditions, i.e., January (left plot) and July (right plot). The temperature and humidity profiles are also shown.

The differences in the results for $\phi = 0^{\circ}$ and $\phi = 180^{\circ}$ are due the effect of the atmospheric transmission on the wavelenght spectrum of light reaching the telescope.

7.3 Results with real data

In section 7.3.1 an analysis similar to the theoretical one presented above will be shown, using real data obtained from the Pierre Auger Observatory to obtain the energy variation. First the TA dataset will be employed in the standard Auger reconstruction presented in section 4.4, and a comparison between theoretical predictions and the results obtained with real data will be shown. After that, the effect of the optical efficiency will be evaluated using the procedure explained in section 4.5. Finally, the results of an analogue comparison performed by the Telescope Array Collaboration that was recently presented in the UHECR2014 Conference, celebrated at Springdale, Utah, USA [32] will be discused and compared with those obtained in this work will be performed.

An analogue procedure will be done for $\Delta X_{\max}$ in section 7.3.2. In section 7.3.3, the effect of this change on the elongation rate, one of the main observables employed in the

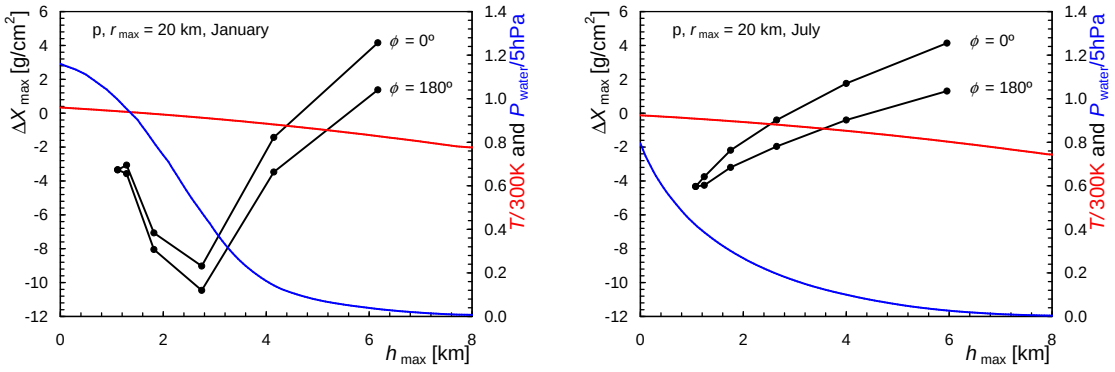

(a) (b)

Figure 7.5: The $X_{\max}$ shift versus the height of the shower maximum for a proton shower with two different orientations. Results are shown for average atmospheric profiles of January (left) and July (right) together with the corresponding temperature and humidity profiles.

determination of the mass composition of UHECRs will be presented.

Unless otherwise stated, the sample used for this analysis includes real data from January 2005 to December 2013. Reconstruction has been carried out using $\overline{\text{Off}}\underline{\text{line}}$ v2r9p2 for both yields, the one used by Auger and the one used in the TA experiment. The cuts employed by the Auger Collaboration for the hybrid spectrum selection (see section 4.4.4 for details) have been applied.

7.3.1 Effect of FY selection on reconstructed energy

The effect of using the FY of TA in the Auger reconstruction

The energy deviation histogram of the full real data sample when the Kakimoto-FLASH dataset is introduced in the Auger standard reconstruction is shown in figure 7.6. The energy of Auger would have increased on average 12.3% if Auger had used the FY model of TA instead. This energy deviation depends on the shower geometry and thus the δE distribution is broadened resulting in a total RMS of 2%, i.e., absolute value of RMS of 2 per cent units.

As shown in section 7.2, δE is expected to depend on the shower-telescope distance. In Fig. 7.7a, the average δE is plotted versus the distance between the telescope and the shower maximum, $r_{\max}$. δE decreases with $r_{\max}$ as expected. Also the larger E the larger the average distance $r_{\max}$ of registered showers (Fig. 7.7b) because very energetic showers

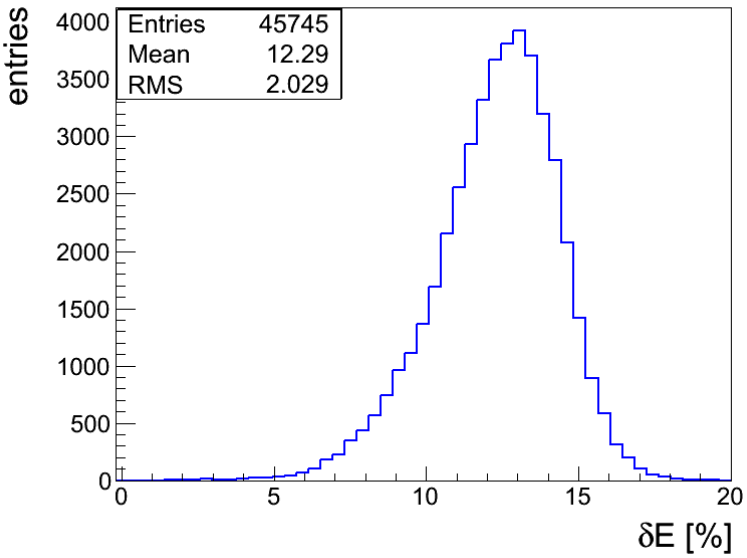

Figure 7.6: Reconstructed values of energy deviations, δE between the Auger and Kakimoto-FLASH dataset using the Offline standard reconstruction

can trigger the telescopes even at large distances. As a result of both correlations, δE turns out to decrease with primary energy (Fig. 7.8) although there is no intrinsic correlation between δE and E.

Other properties of δE are shown in Fig. 7.9. The energy deviation decreases with the fraction of Cherenkov light recorded from the shower, as expected (left plot). Also δE grows with the vertical depth of the shower maximum in the interval 300 - 600 gcm^{-2} with a smooth decrease for deeper showers (right plot).

In Fig. 7.10 a comparison between theoretical predictions from section 7.2 and the real data results are shown. The energy deviation for a shower of 53° and $X_{\rm max} = 677$ gcm^{-2} has been calculated as a function of the distance between the telescope and the shower maximum position $r_{\rm max}$. The theoretical values of δE span the gray area between the continuous line (January) and the broken line (July). The results for real showers with $X_{\rm max}$ values in the interval 660 - 690 gcm^{-2} and $50° < \theta < 55°$ have been split in two subsamples according to the fraction of Cherenkov light. As can be seen, real data follow the theoretical predictions although δE is smaller by an amount that increases with the fraction of Cherenkov light, as expected.

The average 12% deviation in energy can be explained as a combination of three factors:

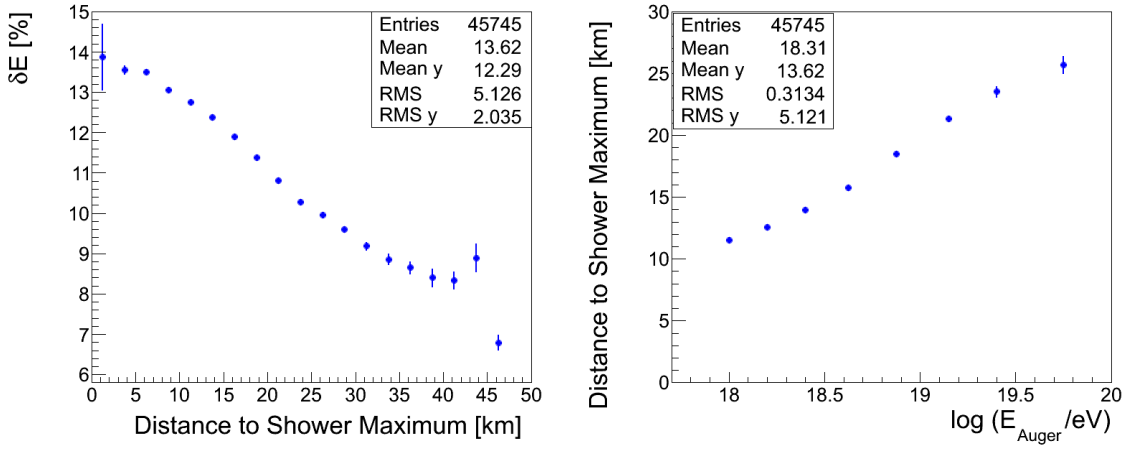

(a) (b)

Figure 7.7: The energy deviations decrease with $r_{\max}$ (left) and this distance to the shower maximum increases with the primary energy (right).

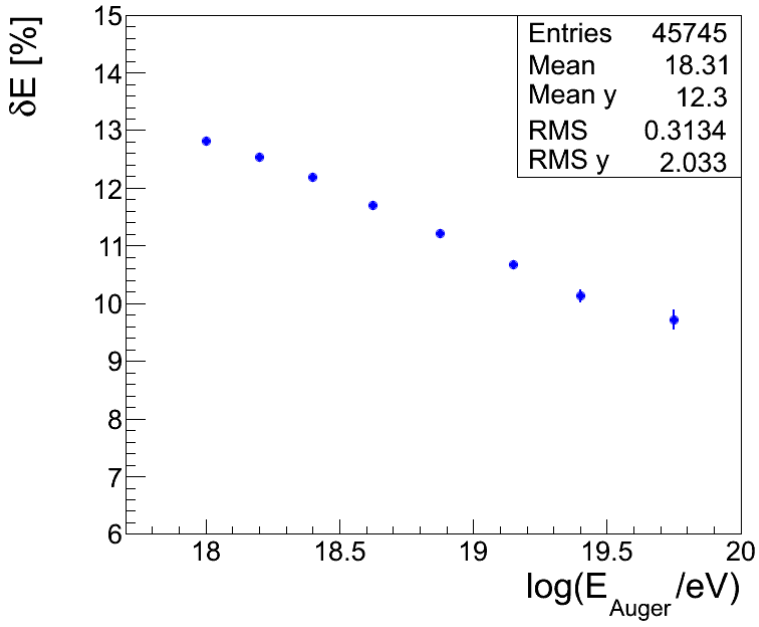

Figure 7.8: Energy deviation versus primary energy. δE decreases with the primary energy due to the combined correlations shown in figure 7.7

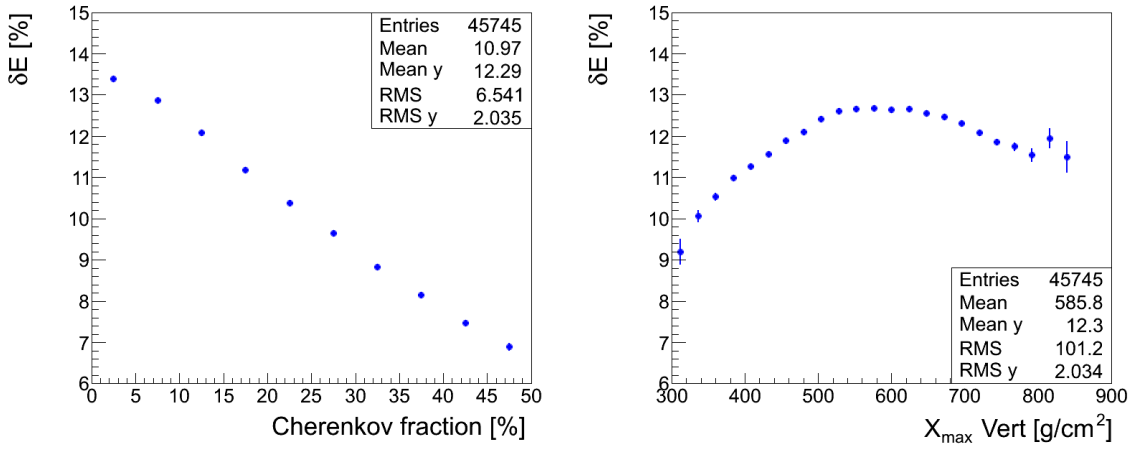

(a) (b)

Figure 7.9: The energy deviation versus Cherenkov fraction (left) and vertical depth of the shower maximum (right).

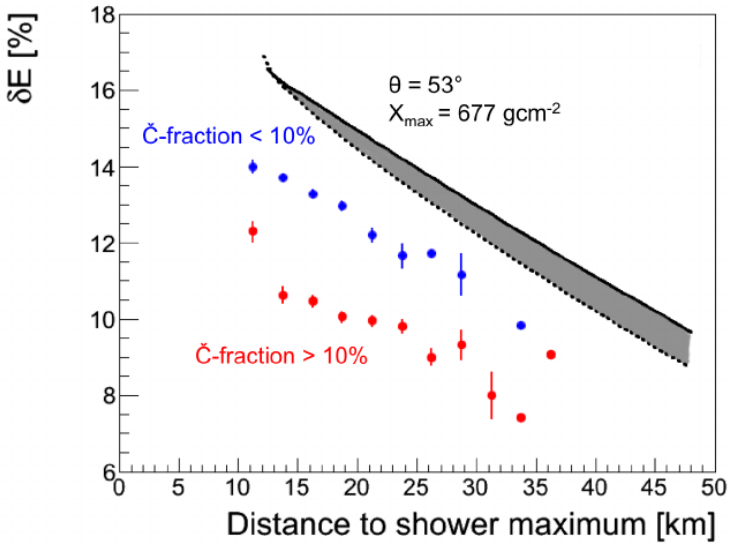

Figure 7.10: Energy deviation versus distance to shower maximum predicted by the analytical model (gray region) and from real data (points). See text for details.

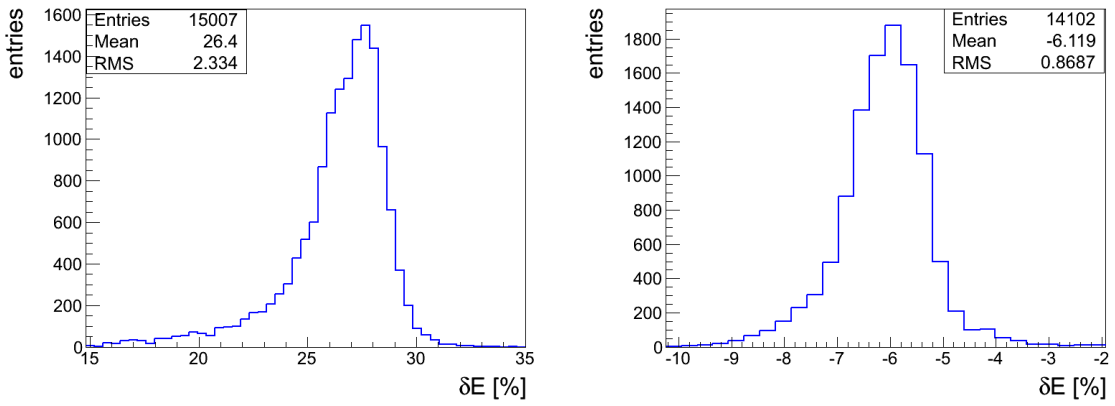

(a) (b)

Figure 7.11: (Left) Effect of replacing the Y_{337} value by that used in the TA collaboration in the AIRFLY dataset. (Right) Energy variations due to the different spectra employed by the TA and Auger Collaboration. See text for details.

the difference between the absolute FY value for the 337 nm band used by Auger and the one used by TA, the difference in the assumed fluorescence spectra and P' values, and the difference in the atmospheric parameters determining the temperature and humidity dependences. The effect of replacing the absolute FY value for the 337 nm used by Auger by that of TA keeping unchanged the remaining parameters of the Auger dataset is a 26.4% shift (Fig. 7.11a). If only the fluorescence spectrum and P' values are changed, keeping the absolute FY of Auger and ignoring temperature and humidity effects, then the effect is a 6% shift in the opposite direction (Fig. 7.11b). As shown in chapter 5, the energy shift due to the temperature and humidity effects exclusively is around 5%, also in the direction that compensates the shift due to the absolute FY. The combination of these three factors yields:

$$\begin{aligned}(1+\delta E_{\mathrm{Auger-TA}}) &= (1+\delta E_{Y_{337}})\cdot(1+\delta E_{\mathrm{Spectrum}})\cdot(1+\delta E_{T+h}) \\ &= (1+0.264)\cdot(1-0.06)\cdot(1-0.05) = 1.127\end{aligned} \tag{7.5}$$

Therefore, $\delta E = 12.7\%$, consistent with the previous result of 12.3% shown in Fig. 7.6.

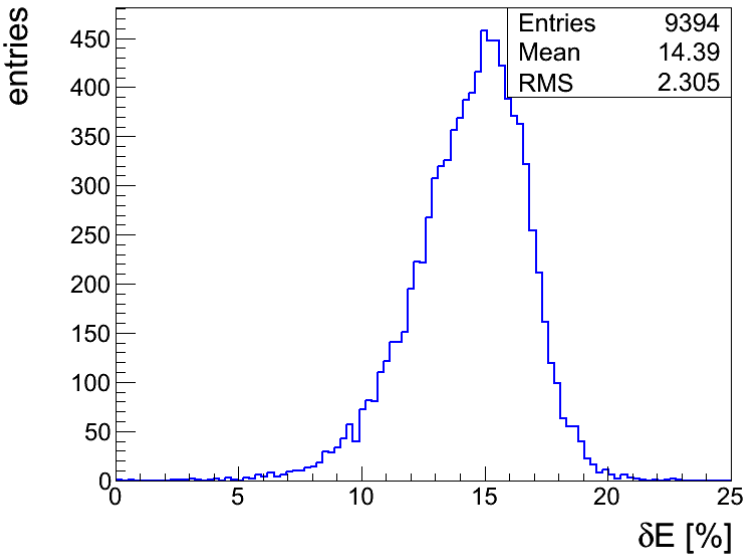

Figure 7.12: Histogram of energy deviations in the relative energy scales of Auger and TA including the effect of the optical filter.

The effect of the optical filter on the relative energy scale

As mentioned above, the relative energy scales of Auger and TA might also be affected by the fact that the optical efficiency of the telescopes are different and both experiments assume different wavelength spectra. The procedure for the evaluation of the relative energy scale was described in section 4.4.4. For this analysis the sample employed was smaller (January 2004 - December 2010). Results are shown in Fig. 7.12. The average value of the energy deviation is 14.3%, i.e., somewhat larger than the one displayed in Fig. 7.6. The actual relative energy scales of Auger and TA may be even larger because this analysis does not include some other possible factors, as will be discussed later.

In Fig. 7.13a the dependence of δE with distance is shown. It follows the same behaviour to the one shown in Fig. 7.7a. The same holds for the correlation between δE and the primary energy (Fig. 7.8 and 7.13b).

In Fig. 7.14, the differences between the standard Auger reconstruction employing the TA FY dataset (red points) and this analysis (blue points) are shown. When the effect of the different optical efficiencies is included, δE is around 2 per cent units higher irrespective of the energy.

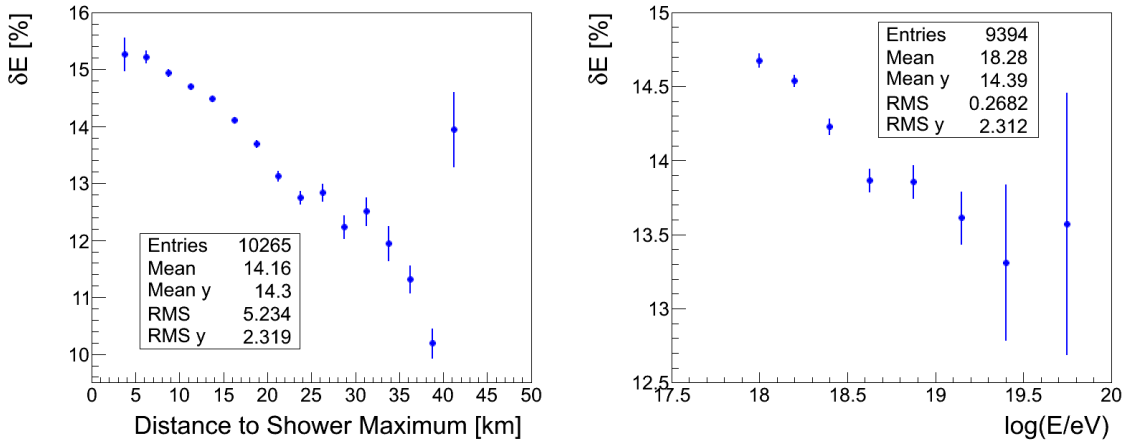

(a) (b)

Figure 7.13: Energy deviations versus distance to the shower maximum (left) and primary energy (right) in the relative energy scales of Auger and TA including the effect of the optical filter.

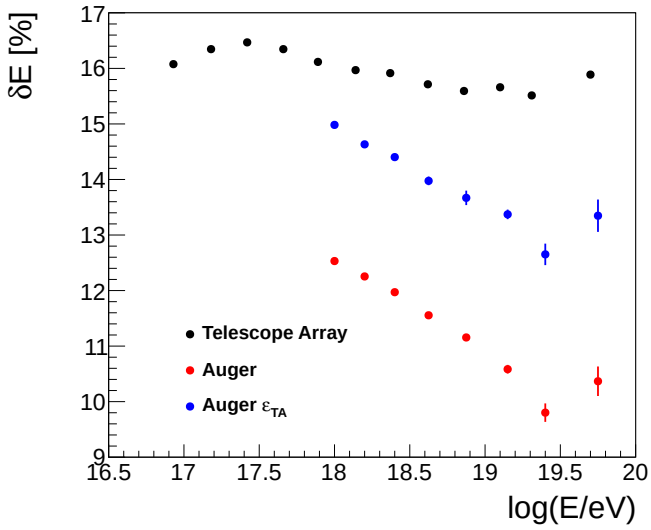

Figure 7.14: Energy deviation versus energy from this work using the Auger standard reconstruction (red points), including the effect of the optical efficiency (blue points) and those reported by the Telescope Array Collaboration using the AIRFLY FY in their reconstruction (black points) [32]. See text for details.

Comparison with a similar analysis by the TA collaboration

The TA Collaboration has recently performed a similar analysis with their data, in which they calculated the energy shift when the FY of TA is replaced by that of Auger in their reconstruction [32]. Black points in Fig. 7.14 represent the results of their analysis for δE with the criterion of Eq. (7.2), that is, using the energy reconstructed for the Auger FY as the reference one. These can be compared directly with the results from this thesis that includes the effect of the different optical efficiency of TA (blue points). As expected from the theoretical analysis, δE is smaller when the analysis is performed using the Auger efficiency (red points). Note that the agreement with the opposite analysis of TA is better when the TA efficiency is used, as predicted.

The results of this work on δE are very close to the ones obtained by the TA Collaboration at low energies (an absolute difference of around 1 per cent unit at 10^{18} eV), although they disagree at increasing energies, as the correlation of δE with energy found by the TA Collaboration is smoother. This discrepancy can be due to several factors. TA has an array smaller than Auger, so TA should register closer showers on average. Therefore, the Rayleigh scattering is not as important as in Auger and the δE values calculated by the TA collaboration should be lower according to our analyses (see Fig. 7.7a and 7.13). The correlation of δE with energy, inherited from the dependence on the shower-telescope distance, may also be expected to be weaker in the case of TA, which is consistent with the results shown in Fig. 7.14. Finally, the differences in the reconstruction algorithms of TA and Auger might have some effect and, as shown above, the Cherenkov fraction also affects δE. The same might happen with the atmospheric monitorization, as the aerosols impact the Rayleigh scattering. More careful cross-checks would be needed to assess the importance of these contributions.

7.3.2 Effect on the shower maximum depth

The effect of change on the FY in the reconstructed $X_{\max}$ values has also been studied. In fig. 7.15 the histogram of $\Delta X_{\max}$ is shown. Auger would have reconstructed $X_{\max}$ values 3.8 gcm^{-2} smaller, on average, if used the TA yield. These deviations are subjected to large fluctuations (RMS of 4.6 gcm^{-2}) because the height of the shower maximum spans a broad interval and also the atmospheric conditions depend strongly on season.

The main source of deviations is the vertical depth at which $X_{\max}$ is reached, mainly due to the atmospheric effects explained in chapter 5. Showers that develop near the ground (i.e. showers with a larger vertical depth) are mainly affected by humidity and have a larger absolute value of $\Delta X_{\max}$ than those that develop upper in the atmosphere,

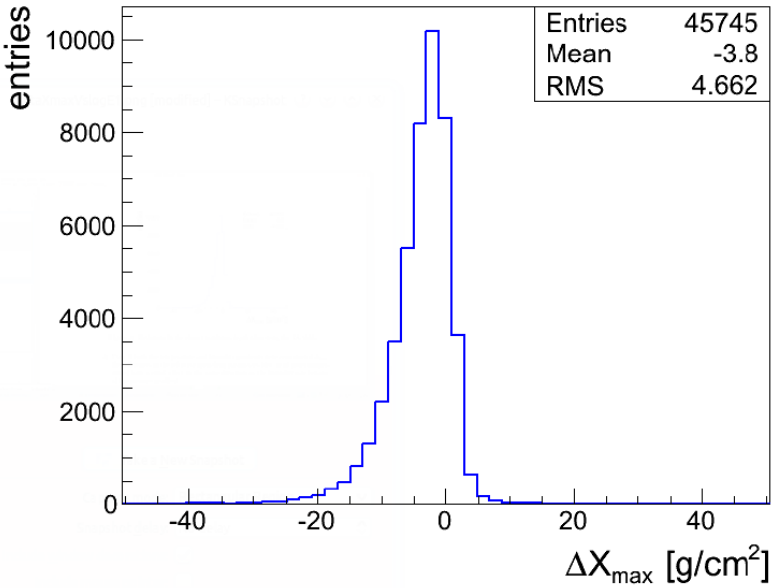

Figure 7.15: Deviations in the reconstructed shower maximum depth between the AIRFLY and the Kakimoto-FLASH datasets.

which are mainly affected by temperature effects (see Fig. 7.16b). It is interesting to note that there is no dependence with primary energy of the shower, as the Rayleigh scattering does not modify the reconstructed $X_{\max}$. This can be seen in Fig. 7.16a. This happens irrespective of the depth at which the shower reaches its maximum, as can be sen in Fig. 7.16b.

The seasonal dependence of $\Delta X_{\max}$ is studied in Fig. 7.17. It ranges from about -2 gcm^{-2} in winter up to -7 gcm^{-2} in summer (left plot). The result for a subsample of data with $660 < X_{\max}(\text{gcm}^{-2}) < 690$ and $\theta < 10^{\circ}$ is also displayed (right plot) together with our theoretical predictions for showers of $X_{\max} = 677.2$ gcm^{-2} with the same range of θ values. The agreement is remarkable.

7.3.3 Effect on the elongation curve

The variaton of $X_{\max}$ with energy (the so-called elongation rate) provides a powerful technique for mass composition analysis, as was explained in sec. 2.3.2. Therefore the effect of a change in the FY on this relevant obsevable might give useful information to understand disagreements between the results obtained by both experiments. For this analysis the same data sample employed in this section has been used (Jan. 2005 - Dec. 2013), applying the more strict cuts for the elongation curve in order to avoid any bias

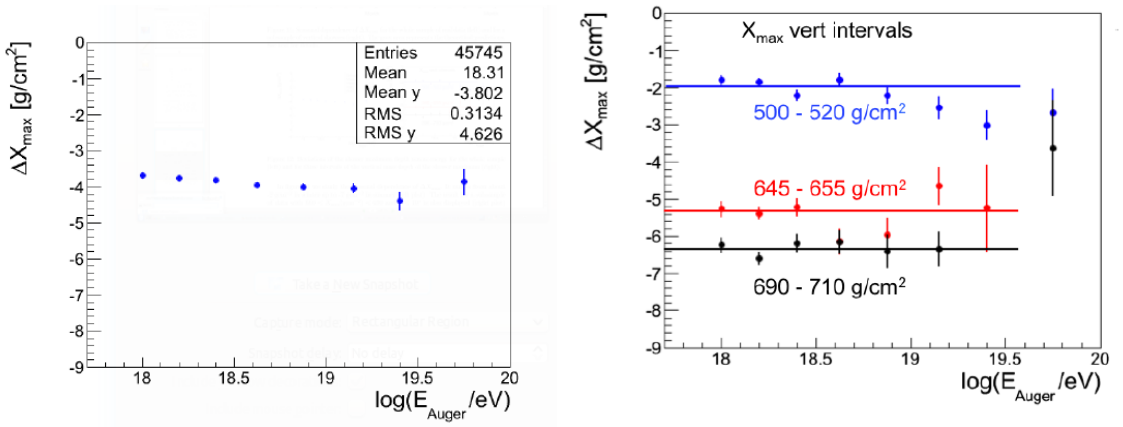

(a) (b)

Figure 7.16: Deviations of the shower maximum depth versus energy for the whole sample (left) and for three intervals of the vertical mass depth of the shower maximum (right).

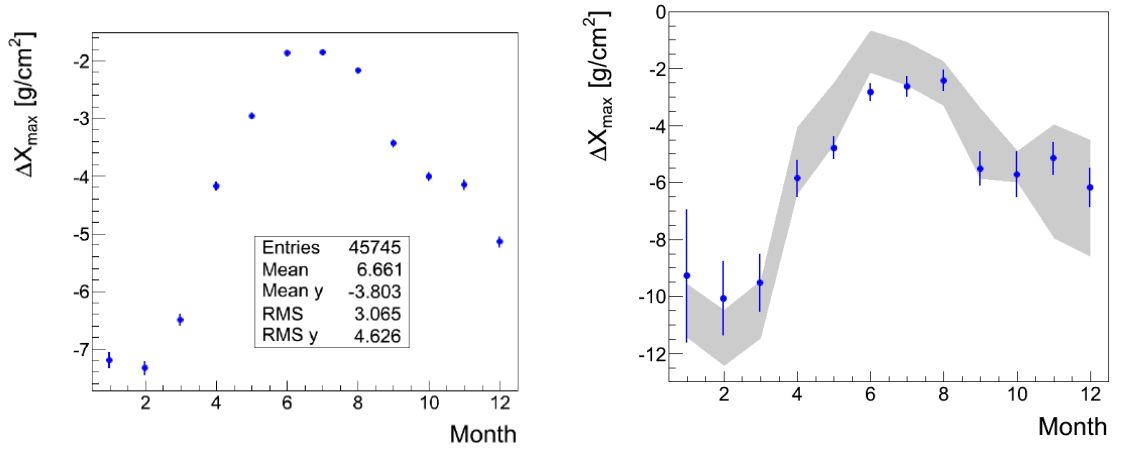

(a) (b)

Figure 7.17: Seasonal dependence of $\Delta X_{\max}$ for the whole sample of real data (left) and for a subsample of vertical showers (right). The gray area represents the theoretical predictions. See text for details.

that could distort the measure of the mass composition. A summary of these cuts can be found in [166].

The elongation curve has been evaluated using real data, and comparing the standard reconstruction, using the FY of AIRFLY and Auger filter and that one with the FY used by TA without changing the filter. The result is presented in Fig. 7.18. As can be observed, the FY replacement leads to a shift in the elongation curve. As shown in the lower panel, this effect is compatible with a simultaneous shift of 12% in energy and 3.8 gcm^{-2} in X_{max}. In fact the migration of events to neighbor energy bins seems to be the main responsible of the discrepancy between both results. Information about mass composition cannot be inferred from these data, as dedicated simulations with the TA yield for different primaries should be performed in order to do so. However, such an small variation in the curve should not affect previous interpretations of mass composition of UHECRs released by the Auger Collaboration.

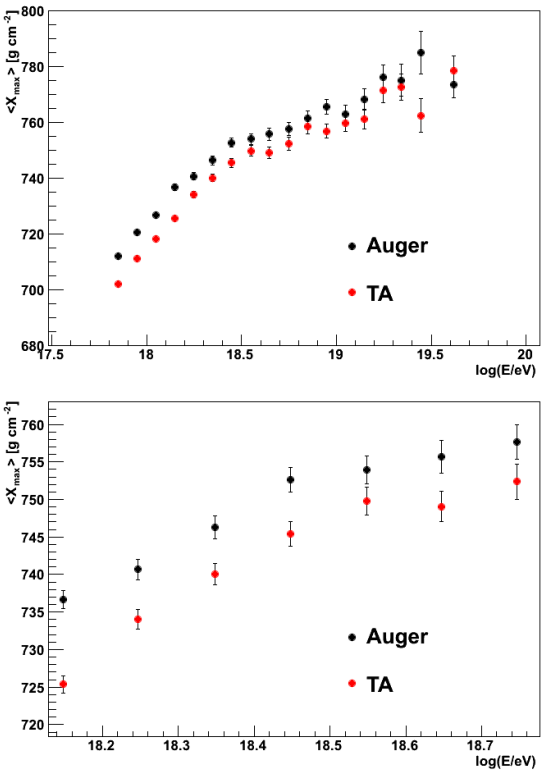

Figure 7.18: Shower maximum depth versus E for the Auger data sample. Results using the Auger FY (black) are compared with those obtained with the FY of TA. The zoom displayed in the lower plot shows that the main contribution to the discrepancy comes from event migration due to the energy shift.

Chapter 8

Conclusions

In this work, a comprehensive analysis of the impact of the fluorescence yield selection in the shower reconstruction parameters of the Pierre Auger Observatory has been carried out. To do so, an analytical method that offers good qualitative and quantitative results compared with a more accurate procedure based on a dedicated reconstruction algorithm i.e. the $\overline{\text{Off}}\underline{\text{line}}$ software employed by the Pierre Auger Collaboration has been developed. In addition, a module for the $\overline{\text{Off}}\underline{\text{line}}$ framework has been developed to study the impact of the fluorescence yield on real data reconstruction. This module is presently used in the official reconstruction of the Pierre Auger Collaboration. The analytical method has been extended to account for the effect of the optical efficiency when different experiments are compared. This procedure has been tested with Monte Carlo simulations and applied to study the relative energy scales of the Auger and TA experiments.

Both methods, analytical and real data reconstruction, have been used to study the effect of temperature and humidity dependence of the FY on the primary energy and shower maximum depth. Water vapor is relevant near the ground, and thus affects mainly vertical showers that develop deeper in the atmosphere and deposit the bulk of their energy close to the ground. Temperature effects, on the other hand, are more important on upper layers, where inclined showers have their maxima. When both temperature and humidity dependences are taken into account their combined effect increases the energy of the shower by around 5%. The impact in the shower maximum is a few gcm^{-2}.

The FY had been the main source of uncertainties in the energy scale of the Pierre Auger Observatory. As a part of the Hybrid Reconstruction task of the Pierre Auger Collaboration, a combined work has been done to reduce these uncertainties. To do so, recent measurements of the FY, including the atmospheric dependences and the absolute value for the 337 nm band, have been introduced in the reconstruction and the new uncertain-

ties in the energy scale have been evaluated. As a result of these and other updates in different aspects of the shower reconstruction, the energy scale of the Auger experiment has increased in about 15% while the uncertainty has decreased from 22% to 15% leading to a significant improvement in the accuracy of the spectrum.

The comparison of the energy spectra of TA and Auger suggests discrepances in the corresponding energy scales. Independent analyses carried out by Auger (presented here) and TA indicate that the different yields assumed by both experiments might account for a significant fraction of the discrepancy in the energy scale. Finally the combined effect of the FY on primary energy and shower maximum depth has a marginal effect on the comparison of elongation rate curves of both experiments.

Appendix A

The AirFluorescenceModel Module for the $\overline{\text{Off}}\underline{\text{line}}$ framework

Prior to the development of the AirFluorescenceModel module, the fluorescence yield was calculated in the $\overline{\text{Off}}\underline{\text{line}}$ framework by selecting the so-called "model" between all the different experimental measurements available. Each fluorescence yield was calculated using the parameterization provided by the authors, including different units and algorithms to calculate the total fluorescence yield. The available datasets were:

- **Kakimoto:** The absolute values in photons/m were obtained from a combination of fluorescence yield measurements of Kakimoto *et al.* [130] and the relative intensities reported by Bunner [56]. Yields were converted to photons/MeV using the electron energy loss data from NIST [167]. The pressure dependence were expressed in terms of the coefficients A and B reported by Kakimoto. Neither humidity nor the extra dependence of the temperature were implemented in this dataset, although the $\sqrt{(}T)$ term asociated to the frequency of molecular collisions was present.

- **Nagano:** Absolute value in photons/m, wavelength and pressure dependence from the paper of Nagano *et al.* [132]. The formulation of Kakimoto *et al.* was used. Humidity and extra temperature effects were neglected in this dataset.

- **Keilhauer:** Absolute values from the fluorescence efficiencies measured by Bunner [56]. The quenching parameters are calculated from experimental values of collisional cross-sections for N-N, N-O and H_2O and radiative lifetimes of the excited molecular levels of nitrogen. The user can select several sets of these quenching parameters. More details of this implementation can be found in [168].

- **Airfly:** Absolute value of the 337 nm in photons/MeV from the fluorescence efficiency of Nagano *et al.* [132]. The relative intensities and P'were those measured by Airfly [27]. Humidity and extra temperature dependence $(P'_{\lambda,\mathrm{w}}, \alpha_\lambda)$ were also taken from Airfly measurements [125]. The formulation used was basically the one described in section 4.2. This fluorescence yield selection was the default selection for the official reconstruction of the Pierre Auger Collaboration prior to AirFluorescenceModel.xml

The Offline framework is very flexible and allows the user to test easily the effect of different approaches to the shower reconstruction. Following this philosophy the user should be able to easily choose any fluorescence yield dataset. This was crucial for the study of the impact of fluorescence yield that is the scope of this thesis, but also for updating purposes if the Pierre Auger Collaboration decides to use different fluorescence yield data.

Offline previous to revision 18824 did not provide this feature because each fluorescence yield option (Kakimoto, Nagano, Keilhauer, Airfly) had its own implementation and formulation, that is, the yield was computed in each case using a different algorithm with configuration files including different parameters. The AirFluorescenceModel.xml implementation aims at reaching the flexibility required by the Offline also in the fluorescence yield evaluation. To do so, a universal algorithm for the calculation of the yield has been implemented, allowing the user to easily switch the fluorescence yield dataset by replacing/building a configuration file that includes all needed parameters. In this appendix, the implementation of the algorithm will be described.

A.1 Algorithm and input data

Of the different formulations available in the literature for the fluorescence yield calculation, AirFluorescenceModel employs the one described in section 4.2. For a given atmospheric condition of pressure P, temperature T and partial water pressure (humidity) P_w, the fluorescence yield for each wavelenght $Y_\lambda(P, T, P_\mathrm{w})$ is:

$$Y_\lambda(P, T, P_\mathrm{w}) = Y_{337}(P_0.T_0, 0) \cdot I_\lambda(P_0.T_0, 0) \cdot \frac{1 + P_0/P'_\lambda(T, P_\mathrm{w})}{1 + P/P'_\lambda(T, P_\mathrm{w})} \tag{A.1}$$

where the characteristic pressures $P'_\lambda(T, P_\mathrm{w})$ for humid air at temperature T are obtained from the corresponding values at reference temperature T_0 for dry air using the relation:

$$\frac{1}{P'_\lambda(T, P_\mathrm{w})} = \frac{1}{P'_\lambda(T, 0)} \left(1 - \frac{P_\mathrm{w}}{P}\right) + \frac{P_\mathrm{w}}{P} \frac{1}{P'_{\lambda\mathrm{w(T)}}} \tag{A.2}$$

In the above expression the characteristic pressures for dry air at temperature T are calculated from

$$P'_\lambda(T,0) = P'_\lambda(T_0,0)\left(\frac{T_0}{T}\right)^{\alpha_\lambda - 1/2} \tag{A.3}$$

and the characteristic pressures for air-fluorescence quenching with water molecules can be calculated with a similar expression:

$$P'_{\lambda\mathrm{w}}(T,0) = P'_{\lambda\mathrm{w}}(T_0,0)\left(\frac{T_0}{T}\right)^{\alpha_{\lambda\mathrm{w}} - 1/2} \tag{A.4}$$

However, there are no available measurements of $\alpha_{\lambda\mathrm{w}}$ and the usual procedure is to neglect the temperature dependence of $P'_{\lambda\mathrm{w}}$. I

To evaluate the fluorescence yield using the algorithm described above the following parameters must be supplied as input:

- The reference temperature T_0 and pressure P_0
- The absolute value in dry air at P_0 and T_0 for the reference wavelength $\lambda = 337$nm, $Y_{337}(T_0, P_0)$.
- The relative intensities for each wavelength for dry air at the reference pressure and temperature $I_\lambda(T_0.P_0, 0)$.
- The characteristic pressures in dry air $P'_\lambda(T_0.0)$.
- The parameters of water quenching $P'_{\lambda\mathrm{w}}(T_0.0)$
- The α parameters for the temperature dependence in dry air, α_λ.
- The α parameters for water quenching, $\alpha_{\lambda,\mathrm{w}}$.

A.2 Offline implementation

The algorithm described in section A.1 has been implemented in the source files AirFluorescenceModel.cc (listing A.2) and AirFluorescenceModel.h. The set of parameters required for the fluorescence yield calculation are given in the configuration file AirFluorescenceModel.xml (listing A.3). Since Offline revision 18224, this universal fluorescence model can be selected via AtmosphereInterfaceConfig.xml. In the AirFluorescenceModel.xml file the desired fluorescence yield option is chosen by means of DataSet (see listing A.3).

Listing A.1: AirFluorescenceModel.xml configuration file. DataSet defines the selected FY option.

```
1 <AirFluorescenceModel>
2   <DataSet> Auger </DataSet>
3 </AirFluorescenceModel>
```

Configuration files for each Offline old models, i. e., Kakimoto, Nagano, Keilhauer and Airfly (named Auger in the AirFluorescenceModel implementation) have been created. In addition, a new general purpose configuration file, called UserDefinedFluorescenceYieldDataSet.xml. As an example of the capabilities of this implementation, the dataset included by default in this UserDefinedFluorescenceYieldDataSet corresponds to the fluorescence yield currently used by the Telescope Array collaboration described in section 4.2.

A.3 Validation tests

In order to validate the new implementation of the fluorescence yield in the Offline framework the subset of golden events from 2009 and 2010 with the cuts described in section4.4.4 were employed. This subsample was reconstructed using Offline v2r5p8-Shannon with both the AirFluorescenceModel module and the previous implementations (Kakimoto, Nagano, Keilhauer and Auger/Airfly) A comparison of the reconstructed shower energy E and maximum shower depth $X_{\max}$ has been performed. The percentage relative deviations between the energy reconstructed with AirFluorescenceModel, E_{AF}, and that of the old Offline implementation, E_{Off},

$$\delta_E = \frac{E_{\mathrm{AF}} - E_{\mathrm{Off}}}{E_{\mathrm{Off}}} \times 100 \ [\%] \tag{A.5}$$

as well as the absolute difference in $X_{\max}$,

$$\Delta_{X_{\max}} = X_{\max,\mathrm{AF}} - X_{\max,\mathrm{Off}} \ [\mathrm{gcm}^{-2}] \tag{A.6}$$

have been evaluated.

A.3.1 AirFluorescenceModel vs Airfly

In figure A.1 we compare the results of FluorescenceModel = Airfly versus FluorescenceModel = AirFluorescence using DataSet = Auger (listing A.6). In this case both algorithms

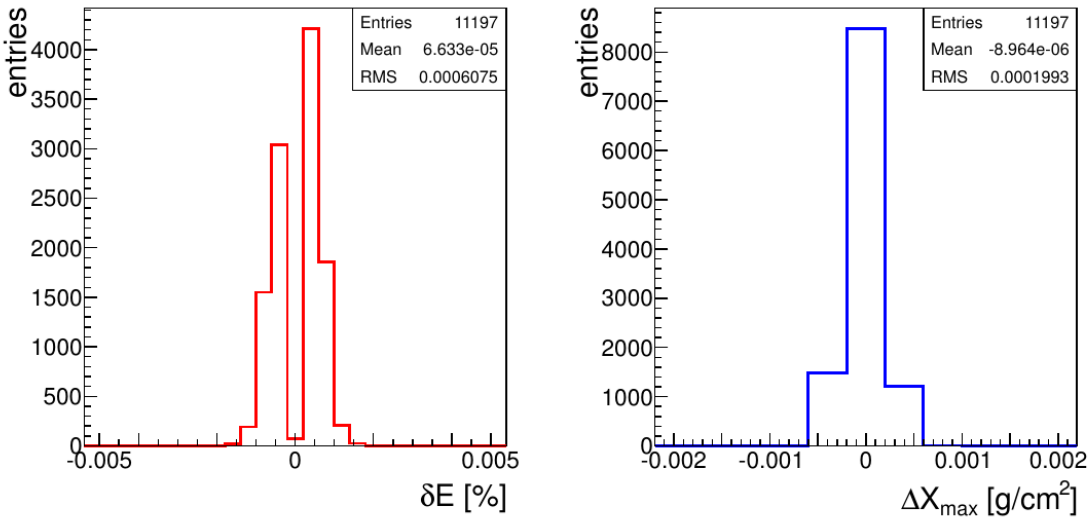

Figure A.1: The comparison on reconstructed energy (left) and $X_{\max}$ (right) between Airfly and AirFluorescenceModel

use the same formulation and FY parameters. Deviations in reconstructed energy are below 2×10^{-3} % and those in $X_{\max}$ are below 10^{-3}gcm^{-2}. As expected, deviations are negligible.

A.3.2 AirFluorescenceModel vs Kakimoto

The comparison of shower reconstruction using FluorescenceModel = Kakimoto versus FluorescenceModel = AirFluorescence using DataSet = Kakimoto (listing A.6) is shown in figure A.2. In this case the energy deviations amounts up to 0.12% and those of $X_{\max}$ up to 0.14 gcm^{-2}. As shown in the figure, the corresponding mean (RMS) values of the δE and $\Delta X_{\max}$ distributions are 0.06% and 0.14 gcm^{-2} respectively.

These minor discrepancies are due to the different input parameters employed in each module. In the old Kakimoto module quenching was evaluated from the air densitiy ρ and the molecular parameter B, while in the AirFluorescence implementation the air pressure and the P'parameter are used instead. For dry air the relationship between ρ and P is:

$$\rho = \frac{P}{R_{\text{air}}} T \tag{A.7}$$

where R_{air} is the specific gas constant for air. On the other hand, the relationship between

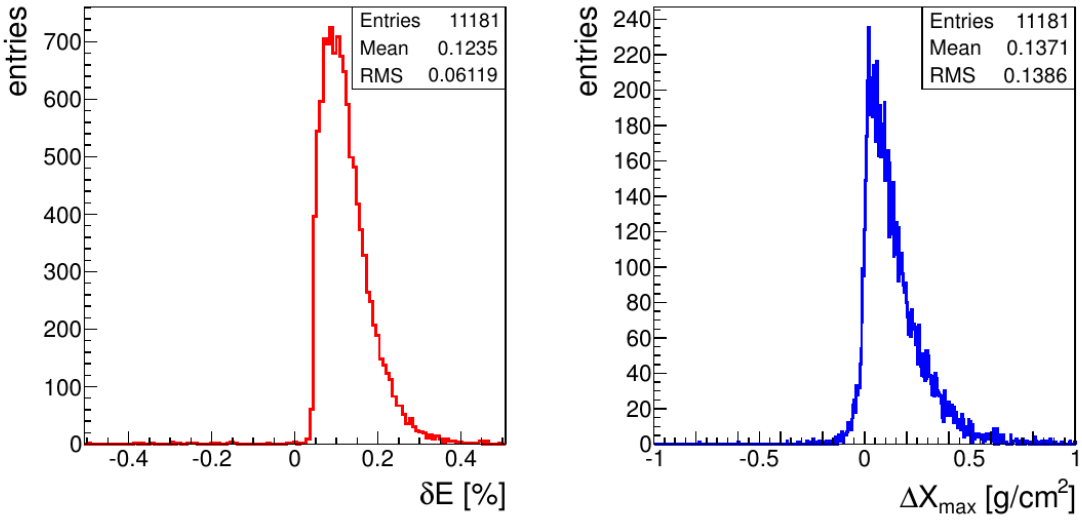

Figure A.2: The comparison on reconstructed energy (left) and $X_{\max}$ (right) between Kakimoto1996 and AirFluorescenceModel

B and $P'$is:

$$\rho B\sqrt{T} = P/P' \tag{A.8}$$

In fact the P'values for the Kakimoto configuration file in the AirFluorescence implementation were calculated using equation A.8 that is correct as far as equation A.7 holds, i.e., for dry air. The atmospheric pressure and air density used in Offline are those from a database of realistic humid air for which equation A.7 is not accurately fulfilled and consequently the relationship between B and P'slightly deviates from A.8.

In order to study the effect of this inconsistency the fluorescence yield within Offline has been calculated in three ways: a) with the previous Kakimoto implementation, $Y_{\rm Off}$, b) with the AirFluorescence implementation, $Y_{\rm AF}$ using the P value from the atmospheric DB and c) with the AirFluorescence implementation, but evaluating the pressure from the ρ value of the atmospheric DB by means of equation A.7, $Y_{{\rm AF}_\rho}$. The percentage difference between $Y_{\rm Off}$ and $Y_{\rm AF}$ has been plotted in Fig. A.3 as a function of the atmospheric depth (δY via P on the left plot). In the right plot the energy deviation δE has been represented as a function of the (vertical) shower maximum depth. Both plots are fully consistent showing that these energy deviations are due to the fact that the AirFluorescence implementation is using a dry air formulation in humid air. As a further test, it has been checked that the yield deviation with respect to $Y_{{\rm AF}_\rho}$ (δY via ρ on the left plot) is smaller than 0.1% and independent of atmospheric depth. That is, that the evaluation of the Kakimoto yield is

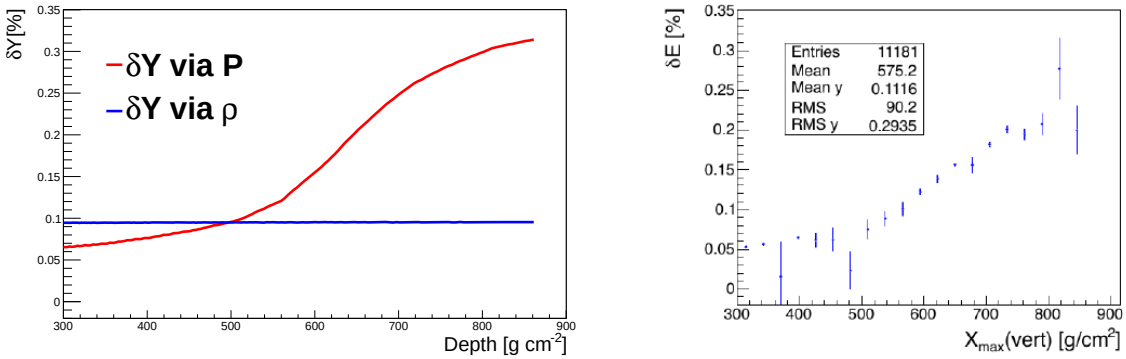

(a) (b)

Figure A.3: Comparison on Fluorescence Yield between Kakimoto and AirFluorescence-Model (left plot). The red line correspond to the reconstruction implemented in the offline (section A.1) while the blue line uses the density as input parameters for the FY calculation (see text for details). The right plot represents the energy deviation δE against vertical maximum depth. It is consistent with the red line in left plot. The sign of δY has been changed for an easier comparison between both plots.

compatible with that of the previous Offline implementation at a level better than 0.1%.

The small deviation of about 0.14 gcm^{-2} in $X_{\max}$ is a consequence of the slope of δY versus depth function (red line) shown in Fig. A.3

A.3.3 AirFluorescenceModel vs Nagano

A comparison similar than the one presented for Kakimoto in the previous section has been carried out for the Nagano fluorescence yield dataset, that is, FluorescenceModel = Nagano (Off) versus FluorescenceModel = AirFluorescence (AF) using DataSet = Nagano (listing A.5).

In this case the direct comparison between both implementations gives an average energy deviation of 0.009% with an RMS value of 0.06% while for $\Delta X_{\max}$ the mean and the RMS are 0.16 and 0.14 gcm^{-2} respectively (see Fig. A.4). In the Nagano implementation a formulation similar to the Kakimoto one is used and therefore a similar inconsistency is also found for this case. In Fig. A.5 is shown that this difference is due to a similar artifact.

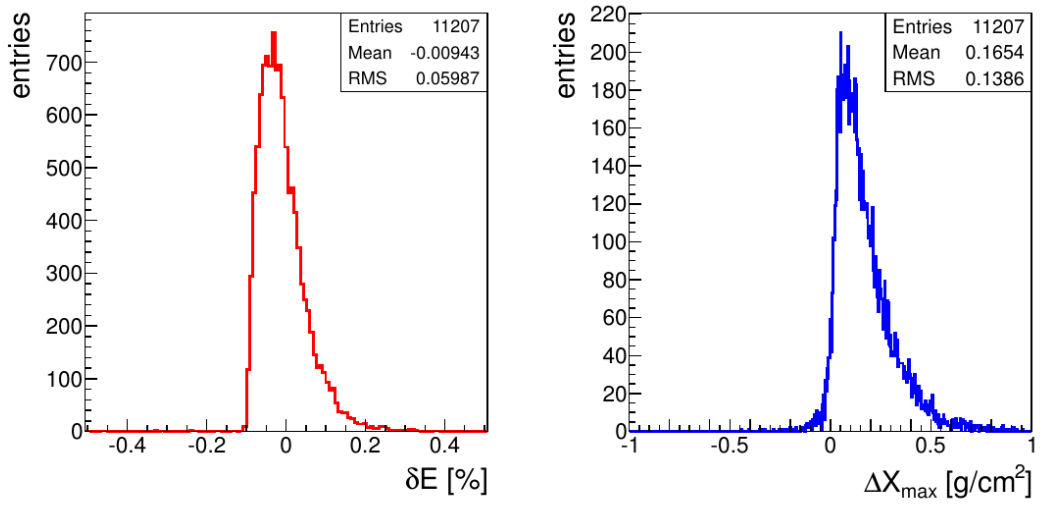

Figure A.4: The comparison on reconstructed energy (left) and $X_{\max}$ (right) between Nagano and AirFluorescenceModel

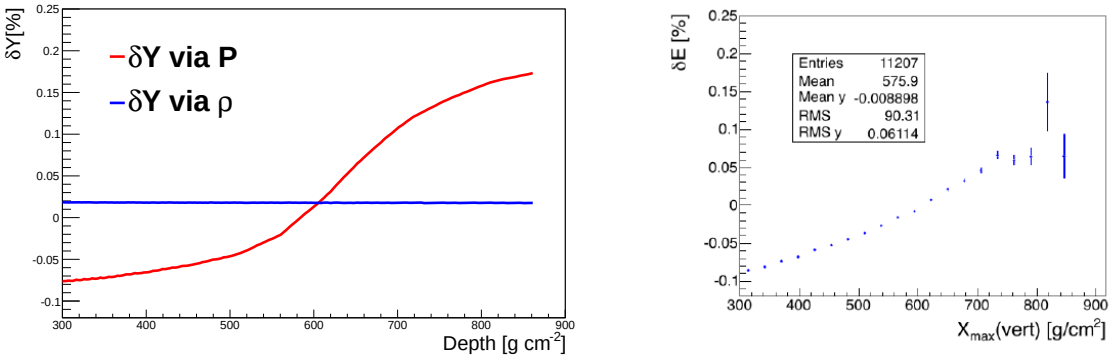

(a) (b)

Figure A.5: Same as Fig. A.3 for the comparison between Nagano and AirFluorescence-Model implementation.

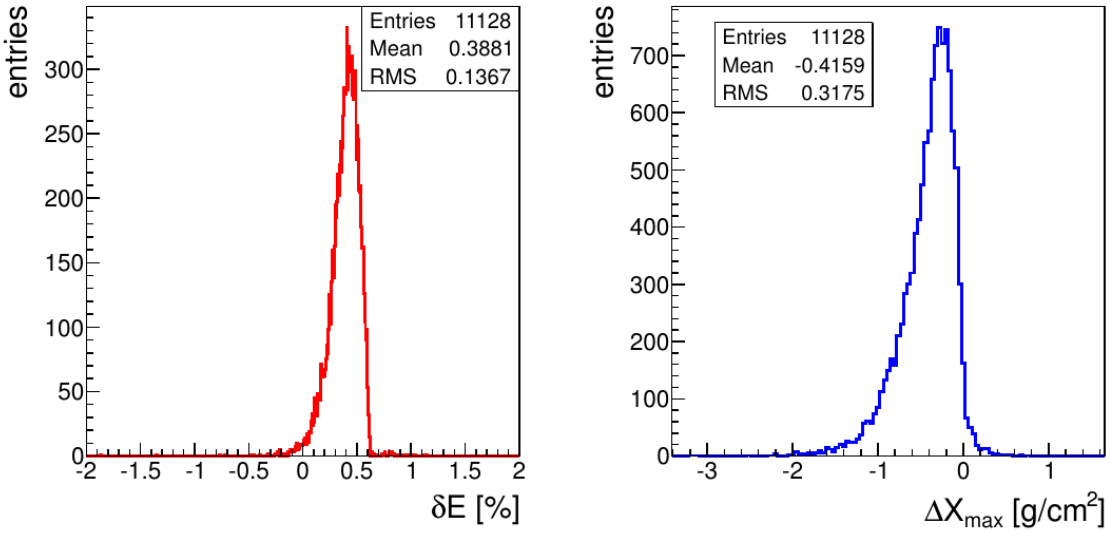

Figure A.6: The comparison on reconstructed energy (left) and $X_{\max}$ (right) between Keilhauer and AirFluorescenceModel

A.3.4 AirFluorescenceModel vs Keilhauer

The translation for this case is slightly more difficult, because the Keilhauer formulation uses more parameters, e. g., lifetimes of the excited molecular levels, cross sections for collisional de-excitation with nitrogen, oxygen and water molecules, etc. Results presented in Fig. A.6 for the Morozov water quenching parameters [144] show a mean deviation of about 0.4% in energy and -0.4 gcm^{-2} in $X_{\max}$. The values employed for this comparison can be found in listing A.7.

Listing A.2: AirFluorescenceModel.cc

```
1  /**
2     \file
3     Implementation of the fluorescence yield production in air.
4
5     \author Diego Garcia Pinto
6     \version $Id$
7     \date 14 Dec 2010
8  */
9
10 static const char CVSId[] =
11   "$Id$";
12
13 #include <sstream>
14 #include <fstream>
15 #include <utl/TabulatedFunction.h>
16 #include <utl/Reader.h>
17 #include <utl/ErrorLogger.h>
18 #include <utl/PhysicalConstants.h>
19 #include <fwk/CentralConfig.h>
20 #include <det/Detector.h>
21 #include <atm/Atmosphere.h>
22 #include <atm/ProfileResult.h>
23 #include <atm/AirFluorescenceModel.h>
24
25 using namespace utl;
26 using namespace atm;
27 using namespace fwk;
28 using namespace std;
29
30 void
31 AirFluorescenceModel::Init()
32 {
33   //INFO(".");
34
35   Branch topB =
36     CentralConfig::GetInstance()->GetTopBranch("AirFluorescenceModel");
37
38   string DataSetSelection;
39   topB.GetChild("DataSetSelection").GetData(DataSetSelection);
40
41   Branch DataSetBranch;
42
```

```
43 #warning Kakimoto and Keilhauer data sets are not fully implemented
44
45   if(DataSetSelection == "eAuger") DataSetBranch = ↩
         topB.GetChild("AugerFluorescenceYieldDataSet");
46   else if (DataSetSelection == "eNagano") DataSetBranch = ↩
         topB.GetChild("NaganoFluorescenceYieldDataSet");
47   else if (DataSetSelection == "eKakimoto") DataSetBranch = ↩
         topB.GetChild("KakimotoFluorescenceYieldDataSet");
48   else if (DataSetSelection == "eKeilhauer") DataSetBranch = ↩
         topB.GetChild("KeilhauerFluorescenceYieldDataSet");
49   else if (DataSetSelection == "eUserDefined") DataSetBranch = ↩
         topB.GetChild("UserDefinedFluorescenceYieldDataSet");
50   else{
51     ERROR("DataSet not implemented");
52     throw utl::NonExistentComponentException();
53   }
54
55   //Branch DataSetBranch = fDataSetReader -> GetTopBranch();
56
57   DataSetBranch.GetChild("wavelength").GetData(fWavelength);
58   DataSetBranch.GetChild("relativeIntensity").GetData(fRelativeIntensity);
59   DataSetBranch.GetChild("relativeIntensityError").GetData(fRelativeIntensityError);
60   DataSetBranch.GetChild("pPrime").GetData(fPPrime);
61   DataSetBranch.GetChild("pPrimeErrorUncorrelated").GetData(fPPrimeErrorUncorrelated);
62   DataSetBranch.GetChild("pPrimeErrorCorrelated").GetData(fPPrimeErrorCorrelated);
63   string tempParam, tempWaterParam, humParam;
64   DataSetBranch.GetChild("collisionalCrossSection").GetData(tempParam);
65   if(tempParam == "eAIRtemp") fTempParam = eAIRtemp;
66   else if(tempParam == "eNONE") fTempParam = eNoTempParam;
67   else{
68     ERROR("Parametrization not implemented");
69     throw utl::NonExistentComponentException();
70   }
71   DataSetBranch.GetChild("alpha").GetData(fAlpha);
72
73   DataSetBranch.GetChild("collisionalCrossSectionWater").GetData(tempWaterParam);
74   if(tempWaterParam == "eAIRWatertemp") fTempWaterParam = eAIRWatertemp;
75   else if(tempWaterParam == "eNONE") fTempWaterParam = eNoWaterTempParam;
76   else{
77     ERROR("Parametrization not implemented");
78     throw utl::NonExistentComponentException();
79   }
80   DataSetBranch.GetChild("alphaWater").GetData(fAlphaWater);
81
```

```
82    DataSetBranch.GetChild("humidity").GetData(humParam);
83    if(humParam == "eAIRhum") fHumParam = eAIRhum;
84    else if(humParam == "eNONE") fHumParam = eNoHumParam;
85    else{
86      ERROR("Parametrization not implemented");
87      throw utl::NonExistentComponentException();
88    }
89    DataSetBranch.GetChild("pPrimeWater").GetData(fPPrimeHum);
90
91
92    DataSetBranch.GetChild("temperature0").GetData(fTemperature0);
93    DataSetBranch.GetChild("pressure0").GetData(fPressure0);
94    DataSetBranch.GetChild("yield337").GetData(fYield337);
95
96
97    ostringstream info;
98    info << "Version: "
99         << "\n"
100     "Parameters:\n"
101     " DataSet: " << DataSetSelection << "\n"
102     " yield337: " << fYield337/(1/MeV) << " [1/MeV]\n"
103     " ref temperature: " << fTemperature0/kelvin << " [kelvin]\n"
104     " ref pressure: " << fPressure0/100/pascal << " [100*pascal]\n"
105     " temp dependence: " << tempParam << "\n"
106     " hum dependence: " << humParam << "\n"
107     " water temp dep: " << tempWaterParam << "\n";
108
109   INFO(info);
110
111 }
112
113
114 const
115 utl::TabulatedFunction&
116 AirFluorescenceModel::EvaluateFluorescenceYield(const double heightAboveSeaLevel)
117   const
118 {
119
120   const Atmosphere& atmo = det::Detector::GetInstance().GetAtmosphere();
121
122   const ProfileResult& tempProfile = atmo.EvaluateTemperatureVsHeight();
123   const ProfileResult& densityProfile = atmo.EvaluateDensityVsHeight();
124   const ProfileResult& pressureProfile = atmo.EvaluatePressureVsHeight();
125   const ProfileResult& pvaporProfile = atmo.EvaluateVaporPressureVsHeight();
```

```
126
127   const double temperature = tempProfile.Y(heightAboveSeaLevel);
128   const double density = densityProfile.Y(heightAboveSeaLevel);
129   const double pressure = pressureProfile.Y(heightAboveSeaLevel);
130   const double vaporPressure = pvaporProfile.Y(heightAboveSeaLevel);
131
132   double fluorescenceYield = 0;
133   fFluorescenceSpectrum.Clear();
134   for (unsigned int iwl = 0; iwl < fWavelength.size(); ++iwl) {
135
136     double current_alpha = (fTempParam == eAIRtemp) ? fAlpha[iwl] : 0;
137     double current_alpha_w = (fTempWaterParam == eAIRWatertemp) ? fAlphaWater[iwl] : 0;
138     double current_pprime_w = (fHumParam == eAIRhum) ? fPPrimeHum[iwl] : 0;
139
140     double pprime = fPPrime[iwl]*pow(fTemperature0/temperature, current_alpha-0.5);
141     /* P'(lambda,T) = P'(lambda,T_0)(T_0/T)^(alpha-1/2) */
142
143     double pprime_w = current_pprime_w*pow(fTemperature0/temperature, current_alpha_w-0.5);
144     /* In a near future, alpha values for water might be available. Presently alpha_w = 0 for all ↩
            wavelengths.
145   P'_w(lambda,T) = P'_w(lambda,T_0)(T_0/T)^(alpha_w-1/2)
146     */
147
148     if(fHumParam == eAIRhum)
149       {
150   if (pprime_w!=0){
151     pprime = (1./pprime)*(1-vaporPressure/pressure) + vaporPressure/(pressure*pprime_w);
152     pprime = 1/pprime;
153   }
154       }
155
156     fluorescenceYield = fYield337*fRelativeIntensity[iwl]*0.01;
157     fluorescenceYield *= (1 + fPressure0/fPPrime[iwl])/(1+pressure/pprime);
158     /* Y(lambda,P,T) = Y(lambda,P_0,T_0) * (1+P_0/(P'(lambda,T_0)))/(1+P/(P'(lambda,T)))*/
159     fluorescenceYield *= density; /* in units g/cm3/MeV as required in the FD reconstruction ↩
            module*/
160
161     fFluorescenceSpectrum.PushBack(fWavelength[iwl], fluorescenceYield);
162
163   }
164
165   return fFluorescenceSpectrum;
166 }
167
```

```
168
169 double
170 AirFluorescenceModel::GetdEdX0()
171   const
172 {
173   // Energy loss evaluated for an electron of .85 MeV
174   return 1; //.658*MeV/(g/cm/cm);
175 }
176
177
178 // Configure (x)emacs for this file ...
179 // Local Variables:
180 // mode:c++
181 // compile-command: "make -C .. -k"
182 // End:
```

Listing A.3: AirFluorescenceModel.xml

```
<?xml version="1.0" encoding="iso-8859-1"?>

<!-- Configuration for AirflyFluorescenceModel -->

<!DOCTYPE AirFluorescenceModel [
<!ENTITY AugerFluorescenceData SYSTEM '@XMLSCHEMALOCATION@/AugerFluorescenceYieldDataSet.xml'>
<!ENTITY NaganoFluorescenceData SYSTEM '@XMLSCHEMALOCATION@/NaganoFluorescenceYieldDataSet.xml'>
<!ENTITY KakimotoFluorescenceData SYSTEM '@XMLSCHEMALOCATION@/KakimotoFluorescenceYieldDataSet.xml'>
<!ENTITY KeilhauerFluorescenceData SYSTEM '@XMLSCHEMALOCATION@/KeilhauerFluorescenceYieldDataSet.xml'>
<!ENTITY UserDefinedFluorescenceData SYSTEM '@XMLSCHEMALOCATION@/UserDefinedFluorescenceYieldDataSet.xml'>
]>

<AirFluorescenceModel xmlns:xsi="http://www.w3.org/2001/XMLSchema-instance"
        xsi:noNamespaceSchemaLocation="@XMLSCHEMALOCATION@/AirFluorescenceModel.xsd">

  <!-- eAuger, eNagano, eKakimoto, eKeilhauer, eUserDefined -->
  <DataSetSelection> eAuger </DataSetSelection>

  <AugerFluorescenceYieldDataSet>
    &AugerFluorescenceData;
  </AugerFluorescenceYieldDataSet>

  <NaganoFluorescenceYieldDataSet>
    &NaganoFluorescenceData;
  </NaganoFluorescenceYieldDataSet>

  <KakimotoFluorescenceYieldDataSet>
    &KakimotoFluorescenceData;
  </KakimotoFluorescenceYieldDataSet>

  <KeilhauerFluorescenceYieldDataSet>
    &KeilhauerFluorescenceData;
  </KeilhauerFluorescenceYieldDataSet>

  <UserDefinedFluorescenceYieldDataSet>
    &UserDefinedFluorescenceData;
  </UserDefinedFluorescenceYieldDataSet>
```

```
38
39 </AirFluorescenceModel>
```

Listing A.4: AugerFluorescenceYieldDataSet.xml

```
<?xml version="1.0" encoding="iso-8859-1"?>

<!-- Configuration for AirFluorescenceModel -->
<!--

   This xml file provides the neccesary data to run the FluorescenceYield module using the
   Nagano-AIRFLY data set:

   - Absolute value of Y_337 for dry air at given P, T conditions:
   Nagano et al., Astrop. Phys. 22 (2004) 235.

   Recently a new measurement by AIRFLY has been published:
   - Precise measurement of the absolute fluorescence yield of the 337 nm band in atmospheric gases
   AIRFLY, Astrop. Phys. 42 (2013) 90.
   You can switch to this new value by commenting/uncommenting the Nagano one.

   - Nitrogen Spectrum (Wavelength):
   AIRFLY, Astrop. Phys. 28 (2007) 41.

   - Relative intensities (and corresponding uncertainties):
   AIRFLY, Astrop. Phys. 28 (2007) 41.

   - Characteristic pressures P' in dry air:
   AIRFLY, Astrop. Phys. 28 (2007) 41.

   - Temperature dependence of collisional cross sections in dry air (alpha parameters):
   AIRFLY presented at 6th AFW L'Aquila (2009); they are updated results from those previoulsy published in
   NIM_A 597 (2008) 50.

   - Characteristic pressures for collisional quenching with water molecules P'_w parameters:
   AIRFLY; presented at 6th AFW L'Aquila (2009); they are updated results from those previoulsy published in
   NIM_A 597 (2008) 50.

   More details on FY data sets in GAP 2010-016 and Astropart. Phys, 34 (2011) 467-475.
  -->

<!-- Nagano-AIRFLY data set -->

```

```
<!-- Pressure and/or temperature at which the fluorescence parameters are given -->

<pressure0 unit="100*pascal">800</pressure0>
<temperature0 unit="kelvin">293</temperature0>

<!-- Absolute value of the fluorescence yield at 337 nm by Nagano -->
<yield337 unit="1/MeV">6.38</yield337>

<!-- New AIRFLY value
 <yield337 unit="1/MeV">7.07</yield337> -->


<!-- molecular spectrum: 34 wavelengths -->
<wavelength unit="nanometer">
  296.2 297.7 302.0 308.0 311.7 313.6 315.9 317.7 326.8 328.5
  330.9 333.9 337.1 346.3 350.0 353.7 357.7 365.9 367.2 371.1
  375.6 380.5 385.8 387.7 388.5 391.4 394.3 399.8 405.0 414.1
  420.0 423.6 427.0 427.8
</wavelength>

<!-- Relative intensities (I_337 = 100) and relative errors -->
<relativeIntensity>
  5.16 2.77 0.41 1.44 7.24 11.05 39.33 0.46 0.80 3.80
  2.15 4.02 100.0 1.74 2.79 21.35 67.41 1.13 0.54 4.97
  17.87 27.2 0.50 1.17 0.83 28.0 3.36 8.38 8.07 0.49
  1.75 1.04 7.08 4.94
</relativeIntensity>

<relativeIntensityError> <!--unit="perCent"-->
  0.29 0.13 0.06 0.10 0.27 0.41 1.4 0.06 0.08 0.14
  0.12 0.18 0. 0.11 0.11 0.76 2.4 0.08 0.04 0.22
  0.63 0.97 0.08 0.06 0.04 1.0 0.15 0.29 0.29 0.07
  0.10 0.11 0.28 0.19
</relativeIntensityError>

<!-- Characteristic pressures (hPa) and errors-->
<pPrime unit="100*pascal">
  18.5 17.3 21. 21. 18.7 12.27 11.88 21. 19. 20.7
  16.9 15.5 15.89 21. 15.2 12.7 15.39 21. 19. 14.8
  12.82 16.51 19. 7.6 3.9 2.94 13.7 13.6 17.8 19.
  13.8 3.9 6.38 2.89
</pPrime>

<pPrimeErrorUncorrelated unit="100*pascal">
```

```
  5.0 4.0 10. 10. 3.8 0.78 0.31 10. 5. 2.6
  3.5 1.5 0. 10. 3.7 0.34 0.25 10. 5. 1.9
  0.45 0.48 5. 1.59 1.72 0.58 3.30 1.1 1.50 5.
  4.0 1.7 0.68 0.64
</pPrimeErrorUncorrelated>

<pPrimeErrorCorrelated unit="100*pascal">
  0.8 0.8 1. 1. 0.8 0.64 0.62 1. 1. 0.8
  0.76 0.7 0.73 1. 0.7 0.64 0.72 1. 1. 0.7
  0.62 0.72 1. 0.5 0.31 0.31 0.7 0.6 0.8 1.0
  0.7 0.3 0.43 0.30
</pPrimeErrorCorrelated>

<!--eAIRtemp, eNONE -->
<collisionalCrossSection> eAIRtemp </collisionalCrossSection>

<!-- alpha values for the temperature dependence of the collisional cross section -->
<alpha>
  0. 0. 0. 0. 0. −0.13 −0.19 0. 0. 0.
  0. 0. −0.35 0. −0.38 −0.22 −0.35 0. 0. −0.24
  −0.17 −0.34 0. 0. 0. −0.79 −0.2 −0.2 −0.37 0.
  0. 0. 0. −0.54
</alpha>

<!-- eAIRhum, eNONE -->
<humidity> eAIRhum </humidity>

<!-- Characteristic pressures for quenchig with water molecules
     pPrimeWater = 0 means here no humidity effect (i.e. pPrimeWater = Inf)
  -->
<pPrimeWater unit="100*pascal">
  0. 0. 0. 0. 0. 1.2 1.1 0. 0. 0.
  0. 0. 1.28 0. 1.5 1.27 1.3 0. 0. 1.3
  1.1 1.4 0. 0. 0. 0.33 1.2 1.1 1.5 0.
  0. 0. 0. 0.6
</pPrimeWater>

<!-- eAIRWatertemp, eNONE -->
<collisionalCrossSectionWater> eNONE </collisionalCrossSectionWater>

<alphaWater>
  0. 0. 0. 0. 0. 0. 0. 0. 0. 0.
  0. 0. 0. 0. 0. 0. 0. 0. 0. 0.
  0. 0. 0. 0. 0. 0. 0. 0. 0. 0.
```

```
127   0. 0. 0. 0.
128 </alphaWater>
```

Listing A.5: NaganoFluorescenceYieldDataSet.xml

```
<?xml version="1.0" encoding="iso-8859-1"?>

<!-- Configuration for AirFluorescenceModel -->
<!--

  This xml file provides the neccesary data to run the FluorescenceYield module using the Nagano data set
  described in M. Nagano et al., Astropart. Phys. 29 (2004) 235

  - Absolute value of Y_337 for dry air at given P, T conditions:
  From fluorescence efficiency reported by Nagano et al.

  - Nitrogen Spectrum (Wavelength):
  From Nagano et al.

  - Relative intensities (no uncertainties):
  Measured by Nagano et al.

  - Characteristic pressures P' in dry air:
  Measured by Nagano et al.

  - Temperature dependence of collisional cross sections in dry air (alpha parameters):
  None

  - Characteristic pressures for collisional quenching with water molecules P'_w parameters:
  None

  More details on FY data sets in GAP 2010-016 and Astropart. Phys, 34 (2011) 467-475.
 -->

<!-- Nagano data set -->

<!-- Pressure and/or temperature at which the fluorescence parameters are given -->

<pressure0 unit="100*pascal">800</pressure0>
<temperature0 unit="kelvin">293</temperature0>

<!-- Absolute value of the fluorescence yield at 337 nm -->
<yield337 unit="1/MeV">6.38</yield337>

<!-- molecular spectrum: 15 wavelengths -->
```

```
41 <wavelength unit="nanometer">
42   316 329 337 354 358 376 381 391 394 400
43   406 414 420 427 428
44 </wavelength>
45
46 <!-- Relative intensities (I_337 = 100) and relative errors -->
47 <relativeIntensity>
48   53.61 17.52 100 12.68 78.34 23.33 28.07 29.61 6.15 12.58
49   11.59 4.03 4.13 3.08 11.89
50 </relativeIntensity>
51
52 <relativeIntensityError> <!--unit="perCent"-->
53   0 0 0 0 0 0 0 0 0 0
54   0 0 0 0 0 0
55 </relativeIntensityError>
56
57 <!-- Characteristic pressures (hPa) and errors-->
58 <pPrime unit="100*pascal">
59   23 40.2 19.2 30.6 18.1 34.1 19.4 5.02 24.2 24.2
60   12.3 19.3 7.3 72 3.86
61 </pPrime>
62
63 <pPrimeErrorUncorrelated unit="100*pascal">
64   0 0 0 0 0 0 0 0 0 0
65   0 0 0 0 0 0
66 </pPrimeErrorUncorrelated>
67
68 <pPrimeErrorCorrelated unit="100*pascal">
69   0 0 0 0 0 0 0 0 0 0
70   0 0 0 0 0
71 </pPrimeErrorCorrelated>
72
73 <!-- eAIRtemp, eNONE -->
74 <collisionalCrossSection> eNONE </collisionalCrossSection>
75
76 <!-- alpha values for the temperature dependence of the collisional cross section -->
77 <alpha>
78   0 0 0 0 0 0 0 0 0 0
79   0 0 0 0 0
80 </alpha>
81
82 <!-- eAIRhum, eNONE -->
83 <humidity> eNONE </humidity>
84
```

```
85  <!-- Characteristic pressures for quenchig with water molecules
86       pPrimeWater = 0 means here no humidity effect (i.e. pPrimeWater = Inf)
87    -->
88  <pPrimeWater unit="100*pascal">
89    0 0 0 0 0 0 0 0 0 0
90    0 0 0 0 0
91  </pPrimeWater>
92
93  <!-- eAIRWatertemp, eNONE -->
94  <collisionalCrossSectionWater> eNONE </collisionalCrossSectionWater>
95
96  <alphaWater>
97    0 0 0 0 0 0 0 0 0 0
98    0 0 0 0 0 0
99  </alphaWater>
100
101 <!-- end of Nagano data set-->
```

Listing A.6: KakimotoFluorescenceYieldDataSet.xml

```
<?xml version="1.0" encoding="iso-8859-1"?>

<!-- Configuration for AirFluorescenceModel -->

<!--

  This xml file provides the neccesary data to run the FluorescenceYield module
  using the Kakimoto-Bunner data set described in detail by B. Dawson in
  "Present and Possible Future Implementations of Fluorescence Yield in FD Analysis"
  Auger Technical Note, GAP-2002-067 (2002). It can be summarized as follows:

  - Absolute value of Y_337 for dry air at given P, T conditions:
  From absolute yields for the three primary bands of nitrogen

  - Nitrogen Spectrum (Wavelength):
  A. N. Bunner, Ph.D. Thesis, Cornell University 1967

  - Relative intensities (no uncertainties):
  A. N. Bunner, Ph.D. Thesis, Cornell University 1967

  - Characteristic pressures P' in dry air:
  Kakimoto et al. NIM A372 (1996) 527

  - Temperature dependence of collisional cross sections in dry air (alpha parameters):
  None

  - Characteristic pressures for collisional quenching with water molecules P'_w parameters:
  None

  More details on FY data sets in GAP 2010-016 and Astropart. Phys, 34 (2011) ↩
      467-475.
 -->

<!-- Kakimoto-Bunner data set -->

<!-- Pressure and/or temperature at which the fluorescence parameters are given -->

<pressure0 unit="100*pascal">1013</pressure0>
<temperature0 unit="kelvin">288</temperature0>

<!-- Absolute value of the fluorescence yield at 337 nm -->
<yield337 unit="1/MeV">5.46023</yield337>
```

```
42
43 <!-- molecular spectrum: 16 wavelength bins-->
44 <wavelength unit="nanometer">
45   280 289 298 307 316 325 334 343 352 361
46   370 379 388 397 406 415
47 </wavelength>
48
49 <!-- Relative intensities (I_334 = 100) and errors -->
50 <relativeIntensity>
51   0. 0. 2.34 0. 10.55 0.81 100 0.45 5.23 107.3
52   1.53 13.53 44.63 3.79 3.25 0.
53 </relativeIntensity>
54
55 <relativeIntensityError>
56   0. 0. 0. 0. 0. 0. 0. 0. 0. 0.
57   0. 0. 0. 0. 0. 0.
58 </relativeIntensityError>
59
60 <!-- Characteristic pressures (hPa) and errors-->
61 <pPrime unit="100*pascal">
62   26.332 26.332 26.332 26.332 26.332 26.332 26.332 26.332 26.332 26.332
63   26.332 26.332 7.494 26.332 26.332 26.332
64 </pPrime>
65
66 <pPrimeErrorUncorrelated unit="100*pascal">
67   0. 0. 0. 0. 0. 0. 0. 0. 0. 0.
68   0. 0. 0. 0. 0. 0.
69 </pPrimeErrorUncorrelated>
70
71 <pPrimeErrorCorrelated unit="100*pascal">
72   0. 0. 0. 0. 0. 0. 0. 0. 0. 0.
73   0. 0. 0. 0. 0. 0.
74 </pPrimeErrorCorrelated>
75
76 <!-- eAIRtemp, eNONE -->
77 <collisionalCrossSection> eNONE </collisionalCrossSection>
78 <alpha>
79   0. 0. 0. 0. 0. 0. 0. 0. 0. 0.
80   0. 0. 0. 0. 0. 0.
81 </alpha>
82
83 <!-- eAIRhum, eNONE -->
84 <humidity> eNONE </humidity>
85
```

```
<!-- Characteristic pressures for quenchig with water molecules
     pPrimeWater = 0 means here no humidity effect (i.e. pPrimeWater = Inf)
  -->
<pPrimeWater unit="100*pascal">
  0 0 0 0 0 0 0 0 0 0
  0 0 0 0 0 0
</pPrimeWater>

<!-- eAIRWatertemp, eNONE -->
<collisionalCrossSectionWater> eNONE </collisionalCrossSectionWater>

<alphaWater>
  0. 0. 0. 0. 0. 0. 0. 0. 0. 0.
  0. 0. 0. 0. 0. 0.
</alphaWater>

<!-- end of Kakimoto-Bunner data set-->
```

Listing A.7: KeilhauerFluorescenceYieldDataSet.xml

```
<?xml version="1.0" encoding="iso-8859-1"?>

<!-- Configuration for AirFluorescenceModel -->

<!--

  This xml file provides the neccesary data to run the FluorescenceYield module
  Based on data in Keilhauer2008FluorescenceModel
  Included parametrizations vapour quenching from T. Waldenmaier (it can be ↩
      swichted to Morozov by
  comment/uncoment the pPrimeWater branch).


 -->

<!-- Keilhauer data set -->

<!-- Pressure and/or temperature at which the fluorescence parameters are given -->

<pressure0 unit="100*pascal">800</pressure0>
<temperature0 unit="kelvin">293</temperature0>

<!-- Absolute value of the fluorescence yield at 337 nm -->
<yield337 unit="1/MeV">6.88</yield337>

<!-- molecular spectrum: 34 wavelengths -->
<wavelength unit="nanometer">
  311.7 313.6 315.9 328.5
  330.9 333.9 337.1 346.9 350.0 353.7 357.7 367.2 371.1
  375.6 380.5 389.4 391.4 394.3 399.8 405.9 414.1
  420.1 427.0
</wavelength>

<!-- Relative intensities (I_337 = 100) and relative errors -->
<relativeIntensity>
  0.81 8.51 25.25 2.62 0.62 2.19 100 1.13 1.31 16.4
  79.58 0.87 3.47 16.27 29.32 0.6 28.62 2.36 10.23 9.84
  0.36 1.81 2.39
</relativeIntensity>

<relativeIntensityError> <!--unit="perCent"-->
  0. 0. 0. 0. 0. 0. 0. 0. 0. 0.
```

```
42   0. 0. 0. 0. 0. 0. 0. 0. 0. 0.
43   0. 0. 0.
44 </relativeIntensityError>
45
46 <!-- Characteristic pressures (hPa) and errors-->
47 <pPrime unit="100*pascal">
48   3.54 6.43 11.05 3.54 6.43 11.05 25.46 3.54 6.43 11.05
49   25.46 3.54 6.43 11.05 25.46 3.54 1.51 6.43 11.05 25.46
50   3.54 6.43 11.05
51 </pPrime>
52
53 <pPrimeErrorUncorrelated unit="100*pascal">
54   0. 0. 0. 0. 0. 0. 0. 0. 0. 0.
55   0. 0. 0. 0. 0. 0. 0. 0. 0. 0.
56   0. 0. 0.
57 </pPrimeErrorUncorrelated>
58
59 <pPrimeErrorCorrelated unit="100*pascal">
60   0. 0. 0. 0. 0. 0. 0. 0. 0. 0.
61   0. 0. 0. 0. 0. 0. 0. 0. 0. 0.
62   0. 0. 0.
63 </pPrimeErrorCorrelated>
64
65 <!-- eAIRtemp, eNONE -->
66 <collisionalCrossSection>
67   eAIRtemp
68 </collisionalCrossSection>
69 <!-- alpha values for the temperature dependence of the collisional cross section -->
70 <alpha>
71   0. -0.09 -0.21 0. -0.09 -0.21 -0.36 0. -0.09 -0.21
72   -0.36 0. -0.09 -0.21 -0.36 0. -0.8 -0.09 -0.21 -0.36
73   0. -0.09 -0.21
74 </alpha>
75 <!-- eAIRhum , eNONE -->
76 <humidity>
77   eAIRhum
78 </humidity>
79 <!-- Characteristic pressures for quenchig with water molecules
80      pPrimeWater = 0 means here no humidity effect (i.e. pPrimeWater = Inf)
81   -->
82 <!-- pPrimeWater from Waldenmaier -->
83 <pPrimeWater unit="100*pascal">
84   0. 0. 2.13 0. 0. 2.13 1.92 0. 0. 2.13
85   1.92 0. 0. 2.13 1.92 0. 0. 0. 2.13 1.92
```

```
86    0. 0. 2.13
87  </pPrimeWater>
88  <!--pPrimeWater from Morozov
89    <pPrimeWater unit="100*pascal">
90      0. 0. 1.39 0. 0. 1.39 1.31 0. 0. 1.39
91      1.31 0. 0. 1.39 1.31 0. 0. 0. 1.39 1.31
92      0. 0. 1.39
93    </pPrimeWater>
94  -->
95
96  <!-- eAIRWatertemp, eNONE -->
97  <collisionalCrossSectionWater>
98    eNONE
99  </collisionalCrossSectionWater>
100
101 <alphaWater>
102   0. 0. 0. 0. 0. 0. 0. 0. 0. 0.
103   0. 0. 0. 0. 0. 0. 0. 0. 0. 0.
104   0. 0. 0.
105 </alphaWater>
106
107 <!-- end of Keilhauer data set-->
```

Listing A.8: UserDefinedFluorescenceYieldDataSet.xml

```
<?xml version="1.0" encoding="iso-8859-1"?>

<!-- Configuration for AirflyFluorescenceModel -->

<!--
   Example of user-defined FY data set.

   This xml file provides the neccesary data to run the FluorescenceYield module using
   the data set presently used by the TA Collaboration (preliminary).

   - Absolute value of Y_337 for dry air at given P, T conditions obtained from absolute value of total light in the 300-400 nm range
   completed with FLASH values for the 400-420 nm range:
   Kakimoto et al. NIM A372 (1996) 527
   The FLASH Coll., Astropart. Phys. 29 (2008) 77-86.

   - Relative intensities (no uncertainties):
   The FLASH Coll., Astropart. Phys. 29 (2008) 77-86.

   - Characteristic pressures P' in dry air:
   Kakimoto et al. NIM A372 (1996) 527

   - Temperature dependence of collisional cross sections in dry air (alpha parameters):
   None

   - Characteristic pressures for collisional quenching with water molecules P'_w parameters:
   None

   More details on FY data sets in GAP 2010-016 and Astropart. Phys, 34 (2011) 467-475.

  -->

<!-- Pressure and/or temperature at which the fluorescence parameters are given -->

<pressure0 unit="100*pascal">1013</pressure0>
<temperature0 unit="kelvin">293</temperature0>

<!-- Absolute value of the fluorescence yield at 337 nm -->
<yield337 unit="1/MeV">4.291387</yield337>

<!-- molecular spectrum: 21 wavelengths -->
```

```
<wavelength unit="nanometer">
  311.7 313.6 315.9 328.5 330.9 333.9 337.1 346.9 350 353.7
  357.7 367.2 371.1 375.6 380.5 391.4 394.3 399.8 405.9 414.1
  420.1
</wavelength>

<!-- Relative intensities (I_337 = 100) and relative errors -->
<relativeIntensity>
  1.96 16.43 34.01 4.26 0.55 0.87 100 0.76 1.15 22.11
  62.72 3.11 6.61 20.8 37.34 44.6 2.02 15.28 7.91 0.16
  0
</relativeIntensity>

<relativeIntensityError> <!--unit="perCent"-->
  0. 0. 0. 0. 0. 0. 0. 0. 0. 0.
  0. 0. 0. 0. 0. 0. 0. 0. 0. 0.
  0.
</relativeIntensityError>

<!-- Characteristic pressures (hPa) and errors-->
<pPrime unit="100*pascal">
  26.56 26.56 26.56 26.56 26.56 26.56 26.56 26.56 26.56 26.56
  26.56 26.56 26.56 26.56 26.56 7.56 26.56 26.56 26.56 26.56
  26.56
</pPrime>

<pPrimeErrorUncorrelated unit="100*pascal">
  0. 0. 0. 0. 0. 0. 0. 0. 0. 0.
  0. 0. 0. 0. 0. 0. 0. 0. 0. 0.
  0.
</pPrimeErrorUncorrelated>

<pPrimeErrorCorrelated unit="100*pascal">
  0. 0. 0. 0. 0. 0. 0. 0. 0. 0.
  0. 0. 0. 0. 0. 0. 0. 0. 0. 0.
  0.
</pPrimeErrorCorrelated>

<!--eAIRtemp, eNONE -->
<collisionalCrossSection> eNONE </collisionalCrossSection>

<!-- alpha values for the temperature dependence of the collisional cross section -->
<alpha>
  0. 0. 0. 0. 0. 0. 0. 0. 0. 0.
```

```
85    0. 0. 0. 0. 0. 0. 0. 0. 0. 0.
86    0.
87  </alpha>
88
89  <!-- eAIRhum, eNONE -->
90  <humidity> eNONE </humidity>
91
92  <!-- Characteristic pressures for quenchig with water molecules
93       pPrimeWater = 0 means here no humidity effect (i.e. pPrimeWater = Inf)
94    -->
95  <pPrimeWater unit="100*pascal">
96    0. 0. 0. 0. 0. 0. 0. 0. 0. 0.
97    0. 0. 0. 0. 0. 0. 0. 0. 0. 0.
98    0.
99  </pPrimeWater>
100
101 <!-- eAIRWatertemp, eNONE -->
102 <collisionalCrossSectionWater> eNONE </collisionalCrossSectionWater>
103
104 <alphaWater>
105   0. 0. 0. 0. 0. 0. 0. 0. 0. 0.
106   0. 0. 0. 0. 0. 0. 0. 0. 0. 0.
107   0.
108 </alphaWater>
109 <!-- UserDefinedFluorescenceYieldDataSet-->
```

Appendix B

Resumen

El Observatorio Pierre Auger es uno de los detectores más importantes en el campo de los rayos cósmicos de ultra-alta energía. El bajo flujo de rayos cósmicos a estas energías extremas obliga a construir detectores con enormes superficies de colección para obtener un número de sucesos estadísticamente relevante. Los detectores que, como el Observatorio Pierre Auger, usan la técnica de fluorescencia, registran la luz producida por las moléculas de nitrógeno ionizadas por el paso del rayo cósmico al desexcitarse. El rendimiento de fluorescencia, Y, es el parámetro que describe el número de fotones de fluorescencia producidos por unidad de energía depositada en la atmósfera. Existen numerosas medidas experimentales de Y y sus dependencias atmosféricas y, a pesar de los esfuerzos realizados en los últimos años, no hay consenso entre los distintos experimentos sobre cuál es la más adecuada.

En este trabajo se ha realizado un breve resumen de la situación del campo de los rayos cósmicos de ultra-alta energía, seguido de una descripción del Observatorio Pierre Auger. Posteriormente se ha analizado el rendimiento de fluorescencia, sus dependencias y las medidas experimentales más recientes, y se han definido dos métodos complementarios para evaluar el efecto de la elección de un conjunto de parámetros determinado en la reconstrucción de la cascada atmosférica producida por el rayo cósmico incidente. Estos métodos han sido empleados para determinar el impacto de las dependencias atmosféricas de Y en los datos experimentales obtenidos por el Observatorio Pierre Auger y, en conjunto con otras mejoras introducidas por la colaboración Auger, actualizar la escala de energía del Observatorio. En el capítulo final se ha estudiado las diferencias aparentes entre Auger y Telescope Array, el otro gran detector de rayos cósmicos en operación actualmente, y cómo éstas pueden ser explicadas en gran parte por los diferentes valores de Y que emplean ambos experimentos.

B.1 Rayos cósmicos de ultra-alta energía

Los rayos cósmicos son partículas muy energéticas, principalmente núcleos atómicos desnudos, de origen extraterrestre. Fueron descubiertos en 1912 por Victor Hess, al descubrir que los niveles de radiación atmosférica crecían con la altura. Los rayos cósmicos fueron la principal fuente experimental para la física de altas energías antes de la construcción de los modernos aceleradores de partículas. El pión y el positrón son dos ejemplos de partículas descubiertas a partir del análisis de los rayos cósmicos. Sin embargo, más de 100 años después de las medidas de Hess, muchos interrogantes sobre su origen y naturaleza siguen sin ser despejados, especialmente para aquellos con energías superiores a 10^{18} eV, los llamados rayos cósmicos de ultra-alta energía (UHECRs por sus siglas en inglés).

El rango de energía de los rayos cósmicos que llegan a nuestro planeta es muy amplio, habiéndose detectado eventos con energías superiores a 10^{21} eV. Sin embargo, como se puede apreciar en la Fig. 2.4, el flujo decae exponencialmente con la energía, con un valor aproximado de 1 partícula por km^2 y siglo para 10^{20} eV. Esta característica está relacionada también con su origen. Los sucesos de más baja energía provienen del Sol, mientras que las fuentes galácticas y extragalácticas son las únicas capaces de acelerar estas partículas hasta alcanzar energías macroscópicas.

Los rayos cósmicos con energías inferiores a 10^{15} eV tienen un flujo lo suficientemente elevado como para ser detectados por métodos directos, principalmente con calorímetros montados en globos aerostáticos o satélites en órbita sobre la Tierra. En cambio los UHECRs requieren otros métodos indirectos para su detección. En este caso se utiliza la propia atmósfera terrestre como calorímetro. Los rayos cósmicos, al interaccionar con partículas de la atmósfera, generan lo que se conoce como cascadas atmosféricas, que pueden ser detectadas por instrumentos situados en la superficie.

Una cascada atmosférica se forma cuando un rayo cósmico de estas energías interacciona con una molécula de la atmósfera genera nuevas partículas que, a su vez, vuelven a interaccionar con otras partículas de la atmósfera. Este proceso continúa hasta que la mayor parte de la energá del rayo cósmico es depositada en la atmósfera y produce un frente de partículas relativistas, principalmente fotones y electrones, que viaja a lo largo del eje definido por la dirección de llegada del rayo cósmico primario.

Basándose en las largas extensiones necesarias para detectar cascadas atmosféricas producidas por un UHECRs incidente se han desarrollado dos técnicas experimentales: redes de superficie y telescopios de fluorescencia. Los primeros consisten, como su propio nombre indica, en una red de detectores equiespaciados que puede alcanzar varias extensiones. A partir de las partículas de la cascada atmosférica que llegan a los detectores de la red se

puede reconstruir la dirección, energía y otros parámetros del primario. Los telescopios de fluorescencia se basan en la luz de fluorescencia producida por las moléculas ionizadas de N_2 de la cascada atmosférica al desexcitarse. El perfil longitudinal de energía depositada se obtiene gracias al rendimiento de fluorescencia, Y, que mide el número de fotones producidos por unidad de energía depositada.

En 1966, y tras el descubrimiento del fondo de radiación de microondas, Greisen y Zatsepin y Kuz'min postularon de manera simultánea la existencia de un fin en el flujo de energía de los rayos cósmicos. Los rayos cósmicos con energías superiores a $5 \cdot 10^{19}$ eV tienen alta probabilidad de interaccionar con el fondo cósmico de microondas, perdiendo parte de su energía. Debido a este proceso no se esperan apenas eventos por encima de estas energías. Se conoce a esta reducción brusca del flujo como corte GZK en honor a sus tres descubridores. Este corte impone también una restricción a la distancia máxima de las fuentes extragalácticas. Por ejemplo, un protón con energía superior a 10^{20} eV detectado en la Tierra solo puede provenir, de acuerdo a esta teoría, de una fuente situada a menos de 50 Mpc ya que de lo contrario su energía se degradaría antes de llegar. Esta restricción podría abrir la posibilidad a la astronomía de rayos cósmicos, puesto que la distorsión en la trayectoria de los rayos cósmicos debida a los campos magnéticos interestelares debería ser despreciable para estas distancias. La dirección de llegada de los UHECRs podría, pues, apuntar a su procedencia.

Los resultados del Observatorio Pierre Auger parecen confirmar la existencia del corte GZK ya apuntada por el telescopio de fluorescencia HiRes, y muestran una cierta correlacin con los núcleos activos de galaxia (AGNs), aunque la significancia de este resultado parece haberse reducido con el tiempo. Telescope Array, tiene unos resultados similares, si bien la correlación con los AGNs es aún más débil. En cuanto a la composición en masa de los rayos cósmicos, los datos presentados por la colaboración Auger apuntan a una presencia importante de núcleos pesados. Telescope Array, por su parte, muestra una composición mayoritariamente protónica.

Una de las diferencias entre ambas colaboraciones concierne al espectro. Aunque existe un factor de escala entre ambos experimentos de alrededor del 20%, las principales características del espectro tales como como su índice espectral así cómo las energías donde este varía, relacionadas con el origen de los rayos cósmicos, son esencialmente consistentes.

B.2 El Observatorio Pierre Auger

Situado en las afueras de la ciudad de Malargüe, en la provincia de Mendoza (Argentina), el Observatorio Pierre Auger es el detector de rayos cósmicos más extenso del planeta

y lleva tomando datos desde 2004. Es el primer detector de UHECRs con un diseño híbrido, que combina la técnica de la red de detectores de superficie (SD) con los detectores de fluorescencia (FD). El SD está compuesto por más de 1600 tanques Cherenkov, que detectan la llegada de una cascada atmosférica a partir de la radiación Cherenkov producida por las partículas de la cascada al cruzar el volumen de agua altamente destilada alojado dentro del tanque. Esta radiación es reflejada por un material reflectante que recubre el interior del tanque y posteriormente recogida por los fotomultiplicadores colocados en su parte superior. El FD, por su parte, está compuesto por 24 telescopios repartidos en 4 edificios ubicados en el permetro de la red. Cada uno de los telescopios cuenta con un sistema óptico que enfoca la luz recogida en una cámara de 440 fotomultiplicadores, cubriendo un campo de visión de 30^{o} en acimut y 28.6^{o} en elevación, de tal manera que cada uno de los edificios cubre un total de 180^{o} en acimut. Un filtro situado a la entrada del telescopio impide la entrada de fotones fuera del rango del UV cercano, limitando así la contaminación debida a otras fuentes lumínicas distintas de la fluorescencia atmosférica.

Esta técnica híbrida permite obtener medidas simultáneas e independientes del mismo evento, algo que produce un mayor control en los errores sistemáticos de ambas técnicas. Además, las debilidades de ambas técnicas quedan mucho más compensadas gracias al diseño híbrido. Así, escaso ciclo útil del FD (de alrededor del 10%, puesto que solo puede ser utilizado en las noches claras sin luna), contrasta con el 100% del SD. Lo contrario sucede con la obtención de la energía depositada que el FD obtiene al integrar el perfil longitudinal del rayo cósmico incidente registrado por los telescopios. Las medidas simultáneas de FD y SD permiten calibrar de manera mucho más precisa el SD sin necesidad de suposiciones sobre la naturaleza del primario.

Para realizar correctamente todas estas medidas el observatorio cuenta con numerosos instrumentos de monitorización atmosférica distribuidos a lo largo de la red. Además, el observatorio cuenta con prototipos para probar la viabilidad de nuevas técnicas de detección de rayos cósmicos que se aprovechan de dos detectores de probada eficiencia para hacer pruebas. Un ejemplo es AERA, una red de antenas de radio que ya ha detectado eventos en la banda de los MHz. Asimismo el observatorio está en constante evolución, con dos actualizaciones que permiten extender el rango de las medidas por debajo de los 10^{18} eV que contemplaba el diseño original.

Un mapa esquemático del Observatorio, que incluye todos los detectores e instrumentos de monitorización atmosférica puede consultarse en la Fig. 3.1.

B.3 Efecto del rendimiento de fluorescencia en la reconstrucción de cascadas atmosfricas

Como se ha mencionado anteriormente, el rendimiento de fluorescencia atmosférica Y es el paramtro que mide el número de fotones de fluorescencia generados por unidad de energía depositada en la atmósfera. Las moléculas de nitrógeno de la atmósfera son excitan por colisión con los electrones y fotones de la cascada atmosférica. Estas moléculas de N_2 se relajan bien emitiendo un fotón de fluorescencia con una longitud de onda en el UV cercano determinada por las transiciones ópticas permitidas, bien mediante desexcitaciones colisionales. La importancia de estas desexcitaciones colisionales depende de paramétros atmosféricos tales como presión, temperatura y humedad. La denominada presión característica P' es una magnitud, definida como la presión a la cual las desexcitaciones colisionales igualan la emisión de un fotón de fluorescencia, que sirve para modelizar la dependencia de Y con la atmósfera.

Para una correcta determinación de Y serán pues necesarios distintos ingredientes: el valor absoluto de fotones por unidad de energía depositada para una banda de fluorescencia de referencia a unas condiciones atmosféricas determinadas, la intensidad relativa del especto de fluorescencia con respecto a esta banda de referencia, el valor de P' en aire seco para la temperatura de referencia y la dependencia de esta magnitud con la temperatura y la humedad, que puede ser obtenida a partir de los parámetros α y P'_w, respectivamente.

No existe un consenso en el campo de los UHECRs sobre el conjunto de parámetros a utilizar para describir Y. El Observatorio Pierre Auger ha actualizado recientemente su descripción del rendimiento de fluorescencia con las últimas medidas realizadas por la colaboración AIRFLY, que incluyen por vez primera las dependencias con la humedad y temperatura de P' . Telescope Array, por su parte, utiliza una combinación de las medidas realizadas por la colaboración FLASH para la medida de las intensidades relativas del espectro y las realizadas por Kakimoto *et al.* para el resto de parámetros. Esta descripción de Y desprecia la dependencia de P' con la temperatura y la humedad. La eficiencia óptica de los telescopios, y su dependencia con la longitud de onda, puede modificar el espectro aparente de fluorescencia, y debe ser tenida en cuenta a la hora de analizar las diferencias entre distintos experimentos. En la Fig. 4.3 puede verse una comparación del Y en aire seco a 1013 hPa y 293 K y la eficiencia óptica de los telescopios de ambas colaboraciones junto a los de HiRes.

Para analizar el efecto de la elección de una descripción de Y se han desarrollado dos métodos distintos. El primero es un método analítico sencillo, basado en la parametrización

del perfil longitudinal de energía depositada en la atmósfera propuesta por Gaisser y Hillas. Si se asume que toda la energía del rayo cósmico incidente se deposita en la atmósfera, al modificar la curva de Gaisser-Hillas obtenida por el experimento 1 por el cociente de los Y a cada altura, la curva modificada será la que habría obtenido el experimento 2 (Eqs. (4.12) a (4.16)). El segundo método utiliza el software de reconstrucción $\overline{\text{Off}}\underline{\text{line}}$ que utiliza la colaboración Auger. Los datos reales obtenidos por el Observatorio Auger se reconstruyen con los distintos rendimientos de fluorescencia y se comparan los valores reconstruidos de la energía E y profundidad a la que la cascada atmosférica alcanza su desarrollo máximo, $X_{\max}$. Para ello, se ha desarrollado un módulo para $\overline{\text{Off}}\underline{\text{line}}$ que calcula el rendimiento de fluorescencia a distintas profundidades atmosféricas a partir de los perfiles atmosféricos que registran los instrumentos de monitorización del Observatorio. Este módulo se emplea hoy en la cadena de reconstrucción oficial del Observatorio.

Como ejemplo, se han mostrado las diferencias en los valores reconstruidos de E y $X_{\max}$ cuando se varía el valor absoluto de la banda de fluorescencia de 337 nm, Y_{337}, usada como referencia por la colaboración Auger. Además, ambos métodos han sido extendidos para evaluar el impacto de la respuesta óptica de los telescopios, y su validez ha sido comprobada mediante simulaciones Monte Carlo. El impacto de estas respuestas ha quedado de manifiesto al comparar la parametrización de Y de TA y HiRes, que utiliza un valor absoluto muy similar pero un espectro diferente, produciéndose variaciones de energía aparentes no achacables únicamente a Y.

B.4 Impacto de las dependencias atmosféricas del rendimiento de fluorescencia

Los métodos descritos en el apartado anterior han sido empleados para evaluar el efecto de las dependencias atmosféricas de Y en la reconstrucción de cascadas atmosféricas. Debido a la forma del perfil atmosférico, los efectos relacionados con el parámetro P'_w serán más importantes cerca del suelo, donde la humedad es mayor. La temperatura, en cambio, influye más en capas superiores de la atmósfera.

Estos efectos se aprecian en las cascadas reconstruidas. Las verticales, que tienen un $X_{\max}$ más profundo, esto es, alcanzan su punto de máximo desarrollo cerca del suelo, muestran variaciones en E y $X_{\max}$ mayores cuando se tienen en cuenta solo las variaciones en Y debidas a la humedad. Lo opuesto es cierto para las inclinadas. Al depositar la mayor parte de su energía en capas más altas de la atmósfera la reconstrucción apenas varía al despreciar P'_w, pero son mucho más sensibles al parámetro α.

Esta dependencia geométrica queda bastante compensada cuando se evalúa el efecto conjunto de ambos parámetros. Tanto el método analítico como la reconstrucción de datos reales muestran que las energías reconstruidas son un 5% superiores en media a las obtenidas al despreciar P'_w y α. El efecto en $X_{\max}$ es bastante inferior, del orden de unos pocos gcm^2, aunque en este caso las dependencias con la geometría o la estación del año deben ser tenidas en cuenta.

Asimismo, cabe destacar que las predicciones del método analítico tienen un acuerdo más que razonable con los datos reales, aunque sobreestiman ligeramente la variación de la energía al no tener en cuenta la producción de luz por efecto Cherenkov.

B.5 La nueva escala de energía del Observatorio Pierre Auger

El rendimiento de fluorescencia es el paramétro más importante a la hora de determinar la energía de una cascada atmosférica detectada por el método de fluorescencia. En el caso del Observatorio Pierre Auger la energía del FD se utiliza también para calibrar el SD. Para ello, se realiza una comparación entre las energías detectadas por el FD y la señal asociada en el SD. Esta curva de calibración servirá después para obtener la energía de los eventos que solo son detectados por el SD.

Es por ello que el valor de la incertidumbre de Y resulta tan importante para el error sistemático en la energía del Observatorio Auger. En este trabajo se ha realizado un estudio exhaustivo de los errores de Y, tanto en el valor absoluto de la banda de 337 nm como de las dependencias atmosféricas o la incertidumbre en la determinación del espectro. Esto, junto a esfuerzos similares en otros puntos de la cadena de reconstrucción realizados dentro del grupo de Reconstrucción Híbrida de la colaboración Auger ha servido para actualizar tanto el valor de la escala de energía de la colaboración como la estimación de las incertidumbres sistemáticas.

El resultado final indica que la energía debe ser aumentada en torno a un 15%, de acuerdo a los estudios realizados, al tiempo que reduce el valor de la incertidumbre del 22% al 14%. Este valor presenta una pequeña dependencia con la energía, creciendo ligeramente a medida que ésta aumenta.

B.6 El efecto de la elección del rendimiento de fluorescencia en Telescope Array y Auger

A pesar de la actualización de la escala de energía del Observatorio Auger, la diferencia con TA sigue siendo bastante elevada, y cifrada en torno a un 15$. Como se ha explicado anteriormente, ambos experimentos utilizan parametrizaciones distintas de Y. En esta tesis se ha realizado un estudio detallado para evaluar la importancia de la elección de Y en las esta diferencia. Es importante destacar que, a pesar de que existe una diferencia de casi el 30% en los valores de Y_{337}, cuando se tienen en cuenta el resto de ingredientes del rendimiento de fluorescencia la diferencia total se reduce.

Cuando los valores de Y empleados por TA se sustituyen en la reconstrucción de Auger se obtiene una variación del 12% en la energía. Esta variación depende mucho de la distancia cascada-telescopio, ya que la luz registrada por los telescopios se ve afectada por la dispersión Rayleigh. A mayor distancia, mayor dispersión y, consecuentemente, menor diferencia en la energía.

Una diferencia notoria entre TA y Auger es la eficiencia óptica de los telescopios. El filtro empleado por TA es más ancho, y permite la entrada de luz de fluorescencia en bandas del espectro que son completamente suprimidas por el filto de Auger. Empleando para ello los métodos desarrollados en el capítulo 4 se ha evaluado que la diferencia entre Auger y TA debida a la elección de Y es de un 14% en media, reduciéndose con la distancia por los motivos explicados anteriormente. Al comparar los resultados con un análisis similar realizado por TA se han observado diferencias del orden del 1% con las presentadas en este trabajo, un acuerdo casi perfecto. El resultado de esta comparación se muestra en la Fig. 7.14.

Un análisis similar se ha realizado para la variación en $X_{\max}$, obteniendo una variación de 4 gcm^{-2}. Como complemento, se ha estudiado el efecto de esta variación en la curva de elongación, uno de los observables más utilizados para la determinación de la composición en masa de los rayos cósmicos. Los resultados muestran que la elección de Y no tiene efectos apreciables, aunque es necesario hacer estudios más detallados para evaluar el impacto por completo.

B.7 Conclusiones

En este trabajo se ha realizado un análisis pormenorizado del efecto de la elección del rendimiento de fluorescencia en los parámetros reconstruidos por el Observatorio Pierre Auger. Para ello se ha desarrollado un sencillo método analítico. Este procedimiento

ofrece buenos resultados cualitativos y cuantitativos cuando se comparan con los obtenidos mediante un método más preciso basado en un algoritmo de reconstrucción como el software $\overline{\text{Off}}\underline{\text{line}}$ empleado por la colaboración Auger. Con el objetivo de obtener un resultado que pueda ser comparado con las predicciones teóricas se ha desarollado un módulo para $\overline{\text{Off}}\underline{\text{line}}$ permita calcular con facilidad Y de acuerdo a las distintas medidas. Este módulo forma parte hoy de la cadena de reconstrucción oficial de Auger. Ambos métodos han sido ampliados para tener en cuenta el efecto de la eficiencia óptica cuando se comparan distintos experimentos. El procedimiento se ha probado mediante simulaciones Monte Carlo y ha sido aplicado para estudiar las escalas de energía relativas de Auger y TA.

Ambos métodos, analítico y reconstrucción de datos reales, se han empleado para estudiar el efecto de la dependencia con la temperatura y la humedad del rendimiento de fluorescencia en la energía y profundidad del máximo de la cascada. El vapor de agua es relevante cerca del suelo y, por tanto, afecta principalmente a las cascadas verticales que se desarrollan en las capas más profundas de la atmósfera y depositan su energía a baja altitud. Los efectos de temperatura, por el contrario, son más importantes en capas superiores, donde las cascadas inclinadas tienen su máximo. Cuando ambas dependencias se combinan, el efecto que producen es un incremento en la energía de la cascada de en torno al 5%, mientras que el máximo varía solo unos pocos gcm^{-2}.

El rendimiento de fluorescencia era la principal fuente de error en la escala de energía del Observatorio Pierre Auger. La tarea de Reconstrucción Híbrida de la Colaboración Auger ha realizado un esfuerzo conjunto para reducir al máximo esta incertidumbre. Para ello las medidas más recientes de Y realizadas por la colaboración AIRFLY, que incluyen las dependencias atmosféricas y el valor absoluto para la banda de 337 nm, se han incorporado a la reconstrucción y las nuevas incertidumbres relacionadas han sido evaluadas. Como resultado de éstas y otras actualizaciones en diferentes aspectos de la reconstrucción de cascadas, la escala de energía del experimento ha sido aumentado un 15% al tiempo que las incertidumbres han sido reducidas del 22% al 15%, lo que ha producido una mejora significativa en la precisión del espectro de energía de los UHECRs.

La comparación de los espectros de energía de Auger y TA sugiere sugiere que las discrepancias entre ambos experimentos pueden estar relacionadas con la escala de energía. Anlisis independientes realizados por Auger (presentados en esta tesis) y TA indican que la elección de distintos rendimientos de fluorescencia puede dar cuenta de una fracción muy importante de estas diferencias. El efecto combinado de Y en la energía primaria y la profundidad del máximo de la cascada tiene un efecto marginal en la curva de elongación de ambos experimentos.

Appendix C

Summary

The Pierre Auger Observatory, with a total area of 3000 km^2 is currently the largest cosmic ray detector made by mankind and it has been taking data since 2004. Located in Malargüe (Argentina) it covers the southern hemisphere sky using a hybrid technique. The Surface Detector (SD), composed of around 1600 water Cherenkov tanks, samples the particles of the EAS that arrive to ground level. The Fluorescence Detector (FD) registers the fluorescence light produced by the atmospheric nitrogen molecules that are excited by the cascade particles.

The SD is calibrated using the calorimetric measurements provided by the FD. A correct determination of the energy deposition via the fluorescence light is of the uttermost importance, as all the analyses performed at the Pierre Auger Observatory rely on the energy estimation provided by the FD. The fluorescence yield (FY) is the parameter that gives the conversion factor between the energy deposition and the number of fluorescence photons produced in the atmosphere. An international combined effort in the past few years has improved the knowledge on the absolute value and the dependences of this parameter, which has been the main source of uncertainty in the primary energy determination of the Pierre Auger Observatory. It is believed that the FY selection is also one of the main source of discrepancies between the UHECR spectrum measured by the Pierre Auger Observatory and the one measured by Telescope Array (located in Utah, USA), the other UHECRs observatory operated presently.

In this work the impact of the FY data used for shower reconstruction has been studied, in particular its effect on the primary energy and the shower maximum depth. To this end, an analytical procedure has been developed and real data of the Auger Observatory has been analyzed using dedicated algorithms.

C.1 Ultra-High Energy Cosmic Rays

More than 100 years after their discovery, there are still open questions regarding the origin, acceleration mechanism and mass composition of cosmic rays, specially for the ones with the most extreme energies, above 10^{18} eV, the so-called Ultra-High Energy Cosmic Rays (UHECRs). These particles are believed to be of extra-galactic origin, and their flux is so low that approximately one cosmic ray of these macroscopic energies reaches the atmosphere of the Earth per square kilometer and year. This extremely low flux makes necessary the construction of very extense detectors in order to collect a sample big enough to study the many interrogants still open about their nature.

When one of these UHECRs impinges the atmosphere it interacts with an atmospheric nucleus, producing secondary particles and initiating a cascade of interactions that propagate along the atmosphere until they decay or reach the ground. The result of this process is what is known as an Extensive Air Shower (EAS) and its features are related to the properties of the incident UHECR.

There are two main techniques for UHECR detection: surface arrays and fluorescence telescopes. Surface arrays sample the density distribution of the particles of the EAS that reach the ground. From this distribution, parameters such as arrival direction of the incident cosmic ray or its primary energy can be inferred. Fluorescence detectors record the fluorescence light produced by the atmospheric N_2 molecules excited by the shower particles. The longitudinal energy deposition profile can be obtained through the fluorescence yield parameter, Y, defined as the number photons per unit deposit energy.

After the discovery of the Cosmic Microwave Background in 1966, Greisen and Zatsepin and Kuz'min postulated independiently the existence of an end of the cosmic ray flux. UHECRs with energies over $5 \cdot 10^{19}$ eV would interact with this radiation, losing part of their energy. This supression is called the CZK cut-off in their honor. Experimental measurements by the HiRes collaboration, confirmed later by the Pierre Auger Observatory and Telescope Array, have proved the existence of the GZK supression at these energies.

The GZK cut-off also imposes a restriction in the maximum distance traveled by an UHECR prior to be detected on Earth. This limit can be potentially used to link the arrival directions of the UHECR with their source, as the interstellar magnetic fields are not expected to heavily distort the trajectory of the particle. The Pierre Auger Collaboration has reported a degree of correlation between arrival directions of UHECRs and Active Galacti Nuclei, although the significance if this result seems to be reducing with time. Telescope Array have reported an even weak correlation than Auger.

Another open question concerns the mass composition of UHECRs. The Pierre Auger

Collaboration has reported a trend towards heavy nuclei with energy, while TA results suggests a mainly protonic composition.

The last difference between both collaborations concerns the spectrum. Although the reported spectra seems to be very different, if the energy is re-scaled by a given factor, the spectra become perfectly compatible within the uncertainties. This suggests that the problem is basically related to the energy scale of the different experiments.

C.2 The Pierre Auger Observatory

The Pierre Auger Observatory, located near the town of Malargüe in the province of Mendoza (Argentina) is the largest facility in the world dedicated to the study of UHECRs. It is a hybrid experiment that uses two different and well established techniques to detect cosmic rays: an array of water Cherenkov tanks, the so-called Surface Detector (SD), combined with fluorescence telescopes, the so-called Fluorescence Detector (FD).

The SD is composed of 1600 water tanks, disposed in an hexagonal grid and separated 1500 m each, and covers about 3500 km^2. The SD is overlooked by 27 fluorescence telescopes deployed in 4 different sites. The SD samples the tail of the EAS at the ground from the Cherenkov light produced when the shower particles cross the water tanks, while the FD registers the fluorescence light emitted by the de-excitation of atmospheric nitrogen. This hybrid technique allows to compensate the individual disadvantages of both detectors. The FD reconstruct the full longitudinal profile of the shower, providing a calorimetric measure of the cosmic ray energy. The small FD duty cycle ($\approx$ 10% considering moonless nights) is compensated by the high statistics of the SD data (100% duty cycle). The shower size at ground measured by the SD is converted into cosmic ray energy using the FD measurements and then avoiding the use of simulations. This allows a significant reduction of the systematic uncertainties because the simulations include the extrapolation of hadronic interaction models well beyond the accelerator energies.

In addition to the FD and SD other instruments are installed to expand the energy spectrum to lower energies as well as to explore new detection techniques. AMIGA is intended to extend the efficiency of the SD to lower energies to about 10^{17} eV with a better mass discrimination. It is composed of an infill array of 61 water Cherenkov tanks separated 750 m with muon counters buried beneath them. The FD low-energy extension, called HEAT, is composed of 3 fluorescence telescopes titled 30^o to detect EAS that develop higher in the atmosphere. AERA is an array of radio antennas who aims to detect the geosynchroton emission of radio waves from EAS in a frequency range from 30 to 80 MHz. AMBER, EASIER and MIDAS are prototypes developed to measure the so-called

molecular bremsstrahlung emission in the GHz band.

As the atmosphere affects the fluorescence emission, a good knowledge of its properties is needed to ensure a reliable reconstruction of the shower. To do so a series of atmospheric monitoring stations are installed across the observatory. Four LIDAR stations located near the FD sites detect clouds and aerosols analyzing the backscatter of light from laser pulses. Two additional laser facilities, the CLF (Central Laser Facility) and XLF (Extreme Laser Facility) are installed in the middle of the array. They shoot UV laser tracks that are recorded by the FD and used to estimate the aerosol distribution of the atmosphere at different heights. A program of balloon measurements was used to obtain precise measurements of the atmosphere above the Observatory This has been substituted by the station of Global Data Assimilation System (GDAS) of the Global Forecast System located near the array.

An schematic layout of the Observatory is presented in Fig. 3.1.

C.3 Effect of the Fluorescence Yield on the air-shower reconstruction

Charged particles of the air shower, mainly electrons/positrons, produce fluorescence radiation that is detected by ground based telescopes. Using this technique, fluorescence telescopes register the longitudinal development of the EM component of the shower providing two relevant parameters. The first one is the total energy deposition, that is a calorimetric measure of the shower energy. The primary energy of the cosmic ray can be evaluated adding the invisible energy (nearly model independent). In addition, the atmospheric depth at which the shower reaches its maximum, $X_{\max}$, is directly measured by this techniqueand as is well known, for a given energy, this parameter is related with the mass of the primary cosmic ray.

In this technique the key parameter is the so called air-fluorescence yield, FY, that is, the number of fluorescence photons produced per unit of energy deposited in the atmosphere. Actually, the fluorescence yield is characterized by a number of parameters: the absolute value at certain reference conditions, the relative intensities of the molecular bands of the air-fluorescence spectrum and and the various parameters determining the atmospheric dependences. They have been measured in dedicated laboratory experiments and available measurements show non-negligible disagreements. Since the shower reconstruction is very sensitive to these parameters, a change in the FY assumption might have implications in the results, in particular the energy spectrum and mass composition of

cosmic rays.

To analyze the effect of the FY selection two different methods have been developed. The first one is a simple analytical method, based on the Gaisser-Hillas parameterization of the longitudinal profile of EASs. Assuming that the primary energy of the primary is deposited in the atmosphere, the G-H profile obtained with a given FY dataset is modified using the FY ratio at each slant depth. The modified curve by this procedure would be the one obtained using the FY dataset that we want to compare. The second method employs dedicated software tools, the $\overline{\text{Off}}\underline{\text{line}}$ framework used in the official Auger reconstruction. Real data obtained by the Pierre Auger Observatory are reconstructed twice using different FY datasets in order to study the differences between shower parameters. To do so, a module of the $\overline{\text{Off}}\underline{\text{line}}$ software that calculates the total FY at given atmospheric conditions has been developed. This module is presently used by the Auger Collaboration in its official reconstruction. As an example, the differences in the reconstructed values of E y $X_{\max}$ when the absolute value of the 337 nm band employed by the Auger Collaboration is changed are presented.

The importance of the optical efficiencies of the fluorescence telescopes employed by different experiments is shown when HiRes and TA FY datasets are compared. The different fluorescence spectra employed by these collaborations produces a non-negligible impact in the reconstructed energy, even when they both use a very similar absolute yield value. Both methods have been extended to take this into account. This extension has been validated using Monte Carlo simulations.

C.4 Impact of the atmospheric dependences of the Fluorescence Yield

Ground-based UHECR experiments that employ the fluorescence technique use the atmosphere as a giant calorimeter. This means that an accurate description of the atmosphere and its properties is mandatory to reduce the systematic uncertainties.As the atmosphere is itself part of the experimental set-up, a complete knowledge of its properti s is crucial to correctly reconstruct the EASs. The fluorescence technique is specially sensitive to atmospheric conditions as the FY is strongly dependent on atmospheric properties, specially pressure, temperature and humidity.

While the pressure dependence of the FY has been known and studied for decades, a comprehensive knowledge and experimental measurements for the humidity and temperature dependences were not available until recently. The recent results measured by the

AIRFLY Collaboration have been implemented in the fluorescence yield dataset employed by the Pierre Auger Collaboration. This is the first time a fluorescence detector has taken into account these dependences.

In this work the impact of these dependences on the shower parameters reconstructed by Auger has been evaluated using the method explained above. Vertical showers that develop deeper in the atmosphere are more affected by humidity variations, while inclined showers that deposit the bulk of their energy in upper atmospheric layers are more sensitive to temperature effects.

This geometrical dependence is compensated when both effects are studied simultaneously. Both the analytical and the real data methods show a 5% shift in the energy when the previously neglected dependences are taking into account, irrespectively of angle. The variation on $X_{\max}$ is at the level of few gcm^{-}2.

C.5 The new energy scale of the Pierre Auger Observatory

The SD energy of the Pierre Auger Observatory is obtained using comparing SD signals in hybrid-detected events with their associated FD energy. The energy of the events detected only by the SD can be obtained using this calibration curve. That means that the Fluorescence Yield is a key parameter not only in the FD reconstruction, but in the whole energy determination of the Pierre Auger Observatory.

The FY had been the main source of uncertainties of the Pierre Auger Observatory. In this work, an exahustive study of these uncertainties, both in the absolute value of the 337 nm band and in the atmospheric dependences, have been presented. This effort has been combined with similar studies performed within the Hybrid Reconstruction task of the Pierre Auger Observatory to update the energy scale of the Pierre Auger Observatory and reduce the value of the systematic uncertainties.

The total shift in the energy scale has been evaluated at around 15%. Systematic uncertainties have been reduced to 14% from the previous 22%, with a slight dependence with the energy.

C.6 The impact of the FY selection on TA and Auger

Even with this actualization in the energy scale of the Auger Observatory, the differences in the energy scale with TA are still very important. In this thesis a detailed study of the impact of the FY selection in the energy scale difference between both experiments have been performed. FY is supposed to be one of the main source of discrepancies, as there

is a difference in the absolute value of the 337 nm band of about 30%, although the other FY parameters compensated somewhat this huge discrepancy.

When the FY values employed by TA are introduced in the Auger reconstruction, a variation of 12% in energy is obtained. This variation heavily depends on the distance shower-telescope, due to Rayleigh scattering attenuation. The bigger the distance, the more attenuated the light and, consequently, the smaller the differences in E.

The optical efficiencies of the Auger and TA telescopes are very different. The Auger optical filter is narrower than the TA one, and bands that are completely supressed in the Auger filter can be relevant in the TA telescopes. Employing the extended methods described in chapter 4, the difference taking into account the optical efficiency has been evaluated at around 14%, with the same telescope-shower distance dependence explained above. A similar study performed by the TA collaboration shows a difference at the level of 1% with those shown in this work. The result of this comparison can be seen in Fig. 7.14.

A similar study on the $X_{\max}$ parameter has been performed, obtaining a slight variation of 4 gcm^{-2}. This variation has been introduced in the elongation curve, an FD observable employed to obtain the mass composition of UHECRs. Results shown that the FY selection has a marginal impact in the elongation rate, although more detailed studies are needed for a complete evaluation of this effect.

C.7 Conclusions

In this work, a comprehensive analysis of the impact of the fluorescence yield selection in the shower reconstruction parameters of the Pierre Auger Observatory has been carried out. To do so, an analytical method that offers good qualitative and quantitative results compared with a more accurate procedure based on a dedicated reconstruction algorithm i.e. the $\overline{\text{Off}}\underline{\text{line}}$ software employed by the Pierre Auger Collaboration has been developed. In addition, a module for the $\overline{\text{Off}}\underline{\text{line}}$ framework has been developed to study the impact of the fluorescence yield on real data reconstruction. This module is presently used in the official reconstruction of the Pierre Auger Collaboration. The analytical method has been extended to account for the effect of the optical efficiency when different experiments are compared. This procedure has been tested with Monte Carlo simulations and applied to study the relative energy scales of the Auger and TA experiments.

Both methods, analytical and real data reconstruction, have been used to study the effect of temperature and humidity dependence of the FY on the primary energy and shower maximum depth. Water vapor is relevant near the ground, and thus affects mainly vertical showers that develop deeper in the atmosphere and deposit the bulk of their energy

close to the ground. Temperature effects, on the other hand, are more important on upper layers, where inclined showers have their maxima. When both temperature and humidity dependences are taken into account their combined effect increases the energy of the shower by around 5%. The impact in the shower maximum is a few gcm^{-2}.

The FY had been the main source of uncertainties in the energy scale of the Pierre Auger Observatory. As a part of the Hybrid Reconstruction task of the Pierre Auger Collaboration, a combined work has been done to reduce these uncertainties. To do so, recent measurements of the FY, including the atmospheric dependences and the absolute value for the 337 nm band, have been introduced in the reconstruction and the new uncertainties in the energy scale have been evaluated. As a result of these and other updates in different aspects of the shower reconstruction, the energy scale of the Auger experiment has increased in about 15% while the uncertainty has decreased from 22% to 15% leading to a significant improvement in the accuracy of the spectrum.

The comparison of the energy spectra of TA and Auger suggests discrepances in the corresponding energy scales. Independent analyses carried out by Auger (presented here) and TA indicate that the different yields assumed by both experiments might account for a significant fraction of the discrepancy in the energy scale. Finally the combined effect of the FY on primary energy and shower maximum depth has a marginal effect on the comparison of elongation rate curves of both experiments.

Bibliography

[1] B. Falkenburg and W. Rhode. "From Ultra Rays to Astroparticles: A Historical Introduction to Astroparticle Physics". *SpringerLink*, 2012.

[2] D. Heck. "The Influence of Hadronic Interaction Models on Simulated Air-Showers: A Phenomenological Comparison". *talk presented at the VIHKOS CORSIKA School, Lauterbad, Germany*, 2005.

[3] R. Battiston *et al.*. "Cosmic ray physics from low to extreme energies: Status and perspectives". *Advances in Space Research*, (37):1834–1840, 2006.

[4] R. Engel J. Blümer and J. R. Hörandel. "Cosmic Rays from the Knee to the Highest Energies". *Progress in Particle and Nuclear Physics*, (63):293–338, 2009.

[5] J. Kirby and S. Lee. Fantastic four # 1. *Marvel Comics Publishing*.

[6] W. D. Apel *et al.*. "KASCADE-Grande measurements of energy spectra for elemental groups of cosmic rays". *Astroparticle Physics*, (47):54–66, 2013.

[7] A. M. Hillas. "The Origin of Ultra-High-Energy Cosmic Rays". *Annual Review of Astronomy and Astrophysics*, (22):425–444, 1984.

[8] A. Schulz [The Pierre Auger Collaboration]. "The measurement of the energy spectrum above 3×10^{17} ev with the Pierre Auger Observatory". *EPJ Web of Conferences*, (53), 2013.

[9] T. Abu-Zayyad *et al.*. "Energy Spectrum of Ultra-High-Energy Cosmic Rays Observed with the Telescope Array Using Hybrid Technique". *Astroparticle Physics*, (In press):arxiv:1305.7273 [astro–ph.HE], 2013.

[10] V. de Souza for the Pierre Auger Collaboration. "An update on the measurements of the depth of shower maximum made at the Pierre Auger Observatory". *Procedings*

33rd International Cosmic Ray Conference, Rio de Janeiro, Brazil, (arXiv:1307.5059 [astro-ph.HE]), 2013.

[11] M. Unger for the Pierre Auger Collaboration. "Mass sensitive observables of the Pierre Auger Observatory". *EPJ Web of Conferences*, (53):04009, 2013.

[12] D. García-Gámez for the Pierre Auger Collaboration. "Observations of the longitudinal development of extensive air showers with the surface detectors of the Pierre Auger Observatory". *Procedings 33rd International Cosmic Ray Conference, Rio de Janeiro, Brazil*, (arXiv:1307.5059 [astro-ph.HE]), 2013.

[13] Y. Tameda for the Telescope Array Collaboration. "Mass composition of UHECRs Measures Stereoscopically by the Telescope Array Fluorescence Detectors". *Procedings 33rd International Cosmic Ray Conference, Rio de Janeiro, Brazil*, 2013.

[14] Telescope Array E. Barcikowski *et al.*for the HiRes, Pierre Auger and Yakutsk Collaborations. "Mass composition working group report". *EPJ Web of Conferences*, (53):01006, 2013.

[15] J. Alvarez-Mu niz, M. Risse for the Pierre Auger Collaboration, G. I. Rubtsov, and B. T. Stokes for the Telescope Array Collaboration. "Review of the Multimessenger Working Group at UHECR 2012". *EPJ Web of Conferences*, (53):01009, 2013.

[16] X. Bertou *et al.*. "Calibration of the surface array of the Pierre Auger Observatory". *Nuclear Instrument and Methods in Physics Research A*, (568):839–846, 2006.

[17] J. Abraham *et al.*. [The Pierre Auger Collaboration]. "Trigger and aperture of the surface detector array of the Pierre Auger Observatory". *Nuclear Instrument and Methods in Physics Research A*, (613):29–39, 2010.

[18] D. Veberic and M. Roth. "Offline reference manual: SD Reconstruction". *Auger Technical Note*, (GAP 2005-035), 2005.

[19] D. Newton, J. Knapp, and A. A. Watson. *Astroparticle Physics*, (26):414, 2007.

[20] J. Abraham *et al.*. [The Pierre Auger Collaboration]. "The fluorescence detector of the Pierre Auger Observatory". *Nuclear Instrument and Methods in Physics Research A*, (620):227–251, 2010.

[21] A. Rovero *et al.*. [The Pierre Auger Collaboration]. "Multi-wavelength calibration procedure for thePierre Auger Observatory Fluorescence Detectors ". *Astroparticle Physics*, (31):305–311, 2009.

[22] D. Kuempel, K.-H. Kampert, and M. Risse. "Gemoetry reconstruction of fluorescence detectors revisited". *Astroparticle Physics*, (30):167–174, 2008.

[23] C. Meurer and Scharf [The Pierre Auger Collaboration] N. "HEAT, a low energy enhancement of the Pierre Auger Observatory". *Astrophysics and Space Science Transactions*, (7):183–186, 2011.

[24] F. G. Schröder [The Pierre Auger Collaboration]. "Radio detection of air showers with the Auger Engineering Radio Array". *Procedings 33rd International Cosmic Ray Conference, Rio de Janeiro, Brazil*, pages arXiv:1307.5059 [astro–ph.HE], 2013.

[25] R. Gaïor [The Pierre Auger Collaboration]. "Radio detection of air showers with the Auger Engineering Radio Array". *Procedings 33rd International Cosmic Ray Conference, Rio de Janeiro, Brazil*, pages arXiv:1307.5059 [astro–ph.HE], 2013.

[26] F. Arqueros, J. Hörandel, and B. Keilhauer. "Air fluorescence relevant for cosmic ray detection - Summary of the 5th fluorescence workshop, El Escorial 2007". *Nuclear Instrument and Methods in Physics Research A*, (597):1–22, 2008.

[27] M. Ave *et al.*. "Measurement of the pressure dependence of air fluorescence emission by electrons". *Astroparticle Physics*, (28):41–57, 2007.

[28] M. Unger *et al.*. "Reconstruction of longitudinal profiles of ultra-high energy cosmic ray showers from fluorescence and Cherenkov light measurements". *Nuclear Instrument and Methods in Physics Research A*, (588):433–441, 2008.

[29] B. R. Dawson *et al.*. "Proposal for an update of the Auger Energy Scale". *Auger Technical Note*, (GAP 2012-124), 2012.

[30] J. R. Vázquez, D. García-Pinto, M. Monasor, and F. Aqrqueros. "The effect of uncertainties in air-fluorescence quenching on the reconstructed shower parameters of ultra-high energy cosmic rays". *Procedings 32nd International Cosmic Ray Conference, Beijing, China*, (http://galprop.stanford.edu/elibrary/icrc/2011/papers/HE1.3/icrc0926.pdf), 2011.

[31] V. Verzi for the Pierre Auger Collaboration. "The Energy Scale of the Pierre Auger Observatory". *Procedings 33rd International Cosmic Ray Conference, Rio de Janeiro, Brazil*, (arXiv:1307.5059 [astro-ph.HE]), 2013.

[32] Telescope Array I. C. Maris *et al.*for the Pierre Auger and Yakutsk Collaborations. "The energy spectrum of ultra high energy cosmic rays". *Talk presented at the UHECR2014 celebrated in Springdale, Utah (USA), avaliable at http://uhecr2014.telescopearray.org/schedule.html*, 2014.

[33] T. Wulf. "Observations on the radiation of high penetration power on the Eiffel tower". *Physikalische Zeitschrift*, (11):811, 1910.

[34] D. Pacini. "Penetrating radiation at the surface of and in water". *Nuovo Cimento*, (VI/3):63, 1912.

[35] V. F. Hess. "Observation of Penetrating Radiation in Seven Balloon Flights.". *Physikalische Zeitschrift*, (13):1084–1091, 1912.

[36] W. Kolhörster. "Measurements of the penetrating radiation in a free balloon at high altitudes". *Physikalische Zeitschrift*, (14):1153, 1913.

[37] J. Clay. *Koninklijke Akademie van Wetenschappen te Amsterdam*, (30):633, 1927.

[38] T. H. Johnson. "The Azimuthal Asimmetry of the Cosmic Radiation". *Physical Review*, (43):834–835, 1933.

[39] L. Álvarez and A. H. Compton. "A Positively Charged Component of Cosmic Rays". *Physical Review*, (43):835–836, 1933.

[40] B. Rossi. "On the Magnetic Deflection of Cosmic Rays". *Physical Review*, (36):606, 1930.

[41] M. Schein, W. P Jesse, and E. O. Wollan. "The Nature of the Primary Cosmic Radation and the Origin of the Mesotron". *Physical Review*, (59):615, 1941.

[42] C. D. Anderson. "The Positive Electron". *Physical Review*, (43):491, 1933.

[43] P. A. M. Dirac. "Quantised Singularities in the Electromagnetic Field". *Proceedings of the Royal Society A*, (A133):60, 1931.

[44] S. Neddermeyer and C. D. Anderson. "Note on the Nature of Cosmic-Ray Particles". *Physical Review*, (51):884, 1937.

[45] J. C. Street and E. C. Stevenson. "New Evidence for the Existence of a Particle Intermediate Between the Proton and Electron". *Physical Review*, (52):1003, 1937.

[46] H. Yukawa. "on the interaction of elementary particles 1". *Proceedings of the Physico-Mathematical Society of Japan*, (17):139–148, 1935.

[47] C.M.G. Lattes, H. Muirhead, G.P.S. Occhialini, and C.F. Powell. "Processes involving charged mesons". *Nature*, (159):694–697, 1947.

[48] B. Rossi. "Directional Measurements on the Cosmic Rays Near the Geomagnetic Equator". *Physical Review*, (45):212, 1934.

[49] P. Auger, R. Maze, and T. Grivet-Mayer. "Extensive cosmic showers in the atmosphere containing ultra-penetrating particles". *Comptes rendus de l'Académie des Sciences*, (206):1721–1722, 1938.

[50] W. Kolhörster, I. Matthes, and E. Weber. "Coupled high-altitude rays". *Naturwissenschaften*, (26):576, 1938.

[51] J. Linsley. "Evidence for a Primary Cosmic-Ray Particle with Energy 10^{20} eV". *Physical Review Letters*, (10):146–148, 1963.

[52] M. M. Winn *et al.*. "The Cosmic Ray Energy Spectrum above 10^{17} eV". *Journal of Physics G*, (12):653–674, 1986.

[53] M. A. Lawrence, R. J. O. Reid, and A. A. Watson. "The Cosmic ray energy spectrum above $4 \cdot 10^{17}$ eV measured by the Haverah Park array". *Journal of Physics G*, (17):733–757, 1991.

[54] K. Suga. *Proceedings of the 5th Interamerican Seminar on Cosmic Rays, La Paz, Bolivia*, (XLIX/2), 1962.

[55] A. E. Chudakov. *Proceedings of the 5th Interamerican Seminar on Cosmic Rays, La Paz, Bolivia*, (XLIX/2), 1962.

[56] A. N. Bunner. "Cosmic ray detection by atmospheric fluorescence". *Ph. D. Thesis, Cornell University*, 1967.

[57] T. Hara *et al.*. "Detection of the atmospheric scintillation light from air showers". *Proceedings of the 11th International Conference on Cosmic Rays, Budapest, Hungary*, (3), 1969.

[58] R.M. Baltrusaitus *et al.*. "The Utah's Fly's Eye Detector". *Nuclear Instrument and Methods in Physics Research A*, (240):410, 1985.

[59] T. Abu-Zayyad *et al.*. "The prototype high-resolution Fly's Eye cosmic ray detector". *Nuclear Instrument and Methods in Physics Research A*, (450):253, 2000.

[60] Particle Data Group. "Review of Particle Physics". *European Physical Journal C*, (3):76, 1998.

[61] J. Matthews. "A Heitler model of extensive air showers". *Astroparticle Physics*, (22):387–397, 2005.

[62] T. K. Gaisser and A. M. Hillas. "". *Proceedings of the 15th International Cosmic Ray Conference, Plovdiv, Poland*, (8):353, 1977.

[63] D. Heck, G. Schatz, T. Thouw, J. Knapp, and J. N. Capdevielle. "CORSIKA: A Monte Carlo code to simulate extensive air showers". *FZKA-6019*, 1998.

[64] G. Z. Moliére. "Theorie der Streuung schneller geladener Teilchen I, Einzelstreuung am abgeschirmten Coulomb-Feld". *Zeitschrift für Naturforschung A*, (2):133, 1947.

[65] J. Matthews. "The Standard Atmosphere, $r_{moliere}$ and Ground Array Systematic Errors". *Auger Technical Note*, (GAP-1998-002), 1998.

[66] K. Kamata and J. Nishimura. *Progress of Theoretical Physics Supplement*, (6):53, 1956.

[67] K. Greisen. *Progress in Cosmic Rays Physics*, (3):60, 1956.

[68] L. O'C. Drury. "An introduction to the theory of the diffusive shock acceleration of energetic particles in tenous plasmas". *Reports on Progress in Physics*, (46):973–1027, 1983.

[69] E. Fermi. "on the origin of the cosmic radiation". *Physical Review*, (75):1169–1975, 1949.

[70] J. Hörandel. "Cosmic ray composition and its relation to shock acceleration by supernova remnants". *Advances in Space Research*, (41):442, 2008.

[71] P. Lagage and C. Cesarsky. "The maximum energy of cosmic ray accelerated by supernova shocks". *Astronomy and Astrophysics*, (125):249–257, 1983.

[72] L. G. Svenishkova. "the knee in the Galactic cosmic ray spectrum and variety in Supernovae". *Astronomy and Astrophysics*, (409):799–807, 2003.

[73] A. M. Hillas. "Can diffusive shock acceleration in supernova remnants account for high-energy cosmic rays?". *Journal of Physics G*, (31):R95–R131, 2005.

[74] J. R. Hörandel, N.N. Kalmykov, and A.V. Timokhin. "Propagation of super high-energy cosmic rays in the Galaxy". *Astroparticle Physics*, (27):119–126, 2007.

[75] V. Berezinsky, A. Z. Gazizov, and S. I. Grigorieva. "Dip in UHECR spectrum as signature of proton interaction with CMB". *Physical Letters B*, (612):147–153, 2005.

[76] K. Greisen. "End to the Cosmic-Ray Spectrum?". *Physical Review Letters*, (16):748–750, 1966.

[77] G. T. Zatsepin and V. Kuz'min. "Upper Limit of the Spectrum of Cosmic Rays". *Journal of Experimental and Theoretical Physics Letters*, (4):7880, 1966.

[78] A. A. Penzias and R. W. Wilson. "A Measurement Of Excess Antenna Temperature At 4080 Mc/s". *Astrophysical Journal Letters*, (142):419421, 1965.

[79] M. Nagano and A. A. Watson. "Observations and implications of the ultrahigh-energy cosmic rays". *Review of Modern Physics*, (72):689–732, 2000.

[80] J. Abraham *et al.*. "Measurement of the energy spectrum of cosmic rays above 10^{18} eV using the Pierre Auger Observatory". *Physics Letters B*, (685):271–280, 2010.

[81] R. U. Abbasi *et al.*. "Observation of the ankle and evidence for a high-energy break in the cosmic ray spectrum". *Physics Letters B*, (619):271–280, 2005.

[82] M. Takeda *et al.*. "Extension of the cosmic ray energy spectrum beyond the predicted Greisen-Zatsepin-Kuz'min cutoff". *Physical Review Letters*, (81):1163–1166, 1998.

[83] M. T. Dova *et al.*. "Time asymmetries in extensive air showers: A novel method to identify UHECR species". *Astroparticle Physics*, (31):312–319, 2009.

[84] R. A. Vázquez L. Cazón and E. Zas. "Depth development of extensive air showers from muon time distributions". *Astroparticle Physics*, (23):393–409, 2005.

[85] C. Baixeras for the MAGIC collaboration. "The MAGIC telescope". *uclear Physics B - Proceedings Supplements*, (114):247–252, 2003.

[86] G. Hermann. "The HESS array: a new system of 100 GeV IACTs for stereoscopic observations ". *Proceedings of the XXXII Rencontres de Moriond, Les Arcs, France*, 1997.

[87] F. Krennrich *et al.*. "VERITAS: the Very Energetic Radiation Imaging Telescope Array System". *New Astronomy Reviews*, (48):345–349, 2004.

[88] M. Actis *et al.*. "Design Concepts for the Cherenkov Telescope Array CTA, An Advanced Facility for Ground-Based High-Energy Gamma-Ray Astronomy". pages arXiv:1008.3703 [astro–ph.IM], 2010.

[89] M. G. Aartsen. *et al.*. "Evidence for High-Energy Extraterrestrial Neutrinos at the IceCube Detector". *Physical Review Letters*, (342):1242856, 2013.

[90] V. S. Berezinsky and A. Yu. Smirnov. "Cosmic neutrinos of ultra-high energies and detection possibility". *Astrophysics and Space Science*, (32):461–482, 1975.

[91] X. Bertou *et al.*. "Tau neutrinos in the Auger Observatory: a new window to UHECR sources". *Astroparticle Physics*, (17):183–193, 2002.

[92] P. W. Gorham *et al.*[ANITA Collaboration]. "Observational constraints on the ultrahigh energy cosmic neutrino flux from the second flight of the ANITA experiment ". *Physical Review D*, (82), 2010.

[93] A. Aab *et al.*. [The Pierre Auger Collaboration]. "A Targeted Search for Point Sources of EeV Neutrons". *Astrophysical Journal Letters*, (789):L64–L68.

[94] R. U. Abbasi *et al.*. "Analysis of large-scale anisotropy of ultra-high energy cosmic rays in HiRes data". *Astrophysical Journal Letters*, (713):L34–L41, 2010.

[95] M. Teshima for the AGASA collaboration. "The arrival direction distribution of extremely high energy cosmic rays observed by AGASA". *Procedings 28th International Cosmic Ray Conference, Tsukuba, Japan*, pages 437–440, 2003.

[96] H. B. Kim and J. Kim. "Update of Correlation Analysis between Active Galactic Nuclei and Ultra-High Energy Cosmic Rays". *International Journal of Modern Physics D*, (22):1350045, 2013.

[97] H. B. Kim and J. Kim. "Correlation Analysis of Ultra-High Energy Cosmic Rays with Active Galactic Nuclei". *AIP Conference Proceedings*, (1367):193–196, 2011.

[98] J. Abraham *et al.*. "Correlation of the Highest-Energy Cosmic Rays with Nearby Extragalactic Objects". *Science*, (318):938–943, 2007.

[99] P. Abreu *et al.*. "Update on the correlation of the highest energy cosmic rays with nearby extragalactic matter". *Astroparticle Physics*, (34):314–325, 2010.

[100] M.P. Véron-Cetty and P. Véron. "A catalogue of quasars and active nuclei: 12th edition". *Astronomy and Astrophysics*, (455):773–777, 2006.

[101] K. H. Kampert for the Pierre Auger Collaboration. "Highlights from the Pierre Auger Observatory". *Procedings 32nd International Cosmic Ray Conference, Beijing, China*, pages arXiv:1207.4823 [astro–ph.HE], 2011.

[102] T. Abu-Zayyad *et al.*. "Search for Anisotropy of Ultra-High Energy Cosmic Rays with the Telescope Array Experiment". *Astrophysical Journal*, (757):26, 2012.

[103] J. Goodman and J. Braun [HAWC Collaboration]. "The HAWC Observatory". *Procedings 32nd International Cosmic Ray Conference, Beijing, China*, 2011.

[104] M. Horvat and D. Veberic. "On shower-front Start time-variation". *Auger Technical Note*, (GAP 2007-057), 2007.

[105] A. M. Hillas. *Procedings 12th International Cosmic Ray Conference, Tasmania, Australia*, (3):1001, 1971.

[106] M. Ave, P. Bauleo, J. L. Harton, R. Knapik, A. Castellina, G. Navarra, and A. Chou [Pierre Auger Collaboration]. *Nuclear Instrument and Methods in Physics Research A*, (578):180, 2007.

[107] F. Arneodo, S. Maldera, and G. Navarra. "A procedure to derive the anode charges for saturated signals from the dynode and anode undershoots". *Auger Technical Note*, (GAP 2005-025), 2005.

[108] I. C. Maris, M. Roth, and T. Schmidt. "A Phenomenological Method to Recover the Signal from Saturated Stations'. *Auger Technical Note*, (GAP 2006-012), 2006.

[109] I. D. Mitri, S. Maglio, and D. Martello. "A method for SD traces saturation recovery'. *Auger Technical Note*, (GAP 2006-075), 2006.

[110] T. Abu-Zayyad *et al.*. "New air fluorescence detectors employed in the Telescope Array experiment ". *Nuclear Instrument and Methods in Physics Research A*, (676):54–65, 2012.

[111] Y. Takahashi [JEM-EUSO Collaboration]. "The JEM-EUSO Mission". *New Journal of Physics*, (11):065009, 2009.

[112] J. Bäuml *et al.*. [The Pierre Auger Collaboration]. "Measurement of the Optical Properties of the Auger Fluorescence Telescopes". *Procedings 33rd International Cosmic Ray Conference, Rio de Janeiro, Brazil*, (arXiv:1307.5059 [astro-ph.HE]), 2013.

[113] M. Tueros [The Pierre Auger Collaboration]. "Estimate of the non-calorimetric energy of showers observed with the fluorescence and surface detectors". *Procedings 33rd International Cosmic Ray Conference, Rio de Janeiro, Brazil*, (arXiv:1307.5059 [astro-ph.HE]), 2013.

[114] S. BenZvi *et al.*. "The Lidar system of the Pierre Auger Observatory". *Nuclear Instrument and Methods in Physics Research A*, (574):171–184, 2007.

[115] B. Fick *et al.*. "The Central Laser Facility at the Pierre Auger Observatory". *Journal of Instrumentation*, (1):P11003, 2006.

[116] P. Abreu *et al.*. [The Pierre Auger Collaboration]. "The rapid monitoring system of the Pierre Auger Observatory". *Journal of Instrumentation*, (7):P09001, 2012.

[117] P. Abreu *et al.*. [The Pierre Auger Collaboration]. "Description of atmospheric conditions at the Pierre Auger Observatory using the Global Data Assimilation System (GDAS)". *Astroparticle Physics*, (35):591–607, 2012.

[118] A. Etchegoyen [The Pierre Auger Collaboration]. "AMIGA, Auger Muon Infill Ground Array". *Procedings 30th International Cosmic Ray Conference, Merida, Mexico*, (arxiv:0710.1646 [astro-ph]), 2007.

[119] A. Schulz [The Pierre Auger Collaboration]. "The measurement of the energy spectrum above 3×10^{17} ev with the Pierre Auger Observatory". *Procedings 33rd International Cosmic Ray Conference, Rio de Janeiro, Brazil*, (arXiv:1307.5059 [astro-ph.HE]), 2013.

[120] J. Jelley *et al.*. "Radio pulses from Extensive Cosmic-Ray Air Showers". *Nature*, (205):327–328, 1965.

[121] P. W. Gorham *et al.*. "Observations of microwave continuum emission from air shower plasmas". *Physical Review D*, (78):032007, 2008.

[122] J. R. Vazquez *et al.*M. Monasor. " The impact of the air-fluorescence yield on the reconstructed shower parameters of ultra-high energy cosmic rays". *Astroparticle Physics*, (34):467–475, 2011.

[123] J. R. Vázquez, J. Rosado, D. García-Pinto, and F. Arqueros. "The effect of the fluorescence yield selection on the energy scales of Auger, HiRes and TA". *EPJ Web of Conferences*, (53):01008, 2013.

[124] Dennis L. Holtermann, Edward K. C. Lee, and Roger Nanes. "Rates of collisionin-duced electronic relaxation of single rotational levels of so_2 ($\tilde{A}^1$ A_2)". *Journal of Chemical Physics*, (77):5327, 1982.

[125] M. Ave *et al.*. "Temperature and humidity dependence of air fluorescence yield measured by AIRFLY". *Nuclear Instrument and Methods in Physics Research A*, (597):50–54, 2008.

[126] M. M. Fraga *et al.*. "Temperature-dependent quenching of UV fluorescence of N_2". *Nuclear Instrument and Methods in Physics Research A*, (597):75–82, 2008.

[127] T. Waldenmeier *et al.*. "Spectral resolved measurement of the nitrogen fluorescence emissions in air induced by electrons". *Astroparticle Physics*, (29):205–222, 2008.

[128] J. Rosado *et al.*. "Measurements of air fluorescence induced by low-energy electrons at low pressures". *Nuclear Instrument and Methods in Physics Research A*, (597):83–88, 2008.

[129] P. Colin *et al.*. " Measurement of air and nitrogen fluorescence light yields induced by electron beam for UHECR experiments". *Astroparticle Physics*, (27):317–325, 2007.

[130] F. Kakimoto *et al.*. "A measurement of the air fluorescence yield". *Nuclear Instrument and Methods in Physics Research A*, (372):527–533, 1996.

[131] B. Dawson. "Present and future implementations of the FY in the Auger Analysis". *Auger Technical Note*, (GAP 2002-067), 2002.

[132] M. Nagano *et al.*. "New measurement on photon yields from air and the application to the energy estimation of primary cosmic rays". *Astroparticle Physics*, (22):235–248, 2004.

[133] M. Ave *et al.*. "Precise measurement of the absolute fluorescence yield of the 337 nm band in atmospheric gases". *Astroparticle Physics*, (42):90–102, 2013.

[134] R. Abbasi *et al.*. "The FLASH thick-target experiment". *Nuclear Instrument and Methods in Physics Research A*, (597):37–40, 2008.

[135] L. Perrone, S. Petrera, and F. Salamida. "Gaisser-Hillas Profiles and FD Simulation ". *Auger Technical Note*, (GAP 2005-087), 2005.

[136] J. Abraham *et al.*. [The Pierre Auger Collaboration]. "A study of the effect of molecular and aerosol conditions in the atmosphere on air fluorescence measurements at the Pierre Auger Observatory". *Astroparticle Physics*, (33):108–129, 2010.

[137] S. Argiro *et al.*. "The offline software framework of the Pierre Auger Observatory". *Nuclear Instrument and Methods in Physics Research A*, (580):14851496, 2007.

[138] R. U. Abbasi *et al.*. "Monocular measurement of the spectrum of UHE cosmic rays by the FADC detector of the HiRes experiment". *Astroparticle Physics*, (23):157–174, 2005.

[139] Telescope Array B. Dawson *et al.*for the HiRes, Pierre Auger and Yakutsk Collaborations. "The energy spectrum of cosmic rays at the highest energies". *EPJ Web of Conferences*, (53):01005, 2013.

[140] F. Arqueros, J. Hörandel, and B. Keilhauer. "Air fluorescence relevant for cosmic-ray detection. Review of pioneering measurements". *Nuclear Instrument and Methods in Physics Research A*, (597):23–31, 2008.

[141] A. E. Grün and E. Schopper. "Die Fluoreszenz von Gasen beider Abbremsungschneller Teilchen ". *Zeitschrift fr Naturforschung A*, (9):55–64, 1954.

[142] D. C. Lillicrap. "Collision quenching effects in nitrogen and helium excited by a 30 keV electron beam". *NASA-TM-X-2842*, 1973.

[143] S. V. Pancheshnyi *et al.*. "Measurements of rate constants of the $N_2(c^3\pi_u, v' = 0)$ and $n2^+(b^2\sigma^+u, v = 0)$ deactivation by N_2, O_2, H_2, CO and H_2O molecules in afterglow of the nanosecond discharge". *Chemical Physics Letters*, (294):523–527, 1998.

[144] A. Morozov *et al.*. "Collisional population channels of the $C_3\pi_u$ state and their impact on the fluorescence analysis of extensive air showers". *Nuclear Instrument and Methods in Physics Research A*, (597):105–109, 2008.

[145] T. Waldenmeier *et al.*. "Measurement of the air fluorescence yield with the AIRLIGHT experiment". *Nuclear Instrument and Methods in Physics Research A*, (597):67–74, 2008.

[146] N. Sakaki *et al.*. " Fluorescence in air excited by electrons from a ^{90} Sr source". *Nuclear Instrument and Methods in Physics Research A*, (597):88–93, 2008.

[147] J. Hersil *et al.*. "Observations of Extensive Air Showers near the Maximum of Their Longitudinal Development". *Physical Review Letters*, (6):22–23, 1961.

[148] I. C. Maris *et al.*. "Energy calibration of the surface detector data: A maximum likelihood method.". *Auger Technical Note*, (GAP 2010-129), 2010.

[149] R. Pesce [The Pierre Auger Collaboration]. "Energy calibration of data recorded with the surface detectors of the Pierre Auger Observatory: an update". *Procedings 32nd International Cosmic Ray Conference, Beijing, China*, (arXiv:1107.4809 [astro-ph.HE]), 2011.

[150] J. Baeuml for the Pierre Auger Collaboration. "Measurements of the Optical Properties of the Auger Fluorescence Telescopes". *Procedings 33rd International Cosmic Ray Conference, Rio de Janeiro, Brazil*, (arXiv:1307.5059 [astro-ph.HE]), 2013.

[151] J. T. Brack *et al.*. "Absolute Calibration of a Large-diameter Light Source". *Journal of Instrumentation*, (8):P05014, 2013.

[152] P. Abreu *et al.*. "Techniques for Measuring Aerosols using the Central Laser Facility at the Pierre Auger Observatory". *Journal of Instrumentation*, (8):P04009, 2013.

[153] L. Valore for the Pierre Auger Collaboration. "Measuring Atmospheric Aerosol Attenuation at the Pierre Auger Observatory". *Procedings 33rd International Cosmic Ray Conference, Rio de Janeiro, Brazil*, (arXiv:1307.5059 [astro-ph.HE]), 2013.

[154] J. Abraham *et al.*. "A study of the effect of molecular and aerosol conditions in the atmosphere on air fluorescence measurements at the Pierre Auger Observatory". *Astroparticle Physics*, (33):108–129, 2010.

[155] D. Gora *et al.*. " Simulation of air shower image in fluorescence light based on energy deposits derived from CORSIKA". *Astroparticle Physics*, (22):29–45, 2004.

[156] M. Giller and G. Wieczorek. " Influence of the scattered Cherenkov light on the width of shower images as measured in the EAS fluorescence experiments". *Astroparticle Physics*, (31):212–219, 2009.

[157] J. D. Roberts. "The role of atmospheric multiple scattering in the transmission of fluorescence light from extensive air showers". *Journal of Physics G: Nuclear and Particle Physics*, (31):1291–1301, 2005.

[158] H.M.J. Barbosa, F. Catalani, J.A. Chinellato, and C. Dobrigkeit. " Determination of the calorimetric energy in extensive air showers". *Astroparticle Physics*, (22):159–166, 2004.

[159] I. Vali no [The Pierre Auger Collaboration]. "A measurement of the muon number in showers using inclined events recorded at the Pierre Auger Observatory". *Procedings 33rd International Cosmic Ray Conference, Rio de Janeiro, Brazil*, (arXiv:1307.5059 [astro-ph.HE]), 2013.

[160] C. Bonifazi [The Pierre Auger Collaboration]. "The monitoring system of the Pierre Auger Observatory: on-line and long-term data quality controls". *Procedings 33rd International Cosmic Ray Conference, Rio de Janeiro, Brazil*, (arXiv:1307.5059 [astro-ph.HE]), 2013.

[161] Telescope Array B. R. Dawson *et al.*for the Pierre Auger and Yakutsk Collaborations. "The energy spectrum of cosmic rays at the highest energies". *EPJ Web of Conferences*, (53):01005, 2013.

[162] Telescope Array O. Deligny *et al.*for the Pierre Auger and Yakutsk Collaborations. "Review of the anisotropy working group at UHECR-2012". *EPJ Web of Conferences*, (53):01008, 2013.

[163] The Pierre Auger and Telescope Array Collaborations. *Procedings 33rd International Cosmic Ray Conference, Beijing, China*, pages arXiv:1310.0647 [astro–ph.HE], 2013.

[164] The Pierre Auger and Telescope Array Collaborations. "Searches for Large-Scale Anisotropy in the Arrival Directions of Cosmic Rays above 10^{19} eV at the Pierre Auger Observatory and the Telescope Array". *The Astrophysical Journal*, (794):172–197, 2014.

[165] A. Bucholtz. "Rayleigh-scattering calculations for the terrestrial atmosphere". *Applied Optics*, (34):2765–2773, 1995.

[166] J. Abraham *et al.*. "Measurement of the Depth of Maximum of Extensive Air Showers above 10^{18} eV". *Physical Review Letters*, (104):091101, 2010.

[167] *http://physics.nist.gov/PhysRefData/Star/Text/ESTAR.html.*

[168] B. Keilhauer *et al.*. "Altitude dependence of fluorescence light emission by extensive air showers". *Nuclear Instrument and Methods in Physics Research A*, (597):99–104, 2008.